



PADERBORN UNIVERSITY
The University for the Information Society



ILH
INSTITUT FÜR
LEICHTBAU MIT
HYBRIDSYSTEMEN

***Molecular adhesion science and
engineering of nanostructured poly(acrylic
acid)/metal oxide interfaces***

Dissertation

submitted by

Mr. Dennis Meinderink, M. Sc.

born on 21.09.1991 in Nordhorn, Germany

in fulfilment of requirements for the degree of

Doctor of Science (Dr. rer. nat.)

at the University Paderborn

Faculty of Science

Department of Chemistry

at the chair of Prof. Dr.-Ing. Guido Grundmeier

Technical and Macromolecular Chemistry (TMC)

2017 - 2020

Examination board:

Chair:

1. examiner and 1. referee:

2. examiner and 2. referee:

3. examiner:

Prof. Dr. Sabine Fechner

Prof. Dr.-Ing. Guido Grundmeier

Prof. Dr. Wolfgang Bremser

PD Dr. Hans Egold

Submission of the thesis:

09.09.2020

Day of examination:

30.10.2020

Printed and published with the approval of the examination board.

Ich, Dennis Meinderink, geboren am 21.09.1991 in Nordhorn, bestätige hiermit eidesstattlich als Autor, dass die Ihnen vorliegende Dissertation „*Molecular adhesion science and engineering of nanostructured poly(acrylic acid)/metal oxide interfaces*“ unter der Betreuung von Herrn Professor Dr.-Ing. Guido Grundmeier von mir eigenständig angefertigt worden ist. Die verwendeten Quellen und Hilfsmittel sind an entsprechenden Stellen genannt, gekennzeichnet und vorschriftsgemäß zitiert. Ich bestätige zudem, dass diese Thesis keiner anderen Prüfungsbehörde in dieser oder ähnlicher Anfertigung vorliegt.

Dennis Meinderink

Paderborn, den 09.09.2020

abstract (English)

The precise knowledge of interfacial adhesion mechanisms of both macroscopic and molecular interactions occurring between (poly)electrolytes and metal oxide surfaces is paramount for several applications in research and industry such as the development of long-term stable coating materials, corrosion protection, and adhesion-promoting thin (hybrid) films employed in, for instance, lightweight constructions. Therefore, this cumulative dissertation analyzes the fundamental understanding of the adhesion mechanisms of macromolecular poly(acrylic acid) (PAA) to nanostructured zinc oxide (ZnO) films and stainless steel substrates as highly technical relevant composite materials.

A thorough understanding of the adhesion mechanisms of PAA at the molecular level can be gained by means of single molecule force spectroscopy (SMFS) on polished stainless steel as well as on electrochemically deposited ZnO nanostructures. Force-distance curves of PAA functionalized atomic force microscopy (AFM) cantilevers were recorded depending on the dwell time and the ZnO structure. The increased occurrence of high multiple rupture events in the case of ZnO nanorods compared to platelet-like ZnO films can be explained by high-energy multi- and bidentate coordinative bonds between the carboxylate groups and the more accessible zinc atoms located at the nonpolar sidewalls. Besides of that, the increase in the dwell time that the carboxylate groups present in PAA chains stay in the close vicinity of the ZnO interphase leads to an increase in the measured molecular adhesion for high-aspect ratio ZnO nanostructures.

To further substantiate the molecular adhesion forces of ZnO/PAA composite materials, hydrothermally deposited ZnO nanostructures on hot-dip galvanized steel (HDG) samples were immersed in dilute aqueous PAA solutions. The macroscopic delamination forces of an epoxy-amine adhesive depending on the ZnO nanostructuring showed a clear improvement through the short-term pretreatment with PAA, which straightforwardly correlate with the results of SMFS showing both the high molecular and macroscopic adhesion promoting properties of PAA/ZnO materials.

Conductive stainless steel substrates could be modified with thin PAA films by an electrochemically initiated polymerization reaction. By means of the controlled deposition of PAA films onto stainless steel substrates, the interfacial adhesion to model epoxy-amine adhesives was significantly improved. In this regard, the influence of the PAA layer thickness on the bonding was assessed by peel-off testing. The best results were obtained for thin films, indicating thus cohesive failure of thicker PAA layers.

Based on these results, PAA was tested as a possible adhesion promoter in combination with ZnO nanostructures such as ZnO tetrapods (ZnO TP). The noticeable increase in adhesion between poly(propylene) (PP) laminates modified with thin hybrid spray coatings of ZnO TP/PAA was successfully demonstrated using shear strength tests. The upstream oxidative plasma pre-treatment resulted in a hydrophilic PP surface, promoting the spreading of the aqueous PAA/ZnO TP dispersions. The elucidation of the adhesion mechanism by shear strength tests and interfacial analysis revealed the strong mechanical interlocking and embedding of the ZnO TP as a kind of “anchor device” between the polymeric materials. The cohesive failure of the ZnO TP was demonstrated using FE-REM and high-resolution TEM images after the tensile tests.

Zusammenfassung (German)

Die genaue Kenntnis der Grenzflächenadhäsionsmechanismen, sowohl die makroskopischen als auch molekularen Wechselwirkungen zwischen Polyelektrolyten und Metalloxidoberflächen ist für verschiedene Anwendungen in Forschung und Industrie von größter Bedeutung, beispielsweise für die Entwicklung von langzeitstabilen Beschichtungsmaterialien, Korrosionsschutz und Adhäsionsvermittlung von dünnen (Hybrid-)Filmen, einsetzbar beispielsweise in Leichtbaukonstruktionen. Daher analysiert diese kumulative Dissertation das grundlegende Verständnis der Adhäsionsmechanismen von makromolekularer Poly(acrylsäure) (PAA) an nanostrukturierten Zinkoxid (ZnO) Filmen und Edelstahlsubstraten als technisch hochrelevante Verbundwerkstoffe.

Ein vollständiges Verständnis der Adhäsionsmechanismen von PAA auf molekularer Ebene konnte durch Einzelmolekül-Kraftspektroskopie (SMFS) an poliertem Edelstahl sowie an elektrochemisch abgeschiedenen ZnO-Nanostrukturen gewonnen werden. Kraft-Abstands-Kurven von PAA-funktionalisierten Cantilevern für die Rasterkraftmikroskopie (AFM) wurden in Abhängigkeit von der Verweilzeit und der ZnO-Strukturierung aufgezeichnet. Das vermehrte Auftreten von Mehrfachbruchereignissen bei ZnO-Nanostäben im Vergleich zu plättchenartigen ZnO-Filmen kann durch hochenergetische mehr- und zweizählige koordinative Bindungen zwischen den Carboxylatgruppen und den zugänglicheren Zinkatomen an den unpolaren Seitenwänden erklärt werden. Darüber hinaus führt die Verlängerung der Verweilzeit, in der die vorhandenen Carboxylatgruppen von den PAA-Ketten in unmittelbarer Nähe der ZnO-Interphase verbleiben, zu einer Erhöhung der gemessenen molekularen Adhäsion für ZnO-Nanostrukturen mit hohem Längenverhältnis.

Um die molekularen Adhäsionskräfte von ZnO/PAA-Verbundwerkstoffen weiter zu untermauern, wurden hydrothermal abgeschiedene ZnO-Nanostrukturen auf feuerverzinkten Stahlproben (HDG) in verdünnte, wässrige PAA-Lösungen immersiert. Die makroskopischen Enthaftungskräfte eines Epoxid-Amin-Klebstoffs in Abhängigkeit von der ZnO-Nanostrukturierung zeigten eine deutliche Verbesserung durch die kurzfristige Vorbehandlung mit PAA, was direkt mit den Ergebnissen der SMFS korreliert, was sowohl die hohen molekularen, als auch die makroskopischen adhäsionsfördernden Eigenschaften von PAA/ZnO Materialein zeigen.

Leitfähige Edelstahlsubstrate konnten durch eine elektrochemisch initiierte Polymerisationsreaktion mit dünnen PAA-Filmen modifiziert werden. Durch die kontrollierte Abscheidung von PAA-Filmen auf Edelstahlsubstraten wurde die Grenzflächenhaftung an Modell-Epoxid-Amin-Klebstoffen signifikant verbessert. In dieser Hinsicht wurde der Einfluss der PAA-Schichtdicke auf die Klebung durch Abziehversuche bewertet. Die besten Ergebnisse wurden für dünne Filme erhalten, was auf ein kohäsives Versagen dickerer PAA-Schichten hinweist.

Basierend auf diesen Ergebnissen wurde PAA als möglicher Haftungsvermittler in Kombination mit ZnO-Nanostrukturen wie ZnO Tetrapoden (ZnO TP) getestet. Die merkliche Zunahme der Haftung zwischen Poly(propylen) (PP)-Laminaten, die mit dünnen Hybridsprühbeschichtungen aus ZnO TP/PAA modifiziert wurden, wurde erfolgreich unter Verwendung von Scherfestigkeitstests demonstriert. Die vorgeschaltete Vorbehandlung mit oxidativem Plasma führte zu einer hydrophilen PP-Oberfläche, die die Spreitung der wässrigen PAA/ZnO-TP-Dispersionen förderte. Die Aufklärung des Adhäsionsmechanismus durch Scherfestigkeitstests und Grenzflächenanalysen ergab die starke mechanische Verzahnung und Einbettung der ZnO TP als eine Art „Ankervorrichtung“ zwischen den Polymermaterialien. Das kohäsive Versagen der ZnO TP wurde nach den Zugversuchen mit FE-REM- und hochauflösenden TEM-Bildern demonstriert.

Preamble

This thesis is structured in a cumulative way and includes four selected peer-reviewed publications which are available in international scientific journals:

1. **Dennis Meinderink**, Alejandro Gonzalez Orive, Simon Ewertowski, Ignacio Giner, Guido Grundmeier, *Dependence of Poly(acrylic acid) Interfacial Adhesion on the Nanostructure of Electrodeposited ZnO Films*, ACS Applied Nano Mater. 2,2 (2019) 831-843
(abbreviated as **1. publication** in this thesis)
2. **D. Meinderink**, C. Kielar, O. Sobol, L. Ruhm, F. Rieker, K. Nolkemper, A. G. Orive, O. Ozcan, G. Grundmeier, *Effect of PAA-induced surface etching on the adhesion properties of ZnO nanostructured films*, International Journal of Adhesion and Adhesives 106 (2021) 102812
(abbreviated as **2. publication** in this thesis)
3. **D. Meinderink**, A. G. Orive, G. Grundmeier, *Electrodeposition of poly(acrylic acid) on stainless steel with enhanced adhesion properties*, Surface and Interface Analysis 50 (2018) 1224-1229
(abbreviated as **3. publication** in this thesis)
4. **Dennis Meinderink**, Karlo J.R. Nolkemper, Julius Bürger, Alejandro G. Orive, Jörg K.N. Lindner, Guido Grundmeier, *Spray Coating of Poly(acrylic Acid)/ZnO Tetrapod Adhesion Promoting Nanocomposite Films for Polymer Laminates*, Surface & Coatings Technology 375 (2019) 112-122
(abbreviated as **4. publication** in this thesis)

The present results are mainly based on publications created during the research project period funded by the *Deutsche Forschungsgemeinschaft* (DFG). The title of the project was “*Vergleichende Studien zur Adhäsion von Polyacrylsäure auf ZnO-Einkristalloberflächen und nanokristallinen ZnO-Schichten*” (engl.: “*Comparative Molecular Adhesion Studies of Polyacrylic Acids on ZnO Single Crystal Surfaces and ZnO Nanocrystalline Films*”) (project number: GR 1709/22-1).

Table of contents

1 Introduction	1
1.1 Relevance of zinc oxide and polymer/zinc oxide interfaces	1
1.2 Motivation and scientific approach	3
2 Fundamentals	6
2.1 Surface chemistry of zinc oxide structures	6
2.2 Synthesis of ZnO nanostructures	8
2.2.1 Hydrothermal and electrochemical synthesis of ZnO nanostructures	9
2.2.2 Gas phases synthesis of 3-dimensional ZnO structures	12
2.3 Theories of adhesion mechanisms	14
2.3.1 Wetting of surfaces	16
2.3.2 Mechanical interlocking	19
2.3.3 Electrostatic/electronic adhesion theory	19
2.3.4 Diffusion theory	19
2.3.5 Electrostatic forces from electrostatic double-layer (EDL)	20
2.3.6 Van der Waals interactions	23
2.3.6.1 Van der Waals forces – Hamaker approach	25
2.3.6.2 Van der Waals forces – Lifshitz theory	26
2.3.7 Hard-Soft Acid-Base (HSAB) principle	28
2.3.8 Hydrogen bridges	30
2.4 Adhesion mechanisms at metal oxide surfaces	31
2.5 Poly(acrylic acid)-ZnO interfaces in advanced materials	33
2.5.1 Examples of PAA-ZnO interface dominated materials	33
2.5.2 Interactions and molecular adhesion studies of poly(acrylic acid) on ZnO surf	34
2.6 Deposition of poly(acrylic acid) films	35
2.6.1 Electropolymerisation and electrografting of poly(acrylic acid)	35
2.6.2 Spray coating	38
2.6.2.1 Basics	38
2.6.2.2 Different setup modifications and classes of spray coating methods	39
2.7 Analytical methods for surface and interface analysis	42
2.7.1 X-ray photoelectron spectroscopy (XPS)	42
2.7.2 Vibrational spectroscopy	44
2.7.2.1 Fourier-transformed infrared reflection absorption spec. (FT-IRRAS)	45

2.7.2.2 Polarization-modulated Fourier-transformed infrared reflection absorption spectroscopy (PM-FT-IRRAS).....	46
2.7.2.3 Raman spectroscopy	47
2.7.3 Electron microscopy: scanning electron microscope (SEM) and transmission electron microscopy (TEM).....	48
2.7.4 Time-of-flight secondary ion mass spectroscopy (ToF-SIMS).....	50
2.7.5 Static water contact angle measurements	51
2.7.6 Atomic force microscope (AFM)	51
2.7.6.1 Basic experimental setup and measurement principles	51
2.7.6.2 Different measurement modes with AFM	52
2.8 Single molecule force spectroscopy (SMFS)	53
2.8.1 Basic explanations and literature review	53
2.8.2 Cantilever functionalization	58
2.8.3 Data interpretation of multiple rupture events and surface roughness	59
2.8.4 Bell-Evans theory: kinetic and thermodynamic values from SMFS	60
2.9 Identification of macroscopic adhesion performance.....	61
2.9.1 90°-peel-test.....	61
2.9.2 Shear test of two parallel connected specimens	62
3 Publications.....	64
3.1 Dependence of Poly(acrylic acid) Interfacial Adhesion on the Nanostructure of Electrodeposited ZnO Films.....	66
3.2 Effect of PAA-induced surface etching on the adhesion properties of ZnO nanostructured films	106
3.3 Electrodeposition of poly(acrylic acid) on stainless steel with enhanced adhesion properties	126
3.4 Spray coating of poly(acrylic acid)/ZnO tetrapod adhesion promoting nanocomposite films for polymer laminates	133
4 Overall discussion and conclusions	157
5 Outlook.....	162
6 List of references	164
7 List of publications and presentations	190

7.1 Peer-reviewed publications.....	190
7.2 Conference presentations.....	191
7.3 Participations at conference contributions.....	191
8 Attachment.....	192
8.1 List of figures.....	192
8.2 List of tables.....	194
8.3 List of abbreviations and acronyms.....	195
8.4 Documentation of experimental details and approaches	197
8.4.1 Dependence of Poly(acrylic acid) Interfacial Adhesion on the Nanostructure of Electrodeposited ZnO Films	197
8.4.2 Effect of PAA-induced surface etching on the adhesion properties of ZnO nanostructured films	200
8.4.3 Electrodeposition of poly(acrylic acid) on stainless steel with enhanced adhesion properties	203
8.4.4 Spray coating of poly(acrylic acid)/ZnO tetrapod adhesion promoting nanocomposite films for polymer laminates	205

1 Introduction

1.1 Relevance of zinc oxide and polymer/zinc oxide interfaces

The range of application fields of zinc oxide (ZnO) is enormous as demonstrated in the reviews of Özgür et al. in *Journal of Applied Physics*¹, Schmidt-Mende et al. in *materialstoday*², Ellmer et al. in *Transparent Conductive Zinc Oxide*³ and Kołodziejczak-Radzimska et al. in *materials*⁴, only to mention a few of them. Starting with the semiconducting properties including a wide band gap of 3.2 eV,^{5,6} it is reasonable that ZnO films, particles and nanostructures are ubiquitous in lots of applications related to photoelectrochemical devices like solar cells.⁷⁻⁹ Their main advantages are the extremely low costs, the physiological harmlessness and the enhanced efficiency of ZnO based materials when used in photocatalytic applications.⁹ Moreover, the benefit from photochemical effects of ZnO nanoparticles in sunscreens¹⁰, in nanocomposite films¹¹ and the redox chemical properties of ZnO nanoparticles¹² should be highlighted. Furthermore, an overview about the gas sensing properties is provided in the review by Zhu et al. in *Sensors and Actuators A: Physical*.¹³ The ZnO surface is in contact with other materials or molecules in all mentioned applications. Thus, the created interfacial region, namely the interface of these two separated phases, is dominated by a lot of complex phenomena and processes.^{14,15} The characteristics of this interface are heavily influenced by physical and chemical properties such as the electronic structure, chemical compositions or (catalytic) reactions of the pure bulk phases.^{14,15} Additionally, another wide fields are the antibacterial and wound healing properties of ZnO materials and surfaces¹⁶⁻²⁰ where ZnO is in contact with bacteria.^{18,21-23} For instance, Yamamoto and Raghupathi et al. showed that the size of ZnO particles affects the antibacterial properties of ZnO.^{24,25} In the context of this thesis, the analysis of the polymer/zinc oxide interface is the most interesting aspect to consider. By taking a deeper look into the molecular interfacial regions at different scales as displayed in Figure 1, it becomes clear that the fundamental analysis of the surfaces and resulting interfaces is essential for a major understanding of adhesion mechanisms.

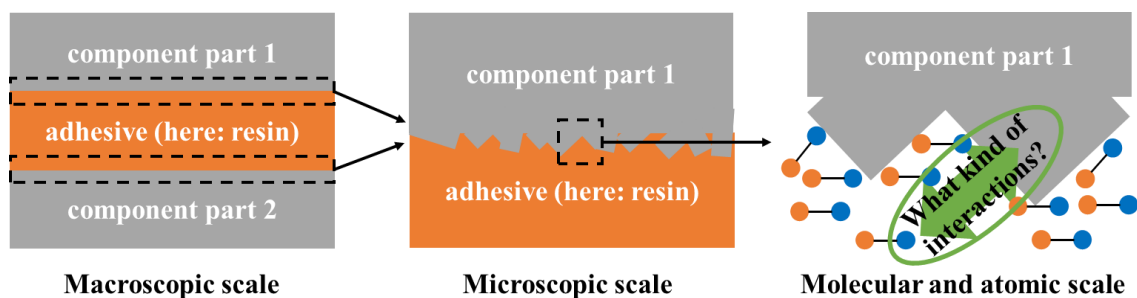


Figure 1. Illustration of the fundamental understanding of interfacial adhesion science resembling different macroscopic and molecular phenomena depending on the wide length scale and time scales of interfacial processes.

The time scale for interfacial and interphasial processes can be in the range of some ps in the context of electronic and atomic structures and up-scaled to some years or decades, taking the long-term construction idea into account. A lot of superposing effects in the time scale (caused, for instance, by the Brownian Movement) as well as in the length scale have to be taken into account during the analysis of interfacial phenomena.^{26,27}

In recent years, a lot of investigations have been performed to understand the microstructural and molecular mechanistic between polymer and metal oxide layers or particles.^{28–36} The simulation of molecular structures in the interfacial region is complex and difficult to understand due to Brownian movement, corrosion properties, instabilities like reorganizations and the complex driving forces of the different materials' surfaces.²⁹ For instance, Kandada et al. demonstrated that the dynamics in molecular scale are important for the charge generation at the polymer/metal oxide interface in ZnO based photovoltaic materials.³⁷ Indeed, the understanding of the effects influencing the adsorption of molecules on metal oxide surfaces is still a broad field of investigations.³⁸ In context of adsorption layers at ZnO interfaces, the studies of Torun et. al. showed that the high water activity in high relative humidity (r.H.) could affect the adsorption of organothiols and organosilanes like 1-octadecanethiol (ODT) and octadecyltriethoxysilane (ODS).³⁶ Indeed, the stability of the interfacial region was shown to be higher in the case of ODT due to the occurrence of S-Zn bonds with high binding energies and the hydrophobic character of the nonpolar chains of the ODT molecules. In the case of ODS, the water molecules are competing against the Si-O-Zn bonds. Indeed, it could be demonstrated that the formation of Si-OH and Zn-OH groups occurred at higher r.H. values detected with an in-situ infrared-based method by the increasing of typical vibration modes of –OH-groups.³⁶ The successful adsorption of molecules with adhesion promoting properties is a key aspect in interfacial engineering. The relevance of surface treatments with plasma followed by adsorption processes of molecules like organophosphonic acid monolayers on engineering materials like Zn-Mg-Al/ZM alloys was investigated by Pohl et al.³⁵ and on ZnO wafers by Zhang et al.³⁹ The corrosion protection behavior and charge transfer properties exhibited by ZM substrates after successive modifications with plasma and adsorbed molecules have been tested by XPS and cyclic voltammetry.³⁵

A recent study of Yang et al. proved the enhancement of the interfacial adhesion exhibited by biocomposite fibers functionalized with ZnO nanowires.⁴⁰ These natural fibers coated with ZnO nanowires and embedded in poly(lactic acid) showed a significant increase in the interfacial shear strength.⁴⁰ The usage of ZnO nanowires as interfacial adhesion promoting films was considered by Ma et al. in a recent study for aramid fibers in composites, too.⁴¹ In addition, functionalized systems with ZnO materials showed an improved resistance for UV radiation.⁴¹

Only few works illustrated the molecular adsorption and adhesion properties of macromolecules on zinc oxide surfaces, which play a key role in the context of this PhD thesis. In a recent research work by Fockaert et al., the authors show the accurate stability of carboxylic acid groups at the polymer-zinc/zinc oxide interface.⁴² Another fundamental investigation of the analysis of the interfacial molecular adhesion mechanistic was performed on stepped polar ZnO(0001)-Zn single-crystals in contact with PAA molecules linked to an AFM cantilever in aqueous solutions by Valtiner et al.⁴³ These results show that the carboxylate groups bind with high adsorption energies, probably via coordinative bonds, to the nonpolar steps and via lower adsorption energies like electrostatic interactions to the hydrogen stabilized polar terraces.⁴³ Ozcan et al. found that the macroscopic adhesion can be increased with the deposition of zinc oxide nanorods on zinc surfaces as evidenced from peel-off testing with a model epoxy-amine resin.³⁴ The presence of adhesion promoting molecules like 3-aminopropylphosphonic acid (APPA) in combination with the ZnO nanorod structures can even enhance the registered macroscopic adhesion.³⁴ However, the characteristics of the molecular adhesion mechanisms on such ZnO nanostructures still remains as an open question. Therefore, this PhD thesis focuses on the fundamental investigations, engineering applications, and molecular understanding of PAA in contact with nanostructured ZnO films on technically relevant surfaces like stainless steel or hot-dipped galvanized steel (HDG).

1.2 Motivation and scientific approach

The main fields in the fundamental research and industries, especially in the automotive and aerospace, are searching for lightweight constructions that satisfy the rapidly increasing profiles of requirements. The most highly charged topic is the reduction of the consumption levels linked with the reduction of CO₂ gas from combustors. Therefore, it is useful to reduce the overall mass or weight, for instance, of vehicles and airplanes.⁴⁴ In their paper about the construction of super light vehicles, Goede et al. mentioned that a reduction in weight of 100 kg leads to savings of around 3.5 l fuel/100 km and 8.4 g CO₂/km.⁴⁵ The idea of minimizing the total mass or, in other words, of finding the lightest possible structure is based on the hybrid construction idea.⁴⁶ From that point of view, it is necessary to identify optimized surface treatments for materials of interest, before these modified multi-materials can be effectively joined with long-term stable properties. One example is the adhesion of two different materials, like metallic parts and polymers as displayed in Figure 2. Thereby, the understanding of the chemical, mechanistical and molecular properties, and especially of the adhesion mechanisms at material interfaces is essential for long-term stable lightweight constructions.^{47–49}

Indeed, the field of interfacial technology has reached a high impact in research and development,⁵⁰ due to the fact that the polymer/metal oxide interfaces can be the point of failures in a bonding.^{38,51} In the context of adhesive bonding and interfacial chemistry, typical environments like high humidity or even more corrosion aggressive media play a key role in corrosion protection and adhesion technology.^{29,30,38,52} Subsequently, the choice of optimum matching multi-

materials, together with possible pre-treatments like the deposition of nanostructures or the application of adhesion promoting thin films with corrosion inhibiting properties, still remains a challenge in the lightweight construction industry and in scientific research.

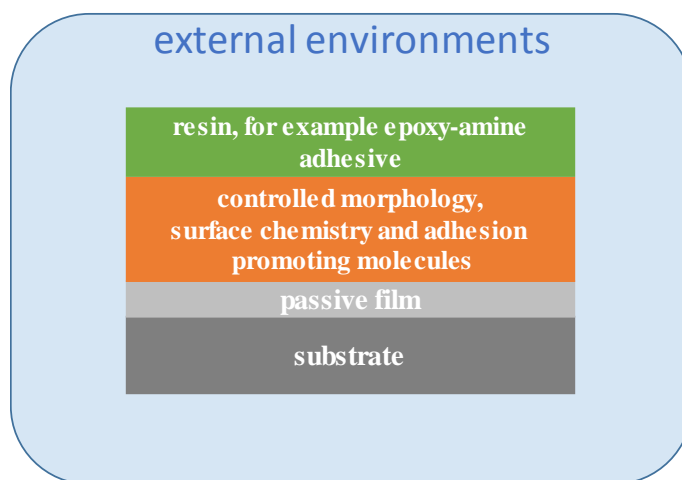


Figure 2. Schematic illustration of join partners with matched surface pre-treatments (orange) and coated with a resin (green) for a possible bonding to other materials.

Within the aims of this work, poly(acrylic acid) (PAA) was investigated regarding its potential use as an adhesion promoter when deposited on stainless steel and nanostructured ZnO surfaces, focusing on both the macroscopic adhesion and the binding mechanisms.

Firstly, the analysis of molecular adhesion mechanisms of hydrothermal and electrochemical deposited nanostructured zinc oxide (ZnO) films on engineering metals and oxides in contact with PAA is investigated by single molecule force spectroscopy (SMFS). So far, the molecular understanding of adhesion of PAA on nanostructured ZnO films had still been an open question. Secondly, the immersion of hot dipped galvanized steel substrates (HDG) in PAA containing water-based solutions is implemented as an easy-to-use application method, underpinning the highly increased macroscopic adhesion properties of ZnO nanostructured films on HDG samples. Thirdly, evidences of the macromolecular PAA as a possible adhesion promoting molecule on mirror polished stainless steel are presented, where the electrochemically induced polymerization of acrylic acid (AA) was chosen as a precise controllable deposition method.

Fourthly, an industrially applicable deposition process of an ultrathin nanocomposite film of PAA/ZnO tetrapods, carried out by spray coating, on poly(propylene) (PP) foils is presented.

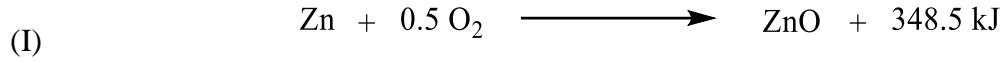
In conclusion, this thesis presents a profound understanding of the PAA/ZnO interface in terms of the deepening of molecular and macroscopic adhesion mechanisms. On top of that, the optimized pre-treatments could be highly interesting for their potential application in industrial processes like

an in-line spray coating step as shown for the investigated PAA/ZnO water-based solutions or the immersion into PAA containing solutions, following the “green chemistry” principles.

2 Fundamentals

2.1 Surface chemistry of zinc oxide structures

The main process for the synthesis of ZnO is described by the following chemical reaction (taken from literature⁶, page 1491):



The reaction (I) shows that ZnO can be generated in high yields by oxidation with oxygen from air. In the latter case, the vapor phase of zinc can be used for the reaction in air (“American proceeding”).⁶ In this regard, the oxidation of pure zinc evaporated in a tube oven has been laid out in the 4. publication⁵³ of this thesis (see chapter “3 Publications”).

ZnO can have two different crystal structures: cubic “zinc blende” and hexagonal “wurtzite structure”.⁶ In the context of this work, the latter structure is the most relevant one. For this reason, the following considerations are limited to the wurtzite crystal structure, which is displayed in Figure 3.

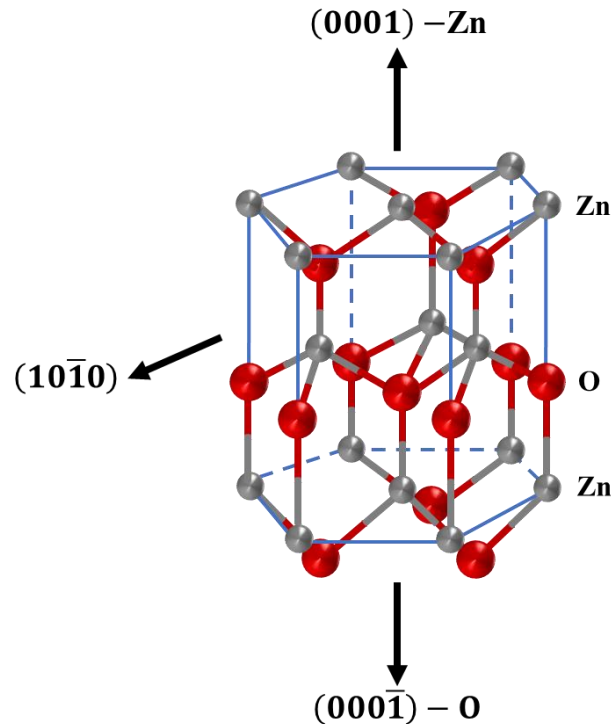


Figure 3. Schematic model of the hexagonal (indicated with blue lines and blue dashed lines) crystal wurtzite structure (based on Noei et al.⁵⁴).

The alternately ordered Zn^{2+} and O^{2-} atoms are growing in the c -axis direction and with a tetrahedral coordination of the atoms in the ZnO Wurtzite crystal structure.⁵⁵ In principle, the topper parts of the ZnO wurtzite structure can exhibit two polar surfaces: $(0001) - \text{Zn}$ terminated and $(000\bar{1}) - \text{O}$ terminated (indicated in Figure 3). The former is resulting in a zinc

side partially positively charged without including a stabilization mechanism, while the latter is terminated in oxygen atoms with a partially negatively charged surface, respectively.⁵⁵ The facets surrounding the topper polar planes mentioned before can be classified as nonpolar sidewalls of the hexagonal structure. Furthermore, the nonpolar ZnO surfaces are more stable without a stabilization mechanism than the polar facets. For instance, it was shown by Parker et al. by means of scanning tunneling microscopy (STM) that the $(10\bar{1}0)$ nonpolar surface has a lower amount of step sizes in comparison with the polar $(000\bar{1})$ equivalent.⁵⁶ The authors mentioned the existence of possible stabilization mechanisms of the polar $(000\bar{1}) - O$ surface.⁵⁶

The anisotropic adsorption of different molecules on the surface is important in all mentioned applications like in the fields of adhesion science, photocatalysis or chemical reactions on ZnO surfaces in semiconductor devices.⁵⁴ For example, the adsorption of small probe molecules like H_2 , CO, CO_2 , NO and HCOOH were tested by Noei et al. with vibrational spectroscopy like in situ FTIR experiments under ultra-high vacuum conditions on different metal-covered metal oxide surfaces including ZnO.⁵⁴ For instance, the clear understanding of the adsorption of hydrogen molecules opens the door for a more efficient hydrogenation reaction in catalysis.⁵⁴

Furthermore, it becomes apparent that a lot of publications deal with the analysis of stabilization mechanisms and the clarification of the crystal structure. Therefore, most of the studies were performed for single crystals with different orientations.^{57–65} Valtiner et al. demonstrated by means of Angle-Resolved High-Resolution X-ray Photoelectron Spectroscopy (AR-HR-XPS) that the outer part of the ZnO(0001)-Zn surface is stabilized by hydroxide groups and that the water molecules play the most important role in the stabilization process on such polar surface facets.⁶³ Additionally, the electronic structures were studied by taking the Zn 3d state of polar ZnO(0001)-Zn with HR-XPS measurements into account.⁶⁵ At the zinc terminated polar (0001) orientation, 0.5 electrons are missing per zinc atom.^{62,63} This can be stabilized by 0.5 monolayers of hydroxyl groups on these surfaces, but the precise amount of adlayers is still an open question.^{62,63,66} However, stabilization mechanisms like metallization, adsorption of hydroxyl groups, oxygen as adatoms, formation of Zn vacancies or other reconstructions on the polar ZnO(0001)-Zn surface are dependent on temperature⁶⁴ and pressure, as shown by Kresse et al. through density-functional theory calculations.⁵⁷ Especially in context of gas sensing properties the mentioned electronic and crystal structures have to be considered.^{67–69} Even the sensitivity and selectivity of gas sensing is dependent on the morphology and in general on the surfaces of ZnO single crystals.^{68,69}

Due to the fact that the ZnO crystal structure is stable, the growth mechanisms are discussed for the different morphologies which could be generated under controlled synthesis conditions. Baruah et al. summed up the most important nanostructures of ZnO like nanowires/nanorods,

nanocombs, nanorings, nanoloops and nanohelices, nanobows, nanobelts and nanocages.⁵⁵ These structures of ZnO can be classified as 1-dimensional nanostructures. If these structures are deposited as a film, it is generally common to define these nanostructures as 2-dimensional ZnO films. The 0-dimensional nanostructures are quantum dots or nanoparticles.⁷⁰ Here the size and aspect ratio is in the close range of one uniform crystal cell.⁷⁰ The different possible structures open the door for a wide range of applications, especially in the field of ZnO/polymer interfaces as discussed above.

2.2 Synthesis of ZnO nanostructures

A lot of reviews deal with the growth synthesis of ZnO materials like the recent ones from Skomska and Zarebska⁷¹, Baruah and Dutta⁵⁵, Ahmad and Zhu⁷², Zhang et al.⁷⁰ and Laurenti⁷³ and Cauda.⁷⁴ Most of the reviews mention that the synthesis of ZnO can be categorized by the phase in which the synthesis takes place:

- 1) reaction in liquid solution
- 2) synthesis in gas phase

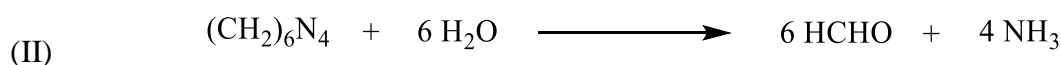
For the control of the aspect ratio, it is important to know how the growth direction of ZnO nanorods, often named nanowires in the literature^{55,70–74}, proceeds under different experimental conditions. The ZnO crystal structure is anisotropic.⁷⁰ Indeed, the growth direction of ZnO nanorods along the *c*-axis is caused by the dependence of the different growth velocities on the different surface planes/crystal orientations. For example, Zhang et al. mention in their review published in the *Journal of Nanomaterials* in 2012 the following order for the growth reaction speeds of the different crystal planes: $v(0001) > v(1011) > v(1010)$.⁷⁰ Zhang et al. demonstrated with a micelle growth reaction controlled by an amphiphilic block polymer, namely poly(ethylene oxide)-poly(propylene oxide)-poly(ethylene oxide) (PEO-PPO-PEO), that the different facets of ZnO have different growth rates.⁷⁵ This anisotropic property in growth is useful for the growth control on substrates where the application needs especially precise facets like in the photocatalysis or gas sensing, where it could be an advantage to have concrete facet orientations on the substrate surface.⁷⁰

The examples show that the crystal structure is a main feature for the optimized performance in the different application fields. Indeed, it is necessary to consider optimized synthesis strategies for the creation of ZnO particles, films and nanostructures. In this context, the following chapters “2.2.1 Hydrothermal and electrochemical synthesis of ZnO nanostructures” and “2.2.2 Gas phases synthesis of 3-dimensional ZnO structures” will be focused on the synthesis of ZnO films and of 3D oriented ZnO tetrapods (ZnO TP) from the gas phase.

2.2.1 Hydrothermal and electrochemical synthesis of ZnO nanostructures

In principle, ZnO nanostructures can be synthesized in liquids using water-based solutions, organic solutions or a mixture of both.⁷⁰ Mainly the use of aqueous solutions opens the door for a nearly green-chemistry with high potential for scale-up processes. Besides, the costs are lower, taking the low possible reaction temperature ($< 90\text{ }^{\circ}\text{C}$) in the whole process context. Due to the usage of lower temperatures in comparison to gas phase synthesis, it is even possible to coat organic substrates with low decomposition or melting temperatures.⁷⁰ In most application cases, the seeded metallic substrate is placed in a heated liquid solution with different precursors containing Zn^{2+} species for the growth of ZnO crystals.⁷⁰ To ensure a homogenous growth, a seed layer can be deposited by spray coating beforehand.⁷⁶ Here, different zinc salts can be sprayed onto hot substrates to create homogenous thin films of ZnO as a seeding layer.⁷⁷ The spray coating as an experimental approach will be described in more detail in chapter “2.6.2 Spray coating” some chapters below.

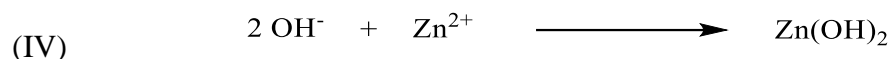
In the context of this work, the zinc nitrate hexahydrate ($\text{Zn}(\text{NO}_3)_2 \cdot 6\text{H}_2\text{O}$) plays a key role in the synthesis of ZnO nanorods. To control the morphology and at least the aspect ratio of the ZnO wurtzite crystals, it is necessary to use, for instance, hexamethylenetetramine ($(\text{CH}_2)_6\text{N}_4$) (HMTA) which could block the nonpolar sidewalls of the ZnO hexagonal crystals in growth processes.⁷¹ However, it is controversially discussed in the literature whether the HMTA is supplying the hydroxyl groups for the chemical reaction and/or is chelating the nonpolar sidewalls.⁷¹ Nevertheless, it is possible to observe the following reactions (II)-(V) in the hydrothermal deposition from a water-based solution containing zinc nitrate and HMTA (taken from Zhang, Ram et al.⁷⁰). The HMTA decomposes by dissolving in water as solvent molecule in reaction (II) (adapted from literature including literature in there):⁷⁰



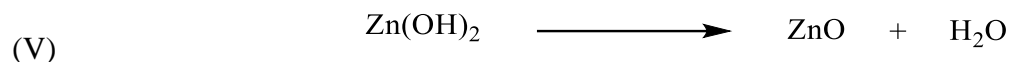
The ammonia molecules increase the pH by supplying hydroxyl ions formulated in reaction (III):⁷⁰



Controlling the concentration of the created hydroxyl ions is one important aspect in the synthesis of ZnO structures. At higher pH values or, in other words, at higher concentrations of hydroxyl groups, the Zn^{2+} ions evolves to zinc hydroxide by supersaturation:⁷⁰



The nanorods growth then occurs under higher temperature by a condensation reaction:⁷⁰

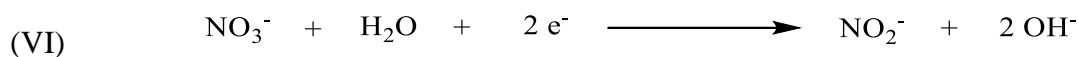


The above chemical reactions underline that controlling the different concentrations is one of the most important aspects in context of the ZnO growth, both for hydrothermal and electrochemical depositions. Within the production of ZnO particles by increasing OH⁻ concentration, the adsorption of these species is favored on the surface as nucleation points.⁷⁰ Indeed, the growth of ZnO nanorods is increased by decreasing the total concentration of HTMA and OH⁻ ions, respectively.⁷⁰ Besides, both reactants zinc nitrate salt and HMTA are well dissoluble in water.^{78,79} This makes these chemicals interesting for more industrially relevant applications. However, the stability diagrams presented in the review from Skompska and Zarebska show that the concentration and pH play the most important role if the Zn²⁺ ions stay in the soluble state or if a supersaturation (displayed in reaction (IV)) is favored.⁷¹ Moreover, it is evident that the concentration equilibrium states are dependent on the temperature of the liquid solution, which has been published by Goux et al. for a zinc chloride water-based system.^{71,80}

The control of the morphology based on the broad range of possible structures is a key point in the synthesis of ZnO nanostructures. Therefore, a lot of additives, pH adjustments and concentration screenings of Zn²⁺ were tested for the optimized growth conditions for the different morphologies of ZnO like ZnO nanorods or nanoplates.^{71,81,82} One key concept in the synthesis of ZnO nanorod films is the adsorption of molecules at the nonpolar sidewalls or even on the polar facets caused by the anisotropic features of ZnO crystals. Different molecules like the mentioned HMTA, citric acid or salts like potassium chloride were used to control the morphology during hydrothermal and electrochemical synthesis.^{71,83} Both components block specific facets of the growing wurtzite ZnO nanostructure to control the growth directions in the desired ways. For instance, the chloride anions are typically used for the adsorption on the polar (0001)-Zn surface to slow down the growth into the direction of the *c*-axis. Therefore, the addition of NaCl or KCl to ZnCl₂ water-based solutions has been proposed.⁷¹ As discussed above, HMTA can interact as a chelating molecule at the nonpolar sidewalls of the wurtzite ZnO crystals to block the growth directions. Consequently, at specific concentration ratios between the additive and the precursor, it is possible to control the growth of ZnO nanorods in both directions: polar surface and nonpolar sidewalls. While blocking the polar surface, the growth of the ZnO crystallites will end in plate-shaped ZnO nanostructures

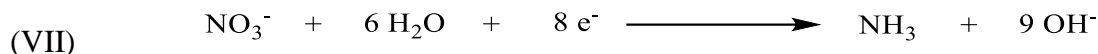
while by blocking the nonpolar sidewalls the structure growth will follow in the c-axis direction resulting in long and small ZnO nanorods/nanowires.⁷¹

The chemical reactions (II)-(V) are the most important during hydrothermal synthesis and can be carried out without any electrochemically induced reactions. With consideration of the applied precursor zinc nitrate in context of this work, two additional reactions should be mentioned for the electrochemical deposition of ZnO nanostructures on metallic substrates:^{71,84}



The produced hydroxide ions from the reduction of the nitrate ions to nitrite ions can then be used for the reaction (IV) to form zinc hydroxide. At increased temperatures from around 50 °C⁷¹ up to 200 °C⁷⁰, which are typically used at the hydrothermal and electrochemical synthesis of ZnO films from aqueous zinc nitrate solutions⁷¹, the supersaturation and the formation of ZnO can occur as displayed in reaction (V).⁷¹

At a negative potentials, the reduction of nitrate to ammonia in water could also be considered:⁷¹



The scientific analysis of the optimization of an electrochemical deposition with zinc nitrate as precursor can be found in the publication of Izaki.⁸⁴ Here, a deposition of zinc oxide particles at higher negative potentials (-1.2 V vs Ag/AgCl) acts as a previous step before a negative potential at -0.7 V vs. Ag/AgCl leads to the formation of hexagonal grains.^{71,84} A lot of more studies dealing with the screening of the parameters for the understanding of the deposition of ZnO structures have been published.^{85–87} An overview can be found in the review of Skompska and Zarebska in *Electrochimica Acta* (2014).⁷¹

To sum up, the important reaction parameters and issues that should be taken into account are:

- 1) ZnO seeding layer
- 2) concentration of precursor
- 3) using an alkaline reagent
- 4) reaction time – growth duration
- 5) pH value at the starting of the reaction
- 6) substrate
- 7) temperature

- 8) additives
- 9) other experimental conditions, like mechanical stirring or external electric field.⁷⁰

2.2.2 Gas phases synthesis of 3-dimensional ZnO structures

In addition to the synthesis of ZnO nanostructures in liquid phases, the synthesis can also be performed in the gas phase. The already mentioned reviews give a broad overview about all publications.^{55,70,72} Based on the chemical reaction (I) for the oxidation of pure zinc, it is deducible that closed experimental approaches with high temperature up to 1500 °C are needed.⁵⁵ Baruah et al. name several gas phase approaches, like vapor phase transport, chemical and physical vapor deposition or the thermal oxidation of metallic zinc.⁵⁵ The former one performed in a tube oven as a gas phase transport reaction is the most relevant one in the context of this work. A lot of publications regarding the synthesis of 3-dimensional ZnO networks/nanostructures with the chemical vapor transport method are available.^{88–98}

In principle, all synthesis approaches are basically performed in an oven or tube oven in which metallic zinc can be evaporated. Besides, the introduction of gas flows is useful for the transport of the products to the end of the tube oven for the condensation of the ZnO structures. Calestani et al. divided the areas in the tube oven into three different sections:⁹⁰

- 1) zinc evaporation zone (700 °C)
- 2) nucleation and growth zone (600-500 °C)
- 3) collection region

The metallic zinc is placed in the region 1), while two gas inlets (oxygen and argon) are used for the transport of the evaporating zinc. As in zone 2) the temperature is slightly lower (600-500 °C), the nucleation and growth of ZnO particles occurs. Within the constant flow rates of the gases, the reacted products will be transported to the end of the tubular furnace where the ZnO nanostructure like ZnO tetrapods (ZnO TP) can be collected on the surface of a quartz tube.⁹⁰ Some experimental details, like the technical implementation are different in the approaches, for instance:

1. the precursor (zinc pellets⁹³, zinc foil⁹⁰, zinc carbonate with graphite⁸⁸),
2. the reaction time (from 5 min⁹³ up to 30 min⁸⁹)
3. and the reactor construction⁹⁹ differs in some publications.

In addition, Roy could show that the different gas compositions like air, argon and nitrogen at different humidity have an influence on the fabrication of ZnO nanostructures like tetrapod nanorods and tetrapod nanowires.⁹² Thereby, the morphology differences caused by different experimental conditions determined their photoluminescence properties.⁹² Good overviews are

available in different reviews regarding ZnO TP from the synthesis up to the applications. Newton and Warburton in *materialstoday* (2007)¹⁰⁰, Modi in *Advances in Natural Sciences: Nanoscience and Nanotechnology* (2015)¹⁰¹, Yan et al. in *Nanomaterials and Nanotechnology* (2015)¹⁰², Mishra et al. (working group of Prof. Adelung) in *KONA Powder and Particle Journal* (2014)¹⁰³ and a recent review from Mishra and Adelung in *materialstoday* (2018).¹⁰⁴

The broad field of applications of these highly interesting materials has opened the door for scientists to develop low-cost and efficient synthesis processes. Mishra and Adelung summed up the most important application fields of ZnO tetrapods or ZnO TP containing materials¹⁰⁴. For example, ZnO TP can be used as “anchors” for the increase of mechanical interlocking between two un-joinable materials like PTFE and PDMS as shown by the working group of Adelung et al.¹⁰⁵ Probably, the broadest application fields are in optical, electronic and photonic devices due to the high surface area of ZnO TP. Here, ZnO TP could decrease the contact areas in nanodevices.¹⁰⁴ Additionally, ZnO has antibacterial properties which could be improved by the use of ZnO TP exhibiting a high surface area in composite materials.¹⁰⁶

All applications underline the need of a ZnO TP synthesis with high yields in short times and therefore with low costs. Therefore, a lot of publications deal with the optimization of the synthesis conditions. Mishra et. al. mentioned flame transport synthesis, DC thermal plasma, hydrothermal, wet chemistry and a few more.¹⁰⁴ In addition to that, it is even possible to synthesize ZnO TP in water-based dispersions as shown by Lupan et al.¹⁰⁷ The authors used an aqueous zinc sulfate and ammonia solution at 90-95 °C for 15 minutes without stirring at pH 10-11. The finishing was performed in an oven at 300 °C to 850 °C for different times.¹⁰⁷ However, to ensure high yields and amounts of ZnO TP powders, two main approaches could be considered: a flame-based synthesis developed in the working group of Adelung et al.^{108,109} and the approach in a tubular furnace as shown, for instance, by Calestani et al.⁹⁰

However, the growth mechanism of ZnO TP is still an open question in the field of ZnO TP, since it is controversially discussed how the resulting crystalline structure starts growing in the mentioned fabrication processes. Ronning et al.⁸⁹ and Newton et al.¹⁰⁰ summed up and reviewed the recent studies about the growth mechanisms and the crystal structure of ZnO tetrapods (ZnO TP). As presented in the FE-SEM images in the 4. publication⁵³ of this thesis, the ZnO TP are constructed of four arms with a hexagonal crystalline structure connected by one core center. While the growth mechanism of the hexagonal nanorod arms in the direction of the c-axis is clear, there is no undisputed crystal structure and growth of the nucleus of the ZnO TP. In principle, all publications mention a model starting with a seed nucleus.^{89,100} Based on the fundamental parameter screening for the optimization of the synthesis conditions, it is evident that the

nucleation and growth is taking place in the vapor phase.¹⁰⁰ Rackauskas et al. could show via gas phase synthesis that the reaction temperature and the Zn vapor pressure strongly influence the morphology of ZnO TP.⁹⁷ However, the SEM images show that the fundamental structure of the ZnO TP remains constant: four arms connected with one center.⁹⁷ Most of the authors conclude that the growth starts in a core like the nucleation of particles and continues by growing the four arms.^{100,110–112} Two mainly possible crystalline structures between the core and the arms of the ZnO TP have been proposed in the literature:^{89,100}

- 1) the “tetrahedral zinc blende core” with four wurtzite hexagonal nanorod arms published by Yu et al. in 2004¹¹³ and for CdTe¹¹⁴, respectively
- 2) the “octa-twin model” of Iwanaga et al. in 1993¹¹⁵ and described in other publications of Iwanaga et al.^{112,116,117}

Both models start at the core center which is the most critical point according to the current literature.⁸⁹ The first model contains the nucleus theory starting with a tetrahedral zinc blende as the core.¹⁰⁰ The facet (111) in the zinc blende could link the $(000\bar{1}) - O$ plane in the wurtzite crystal structure of the four arms as published for the CdTe crystalline structure.¹¹⁴ The second model, firstly developed by Iwanaga et al.,¹¹² is based on the theory of eight tetrahedral crystals in the core center of ZnO TP forming one octahedron.^{100,112}

2.3 Theories of adhesion mechanisms

The understanding of the molecular adhesion mechanisms at oxide interfaces is essential for the effective and long-term joining in manufacturing engineering (DIN 8593) mentioned in the context of lightweight constructions. The optimization of the macroscopic, microscopic, molecular and atomic interactions between two components (bonding) like, for example, a resin (adhesive) and a metallic substrate (adherends), is one of the most important aspects in fabrication of long-term joinings.¹¹⁸

In the context of the analysis of failures in joints/bonding, it is interesting to determine the weakest component responsible for the adhesion failure in order to find optimized pre-treatments or materials like adhesives.¹¹⁸ There are some adhesion failures which can be observed: in some cases, typical cohesive failures in the adhesives or in the component parts occur. Another possibility is the most complex situation, where the break of harnessed structures takes place at the interfacial near region. In most situations, it is difficult to precisely distinguish on which component (adhesive, adhesion promoting molecules or nanostructures) the failure takes place or has started.¹¹⁸ Therefore, it is essential to bridge between the molecular, microscopic scaled processes and adhesion, and the macroscopic measured adhesion forces as displayed in Figure 4.

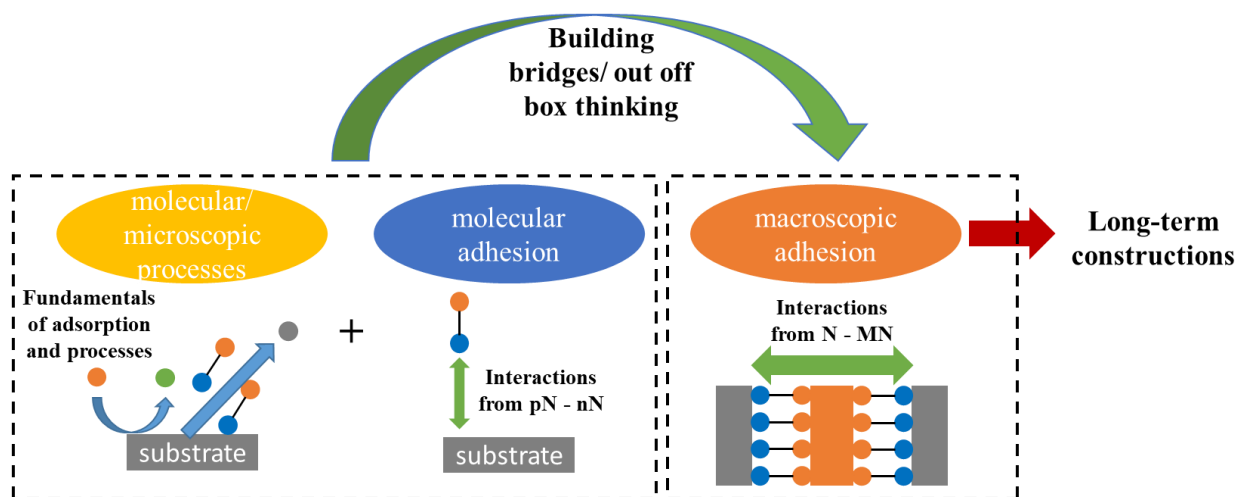


Figure 4. Schematic demonstration of the bridging between the microscopic, molecular interfacial adhesion processes and the macroscopic adhesion theory and praxis. Closing the gap between these two differently scaled “worlds” is necessary for optimized long-term constructions.

However, there are a lot of complex superposing length and time scaled processes which are implemented from macroscopic up to atomic effects. For the fundamental understanding of the total macroscopic measurable adhesion force, the analysis of the interfacial regions is needed. In general, there are different “classes” of adhesion mechanisms (often also called “adhesion theories” like mentioned by Ebnesajjad et al.¹¹⁸ with corresponding literature in there) which will be explained in the following paragraphs and chapters. This leads to lot of different classifications and theories of adhesion science in the literature.^{118–120} The general classification of adhesion mechanisms displayed in Figure 5 is based on mechanical, physical and chemical driving forces and causes, respectively.

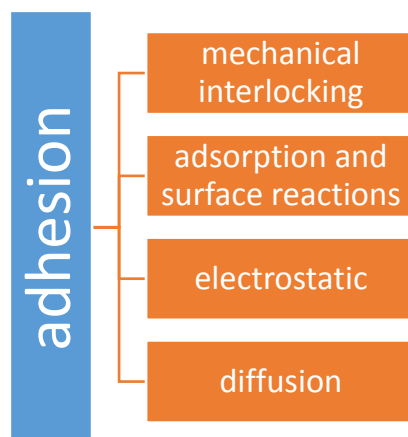


Figure 5. Theoretical mechanism theories for adhesion (based on the text published by Ebnesajjad¹¹⁸).

All of the displayed adhesion mechanisms are important for the performance of the interfacial bonding and cohesive properties and only their overall understanding lead to the best adhesive results for of surfaces and adhesives. In addition, the wettability and the morphology play a significant role in the field of the adsorption properties.

The chemical and physical bases for these phenomena are related to different adsorption and binding processes which are summarized in the Figure 6.

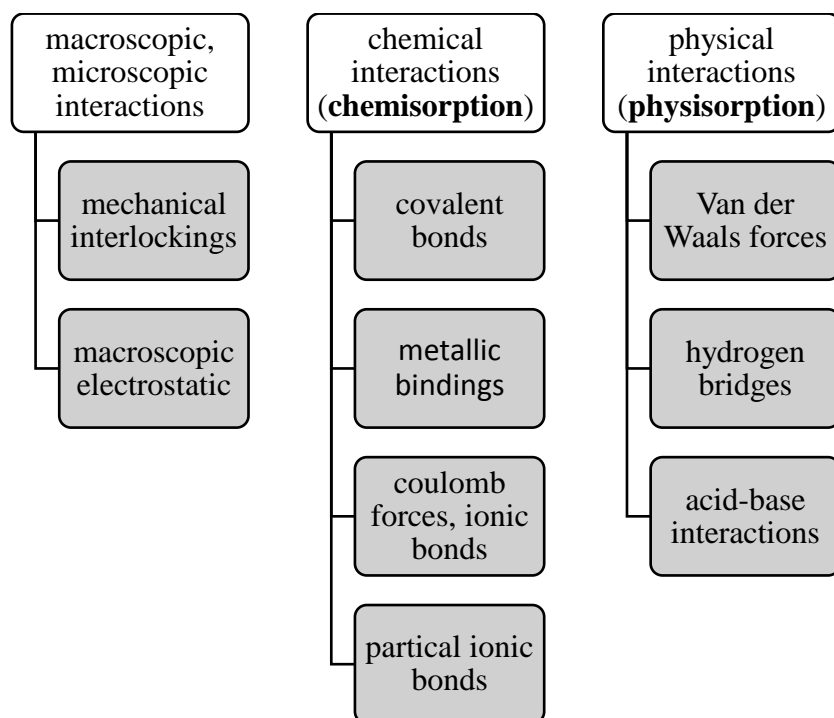


Figure 6. One possible classification of basic adhesion mechanisms and binding forces
(based on literature ^{15,119,121}).

However, in reality a strict differentiation of the adhesion mechanisms with the corresponding interactions is difficult to predict and propose. In addition, all adhesion mechanisms have overlapping features and properties. Consequently, a combination of different mechanisms is present in real interfaces. All mentioned bindings forces will be explained in more detail in the following subchapters.

2.3.1 Wetting of surfaces

In context of adhesion mechanisms and optimization of process steps including the surface pretreatment, it is very important to understand the wetting behavior of adhesives on the chosen substrates. The distances between the molecules of the two components is essential.^{26,119} The intermolecular interactions are described with the help of the two-parameter model of Lennard-Jones, called “Lennard-Jones potential”, illustrated in Figure 7.²⁶

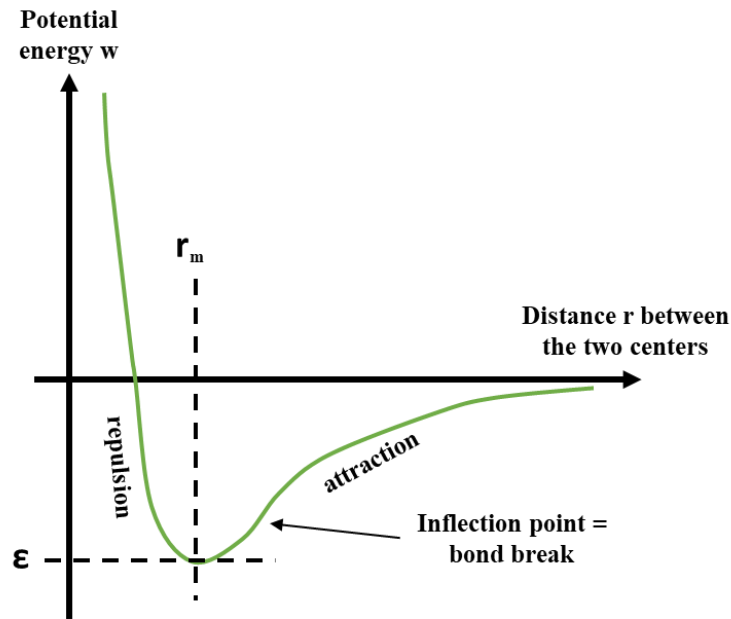


Figure 7. “Lennard-Jones potential“ (based on Kendall²⁶).

The green curve in Figure 7 represents the sum of energies of the attractive and repulsive interactions between two atoms dependent on the distance r with the bond energy ε and the bond length r_m .²⁶ For the Lennard-Jones potential a proposed equation from Kendall reads:²⁶

$$(1) \quad w = 4\varepsilon \left[-\left(\frac{r_m}{1.12 r}\right)^6 + \left(\frac{r_m}{1.12 r}\right)^{12} \right]$$

The first term in (1) represents the attractive interactions, which have a negative sign, while the repulsive interactions are given by the positive term with 12 in the exponent.

Habenicht mentioned that a distance of 0.1 to 1.0 nm between the valence forces results in possible interfacial chemical reactions and binding interactions.¹¹⁹ Thus, an affinity of the adhesive to wet the adherend is useful for the formation of interactions with higher energetic levels.¹¹⁹

A good example for the description of wettability is a sessile drop of a liquid phase from, for instance, the adhesive on a solid phase/substrate. While the liquid phase creates a change of surface area dA on the solid surface of a metallic substrate, the energy dW that will be needed for this process can be written as follows:¹⁵

$$(2) \quad dW = \gamma_1 dA$$

An important parameter within the equation (2) for liquids at constant pressure p and temperature T is the surface energy or the surface tension γ_1 given in J/m^2 or N/m .^{15,122} The outer layers of molecules in the liquid phase create a net surface tension due to the missing of their nearest

neighbors in comparison to the bulk liquid phase.¹⁵ In more qualitative terms, the surface of the liquid needs to reduce the total surface area to reach the lowest energetic state while the surface tension is the operating tension.¹⁵ A quantitative summary of three tension vectors in equilibrium state (compare chapter “2.7.5 Static water contact angle measurements”) is given by the Young’s equation:¹⁵

$$(3) \quad \gamma_{lg} \cos(\theta) = \gamma_{gs} - \gamma_{ls}$$

For instance, in the case of $\gamma_{gs} > \gamma_{ls}$ the right-hand of equation (3) will be negative. Therefore, the left-hand side has to be negative as well, which implies a contact angle $\theta > 90^\circ$. In this case, the wetting of the surface is hindered or in other words, the surface wetting with the liquid is not possible. For instance, a hydrophilic surface will create a contact angle θ of lower than 90° .¹⁵

With regards to the adhesion and based on the sessile drop methods (compare chapter “2.7.5 Static water contact angle measurements”), it is possible to define the adhesion work W_A . This work is necessary to separate two joined phases with a contact area A and is described by the Dupré-equation:¹¹⁹

$$(4) \quad W_A = \gamma_{lg} + \gamma_{gs} - \gamma_{ls}$$

Here, the total adhesion work W_A could be positive or negative based on the values from the different surface tensions: liquid-gas γ_{lg} , gas-solid γ_{gs} , liquid-solid γ_{ls} . The former case ($W_A > 0$) means that some energy is in excess and the latter case describes the vice versa.¹¹⁹ The combination of equations (3) and (4) results in the Young-Dupré equation which reads as follows:¹¹⁹

$$(5) \quad W_A = \gamma_{lg}(1 + \cos(\theta))$$

Equation (5) underlines the importance of wetting in the context of adhesion. With a contact angle of $\theta = 0^\circ$, the surface will be completely wetted and the adhesion work results in a maximum value:¹¹⁹

$$(6) \quad W_A = 2\gamma_{lg}$$

The maximum adhesion work W_A in this case equates to the cohesive work W_C of the liquid phase spreading on the surface.¹¹⁹

2.3.2 Mechanical interlocking

Mechanical interlocking can occur at the macro- and nano-scopic scale where a mechanical locking between two solid phases lead to an anchoring of both phases. For instance, when a cured polymer is in contact with a metallic substrate, the polymer chains can interlock with the pores, gaps, cracks or fractures of the metallic component. This leads to an increase of the total adhesion force in the direction of the locking. In the context of this adhesion mechanism, it is important to mention the measurement of the surface roughness and specific surface area which indicates the possibility for mechanical interlocking.^{15,118,120} While these factors could give a hint, there could, however, also be strong adherence even in the case of flat or smooth substrates.¹¹⁸

2.3.3 Electrostatic/electronic adhesion theory¹¹⁸

It is clear that all materials have an electronic structure caused by their molecular structures. Thus, all materials have an electrostatic effect when they come into contact.¹¹⁸ Consequently, there will be an electrical double layer (EDL) in the 2-phase interface, which leads to electrostatic forces affecting the adhesion, for instance, between a polymer and metal.¹¹⁸

2.3.4 Diffusion theory

The molecules of the two components (adhesive and adherend) affect the adhesion mechanisms caused by the Brownian Movement.^{121,123} The resulting concentration differences and gradients in the interface lead to a steady state of diffusion.¹²¹ Here, the concentration changes are independent on time, and a fluctuation F_x can be summarized in the first Fick's law in x-direction with the diffusion constant D (adapted from literature including literature in there):¹²¹

$$(7) \quad F_x = -D \left(\frac{\delta c}{\delta x} \right)$$

A more realistic description of the diffusion includes the concentration changes with time. Due to the unbalanced state, the second Fick's law has to be written with all three spatial dimensions x , y and z (adapted from literature including literature in there):¹²¹

$$(8) \quad \left(\frac{\delta c}{\delta t} \right) = D \left(\frac{\delta^2 c}{\delta x^2} + \frac{\delta^2 c}{\delta y^2} + \frac{\delta^2 c}{\delta z^2} \right)$$

In addition, the diffusion constant D is influenced by the “strength of the atomic bond of the solid” and by the “mechanism for diffusion” like mentioned by Lee et al. with corresponding literature in there.¹²¹ Glasstone, Laidler, and Eyring could show that the diffusion constant D is dependent

on the elementary jump length λ and the temperature T mentioned by Lee.¹²¹ The following equation (9) features further constants like Boltzmann's constant k , Planck's constant h , F^\ddagger defined as standard free energy of activation per mole, the free energy at the ground state F , the elementary jump length of particles λ and the activation energy per molecule at 0 K expressed as ϵ^0 , which affects the diffusion constant D (adapted from literature including literature in there):¹²¹

$$(9) \quad D = \lambda^2 \frac{kT}{h} \cdot \frac{F^\ddagger}{F} \cdot \exp\left(-\frac{\epsilon^0}{kT}\right)$$

Especially in the case of two adhered polymers being in contact, the diffusion has a strong influence on the adhesion.^{118,121}

2.3.5 Electrostatic forces from electrostatic double-layer (EDL)¹⁵

Due to the high dielectric constant of water ($\epsilon_{H_2O} = 78.4$ at 25 °C)¹⁵, the hydration of metal ions from metals in water-based electrolytes can be favored and lead to charged metal surfaces.¹⁵ Based on electrostatic interactions of positively and negatively charged ions and surfaces, the surfaces adsorb ions or separate ions from the surface, creating an electric field. The adsorbed counter ions forming different layers on the surface are summarized as “electric double layer” (EDL).¹⁵

In principle, there are different models describing the complex adsorption states and layers of the EDL. The first adsorbed layer of counter ions was described by Helmholtz. The counter ions are adsorbing at the counter charged positions and cannot reach a thickness higher than a molecular layer like in a plate capacitor named the “Helmholtz layer”.¹⁵ This simplest model was improved by Gouy and Chapman by taking the thermal fluctuation of ions into account. The model was complemented by the addition of an extended “diffuse layer” where the counter ions could also be removed from the charged surface and move into the diffuse layer.¹⁵ Otto Stern (Nobel prize in physics in 1943¹⁵) published a combination of both models from Helmholtz and the diffuse layer theory into his “Stern layer” model illustrated in Figure 8. The model contains an inner layer named Stern layer and an outer part called diffuse layer or Gouy layer from the Gouy-Chapman model. In the latter, it is possible to express the Poisson-Boltzmann statistic for the mobile ions for the coordinate normal to the plane x in the diffuse layer (for an infinitely extended planar surface) (adapted from literature including literature in there):¹⁵

$$(10) \quad \frac{d^2\psi}{dx^2} = \frac{c_0 e}{\epsilon \epsilon_0} \cdot \left(\exp\left(\frac{e\psi(x)}{k_B T}\right) - \exp\left(-\frac{e\psi(x)}{k_B T}\right) \right)$$

2 Fundamentals

Equation (10) contains the bulk concentration c_0 , e as the elementary charge constant, the relative permittivity ϵ , the vacuum permittivity/electric constant ϵ_0 , k_B for Boltzmann's constant, T for the temperature and $\psi(x)$, the potential dependent on the distance x from the surface with $\psi_0 = \psi(x = 0)$ defined as “surface potential”. This surface potential ψ_0 is marked in the Figure 8 as the inner Helmholtz plane (IHP) and contains the permanent adsorbed ions and water molecules. The latter have been illustrated as circles with their dipole moments as arrows.

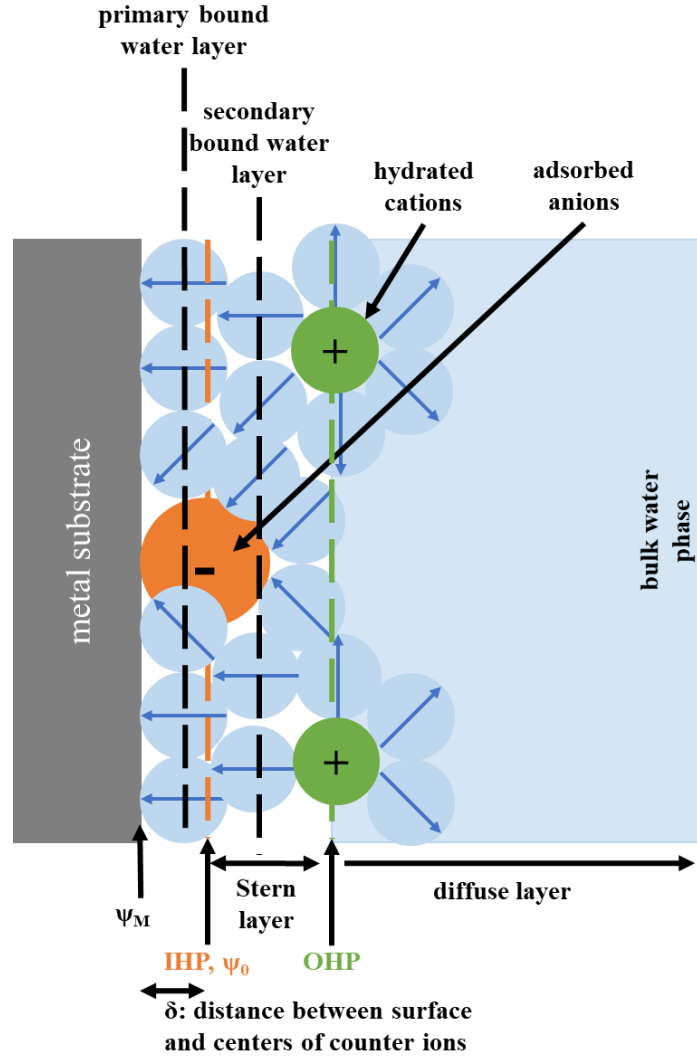


Figure 8. Principal structure of the electric double layer based on the Stern model (adapted from Butt et al. including literature in there¹⁵).

In context of charged surfaces, the “zeta potential ζ ” is a characteristic value for the description of interfacial processes. As illustrated in Figure 8 the EDL is a result of specific adsorbed ions which are more or less fixed on the surface. Consequently, some adlayers on the surface lead to shear plane with a specific distance to the surface where the ions start to be movable. At this position/ shear plane the zeta potential ζ is measurable and represent the hydrodynamic interfacial region.¹⁴

2 Fundamentals

For “low” potentials in the range of $e|\psi| \ll k_B T$ (at room temperature around $\psi \leq 25$ mV), it is common to approximate equation (10) to (adapted from literature including literature in there):¹⁵

$$(11) \quad \frac{d^2\psi}{dx^2} = \frac{c_0 e}{\epsilon \epsilon_0} \cdot \left(1 + \frac{e\psi}{k_B T} - 1 + \frac{e\psi}{k_B T} \pm \dots \right) \approx \frac{2c_0 e^2}{\epsilon \epsilon_0 k_B T} \cdot \psi$$

In the literature this expression is commonly called as the “linearized Poisson-Boltzmann equation” which has the following solution (adapted from literature including literature in there):¹⁵

$$(12) \quad \psi(x) = C_1 \cdot \exp\left(-\frac{x}{\lambda_D}\right) + C_2 \cdot \exp\left(\frac{x}{\lambda_D}\right)$$

The constants C_1 and C_2 can be found as $C_1 = \psi_0$ and $C_2 = 0$ when defining the following boundary conditions:¹⁵

- 1) The potential at the surface $x=0$ is the surface potential ψ_0
- 2) for infinitely large distances x , the potential ψ will be zero¹⁵

Then, equation (12) can be written as (adapted from literature including literature in there):¹⁵

$$(13) \quad \psi(x) = \psi_0 \cdot \exp\left(-\frac{x}{\lambda_D}\right)$$

Therefore, λ_D is the Debye length, which is the length at which the potential ψ has decreased to $1/e$ (e means Euler’s number in this case) and is given by the following expression (adapted from literature including literature in there):¹⁵

$$(14) \quad \lambda_D = \sqrt{\frac{\epsilon \epsilon_0 k_B T}{e^2 I}}$$

In equation (14), the variable I is the ionic strength in particles per m^3 to set the Debye length in m.¹⁵

The fact that the adhesion force depends on the surface potential and the Debye length can be shown by taking the example from Butt et al. for two identical surfaces brought in contact which are approximated as infinitely extended solids.¹⁵ The repulsive force per unit area $f(x)$ dependent on the distance x can be expressed in the following way (adapted from literature including literature in there):¹⁵

$$(15) \quad f(x) = \frac{2\epsilon\epsilon_0}{\lambda_D^2} \cdot \psi_0^2 \cdot \exp\left(-\frac{x}{\lambda_D}\right)$$

In general situations it can be said that the electrostatic double layer force is exponentially decreasing with the quotient distance x /Debye length λ_D . Furthermore, it can be used for the DLVO (from Derjaguin, Landau, Verwey and Overbeek) theory in combination with the attractive van der Waals forces. For more information, the reader is referred to the literature.¹⁵

2.3.6 Van der Waals interactions

Johannes Diderik van der Waals could show that all molecules, even nonpolar ones, have electrostatic interactions.¹⁵ His first observation of condensed gases as liquids by reduced thermal movement was that every molecule and, identified later, even two bodies have these van der Waals forces.^{15,26}

The simplest interaction between two charged ions or charges is the electrostatic interaction which is called Coulomb force $f(D)$ and expressed in the following general equation in vacuum state (adapted from literature including literature in there):¹⁵

$$(16) \quad f(D) = \frac{q_1 \cdot q_2}{4\pi\epsilon\epsilon_0 D^2}$$

Here, q_1, q_2 are the charges and D the distance between these two charges.

However, some molecules have no net electric charge.¹⁵ For that reason, it is more interesting to take a look at the monopole-dipole interaction. The dipole is considered fixed without any movement (theoretical approach). By taking the thermal energy resulting in random fluctuations of the dipole into account, one obtains the following expression for the free energy $W_{m-rd}(D)$ of a monopole-rotating dipole (m-rd) (adapted from literature including literature in there):¹⁵

$$(17) \quad W_{m-rd}(D) = -\frac{q^2 \mu^2}{6(4\pi\epsilon_0)^2 k_B T D^4}$$

The thermal energy is given by $k_B T$, the distance D means the path between the middle of the length of the dipole moment μ and the charge q . With increasing temperature T , the free energy $W(D)$ of the charge-dipole interaction will decrease caused by random movements including suboptimal orientations. Additionally, the free energy $W(D)$ will reach zero at infinite thermal

energy or distance.¹⁵ The dipole moment μ can be expressed as the integral of the total charge q over the total volume V (adapted from literature including literature in there):¹⁵

$$(18) \quad \vec{\mu} = \int q(\vec{r})\vec{r}dV$$

A more relevant interaction mentioned in this context are the Keesom interactions. These permanent dipoles interact due to their dipole moments which are influenced by thermal movements mentioned above for the monopole-rotating dipole.¹⁵ For this molecule interacting situation under thermal influence, the following equation can be given for the free energy of two rotating dipoles (rd-rd) (adapted from literature including literature in there):¹⁵

$$(19) \quad W_{\text{rd-rd}}(D) = -\frac{\mu_1^2 \mu_2^2}{3(4\pi\epsilon_0)^2 k_B T D^3}$$

Moreover, the interactions called Debye forces can be placed in the context of van der Waals forces. Here, an induced dipole moment (id) is newly-created, for instance, by a charge or by a permanent dipole moment in a polarizable molecule.¹⁵ In the first case, the Helmholtz free energy between a monopole m with the charge q and an induced dipole moment μ_{ind} is given by the following equation (adapted from literature including literature in there):¹⁵

$$(20) \quad W_{\text{m-id}}(D) = -\frac{q^2 \alpha}{2(4\pi\epsilon_0)^2 D^4}$$

With the polarizability α and the electric field strength E (adapted from literature with literature in there):^{14,15}

$$(21) \quad \mu_{\text{ind}} = \alpha E$$

In the latter case of a stabile dipole and the corresponding induced dipole, equation (20) changes to (adapted from literature including literature in there):¹⁵

$$(22) \quad W_{\text{m-id}}(D) = -\frac{\mu^2 \alpha}{(4\pi\epsilon_0)^2 D^6} = -\frac{C_{\text{ind}}}{D^6}$$

The third category is built up by the London or Dispersion interactions which explain the interactions between complete nonpolar molecules like, for instance, poly(propylene) in the

context of this work. In this case, the high-frequency (for example 10^{15} - 10^{16} Hz¹⁵) electronic fluctuations of the electron densities lead to a temporary induced dipole moment by the neighbored molecules. Therefore, the calculation can only be performed by using quantum mechanical methods which are not considered in this work.¹⁵ In general, it can be summarized that all mentioned contingents are in total called the van der Waals forces.

In the following chapters “2.3.6.1 Van der Waals forces – Hamaker approach¹⁵” and “2.3.6.2 Van der Waals forces – Lifshitz theory” the van der Waals interactions between molecules and solids will be explained by fundamental approaches.

2.3.6.1 Van der Waals forces – Hamaker approach¹⁵

The total van der Waals forces between two dipoles can be summed up by taking into account all three mentioned dipole-dipole interactions mentioned above: Keesom, Debye and London. These can be summarized in a constant C_{AB} which means the summation of all constants of all three contributions as used, for example, for the Debye interactions in equation (22) as C_{ind} . The Hamaker approach or microscopic approach for determining the resulted adhesion force based on van der Waals interactions starts with the interaction between a molecule A and a solid body B, where D is the distance from each other and x is the distance between the particles in the condensed material of the body B to the surface of the body B. To create an overall force of the separated body and particle, an integration of the molecular density ρ_B over the solid B has to be performed. It is even possible to do this for two bodies A (with molecular density ρ_A) and B by integration over the volumes. One assumption is that the two bodies are infinitely large and another one is that the molecules in the two bodies are not affecting each other.^{15,124} “The van der Waals energy per unit area is”¹⁵ (adapted from literature including literature in there):¹⁵

$$(23) \quad W_{2 \text{ surf}}^A = \frac{V}{A} = -\frac{\pi C_{AB} \rho_A \rho_B}{6} \int_0^\infty \frac{dx}{(D+x)^3} = -\frac{\pi C_{AB} \rho_A \rho_B}{12D^2}$$

With the Hamaker constant A_H and the force f^A per unit area the following equation for the two flat surfaces with the distance D between them can be obtained (adapted from literature including literature in there):¹⁵

$$(24) \quad f_{2 \text{ surf}}^A = -\frac{dW_{2 \text{ surf}}^A}{dD} = -\frac{A_H}{6\pi D^3}$$

This approach can also be performed for two spheres, where R_1 and R_2 are the radii of the spheres and D the distance between them. For the van der Waals energy the following equation (25) arises (adapted from literature including literature in there):¹⁵

$$(25) \quad W_{2 \text{ spheres}} = - \frac{A_H}{6D} \frac{R_1 R_2}{R_1 + R_2}$$

Consequently, the following force law can be written as (adapted from literature including literature in there):¹⁵

$$(26) \quad f_{2 \text{ spheres}} = - \frac{A_H}{6D^2} \frac{R_1 R_2}{R_1 + R_2}$$

An analogous procedure leads to equation (27) for the case of a flat, planar surface in contact with a sphere of radius R_p (adapted from literature including literature in there):¹⁵

$$(27) \quad W_{\text{surf-sphere}} = - \frac{A_H R_p}{6D}$$

It follows for the force (adapted from literature including literature in there):¹⁵

$$(28) \quad f_{\text{surf-sphere}} = - \frac{A_H R_p}{6D^2}$$

Due to the assumptions of an infinite large body, the Hamaker approach fails at non-ideal system including roughness like step edges, holes, gaps etc. Thus, the contributions cannot be aggregated additively. In addition, at higher and lower distances these two effects are strongly influencing this theoretical approach of Hamaker.^{15,125} One popular example for high van der Waals forces is the Gecko. He has a lot of spatulas which can fit the low roughness even on mainly flat surfaces to increase the contact area.¹⁵

2.3.6.2 Van der Waals forces – Lifshitz theory

Van der Waals forces are based on electric-magnetic fluctuations between contacting particles. Furthermore, all particles in condensed materials have individual oscillators which can be described by different optical experiments.^{15,126} Starting with the same approach as in the Hamaker method, the most prominent case is the contact of two plates/slabs. For this, three different dielectric bodies (two plates and one for the gap in-between) are useful for the description.¹⁵ This

idea of Dzyaloshinskii and Pitaevskii was the extension of the model of Lifshitz¹⁵ and it will in the following be referred as the Lifshitz theory. The main goal of this theory is the calculation of the Hamaker constants and forces from optical dielectric properties.^{124,126} The theory is based on the exchange of virtual photons between the three materials. The larger the distance x between the two plates, the longer is the path of the virtual photons.¹⁵ Consequently, at higher distances x the interactions are hindered by the phase separation or the film in-between.¹⁵ Moreover, a total Hamaker coefficient A_{123} has to be introduced in the context of the Lifshitz theory. Thereby, the magnetic contributions can be neglected in the most cases, simplifying the equations.¹⁵

It is possible to find an approximate equation for the case of two plates in contact with a film with a thickness l , which can be found in the literature.^{15,126} However, a numerical calculation of A_{123} can be formulated as (adapted from literature including literature in there):¹⁵

$$(29) \quad A_{123} = \frac{3}{2} k_B T \sum_{m=0}^{\infty} ' \sum_{s=1}^{\infty} \frac{[\Delta_{13}(i\omega_m) \Delta_{23}(i\omega_m)]^s}{s^3}$$

Here, k_B is Boltzmann's constant and T is the temperature. In addition, the following equation (30) is considered (adapted from literature including literature in there):

$$(30) \quad \Delta_{ij} = \frac{\varepsilon_i(i\omega_m) - \varepsilon_j(i\omega_m)}{\varepsilon_i(i\omega_m) + \varepsilon_j(j\omega_m)}$$

The ω are the so-called Matsubara angular frequencies¹⁵, while the London dispersion dielectric response function $\varepsilon(i\omega)$ can be described by the Kramers-Kronig expression (adapted from literature including literature in there):¹⁵

$$(31) \quad \varepsilon(i\omega) = 1 + \frac{2}{\pi} \int_0^{\infty} \frac{\omega' \varepsilon''(\omega')}{\omega'^2 + \omega^2} d\omega'$$

Here, ε'' is the imaginary part of the dielectric function.

Finally, to create an easier to handle expression for A_{123} , it is common to reduce the sum over s in equation (30) to its first summand (adapted from literature including literature in there):¹⁵

$$(32) \quad A_{123} = \frac{3}{2} k_B T \sum_{m=0}^{\infty} ' [\Delta_{13}(i\omega_m) \Delta_{23}(i\omega_m)]$$

Based on equation (32), the Hamaker constant depends only on the differences in the dielectric properties of the materials 1, 2 and the layer 3 in-between.¹⁵ It is problematic that the $\varepsilon(i\omega)$

functions are not available for the whole relevant frequencies iv. Consequently, some approximations should be used to access the Hamaker constant more easily. For example, the Tabor-Winterton approximation leads to a dielectric response function $\varepsilon(i\omega)$ with the refractive index n and the plasma frequency ν_e around $3 \cdot 10^{15}$ Hz (adapted from literature including literature in there):^{15,126}

$$(33) \quad \varepsilon(i\omega) = 1 + \frac{n^2 - 1}{1 + \frac{\omega^2}{(2\pi\nu_e)^2}}$$

It follows with equation (32) for the Hamaker constant A_{123} (adapted from literature including literature in there):^{14,15}

$$(34) \quad A_{123} = \frac{3}{4} k_B T \left(\frac{\varepsilon_1 - \varepsilon_3}{\varepsilon_1 + \varepsilon_3} \right) \left(\frac{\varepsilon_2 - \varepsilon_3}{\varepsilon_1 + \varepsilon_3} \right) + \frac{3h\nu_e}{8\sqrt{2}} \frac{(n_1^2 - n_3^2)(n_2^2 - n_3^2)}{\sqrt{n_1^2 + n_3^2} \sqrt{n_2^2 + n_3^2} \left(\sqrt{n_1^2 + n_3^2} + \sqrt{n_2^2 + n_3^2} \right)}$$

where h is the Planck constant.

Four main approximations have to be taken into account:¹⁵

1. Ultraviolet (UV) contribution is the most significant part – other frequencies are ignored
2. UV absorption is a close band – a single oscillator model is sufficient
3. Resonance frequency is in all three materials equal to the plasma frequency ν_e
4. Estimation: $n^2 = \varepsilon_{vis}$ – refractive indices are in the range of the visible light¹⁵

To sum up, all three materials have the same ionization frequencies. The first term of equation (34) contains the Keesom and Debye interactions ($\omega = 0$) while the second term contains the London dispersion interactions.¹⁵ For instance, in vacuum conditions ($n_3 = 1$) the second term can be neglected due to its small contribution and in the case of water with a high dielectric constant the first term will be significantly smaller than the second term in equation (34).¹⁵

2.3.7 Hard-Soft Acid-Base (HSAB) principle¹²¹

Another reasonable concept of molecular interactions in context of PAA/ZnO systems of this thesis are the acid-base or electron-donor-electron-acceptor interactions based on the principle proposed by Lewis.^{121,126} These interactions can have highly bonding energies around 80 kJ/mol¹⁴ which makes these kind of interactions very interesting for interfacial adhesion-promoting nanotechnology.^{127,128} Basically, all molecular interactions not categorized before, like hydrogen bridges or electrophile-nucleophile interactions can be classified as acid-base interactions.¹²¹ In

principle, a base with an electron pair interact with an acid having a partially positively charged character to create an acid-base complex.¹²¹

Now, the question arises how these charge transfers could be realized and explained by fundamental concepts. First, it is useful to introduce the meaning of the HOMO (highest occupied molecule orbital) and LUMO (lowest occupied molecule orbital) from frontier orbital concept.¹²¹ In principle, Figure 9 illustrates, on the left-hand side, the interactions between two discrete molecules and, on the right-hand side, the interaction possibilities of orbitals of one molecule with the surface of a metal.

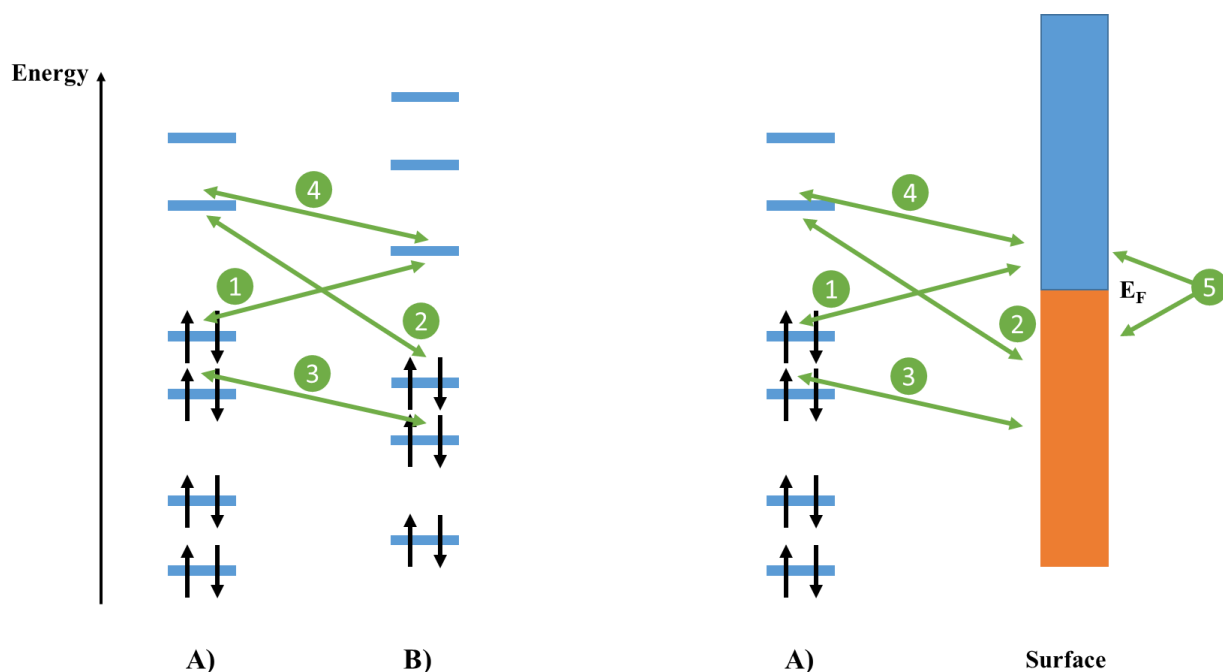


Figure 9. Schematic summary of orbital interactions - left side: interactions in discrete molecules, right side: molecule-surface orbital interactions (based on Hoffmann et al.¹²⁹ including literature in there).

The interactions of an electron-donor with an electron-acceptor are pointed out with the green lines marked with 1 and 2 in the left-handed side in Figure 9. In charge-transfer 1, the HOMO of the first molecule A) (electron-donor or base) is transferring charge/electrons to the LUMO of the other molecule B) (electron-acceptor or acid) by a two-orbital – two-electron stabilizing interaction and vice versa in 2.¹²⁹ This could also lead to a molecule-surface interaction as illustrated on the right side in Figure 9. The Fermi level marked as E_F can be described as the HOMO of the metal on top of the valence band.^{121,129} These electrons can be transferred to the LUMO of the molecule (green line 2 on the right side). A repulsive interaction illustrated by green line 3 in both cases (molecule-molecule and molecule-surface interaction) means an interaction between two fully occupied orbitals (two-orbitals, four-electron interaction), leading to destabilizing interaction properties.¹²⁹ In comparison to 3, the green line 4 generates no energy (de-)stabilizing effect for two interacting molecules. Interestingly, in the case of the molecule-surface interaction the LUMO

of the molecule can be reduced by a bonding process caused by the continuum properties of the levels in the metal.^{121,129} Reaching an energy level lower than the Fermi level generates a net energy effect on the surface.^{121,129} All mentioned interactions are influencing the energy levels of the metal. These primary interactions are mainly compensated by the electrons of the metal from the bulk to open the possibility to form bindings to adsorbates on the surface. Finally, a second different option in comparison to the molecule-molecule case is possible in the case of the molecule-surface: interaction 5 in Figure 9. The fluctuation of electron density around the Fermi levels open the door to shift electrons from the valence band into the conduction band.¹²⁹

A general qualitative description based on the mentioned frontier orbital concept leads to the main aspects of the HSAB principles (adapted from literature¹²¹ including literature in there):

1. The energy level of the LUMO of acids/electron-acceptors (hard electrophiles – mostly positively charged) is high – for soft electrophiles (could be positively charged, but not essential) the opposite applies with a low-energetic LUMO¹²¹
2. Negatively charged hard nucleophiles (bases, electron-donors) consist of a low-energy HOMO while soft nucleophiles have a high-energy HOMO¹²¹

2.3.8 Hydrogen bridges

The hydrogen bridges are only possible when a characteristic structure can be found in the two attracting molecule species as described above as donor-acceptor interactions.¹²³ Therefore, the interactions are only possible when two atoms in the molecules have high differences in their electronegativities that an interaction like A-H---B occur.¹²³ The most prominent atoms are N, O and F which lead to hydrogen bridges.¹²³ One typical description of hydrogen bridges is the overlapping of atom orbitals for the creation of temporary molecule orbitals. More details can be found in the literature.¹²³ At least the total reduction of the energies from the molecules leads to a generation of a hydrogen bridge.

The most well-known example for hydrogen bridges can be found in water molecules where one O-H group is interacting with the free electron pair of an O-atom from another water molecule. For the creation of such short-range interactions, it is necessary that both species have a short distance. Consequently, hydrogen bridges contribute to the total adhesion, having a relatively high binding energies of around 20 kJ/mol¹²³ (or 10-25 kJ/mol^{14,15}) up to 40 kJ/mol when involving fluorine.^{14,15}

However, the transfer from the model based interpretations of interfacial forces and degradation phenomena to real buried polymer/metal oxide interfaces is still a challenge.¹²⁷

2.4 Adhesion mechanisms at metal oxide surfaces

The previous chapter “2.3 Theories of adhesion mechanisms” demonstrated the presence of different adhesion phenomena playing a major role in adhesion properties of materials. Indeed, in the case of metal oxide surfaces the most of these effects strongly influence the molecular adhesion properties.

Firstly, it could be seen that charging and electrostatic effects dominate the structure and composition of the EDL. Here, the isoelectric point (IEP) is an important value. It is defined as the electrolyte condition/state where the concentration(pH) of surface-potential-determining ions like hydroxyl or hydronium ions form a total zeta potential of null ($\zeta = 0$).¹⁴ Moreover, the surface charge σ is affected by the surface groups charging the surface and can be determined under specific conditions (low potentials, one-dimensional Poisson equation and for large distances the potential is zero) by the Grahame equation (adapted from literature including literature in there):¹⁴

$$(35) \quad \sigma = \frac{\epsilon\epsilon_0\psi_0}{\lambda_D}$$

In contrast to the IEP, the surface charge σ given in equation (35) is zero at the “point of zero charge” (PZC). The IEP and the PZC are highly influenced by the surface composition, defects, homogeneities etc. In the case of metal oxides such as ZnO, TiO₂ and Al₂O₃ the surface groups are able to dissociate: ion release and take up.¹⁴ For instance, a polar ZnO(0001)-Zn surface has a stabilization mechanism with an adlayer of hydroxyl groups like shown in following Figure 10.

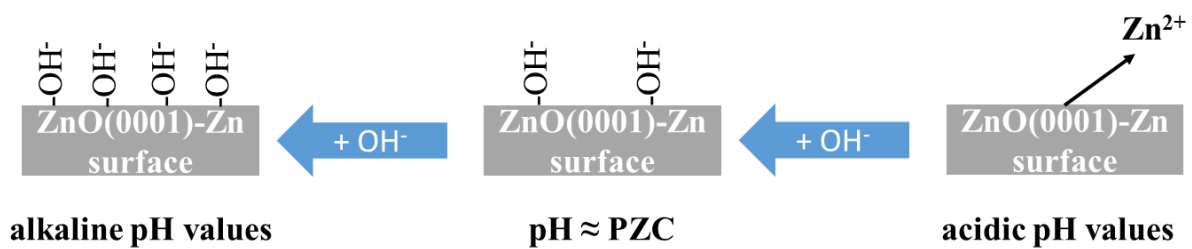


Figure 10. Schematic illustration of equilibrium reactions at different pH values ranging from alkaline values to acidic pH values for an ideal polar ZnO(0001)-Zn surface (based on Valtiner et al.^{27,62–64}).

With regard to the molecular adhesion, the PZC and IEP under defined experimental conditions (chemical surface composition, surrounding media/electrolyte components, morphology, etc.) determine the surface charging and hydroxylation. Both would strongly affect the molecule-surface interactions, as previously explained in chapter “2.3 Theories of adhesion mechanisms”. For instance, a highly hydroxylated surface like polar ZnO(0001)-Zn under alkaline conditions offer the possibility of hydrogen bridges, while at the PZC a neutral surface charge would slow

down the affinity for the adsorption of charged molecules (compare electrostatic interactions/coulomb interactions above). In the case of a mainly hydroxylated stainless steel surface (FeOOH) and a D-Ala-D-Ala peptide used by Landoulsi et al., hydrogen bonds and van der Waals are favored.¹³⁰

The latter dispersive interactions in the particle level depend on the electronical properties of the interacting materials and the medium in-between like demonstrated above in equation (32) for the determination of the Hamaker constant. Therefore, the calculation/determination of the Hamaker constants of the pairing (media 1, 2 and 3) based on the different dielectric functions is essential for the fundamental understanding of van der Waals interactions at metal oxide surfaces. For instance, with the use of the Hamaker constant, the calculation of the presented forces in chapter “2.3.6 Van der Waals interactions” can be performed and compared with experimental data.

Moreover, the electron acceptor and electron donor properties (acid-base interactions) (see chapter “2.3.7 Hard-Soft Acid-Base (HSAB) principle¹²¹”) like chloride are involved in the corrosive and adhesive interfacial interactions and can lead to the collapse of metal oxide–polymer interactions.^{131,132} A prominent example is the amine- Al_2O_3 interaction where the electron pair of the amine can interact as the electron donor while the partial positively polarized aluminum atom of the metal oxide surface is the electron acceptor. This “Lewis-like mechanism” can also be described in the case of $\text{Al-OH}\cdots\text{N}$ -interactions. In the case of organic contaminations, typical “monodentate and bidentate metal-bond surface complexes” can be formed.¹³³ For instance, the interfacial bonding mechanisms also influence the interphase formation and are very interesting for epoxy-amine resins like used in this PhD thesis.¹³⁴

Indeed, the chemical and electronical surface chemistry is an essential factor for the performance and properties of the interfacial adhesion. However, in the context of surface engineering the most common adhesion mechanism is based on mechanical interlocking on defined grown oxide layers and (nano-)structures resulting in a higher contact surface area while reaching an improved macroscopic adhesion performance. With this aim, a lot of methods for pretreatment of metal alloys and oxides have been established like mechanical (e.g., blasting with alumina grit or with glass beads¹³⁵, ultrasonication^{136,137}) and chemical treatments^{138, 139}. For instance, the deposition of ZnO nanorods on zinc substrates for adhesion enhancement³⁴ and the growth of nanotubes on Ti surfaces for influencing the bone cell-material interaction¹⁴⁰ and cell adhesion¹⁴¹ are available in the literature.

Moreover, in context of macroscopic adhesion of metal oxides in light weight constructions and adhesive bonding, aluminum materials with defined oxide surfaces are essential.^{138,142} Consequently, a lot of pretreatments for aluminum alloys have been developed and reviewed.⁴⁷ For instance, Johnsen et al. have demonstrated that the different anodization parameters of the Al

alloy AA6060-T6 like several acid concentrations, current densities and bath temperatures, to mention only a few, strongly influence the bonding performances of the XD4600 epoxy adhesive under different relative humidities.¹³⁸ TEM cross-sections showed the interfacial thick oxide layers in contact with the epoxy adhesive. Moreover, the work of Dillingham et al. showed the analysis of the interfacial structure of Al-epoxy adhesive joints for the improvement of structural bonds.¹⁴³

2.5 Poly(acrylic acid)-ZnO interfaces in advanced materials

2.5.1 Examples of PAA-ZnO interface dominated materials

Macromolecular PAA has broad fields of applications like in medicine, pharmacy (drug delivery), nanotechnology and material science.^{144–148} The most popular application of poly(acrylic acid) materials is based on their superabsorbent properties. For instance, Zhao et al. studied the superabsorbent capabilities for ethanol of PAA synthesized via radical polymerization and Zn^{2+} ions as a cross-linking component.¹⁴⁹ The authors showed that a concentration of 83.2 mmol/l of Zn^{2+} ions leads to the highest absorption capacity of around 160 g ethanol per g PAA salt.¹⁴⁹ Many publications where zinc ions are in contact with PAA are available.^{150–153} For instance, Abzaeva et al. have focused their study on the zinc carboxylate (defined as ziacrlyl) of the PAA salt as a drug for pharmacological properties due to its antimicrobial, hemostatic and wound-healing properties.¹⁵³ The authors checked the healing process of skin burns and aseptic skin wounds in mice.¹⁵³ In addition, tests involving different microorganism species in contact with different ziacrlyl concentrations were carried out.¹⁵³ Another broad field of PAA/zinc applications is associated with cements containing different PAA/ZnO-apatite mixtures for dental applications.^{154,155}

Consequently, many fundamental studies dealing with ZnO particles in contact with PAA can be found, some works even deal with composites of ZnO and PAA.^{156,157} Padilla et al. have tested a cured ZnO/PAA mixture without water.¹⁵⁷ For different ZnO/PAA ratios and curing times they analyzed mechanical properties such as compressive strength and fracture strength.¹⁵⁷

Another interesting study of the production of a zinc-PAA based material was published by Chen et al. in *Crystal Growth and Design* in 2009.¹⁵⁸ The authors were able to use PAA-assisted electrospinning for the synthesis of polycrystalline zinc-oxide nanotubes.¹⁵⁸ Zn^{2+} ions stabilized the polyanion in aqueous solution to prepare nanofibers in the first step. At higher temperatures the calcination, degradation of the polymer matrix, and the formation of ZnO in the outer layers occur. Due to the decomposition of the polymer at higher temperatures, the nanofibers starts to become hollow.¹⁵⁸

The work by Brostow et al. opens the door for polymer coatings fabricated from aqueous solutions to create PAA/zinc diacetate hybrid composites.¹⁵⁹ The as-produced materials can be used as coatings with “high durability and low friction”¹⁵⁹ properties.

2.5.2 Interactions and molecular adhesion studies of poly(acrylic acid) on ZnO surfaces

A fundamental study on the adsorption of PAA for different oxidized metals including Si, Ti, Fe, Al, Cu and Ni was performed by Leadley and Watts.¹⁶⁰ PAA shows different bonding mechanisms from hydrogen bonding, weak basic interactions via the carboxylate anion state, and a strong base interaction via an acyl nucleophilic attack.¹⁶⁰ Yan et al. demonstrated that PAA-Zn/ZnO films strongly improve the anti-corrosion properties on iron substrates in NaCl solutions.¹⁵² The adsorption of pure PAA on iron leads to a weak anti-corrosion performance while the complexation of the Fe-PAA films with solutions containing Zn^{2+} show the highest anti-corrosion properties in impedance spectra.¹⁵²

In the context of this thesis, the adsorption mechanisms of PAA on ZnO-surfaces are of high relevance. In a first approximation, the complexation properties of zinc in solution of PAA molecules are considered. Here, the work of Tomida et al. should be mentioned.¹⁵¹ They found that with divalent zinc ions the following complexations are possible in aqueous solutions: LZn^+ , L_2Zn , $\text{L}_2\text{Zn}(\text{HL})_2$, (L denotes the ligand here PAA with carboxylate groups) depending on the pH of the solution and the ratio of the concentrations of zinc ions and PAA.¹⁵¹ Further fundamental studies, including the kinetic analysis of the reaction between zinc oxide and PAA, has been carried out by Wu et al. with infrared spectroscopy.^{161,162} Based on these results, a binding state of a mono- and bivalent behavior between zinc and PAA was proposed.¹⁶¹ However, it has to be noted that these situations are fundamental approaches for the analysis of binding states in liquid and occurring between free metal ions, and, consequently, may vary at ZnO surfaces.

In a more surface-related study, Degen et al. performed a fundamental analysis of the adsorption of poly(acrylic acid) on ZnO powders.¹⁶³ The positive surface charge of the ZnO particles has a strong influence on the adsorption capabilities of the dispersant. In addition to that, Dang et al. showed the ZnO particle dissolution with sodium PAA salt suspensions at pH 7.¹⁶⁴

Another relevant publication with regard to the adhesion properties of PAA coatings on metal oxides like zinc phosphate hydrate has been reported by Sugama et al. in the *Journal of Materials Science* in 1984.¹⁶⁵ This work indicates that the PAA macromolecules change their conformation in order to carry out acid-base interaction on the hydroxyl rich metallic surface. The COOH groups are able to perform chemisorption on the polar OH groups of the metallic surfaces.¹⁶⁵ The authors could find a shoulder in infrared data in the case of zinc phosphate hydrate coated on iron samples at 1550 cm^{-1} assigned to COO^- groups performing the acid-base surface interaction.¹⁶⁵ The acid

COOH groups could hypothetically realize a divalent metallic crosslinking reaction by forming $\text{Zn}^{2+}\text{-OOC-}$ interactions.¹⁶⁵ Due to the high hydrophilicity of PAA, the coating with PAA to metallic surfaces could have excellent adhesion properties supported by a good spreading on hydroxyl group rich metal surfaces which even exhibit a good penetration of microstructures for high mechanical interlocking.¹⁶⁵

An atomic force microscopy (AFM) based approach for the adsorption study of PAA on stepped polar ZnO(0001)-Zn and nonpolar (10-10) surfaces of single crystals was done by Kunze et al.¹⁶⁶ The authors mentioned a “diffusion and trapping mechanism”¹⁶⁶ where the low adsorption energies on the hydroxyl-stabilized polar ZnO(0001)-Zn caused by low Van der Waals interactions and hydrogen bridges lead to a relative mobility for the PAA chains.¹⁶⁶ Electrostatic interactions through the solid-liquid interface were proposed as the major driving force for the deposition of PAA (macro-)molecules from the surrounding liquid medium. After this step, the diffusion of the chains to the edges of the nonpolar step edges takes place based on stronger binding mechanisms.¹⁶⁶ Here, high energetic interactions by coordinative bindings are suggested.¹⁶⁶ The specific adsorption at the nonpolar edges underline the results from Valtiner et al. who measured the molecular adhesion of PAA to edged polar ZnO(0001)-Zn single crystal surfaces.⁴³ Both results support the idea that the adsorption of PAA occurs especially with high adsorption energies at nonpolar facets of hexagonal ZnO crystals. However, the results obtained from these fundamental approaches dealing with the assessment of the molecular adhesion properties of PAA on single crystalline surfaces cannot be straightforwardly extrapolated to industrially relevant materials. On these technically relevant surfaces, additional parameters such as the roughness or systematically nanostructuring have to be taken into account as well. Therefore, the 1. publication of this PhD thesis investigates the molecular adhesion on real nanostructured surfaces.¹⁶⁷

2.6 Deposition of poly(acrylic acid) films

2.6.1 Electropolymerisation and electrografting of poly(acrylic acid)

The electrochemical approach for the coating of conductive materials with polymers has reached high scientific attention. The coating with grafted polymers produced by electrochemical induced polymerization has a lot of possible applications making this technique very interesting for future investigations.¹⁶⁸ One broad field of applications would be the corrosion protection based on the hindering and blocking properties of polymer layers on metallic parts with complex geometries.^{169–173} For instance, the group of Sabbatini could demonstrate that poly(acrylic acid) films were successfully deposited via electropolymerisation on titanium substrates which opens the door for physiological coatings with anti-corrosion and bioactive properties.¹⁷⁴ Another advantage of using electropolymerisation, is, in general, the precise control of the film thicknesses^{175,176} and

compositions by controlling the electrochemical parameters (e.g.: potential, time, current density) and electrolyte compositions (e.g.: different concentrations, simultaneous use of different monomers, pH, solvent).^{177–179} Indeed, electropolymerisation is an optimum tool for the precise and controlled deposition of polymer films like PAA on gold substrates from Zn^{II} based solutions demonstrated by Wang et al.¹⁷⁶

The interfacial regions have an immense influence on the electropolymerisation process and vice versa. Hung et al. increased the mechanical properties, especially the interfacial adhesion, of carbon fibers coated with the result of the electropolymerization of phenol, *m*-phenylenediamine and acrylic acid as monomers in epoxy resin composites.¹⁷⁰ Indeed, the enhancement in adhesion was also demonstrated by Bauer et al. on carbon fiber reinforced plastics by coating with PAA exhibiting different film thicknesses.¹⁸⁰ In addition, Subramanian et al. showed that the electropolymerisation on graphite fibers is successfully working for different copolymers including carboxyl functions.^{181–183} However, the usage of electropolymerisation with acrylic acid for the deposition of adhesion promoting thin coatings is still an open field. Furthermore, it is important to distinguish how the deposited coating interacts with the outer layers of the metallic oxide, which is strongly depending on the deposition method/conditions. The following Figure 11 presents polymer-surface interactions. Two different binding mechanisms of the polymer in the surface can be distinguished: i) physisorption and ii) covalent grafting of the polymers to the surface. Depending on the polymer and its deposition, different structures of the resulting polymer layer are formed. For instance, a physisorbed diblock copolymer has two different blocks with different functional groups (illustrated in orange and blue lines in image 1) in Figure 11. The blue polymer block called “block A” has a strong affinity to interact with the surface and it could be poorly soluble in the solvent. The second block, named “block B”, in this “A-B” diblock copolymer would be very soluble in the solvent. The “Brush” structure leads to a high density of the polymer and interacts with higher affinity to the solvent. Here, the radius of gyration of the polymer is an important feature which can be found in the literature in more detail.¹⁵

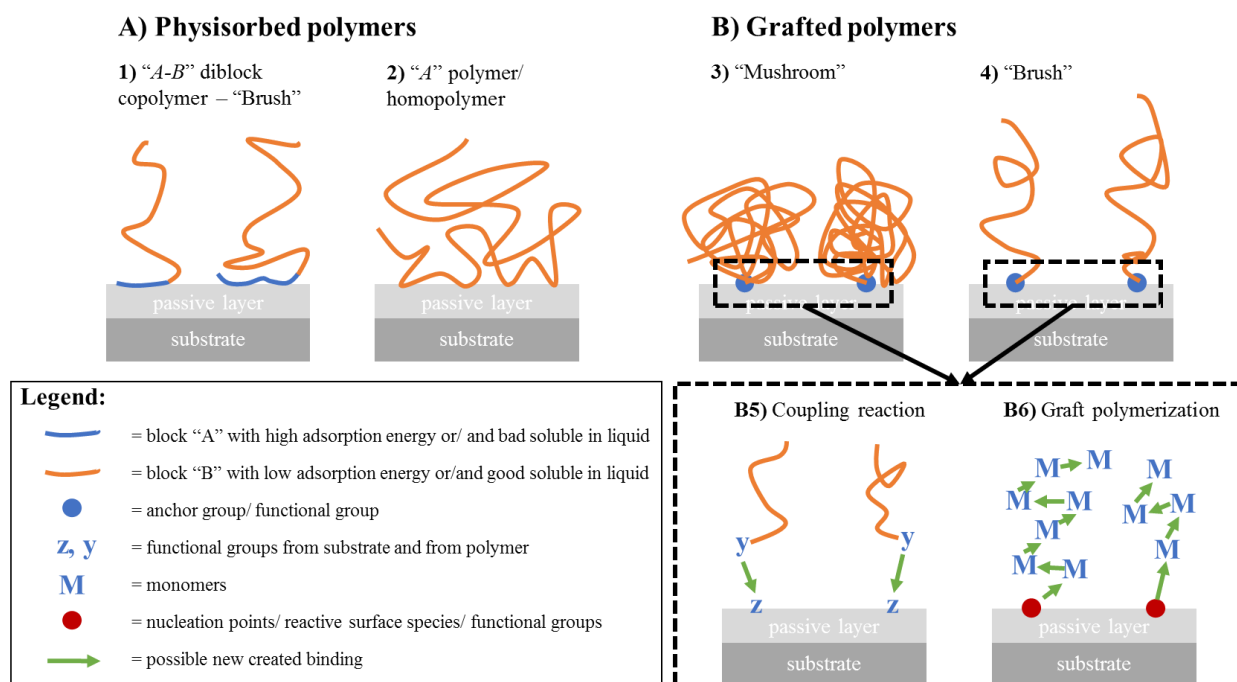


Figure 11. Schematic demonstration of deposited polymers on metallic substrates. The images in A) show physisorbed polymers: 1) diblock copolymer where one block strongly adsorbs on the passive layer, 2) homopolymer interacting with the passive layer. The grafted polymers in the images in B) show the “mushroom” like state in 3) and in 4) the “brush” state is illustrated. Both situations in B) could be generated via a “direct coupling reaction” or a “graft polymerization” with monomers (images adapted from and based on Butt et al.¹⁵ and from Uyama et al.¹⁸⁴ including literature in there).

In the case of a homopolymer, weak interactions with both the solvent and the surface (compare image 2) in Figure 11 can be observed. Then, only van der Waals, electrostatic interactions or hydrogen bridges can lead to low adsorption on the surface (compare chapter “2.3 Theories of adhesion mechanisms “). It is also possible to have polyelectrolytes under specific conditions, which opens the door for more complex adsorption processes due to electrostatic intra- and interactions.¹⁸⁴

The grafting of polymers on surfaces is illustrated in the Figure 11 B). The polymer density on the surface dependent on e.g. the polymer length is affecting the two different states of the grafted polymers: “mushroom” like deposition and “brush” state explained one paragraph before for the physisorbed polymers. Another interesting aspect is the growth mechanism of grafted polymers. In principle, two different mechanisms are possible: the direct coupling reaction of two functional groups (marked with “y” and “z” in image B5) in Figure 11) or the polymerization directly starting at the surface containing some starting points or “nucleation” points. To mention one example for grafting of poly(acrylic acid) on an oxide surface, Barroso-Bujans et al. investigated the grafting of PAA on aluminum with the free radical polymerization and chemical vapor deposition of acrylic acid with thermal polymerization.¹⁸⁵

Electrochemically initiated polymerization is based on a transfer reaction by means of polarization of the working electrode being in the most cases the metal substrate. The electropolymerisation of AA is possible due to the high chemical reactivity of the commonly used monomers. For example, the initiation of AA could even be started by the use of metallic centers like zinc cations¹⁸⁶ or copper cations.^{187,188} In general, there are two different possible ways to generate reactive species on the surface of the working electrodes (compare image B6) in Figure 11: the transfer of electrons to form a radical-anionic or an anionic species of the AA monomer.¹⁸⁹ Therefore, it is necessary to have an initiator molecule or cations like zinc cations which could be solved in the liquid phase of the electropolymerisation. Some authors are proposing that these Zn^{2+} cations could be adsorbed, reduced, and transfer electrons to the monomer molecules.^{175,180,189} A radical-anionic monomer-zinc species could then start the polymerization which is conventionally known as chain polymerization.¹⁸⁸ Anionic species are very instable regarding the reaction with other molecules like water or acids. In addition, the radicals can even react with oxygen (biradical character) and form stable species. So, to prevent the stop of the reaction, it is necessary to create oxygen free conditions.^{175,180} However, the exact reaction mechanisms, especially the initiation of the reaction at the interface, are still open questions and they are strongly depending on the complete system and experimental conditions, especially on the employed monomers.^{190–192} Indeed, it is difficult to differentiate between the grafted polymerization and the polymerization with strongly physisorbed polymers created by electrochemically initiated polymerization. Both show highly adhesion promoting properties in the case of acrylic acid.^{175,180}

2.6.2 Spray coating

2.6.2.1 Basics

A deposition method, simpler than the electropolymerization, for the coating of samples with defined film thicknesses would be the spray coating process. The probably broadest field of application is the automatic painting process in commercial production where a lot of patents can be found.¹⁹³ Thus, a spray nozzle/jet is connected to two tubes: the first one is used for the transport of a gas phase into the nozzle, while the second one is connected to a storage vessel filled with the spray coating solution. A schematic setup is displayed in the Figure 12.

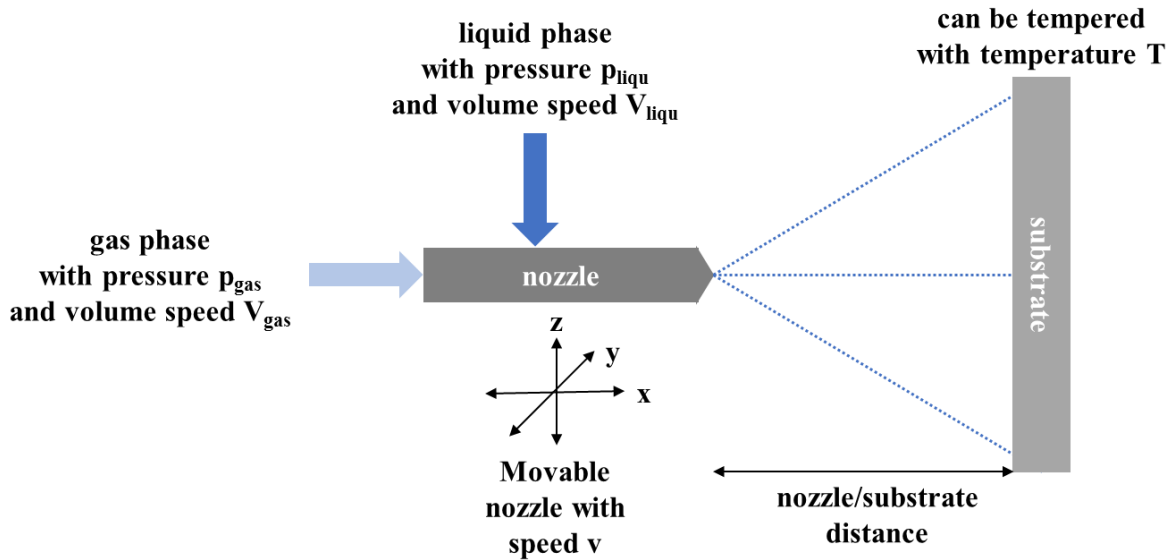


Figure 12. Basic illustration of an experimental spray-coating setup.

A lot of parameters influence the spray coating process, including the pressure and volume speeds of the liquid and gas phases, the motor speed of the nozzle or the sample, the nozzle/substrate distance and the substrate/fluid temperature.

Firstly, the injection system is important for the controlled pumping of the fluids.¹⁹⁴ Pawlowski mentioned three different general systems:¹⁹⁴

1. Liquid jet injection
2. Injection with atomizer
3. Penetration of liquid into jet

The first case describes the escaping liquid jet directly from a tube system. The geometry of the jet can be controlled by the tube itself. The second case contains, for example, a pneumatic nozzle with the use of two fluids. The external energy could be generated by controlled pressure or centrifugal forces as mentioned by Pawlowski.¹⁹⁴ The last case includes all experimental setups where a jet will be penetrated by the liquid. For that, a flame or a plasma phase could be entered by a liquid phase containing the coating material or precursors.¹⁹⁴

2.6.2.2 Different setup modifications and classes of spray coating methods

Caused by the complexity of the generally simple spray coating process, a lot of different groups or classifications of spray coating processes could be found in the literature, for example:

- 1) Cold spray coating/cold spraying^{195–197}
- 2) Thermal spray coating/thermal spraying^{198,199} including flame spray coating and plasma spray coating/plasma spraying^{200,201}
- 3) Spray pyrolysis²⁰²

- 4) Ultrasonic spray coating^{203,204}
- 5) Electrostatic spray coating^{205,206}
- 6) Layer-by-Layer (LbL) spray process^{207,208}
- 7) Airbrushing²⁰⁹

These classes are distinguished by their particular spray setup or by the materials used. For instance, the cold spraying, including powder spray coating, apply a solid powder (metals, ceramic, composites or polymers) by using a “de Laval” nozzle. With this convergent-divergent geometry, the particles could reach high speeds around 300 to 1200 m/s.¹⁹⁷ This differs from thermal spraying, where the particles do not reach the melting temperature in the gas stream.^{196,197} In context of thermal spraying, the material is directly melted inside the spraying system before it hits the surface of the substrate. This is typically used in industry sectors.^{198,199}

Plasma spray coating is linked to the flame spray coating process, in which a plasma jet could be generated between a cathode and an anode realizing an electric field. A plasma gas inlet can control the gas stream while a powder injection can be installed in front of the anode.²¹⁰

Moreover, thermal energy can also be applied to the substrate resulting in a tempered surface with a fixed temperature. A hot plate in the setup illustrated in Figure 12 can also be used. By spraying a salt or precursor solution onto the sample surface, the decomposition of the salt can be realized.²⁰² For instance, a zinc nitrate solution can be used for the deposition of ZnO films on basically every substrate.^{211,212}

An extra tool that generates ultrasonic vibrations in the spray nozzle open the door for ultrasonic assisted spray coating processes.^{203,204,211} For example, Tait et al. could precisely control the donor/acceptor ratio and thickness of ultrasonic spray coatings for organic solar cells.²⁰⁴ The experimental setup consists of two concurrent and coaxially pumped solutions containing donor and acceptor components to the ultrasonic nozzle.²⁰⁴

Furthermore, the electrostatic spray coating is a spraying process where an electrostatic atomizer is used.²⁰⁶ Here, the solution can be charged with a high voltage resulting in a net charge in the droplets. Due to repulsive interactions, the control of the droplets is improved.²⁰⁶ For instance, Kim et al. used electrostatic spraying for the deposition of silver nanowires on poly(carbonate) substrates.²¹³ Actually, the different setups and configurations can be combined to improve their effectiveness. For instance, the electrostatic spraying can be coupled with the ultrasonic spray pyrolysis as shown by Chang et al.²¹⁴

The Layer-by-Layer (LbL) process, typically carried out by dip coating, can also be performed by spraying methods.²⁰⁷ Alternating spray solutions (polycation solution – rinsing - polyanion solution - rinsing) can be used as spray cycles for the deposition of multilayered coatings.^{207,208}

In context of the 4. publication of this thesis, regarding the spray coating of poly(propylene) foils with ZnO tetrapod/PAA dispersions, the Layer-by-Layer (LbL) technique of ZnO nanoparticles/PAA on glass substrates from Eita has to be mentioned.²¹⁵ Their 120 nm thick layers (20-bilayers) show a high porosity and surface roughness, resulting in superhydrophilic properties.²¹⁵ Based on the UV resistance and hindering properties of ZnO particles, these transparent films exhibit even UV-blocking and antireflective behavior with PAA in the visible range.²¹⁵ The adhesion properties of these films have not been analyzed. The combination of the work of Abzaeva et al.¹⁵³ and Eita et al.²¹⁵ could lead to excellent sun-protecting films for human skins with even antimicrobial, hemostatic and wound-healing properties. In addition to that, Shaik et al. have shown that modified PAA-zinc composites have anti-microbial properties against various pathogens²¹⁶, which supports the broad field of applications for PAA-Zn materials already shown above. However, the stabilization of dispersions remains quite a challenge. Thus, the composition of the dispersions/suspensions containing ZnO and PAA for spray coating or LbL processes in particular have to be clear before usage. Kislenko et al. have analyzed the effect of the zinc ion concentration of PAA/ZnO dispersions²¹⁷ and the adsorption of PAA on ZnO particles.²¹⁸ It has to be noted that these experiments were performed under accumulation in a centrifuge setup. The complex adsorption procedure of PAA on ZnO particles is overlapped with a lot of other processes: formation of aggregates, flocculation, formation of salts and desorption from formed salts.²¹⁷ In addition, Rabie et al. proved the temperature dependence of the reaction of PAA with ZnO, for example.²¹⁹ The initiated complexation creating carboxylate salts is very fast and is based on ionic character.²¹⁹ Interestingly, the reaction of ZnO with PAA could be increased by choosing low temperatures.²¹⁹ However, Radyum et al. underlined that the PAA containing solutions are able to stabilize ZnO dispersions.²²⁰

According to this PhD thesis in context of the 4. publication, airbrushing/spray coating without advanced experimental configurations has to be mentioned. Here, a similar construction based on a carrier gas and liquid inlet displayed in Figure 12 combined with a fine nozzle can be used.²²¹ Even a hotplate can support the deposition process as shown by Li et al. for the fabrication of carbon nanotube films by airbrushing on glass plates.²²² In general, airbrushing is a simple and low-cost process, and can be automatized.

With regard to the modification of surfaces with of adhesive films based on poly(acrylic acid)/ZnO dispersion, to the best of our knowledge, there are no publications available that consider its deposition via spray coating/airbrushing processes. However, the deposition of different coatings with airbrushing is a common method,^{223–226} which underlines the contribution to the scientific field regarding spray coating achieved by the 4. publication of this PhD thesis.

2.7 Analytical methods for surface and interface analysis

2.7.1 X-ray photoelectron spectroscopy (XPS)

The surface analysis with X-ray photoelectron spectroscopy (XPS) based on the emission on photoelectrons caused by the photoelectric effect leads to information about the elementary chemical surface composition, the oxidation states of each element, and binding states.^{227,228} Therefore, this method is essential in material science and nanotechnology.

With the use of high energetic electromagnetic and monochromatic radiation generated by an X-ray source, the excitation of core near electrons can be realized as illustrated in Figure 13.

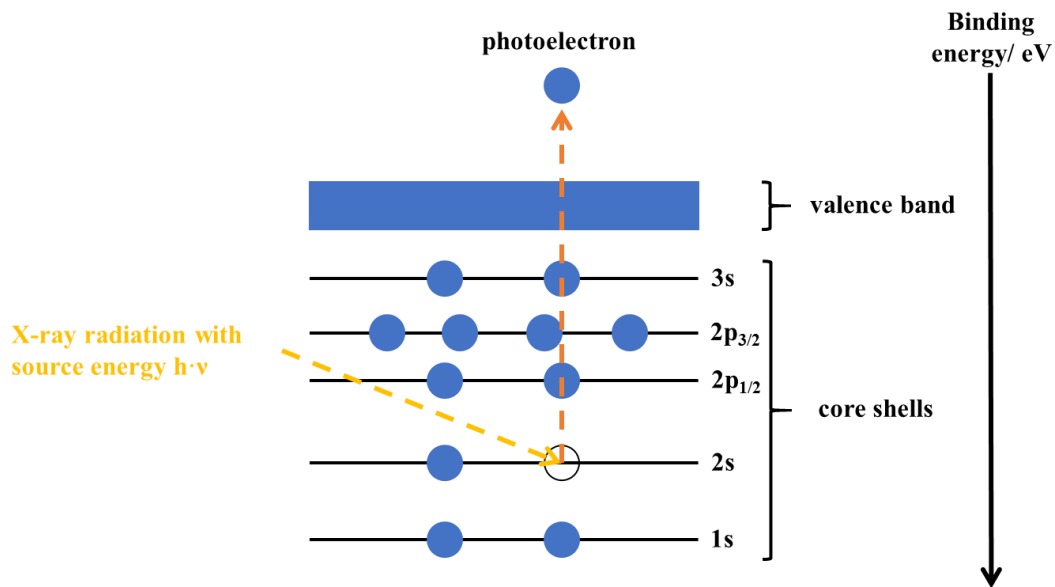


Figure 13. Schematic illustration of the photo effect releasing one photoelectron from inner core shell 2s excited by X-ray radiation (based on Sabbatini et al.²²⁷ including literature in there).

The emitted photoelectrons have a specific kinetic energy E_{kin} , which can be summarized in the following equation (36):²²⁷

$$(36) \quad E_{\text{kin}} = h \cdot \nu - E_{\text{BE}} - f - K$$

The energy balance contains the following symbols: h denotes Planck's constant, ν denotes the frequency of the electromagnetic radiation, E_{BE} is the binding energy of the electron of the corresponding element in the specific orbital, f is the work function of the spectrometer and K is a correction term.²²⁷ The latter is crucial in the case of charging of the sample as underlined by the following reaction, where M denotes the metal/element and e^- is the emitted photoelectron:²²⁹



Especially in the case of isolators such as polymers, the neutralization of the sample with an electron beam is beneficial. It is also evident that one element/atom can also emit more than one photoelectron simultaneously due to the fact of exhibiting several orbitals (compare Figure 13) and oxidation states.

With the knowledge of the primary source energy of the X-ray radiation ($h\nu$) and the spectrometer parameters for the work function ϕ , the calculation of the binding energy and the kinetic energy is possible, which is characteristic for each element depending on the chemical surrounding. Thereby, attached atoms or molecules results in shifting of the binding energy. It is common to record a spectrum where the counts per second versus the kinetic or binding energy in eV can be plotted. The higher the electrostatic attraction of the atom and the corresponding electrons, the lower the corresponding kinetic energy of the emitted photoelectrons. A energetic separation of the photoelectrons can be realized with a hemispherical electron energy analyzer under different pass energies, for instance.²²⁷

In this PhD thesis, the angle-resolved high-resolution XPS (AR-HR-XPS) setup was also used to check the surface state after a preconditioning treatment of a mirror polished stainless-steel substrate. The information depth, depending on the take-off angle θ of the photoelectrons, gives hints about the different chemical concentrations in the inner and outer part of the sample surface. The following Figure 14 illustrates the geometrical paths of the X-radiation and photoelectrons in AR-HR-XPS measurements.

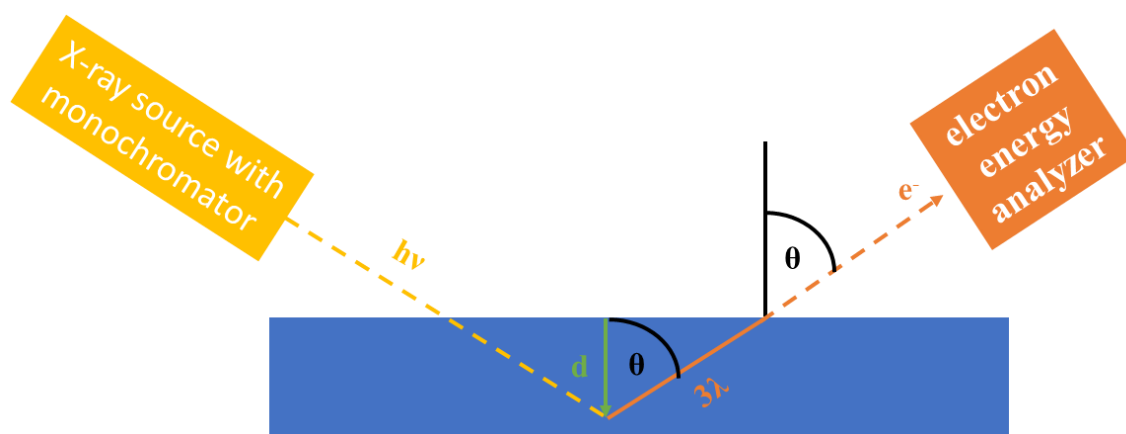


Figure 14. Illustration of the geometrical pathway of the X-radiation and the emitted photoelectrons from a metallic substrate (based on Bluhm²³⁰ and Sabbatini et al.²²⁷ including literature in there).

Here, $h\nu$ is the energy of incident X-rays, d the information depth, λ the inelastic mean free paths (IMFP) of the photoelectrons and θ the take-off angle. Typically, the length at which electrons escape is estimated to be 3λ .^{231,232} In these publications the angle with respect to the surface chosen is obviously $90^\circ - \theta$. It becomes clear that the information depth d depends on the take-off angle.

With this technique it is possible to measure depth profiles and to detect, for instance, low surface concentrations in the outer regions like an adsorbed hydroxide layer on polar ZnO(0001)-Zn single crystals.⁶² Valtiner et al. could demonstrate with AR-HR-XPS that the total hydroxide surface concentration, determined from the O 1s peak, increase with increasing take-off angle θ , which leads to the interpretation of a hydroxide stabilized polar ZnO(0001)-Zn surface.⁶² In more general words, Watts et al. mentioned a “bulk angle” where metallic components are more intense and a “surface angle” where the oxide peak of the native metal oxide has a relatively higher intensity.²³³

2.7.2 Vibrational spectroscopy

Vibration spectroscopy comprises a vast set of helpful techniques for the identification and characterization of molecules in material science and chemistry. Based on the excitation of vibration modes of rotations and oscillations (symmetric/asymmetric, valence and deformation vibration modes) with electromagnetic radiation, the principle of the harmonic oscillator can be applied, as mentioned in the literature.^{123,228,234} The absorption takes place due to the precise energetic level of the irradiation like in the infrared region and the corresponding energy levels of the vibration modes. For instance, wavelengths in the infrared range are located between around 700 nm until 1 mm. Further, this region is separated in the “far infrared” region between around 10 μm until 1 mm and the “near infrared” region from around 10 μm to 700 nm in the literature.¹²³ At higher wave lengths, the microwave range starts, where the rotation modes are the most prominent ones. In the other direction to lower wavelengths > 700 nm electron excitations can start.¹²³

In principle, the absorption of electromagnetic radiation with an energy $h\nu$ leads to an induced dipole moment or a change in the dipole moment of the molecule during the vibration (selection rule: infrared-active). According to the law of Einstein, the energy difference ΔE between two different states can be formulated based on the energy balance like:¹²³

$$(37) \quad \Delta E = h \cdot \nu = h \cdot \frac{c}{\lambda}$$

Here, ν denotes the frequency of the electromagnetic radiation and h is Planck’s constant. Typically, the energy is expressed in wave numbers $\tilde{\nu}$ which are proportional to the energy difference. The absorbed radiation will change to thermal energy within the vibration of the molecule. Each functional group exhibits different vibration modes with respective resonance frequencies which opens the door for the identification of molecules.^{228,234,235}

In the following two infrared techniques used in this thesis are outlined.

2.7.2.1 Fourier-transformed infrared reflection absorption spectroscopy (FT-IRRAS)

Infrared spectroscopy has reached high applicability in material science and chemistry caused by the invention of the Michelson interferometer. The principle construction is displayed in Figure 15. The general idea is based on the movable mirror with a path way x and a semi-permeable mirror to create constructive interferences from the wave lengths at the end of the interferometer.²³⁵

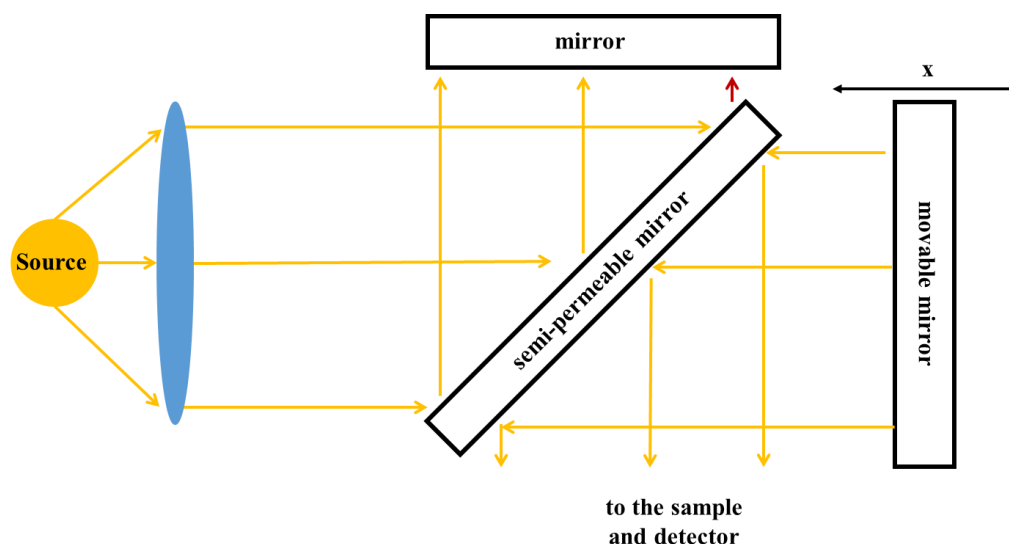


Figure 15. Basically construction of a conventional Michelson interferometer (based on Günzler, Gremlich²³⁵ including literature in there).

The polychromatic radiation in the wave length range of far and near infrared hit a semi-permeable mirror which leads to a splitting of the complete radiation to two half path ways with a length difference of $2x$ within the recombination on the semi-permeable mirror.²³⁵ The precise movement of the mirror can be used to control the position of constructive and destructive interferences, resulting in that every position x of the mirror equals to a wave number $\tilde{\nu}$.²³⁵ This modified infrared radiation can interact with the sample and hit a detector connected to a computer. In this PhD thesis, the infrared reflection absorption spectroscopy (IRRAS) was used where the radiation from the interferometer hits the sample (compare following Figure 16) and the reflected photons are detected by the detector.

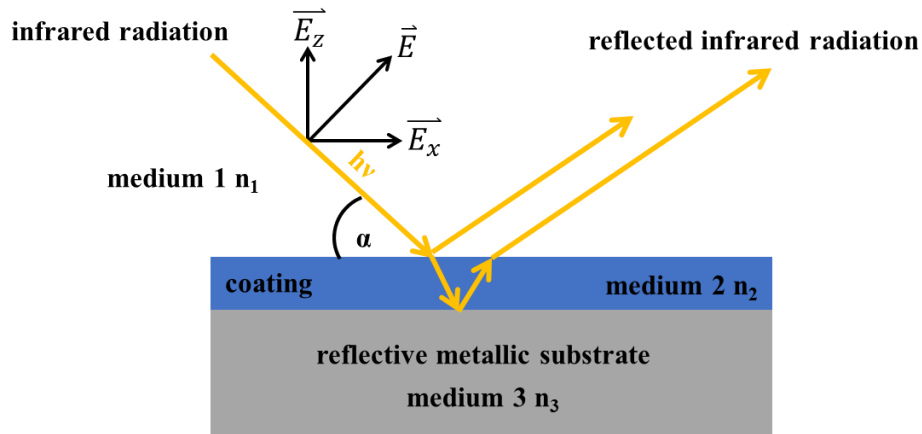


Figure 16. Schematic illustration of the application of infrared reflection absorption spectroscopy (IRRAS) on a metallic sample with a coating (based on Grundmeier et al.²³⁶ including literature in there).

The interferogram (intensity versus position x of the movable mirror) can be transformed to a single channel spectrum (SCS) by means of Fourier-Transformation (FT). By measuring a reference sample without any chemical or physical changes, the SCS of the sample can be divided with the reference SCS to finally generate an infrared spectrum (transmission or absorbance versus wave number in cm^{-1}). The main advantage is the short measuring time depending on the chosen resolution of the device, while drawbacks are the measurement of a reference and roughness effects of the sample's surface. Here, the resolution R is limited by the maximum possible way length x of the movable mirror like:²³⁵

$$(38) \quad R = \frac{1}{2x}$$

For a resolution of 4 cm^{-1} , which was commonly used in all publications of this PhD thesis, a pathway of 0.125 cm was sufficient. The movement speed of the mirror can be controlled to high values. Consequently, the fabrication of an infrared spectrum is possible within some seconds.^{234,235}

2.7.2.2 Polarization-modulated Fourier-transformed infrared reflection absorption spectroscopy (PM-FT-IRRAS)

The surface characterization of ultra-thin layers or coatings could be performed with the PM-FT-IRRAS measurements. The decomposition of the electric field vector of the electromagnetic wave of the infrared radiation and its polarization (parallel (p) or perpendicular (s) to the plane of incidence) play important roles. This has been illustrated in the following Figure 17.

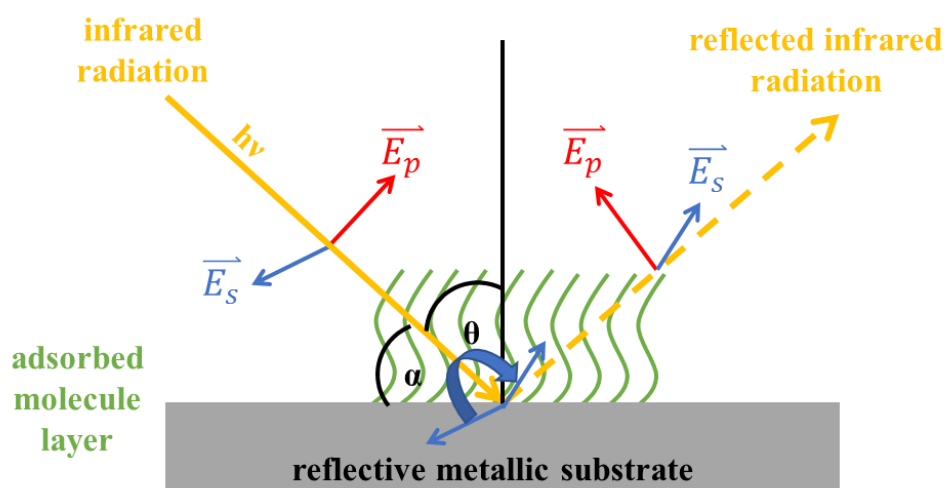


Figure 17. Schematic illustration of reflected infrared radiation with decomposition of the electric field vector (based on Grundmeier et al.²³⁶ including literature in there).

It becomes clear that the electric field component \vec{E}_p (p denotes p-polarization) is similar to the sample normal for high angle of incidence θ , which is increasing the surface sensitivity by a factor of around 25.²³⁷ In fact, the principle of the polarization of dipoles oscillating on the surface has been described by Grundmeier et al. for PM-IRRAS experiments.²³⁶ The dipole moments can be divided into two different groups: dipole moments from the surface of the metal (so called image dipoles) and dipole moments from the adsorbates on the surface. Both groups compensate their dipole moments each other due to electrostatic interactions and can be orientated parallel to each other and perpendicular to the surface plane which enhance the surface sensitivity as mentioned above for high angle of incidence. The other case where both groups are parallel to the surface plane and parallel to each other leads to the “compensation of the infrared active transition dipole moment.”²³⁶ This fact can be used by changing the polarization of the infrared radiation: the surface information from s- and p-polarized IR light is different caused by the independence of the s-polarized IR light from the angle of incidence while the p-polarization of the IR-light is enhanced. In PM-IRRAS experiments, both polarizations could be measured simultaneously for the IR light coming from the Michelson interferometer (compare Figure 15) by using a photoelastic modulator (PEM) made of zinc selenite (ZnS) after the polarizer unit.²³⁶ The main advantage of the resulting differential reflectance spectrum is that no reference has to be measured and the atmosphere has been automatically removed. Further mathematical details are available in the literature.^{234–237}

2.7.2.3 Raman spectroscopy

Similar to IR spectroscopy, Raman Spectroscopy enables the detection of rotation or vibration modes of inorganic and organic molecules and oxide surfaces, leading to the identification and

characterization of unknown substances. The mutual exclusion rule for Raman spectroscopy is the change in the polarizability α of a molecular structure during its rotation or vibration of the functional group, respectively.^{123,238}

An excitation of the material can be realized by a laser beam, that is, by monochromatic electromagnetic radiation. Consequently, Raman and Rayleigh elastic scattering can be observed.¹²³ The electric dipoles of the molecules interact with the photons, which results in vibration modes of the analyzed material. The induced dipole moment μ satisfies a linear equation involving the electromagnetic field E and the polarizability α :

$$(39) \quad \mu = \alpha \cdot E$$

The inelastic interaction of the source radiation's energy is transferred to the sample. The most intense peak in the detected spectrum is the Rayleigh-peak of the initial radiation. It can be eliminated by a Rayleigh filter at this wavelength. Inelastic scattering can be noticed as Stokes lines and anti-Stokes lines. Here, an energy shift ΔE between the incident photons and the emitted photons can be detected with a charge-coupled device (CCD) detector (compare chapter "2.7.2 Vibrational spectroscopy").^{234,239}

Some advantages can be mentioned of this measurement technique: microscopy is optional caused by the usage of a coupled microscope, confocal measurements, easy operations, measurements in water and so on.²³⁸

In this PhD thesis the Raman spectroscopy was used for the additional identification and characterization of zinc oxide structures generated in the mentioned tubal furnace setup (compare 4. publication in chapter "3 Publications").

2.7.3 Electron microscopy: scanning electron microscope (SEM) and transmission electron microscopy (TEM)

The exploration of the morphologies of materials with SEM and TEM techniques is essential in material science and nanotechnology. Here, a focused electron beam generated, for instance, with a field-emission (FE) electron gun, can be used for a scanning electron microscope (SEM). This primary electron (PE) beam can be focused with condenser lenses and scan coils control the scanning of a material (compare following Figure 18).

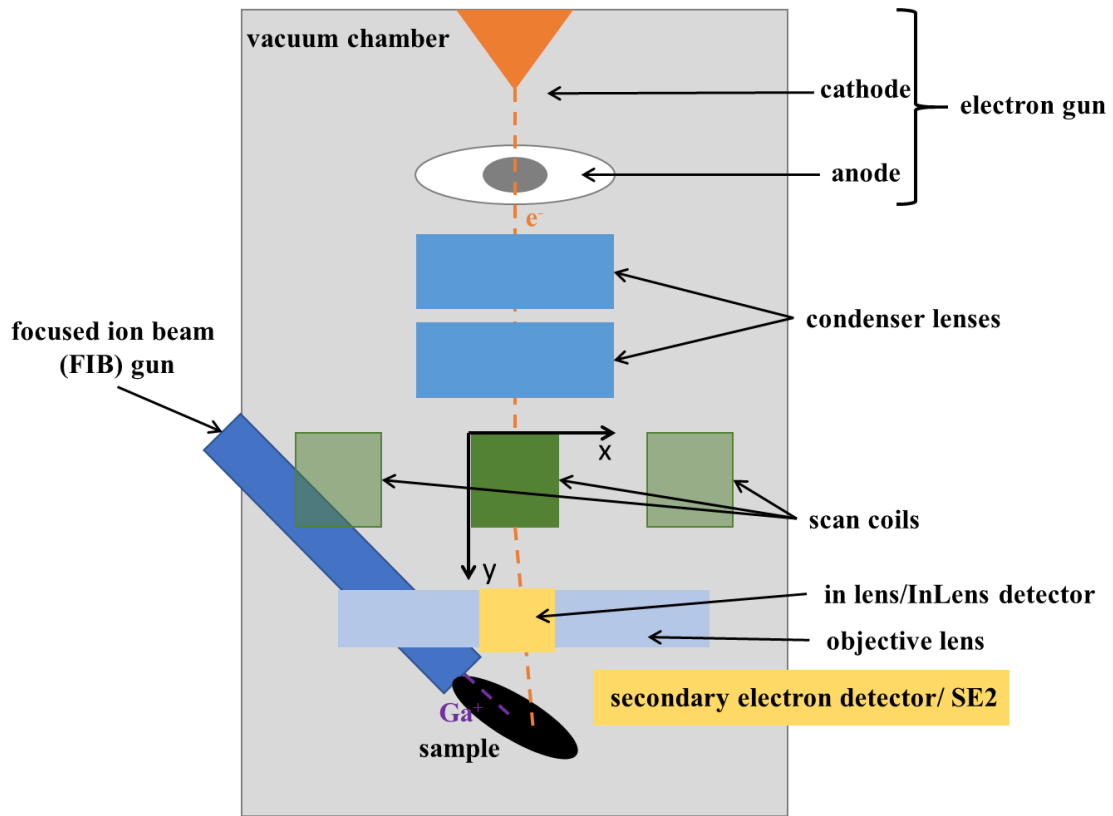


Figure 18. Schematic construction of the main elements in a typical scanning electron microscope (based on Egerton et al.²⁴⁰ including literature in there).

The PE interact with the material of the sample and produce various phenomena (only the most important ones in context of this PhD thesis are mentioned):

- 1) secondary electrons (SE): elastic scattering, low energy
- 2) back scattered electrons (BSE): elastic scattering, high energy
- 3) transmitted, diffracted electrons (TE): penetrating the material
- 4) photoelectrons: based on the Auger-effect
- 5) high energetic radiations: like X-ray with characteristic energies, useful for energy disperse microscopy X-ray spectroscopy (EDX)²⁴¹

The type of interaction and the intensity strongly depend on the energetic level of the PE. The higher the energy, the higher the penetration depth of PE (“potential bulb” displayed in Zhou et al.²⁴¹). For this PhD thesis, the SE are detected by a secondary electron detector and an in lens/InLens detector. The former collects the electrons scattered to the side of the sample while the latter detects the electrons coming directly from the direction of the surface normal. In transmission electron microscopy, the electron completely penetrating the sample can be detected. More details can be found in the literature.^{240,241}

2.7.4 Time-of-flight secondary ion mass spectroscopy (ToF-SIMS)

Precise identifications of chemical surface compositions can be realized with the use of ToF-SIMS, for instance. The principle of secondary ion mass spectroscopy is based on the bombardment of a substrate using a primary particle beam consisting of Ar^+ , Bi_3^+ , Ga^+ ions and other ones.²⁴² A schematic image can be found in the following Figure 19.

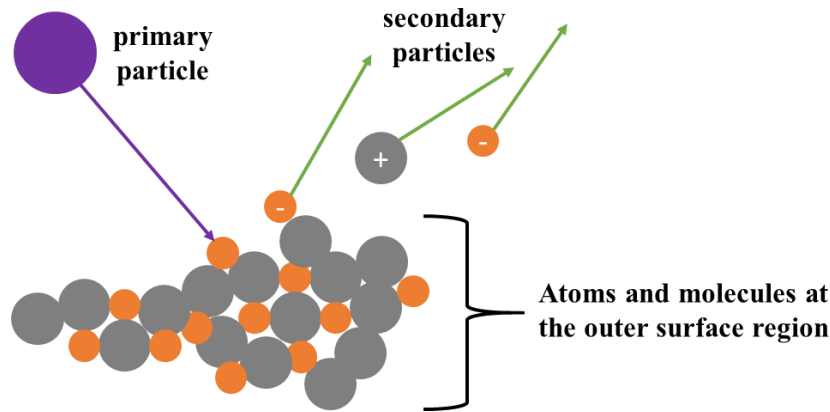


Figure 19. Schematic illustration of secondary ions fabricated by collisional process with primary particle (based on Vickerman and Briggs²⁴² including literature in there).

Most of the secondary particles are electrically neutral, while charged particles ionized by the primary particles from a liquid metal source can be analyzed by the typical mass spectroscopy via the m/z ratios of the generated fragments.^{228,242} The fragments of the first few nanometers of the surface are ramped up in an electric field which has the following energy balance (based on literature²²⁸ including literature in there):²²⁸

$$(40) \quad zU_B = \frac{1}{2}mv^2$$

Here, the potential electric energy of the particles with the corresponding charge z and the acceleration potential U_B is transformed into kinetic energy (m is the mass of the corresponding particle and v the velocity).²²⁸ After this acceleration step, all secondary particles have the same kinetic energy E_{kin} and reach a drift segment with length l without any present field. Based on the different m/z ratios of the fragments, heavy low charged secondary ions need a longer time to traverse the drift path.^{228,242} With the help of equation (40) and the simple “length l -time t law”^{228,242}

$$(41) \quad t = \frac{l}{v}$$

the following separation of the particles regarding their m/z ratios is possible:^{228,242}

$$(42) \quad \frac{m}{z} = \frac{2U_B t^2}{l^2}$$

2.7.5 Static water contact angle measurements

An experimental approach to prove the wettability (hydrophilic and hydrophobic properties of the surface in contact with water) is the measurement of the contact angle (compare chapter “2.3.1 Wetting of surfaces”). This fact becomes clearer by taking a look at a basic thermodynamic view of a sessile drop of liquid (l) on a solid surface (s) in gas phase (g) as illustrated in Figure 20.

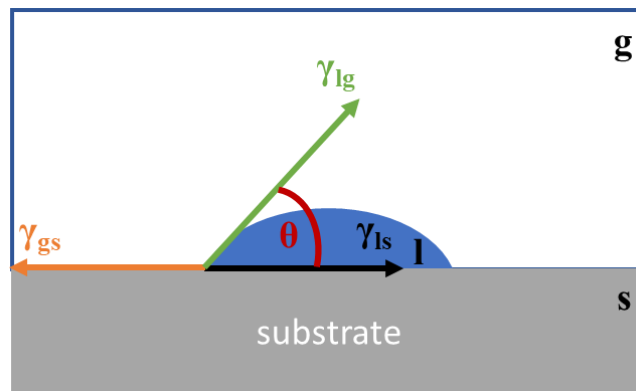


Figure 20. Schematic illustration of surface tension and contact angle (adapted from Habenicht¹¹⁹ and Butt et al.¹⁵ including literature in there).

Here, the surface tension of the liquid is given as γ_{lg} ($=\gamma_l$), the surface tension of the substrate γ_{gs} and the surface tension between the liquid and the solid phase γ_{ls} are in thermodynamic equilibrium by creation of the contact angle θ .¹¹⁹ This angle indicates whether the surface is hydrophilic or hydrophobic in the case of water: the lower the contact angle θ , the higher the wettability of the substrate. The three-phase contact line is often called the wetting line.¹⁵ However, the definition of wetting depends on the definition and the literature. For example, Habennicht defines a surface with a contact angle of $> 90^\circ$ as “incomplete wetting”¹¹⁹ while Butt et al. and with the literature in there are referring to a liquid which “is said not to wet the solid”.¹⁵

2.7.6 Atomic force microscope (AFM)

2.7.6.1 Basic experimental setup and measurement principles

The experimental setup of an AFM is displayed in Figure 21. A laser beam is focused on a cantilever with a tip (diameter in the range of 5-50 nm¹⁵) movable by a piezo-actuator. In some apparatus it is even possible to move the sample instead of the cantilever-tip by a piezo.¹⁵ The piezo effect opens the door for a precise movement in all three dimensions in the nanometer range.

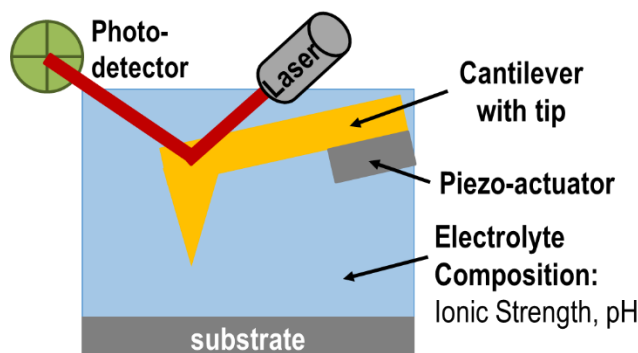


Figure 21. Schematic image of the experimental setup of an atomic force microscopy (AFM) (based on the poster presentation at the ICAS conference in Pisa in 2019 and on Butt et al.¹⁵ including literature in there).

While measuring the reflected deflection of the bended cantilever in contact with the surface with a photodiode and scanning the substrate, it is possible to have an electric signal from the photodiode dependent on the 3D-position. Thus, a calibration of the cantilever is necessary to convert the electronic values into forces and distances.²⁴³ For the precise determination of the spring constant K_c , which is essential for the calibration process, several methods are summarized by Butt et al.¹⁵ Thereby, the error of the cantilever calibration is estimated to be within the range of 5 % according to Bouchiat et al.²⁴⁴

2.7.6.2 Different measurement modes with AFM

AFM offers the possibility to obtain a tridimensional representation/image of the topography of a substrate's surface. This can be performed in liquid under atmospheric conditions and in a gas phase under atmospheric conditions or in vacuum. In principle, three different cantilever-substrate interactions can be used to scan the surface:

- 1) Contact mode
- 2) Intermittent contact mode
- 3) Non-contact mode

Thereby, only the first two modes were used in the context of this PhD thesis. In the first mode the scanning cantilever is directly in contact with the surface²⁴⁵, which can be used, for instance, for the investigation of tribological properties.²⁴⁶ The resulting bending of the cantilever can then be transferred from an electronic signal into a length via the mentioned calibration step of the cantilever. After the successful calibration of the tip, the applied force to approach the tip in contact with the surface can be set (on a scale of smaller than nN). However, it is possible to destroy the cantilever or the sample by applying too much force. This depends strongly on the properties of the cantilever such as its geometry and its material. For example, by using silicon cantilevers

incorporating pyramidal geometries and a sharp diamond-like tip, a huger variety of loading forces can be applied to the sample and high-resolutions are obtainable as well.²⁴⁵

In the intermittent contact mode, the cantilever tip is not constantly in contact with the surface: it is oscillating at its maximum resonant frequency with a defined amplitude in the nanometer range. The cantilever-sample distance is controlled by keeping the amplitude of the oscillating cantilever using an electronic feedback. As a major advantage, the suppression of the lateral forces occurring in the contact mode (when tip and sample are in close mechanical contact) allows to obtain, in general, better lateral resolution in the intermittent contact mode. As a consequence of the tip-surface interaction, a phase lag between the external excitation of the cantilever and the electronic signal registered at the detector, i.e. a phase shift (contrast), is related to the occurrence of (nano)domains on the surface exhibiting differential physicochemical properties. A brief overview about dynamic atomic force microscopy methods can be taken from the review publication by García et al.²⁴⁷

2.8 Singe molecule force spectroscopy (SMFS)

2.8.1 Basic explanations and literature review

The measurement of molecular adhesion forces is a difficult topic. Several experimental approaches can be found in the literatures.¹⁵ For instance, the surface force apparatus (SFA), atomic force microscopy (AFM)-based setups, optical tweezers, total internal reflection microscopy, and magnetic tweezers are mentioned by Butt et al.¹⁵ and Roy.²⁴⁸ However, in context of this PhD thesis the atomic force microscope (AFM)-based force distance spectroscopy, especially with single molecules, is the main advanced experimental approach considered herein. The measurement of the surface force comes with two main difficulties:

1. Short lengths/distances with forces in the range of pN up to nN and
2. Control of sensitive detection under highly challenging rough surfaces with possible contaminations¹⁵

Both requirements can be solved with an AFM-based equipment invented and published by Binnig et al. in 1986 in *Physical review letters*²⁴⁹ that enables atomic resolutions and sensitivities.^{249,250}

Several experimental approaches are conceivable depending on the modification of the cantilever^{250,251} and the usage of theoretical models for surfaces forces.¹²⁴ Three main classes can be mentioned in this context of adhesion forces measured with AFM based concepts:

1. chemical force microscopy (CFM)/spectroscopy^{252–257}
2. colloidal force spectroscopy (CFS)/microscopy^{258–264}

3. single molecule force spectroscopy (SMFS)^{265–269}

All three mentioned approaches are based on the modification of the tip, either the surface (CFM), by attaching molecules (SMFS) or colloids (CFS). Obviously, it is still possible to perform microscopy imaging with the modified cantilevers, but it is influenced by the attached species. However, all three classes can also be used for the measurement of force-distance curves, which implies the forces occurring between the tip and substrate surface.

It is possible to chemically modify a cantilever with a self-assembled monolayer (SAM) and measure the interactions between this SAM and a well-defined surface. This method is called “chemical force microscopy” (CFM).^{252,253} Frisbie et al. published a fundamental analysis of the interactions of different functional groups with CFM.²⁵³ The authors can found a molecular force of 8.7 nN for –COOH/-COOH interactions, while the –CH₃/–CH₃ interaction is much lower at 2.7 nN because it is limited to van der Waals forces.²⁵³ Interestingly, the authors derived from the Johnson-Kendall-Roberts (JKR) model that the contact area between surface and tip has been 10 nm², which means that around 50 functional groups are simultaneous in contact.²⁵³ Another comparative work for the adhesive force analysis of several functional group pairings was performed by Clear et al.²⁵⁷ In addition to that, Noy et al. could show that the ionic strength of the medium affects the electrostatic interactions of “COO[–]/NH₃⁺ tip/surface”.²⁵⁵ Therefore, 11-mercaptoundecanoic acid was attached by thiol-gold chemistry while the silicon surface was modified with 3-aminopropyltriethoxysilane.²⁵⁵ With increasing salt concentration (NaCl) at pH 6.5, a decrease in the measured forces could be observed. The decreasing Debye length λ_D with increasing salt concentration lead to a higher shielding of the functional groups by ions, resulting in lower charge-charge interactions.²⁵⁵ Moreover, the pH dependence at high and low values showed lower adhesion forces than at neutral pH. Thus, the hypothesis of charge-charge interactions at neutral pH has been proven.²⁵⁵ Another example for the usage of CFM is the analysis of single live cells as shown by Dague et al.²⁵⁶ The authors modified the cantilever tip with –CH₃-terminated alkanethiols via gold-thiol chemistry.²⁵⁶ These results showed an rise in the adhesion force obtained for increased surface fractions containing –CH₃ groups caused by a boost in the hydrophobicity.²⁵⁶

The modification by the attachment of colloids to the cantilever tip can be categorized by “colloidal force microscopy” and “colloidal force spectroscopy”.²⁶¹ Ducker et al. published a fundamental study of the use of an AFM to measure the forces between a planar surface and a colloid attached to the tip.²⁶¹ A classic example was published by Biggs et al. who attached a poly(styrene) sphere to a cantilever tip.²⁷⁰ Based on that, Wong et al. could develop the covalent modification of single-walled carbon nanotubes (SWNTs) as microscopy tips.²⁷¹ The advantage of this approach is the

high tip-surface distance resulting in a higher lateral resolution of the force-distance curves and imaging microscopy. Besides, the authors could attach different functional terminations such as carboxylic acid groups to the SWNTs.²⁷¹ In a further study, the authors demonstrated the high-resolution imaging with carbon nanotube modified tips applied to biological probes such as amyloid- β 1-40 (A β 40) fibrils.²⁷² Additionally, a broad field is the measurement of particle-particle interactions performed by modified AFM tips with different colloids.^{258,260,262–264} For instance, the review of Harrison et al. summarizes the colloidal force microscopy as a measurement tool for the understanding of capillary forces in nanoparticle adhesion.²⁶⁴ In addition, the review of Kappl and Butt²⁶² showed a brief overview of the most important parameters to take into account regarding the measurement of colloidal probe techniques by AFM like the calibration of spring constants, applied load and contact time, humidity, and surface roughness.²⁶² In this context, Fuji et al. showed that the surface geometry structure of silica particles influences the adhesion force.²⁷³ The presence of capillary bridges up to capillary condensation leads to an adhesion force measured by AFM.²⁷³

However, for both CFM and CFS single adsorption events are not accessible. In this regard, single molecule force spectroscopy (SMFS) is an interesting experimental approach where the key point is the modification of the cantilevers with long molecules like in the case of macromolecular polymer chains.^{274–277} A fundamental study of this kind of adhesion force measurement was published by Noy et al.²⁶⁷ Figure 22 summarizes the transfer from the electronic signal collected in V into a force in the range of nN dependent on the piezo displacement. The repulsive linear part in a typical force-distance curve can be fitted to the Hook's law to obtain the sensitivity of the cantilever from the slope in nm/V (piezo-displacement versus photodetector signal). The combination with the spring constant K_c given in N/m obtained, for example, from the thermal tune calibration method due to thermal fluctuations, leads to a force in nN. In principle, the spring constant K_c of a rectangular cantilever could be calculated with equation (43) (taken from literature¹⁵ including literature in there):¹⁵

$$(43) \quad K_c = \frac{Ewd^3}{4L^3}$$

Here, E denotes the Young modulus, w the width of the tip, d the thickness of the tip and L the length of the cantilever.¹⁵ Besides, the geometry of the tip on the cantilever plays an important role in the quantitative and reproducible analysis with AFM experiments based on force-distance

mappings.²⁷⁸ Ferreira et al. demonstrated with milled tips produced with a focused ion beam (FIB) that a significant difference in the adhesion forces was found.²⁷⁸

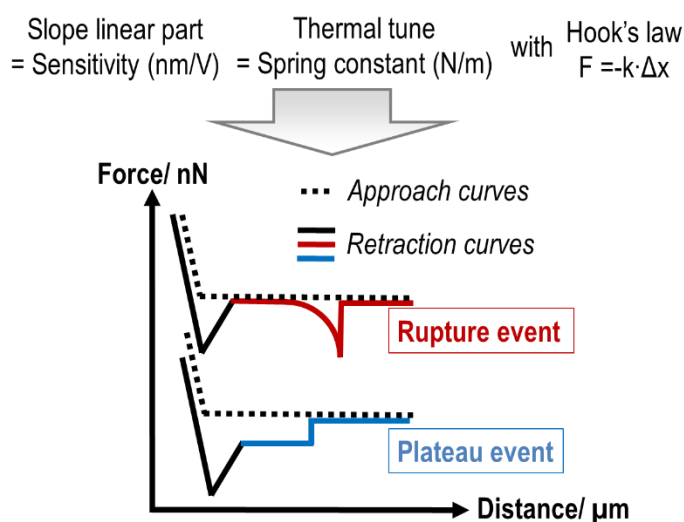


Figure 22. Combination of sensitivity and spring constant with law of Hook for the generation of final units. The result is a force in nN versus distance in μm curves, for example (based on the own poster presentation at the ICAS conference in Pisa in 2019).

When the tip is brought into contact with the surface, the polymer chains and their functionalities interact with the surface functional groups such as hydroxyl groups. When the tip is withdrawn afterwards, this interaction has to be broken. Thus, the force-distance curves collected for the desorption, namely retraction curves, of the polymer chains attached to the cantilever tip depend both in shape and total force values on these interactions. Geisler et al. stated that the SMFS approach is similar to a “nano-peel test”.²⁶⁸ In the literature there are mainly two different kinds of events in the force distance curves: (multiple) rupture events and plateau events/plateaus as displayed in Figure 22 as red and blue colored curves, respectively.²⁷⁹

In the latter case, the desorption is in an equilibrium state where all bindings are based on weak interactions such as electrostatic or van der Waals interactions, thus breaking successively in a row.²⁷⁹ Thereby, no extension/stretching of the polymer chains is present and all polymer functions interact (simultaneously) with the surface. Thus, no specific adsorption could be detected.²⁷⁹

The reason for (multiple) rupture events could be (a) specific interaction(s) between (several) two functional groups. The functionalized cantilever marked by an “x” in Figure 23 approaches to the surface in the steps 1) and 2) until the molecules and the cantilever tip reach the interfacial region and finally touch the surface in the contact mode with a fixed force, for instance, 4 nN. This complete curve is defined as the “approach curve” and drawn as a dashed line in Figure 23.

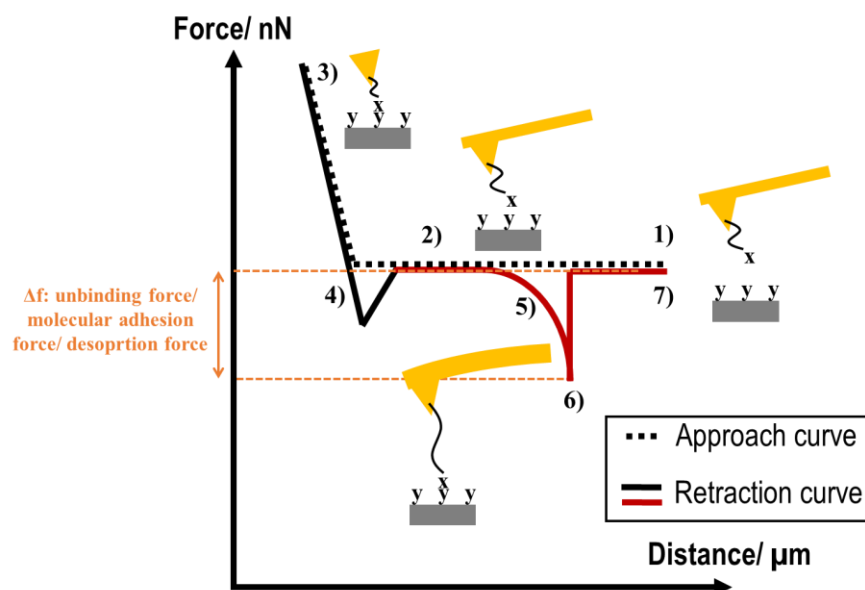


Figure 23. Schematic illustration of the explanation of rupture events in force distance curves in single molecules force spectroscopy (based on Lee et al.²⁸⁰ and Bizzarri et al.²⁸¹ including literature in there).

After the approaching step, the molecules can interact with the surface layer of the substrate and can specifically bind to a functional group marked as “y” of the surface (point 3) in Figure 23). The dwell time until the retraction should start can be set in the software of the AFM. This opens the door for kinetic studies, leading to a fundamental understanding of the processes of bindings. The retraction curve (solid black and red line) starts at 3) with the nonspecific interaction/force of the cantilever tip till position 4) in Figure 23. This force results from the interaction of the cantilever tip with the surface.²⁸⁰ The further retraction leads to the extension/stretching of the interacting molecules/polymer chain resulting in a “x-y” interaction displayed in position 5) in Figure 23. Afterwards, a maximum (point 6)) can be detected in the retraction curve. This specific unbinding force/molecular adhesion force/desorption force represents the interaction between the surface and the attached molecules at the cantilever.²⁸⁰

To sum up the most important interpretations of SMFS events: plateau events are caused by mobile polymer chains, where the interactions are reversible caused by equilibrium state forces and the interactions are relatively weak (van der Waals, electrostatic and hydrogen bridging). Rupture events are specific, irreversible interactions caused by immobilized chains with strong interactions like covalent, coordinative or chelate bindings.^{248,282}

A lot of publications in the field of SMFS can be mentioned, especially of the working group of Gaub.^{283–285} In addition to the usage of polymers attached to the cantilevers, it is even possible to link biomolecules such as proteins, peptides and deoxyribonucleic acid (DNA) molecules to the cantilever tip. The analysis of protein/DNA-surface interactions via SMFS represents a broad field in the biochemistry sector.^{265,286} For instance, Geisler et al. used a spider silk protein.²⁸⁶ Gilbert et

al. used an antibiotic-modified tip to measure possible ligands on living bacteria.²⁸⁷ Bouchiat et al. were able to show the successful fitting of the worm-like chain (WLC) model to force distance curves of extended DNA molecules.²⁴⁴

Besides adsorption, different systems can be investigated as well. For instance, Hugel et al. investigated the elasticity of polymer chains of poly(vinylamine).²⁷⁵ Another example was established by Sonnenberg and co-workers of the working group of Gaub who investigated the quantification of SMFS of poly(*L*-glutamic acid) (PLE) and calcite crystals.²⁸⁸ Anisotropic interactions of different facets of the calcite under pH control and the calcium concentration lead to a helpful correction for the polypeptide-mineral system by the polymer-controlled crystallization.²⁸⁸ For a better overview, the reader is referred to the publication of Friedsam, Seitz and Gaub about SMFS.²⁷⁹

2.8.2 Cantilever functionalization

The functionalities can easily be controlled to study the interactions of interest. In the context of this work and in most of the published SMFS reports, a prior cantilever modification performed with thiol-gold chemistry was done to attach in a second linking step a polymer to the first molecule layer. Here, the already mentioned SAM's are useful for the first modification step of the cantilever: the molecules in the SAM have on one end a thiol/H-S-functionality to give rise to an Au-S-bond with the gold-coated AFM tip. The other end of the linear molecule in the SAM has a chemical function (e.g. $-\text{NH}_2$, $-\text{OH}$), which acts as an anchoring/ linking group for known coupling reactions. The functionalization with PAA chains, relevant for this work, has been summarized by Friedsam et al.²⁷⁹ After a gold coating of the cantilevers and successive cleaning steps, the adsorption of *11*-mercaptoundecan-*1*-ol was done in ethanoic solution.²⁷⁹ The coupling reaction to link the PAA chains to the alcoholic functionality was performed with ethylenediamine (EDA), *N*-Hydroxysulfonosuccinimide sodium salt (S-NHS) and *N*-(3-(dimethylamino)propyl)-*N'*-ethylcarbodiimide hydrochloride (EDC hydrochloride).²⁷⁹ The prepared cantilevers showed very long-term stable properties and can be used for different samples with various polyelectrolytes, for example, PAA on ammonium-functionalized silicon, as shown by Friedsam et al.²⁸⁹

A key aspect becomes clear at this point: the intramolecular bonds based on covalently interactions have to be much stronger than the irreversible binding process at the surface to prevent the destruction of the polymer structure.²⁸⁹ This is a typical limitation of SMFS. As described above, most of the cantilever modifications are based on the Au-S-binding. Therefore, a lot of studies analyzed the Au-S-bond which is stated to be the weakest bonding in the majority of cases.^{290–293} However, the unbinding force for the Au-S is necessarily higher than the unbinding interactions

measured between the PAA and the ZnO surface.^{43,167} For instance, Xue et al. (in *Nature Communications*) quantified the thiol-gold interactions under different influences such as pH and oxidized Au.²⁹³ They mentioned a binding force of around 1.5-2.2 nN²⁹³ while other authors mentioned an Au-S-force between 1.2 and 1.7 nN.^{43,292} A clear proof for the fact that the molecules attached to the cantilever are still stable is the comparison of the collected curves at the beginning and at the end of all measurements. With regard to our manuscript (publication 2.), it should be noted that, even after obtaining desorption values in the range of up to 1.7 nN, similar multiple rupture force profiles were subsequently registered, indicating that the integrity of the as-prepared PAA layers has not been significantly affected. Moreover, the dwell-time dependence of the measured forces further indicates that the desorption of carboxylates at the ZnO/electrolyte interface dominate the obtained data.¹⁶⁷ Moreover, Friedsam et al. showed that a SAM including a thiol-gold binding linked to PAA is long-term stable.²⁸⁹ Although their force values were lower than 300 pN, it underlined the excellent advantage of SMFS: rebinding events after every force-distance curve.²⁸⁹

2.8.3 Data interpretation of multiple rupture events and surface roughness

In some cases, it is even possible to have multiple rupture events in one force-distance curve. In this case, more than one molecule interacts with the surface and create an overlapping of the events.²⁹⁴ Moreover, more than one functional group of one molecule can bind to several positions/functional groups on the surface. For instance, Li et al. and Liu et al. studied the interactions of a single crystal TiO₂ (rutile) surface and a 3,4-dihydroxyphenylalanine (DOPA) modified cantilever with SMFS.^{295,296} Based on the knowledge of the high adhesion properties of DOPA to wet surfaces, the authors found different binding mechanisms explaining the wide range of adherence.²⁹⁵ The binding forces are ranging from 40-800 pN, underlining the wide adhesion possibilities.²⁹⁵ The results showed multiple rupture events depending on the crystal orientation of the TiO₂ surface. The hydroxyl groups of DOPA could interact via hydrogen and coordinative bonds to the different TiO₂ facets. Furthermore, the results illustrated as typical histograms of the number of events versus the corresponding molecular adhesion force, showed two possible Gaussian fits.²⁸⁰ The multiple rupture events and the double fittings could be explained by two coordinative bindings on (110) and (100) surfaces of TiO₂.²⁸⁰

Regarding the effect of a higher roughness of a surface in terms of more accessible surface points to adhere for polymers in comparison to the smoother single crystals mentioned before, Geisler et al. demonstrated that the morphology does not affect the SMFS values, as highlighted by molecular dynamic simulations.²⁶⁸ The authors explained that the adsorption energies per molecule are similar on rough surfaces.²⁶⁸ To the best of our knowledge, especially the measurement via SMFS

on nanostructured surfaces has not been investigated in detail, but can be found in the 2. publication of this PhD thesis.

2.8.4 Bell-Evans theory: kinetic and thermodynamic values from SMFS

At this point it is useful to mention the Bell-Evans theory^{297–299} for the determination of kinetic and thermodynamic parameters of the bonding process as in receptor-ligand interactions measured by SMFS. The Bell-Evans theory was developed for cell-cell adhesion phenomena.^{297,298,300} The typical analysis based on the Bell-Evans theory is the variation of the loading rate r at different retraction rates v . With the spring constant K_C of the cantilever, it is possible to calculate the loading rate r from equation (44):²⁹⁹

$$(44) \quad r = v \cdot K_C$$

According to the Bell-Evans theory a dependence on the mean rupture forces F and the logarithmic loading rate r is found to be (based on literature^{301,302} including literature in there):^{301,302}

$$(45) \quad F(r) = \frac{k_B T}{\chi_\beta} \cdot \ln \left(\frac{r \chi_\beta}{k_{\text{off}} k_B T} \right)$$

It can also be formulated as:

$$(46) \quad \tau = \frac{1}{k_{\text{off}}}$$

The following Table 1 summarizes the physical interpretations of the parameters used in the equations (45) and (46).

Table 1. Summary of the parameters containing in the Bell-Evans theory.

symbol of the parameter	meaning	units
k_B	Boltzmann's constant	$\text{m}^2 \cdot \text{kg} \cdot \text{s}^{-2} \text{K}^{-1}$
T	temperature	K
χ_β	distance between the bound state and transition state; height of the energy barrier ^{130,298,302}	pm
k_{off}	thermal off rate; dissociation rate at equilibrium ³⁰²	s^{-1}
τ	lifetime of the complex; bound-state lifetime ³⁰¹	s

It becomes clear that important parameters could be extracted from SMFS experiments by plotting the mean rupture force F from Gaussian fits of corresponding histograms against the logarithmic loading rate r . The intercept gives the information of χ_β , while the slope with the value of χ_β lead to the thermal off rate k_{off} which is itself inverse to the lifetime τ of the bound state. Moreover, it is even possible based on the transition state theory with the use of k_{off} to calculate the total free energy ΔG where h is Planck's constant (based on the literature^{298,301,303} including literature in there):^{298,301,303}

$$(47) \quad \Delta G = -k_B T \ln \left(\frac{k_{\text{off}} h}{k_B T} \right)$$

It has to be noted that this model only fits rupture events and not plateau events due to equilibrium processes like plateaus being independent of the retraction rate.

2.9 Identification of macroscopic adhesion performance

2.9.1 90°-peel-test

Not only the molecular adhesion based on the applied AFM based methods are interesting for the analysis of adhesion mechanism. In fact, the macroscopic adhesion force measured by 90°-peel-tests opens the possibility for a comparative and quantitative measurement of macroscopic peel-off forces. Within this experimental approach, model adhesive films like an epoxy-amine resin could be applied and cured on metallic samples without or with adhesive films (compare following Figure 24).³⁰⁴

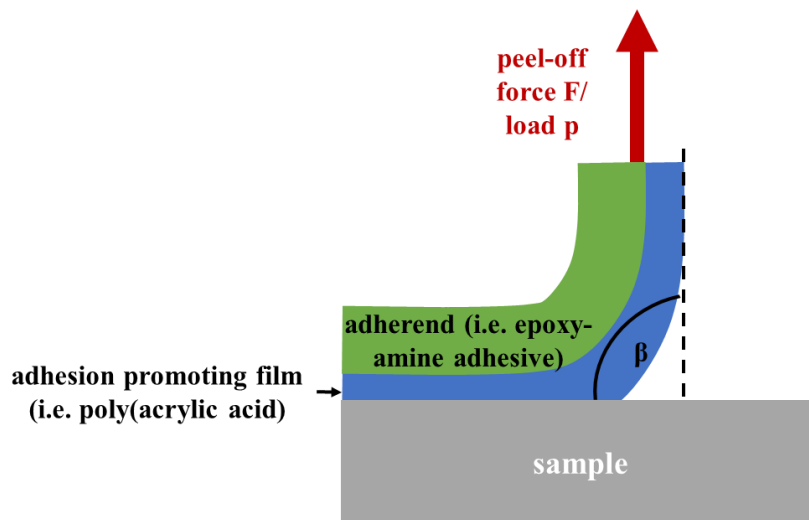


Figure 24. Schematic image of the measurement principle of a peel-test (based on Crocombe and Adams³⁰⁴ including literature in there).

The needed peel-off force can easily be measured by a force meter and gives a hint of the adhesion performance of joins. The load p or force F depends on the peel angle β .³⁰⁵ The latter one is fixed to 90° in all experiments. The peel-off forces are applied continuously on an adhesive film in a short time segment. To gain comparable results, the peel-off forces in N have to be normalized to the width of the detached film resulting in typically N/mm units. An advantage compared to the SMFS is that the free-standing surfaces can be analyzed by different surface analytics to investigate the adhesion mechanism and failure.

2.9.2 Shear test of two parallel connected specimens

A simple shear test was used in the 4. publication for the analysis of the interfacial forces due to the spray coating with water-based solutions containing ZnO tetrapods and poly(acrylic acid). The shearing of two specimens with a shear testing machine is well-known and could be performed in a straightforward way as displayed in Figure 25.³⁰⁶ Even the analysis of adhesion failures of small structures can be performed with the usage of simple shear test setups as shown by Schammler et al.³⁰⁷

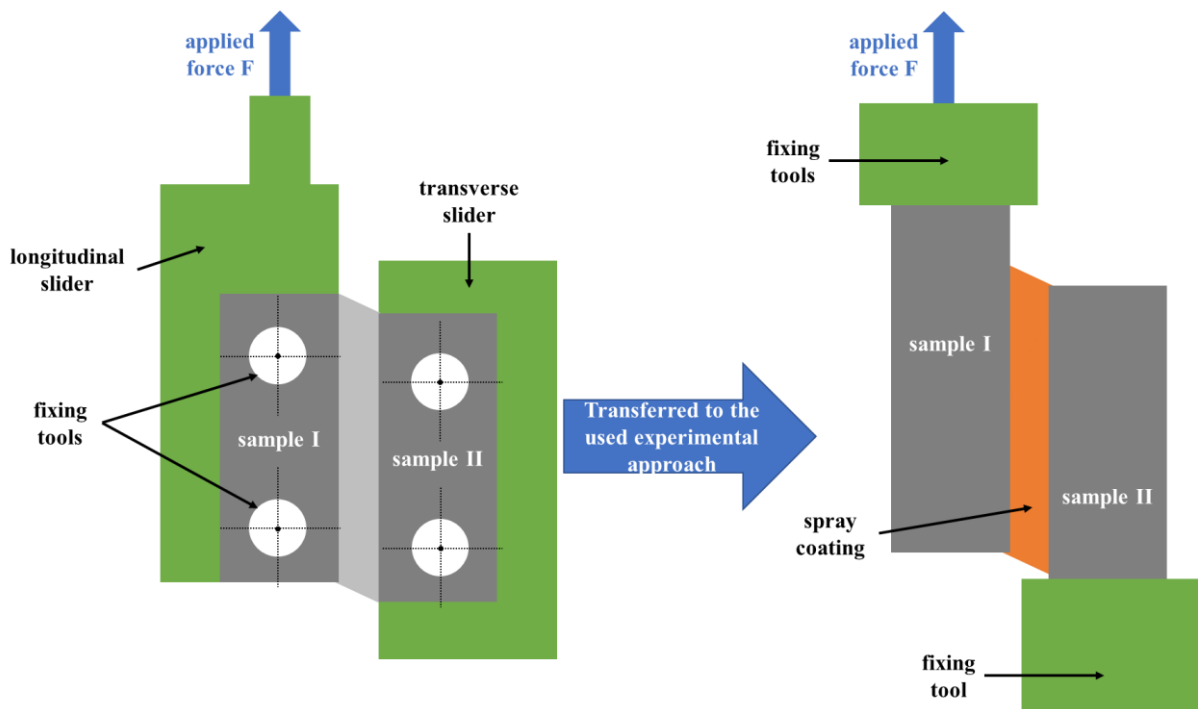


Figure 25. Schematic image of a simple shear test (left side, based on G'Sell et al.³⁰⁶ including literature in there) and the used approach in the 3. publication⁵³ of this thesis (right side).

A standard hydraulic tensile machine can apply the force to the longitudinal slider which is connected to sample I. With a transverse slide the sample side II is mounted. Here, a normal force can also be applied to stabilize the mounted construct (not shown in Figure 25). Further information can be found in the literature.³⁰⁶

For this PhD thesis, the experimental setup of the peel-test was used to apply the force F to a sample slide I which is fixed to the force meter and which is connected via a spray coating to a fixed sample II (right side illustrated in Figure 25 – compare 4. publication of this PhD thesis). The complete laminates were exposed to high humidity for a constant time. Consequently, the adhesive hybrid coating of the spray process loses its adhesive performance due to the migration of water at the interface. Indeed, the experimental results in the 4. publication showed an interfacial breakage.⁵³ Therefore, this setup could be used for the comparative investigation and proof of the different spray coatings. The forces were normalized to the joining area of the two samples to get N/cm^2 , respectively.

3 Publications

For this cumulative dissertation the following four first-author publications peer-reviewed in international journals were selected:

1. **Dennis Meinderink**, Alejandro Gonzalez Orive, Simon Ewertowski, Ignacio Giner, Guido Grundmeier, *Dependence of Poly(acrylic acid) Interfacial Adhesion on the Nanostructure of Electrodeposited ZnO Films*, ACS Applied Nano Mater. 2,2 (2019) 831-843
(abbreviated as **1. publication** in this thesis)
2. **D. Meinderink**, C. Kielar, O. Sobol, L. Ruhm, F. Rieker, K. Nolkemper, A. G. Orive, O. Ozcan, G. Grundmeier, *Effect of PAA-induced surface etching on the adhesion properties of ZnO nanostructured films*, International Journal of Adhesion and Adhesives 106 (2021) 102812
(abbreviated as **2. publication** in this thesis)
3. **D. Meinderink**, A. G. Orive, G. Grundmeier, *Electrodeposition of poly(acrylic acid) on stainless steel with enhanced adhesion properties*, Surface and Interface Analysis 50 (2018) 1224-1229
(abbreviated as **3. publication** in this thesis)
4. **Dennis Meinderink**, Karlo J.R. Nolkemper, Julius Bürger, Alejandro G. Orive, Jörg K.N. Lindner, Guido Grundmeier, *Spray Coating of Poly(acrylic Acid)/ZnO Tetrapod Adhesion Promoting Nanocomposite Films for Polymer Laminates*, Surface & Coatings Technology 375 (2019) 112-122
(abbreviated as **4. publication** in this thesis)

The scientific understanding of the molecular adhesion mechanism of poly(acrylic acid) (PAA) molecules on technically relevant substrates such as zinc oxide (ZnO) surfaces had still been an open question. Single molecule force spectroscopy (SMFS) with poly(acrylic acid) was performed on preconditioned stainless steel and nanostructured ZnO films electrochemically deposited on stainless steel to understand the molecular adhesion mechanisms like coordinative interactions to nonpolar ZnO surfaces (**1. publication**).

This established molecular adhesion model was used to tentatively transfer the adhesion promoting properties of PAA/ZnO materials to steel. The latter was done by means of the immersion of industrially relevant hot dipped galvanized steel (HDG) modified with ZnO nanostructured surfaces in dilute aqueous PAA solution including the proof of the macroscopic adhesion properties (**2. publication**). This work completed the understanding and evidence of the molecular adhesion properties by measuring the macroscopic adhesion via a model epoxy amine resin. These

results are in full agreement with the conclusions obtained from SMFS experiences. So, the molecular adhesion model could be extended to macroscopic systems.

Based on the results generated from Bauer, Meinderink et al. via electropolymerization of acrylic acid on carbon fiber reinforced plastics¹⁸⁰, the adhesion promoting properties of poly(acrylic acid) were tested on stainless steel substrates to prove the applicability as a macromolecule for the subsequent experimental approaches (**3. publication**). These results showed a significant enhancement in the macroscopic adhesion forces by variable PAA thicknesses controlled via the electrochemical conditions (here: constant current density with different deposition times). A possible interfacial failure in the PAA layer has been proposed.

The strong binding mechanisms such as coordinative bonds between the ZnO nanostructures and deprotonated PAA molecules established via SMFS and immersion/macromolecular adhesion experiments were combined in the development of a technically interesting spray coating process of ZnO tetrapod/PAA nanocomposite films on poly(propylene) (PP) foils (**4. publication**). Here, the cohesive failure in the core crystal structure of ZnO tetrapods (ZnO TP) and the adhesion promoting properties were demonstrated.

All in all, the total work of the selected four publications complete the understanding of the macroscopic and molecular adhesion mechanisms of PAA on technically and industrially relevant surfaces including stainless steel, ZnO nanostructured films and poly(polypropylene) foils. The generated benefits and knowledge open the door for the application of PAA/ZnO systems as adhesion promoting composite layers.

3.1 Dependence of Poly(acrylic acid) Interfacial Adhesion on the Nanostructure of Electrodeposited ZnO Films

The publication (**1. publication** of this PhD thesis) presented below and written by D. Meinderink, A. G. Orive, S. Ewertowski, I. Giner and G. Grundmeier with the title “*Dependence of Poly(acrylic acid) Interfacial Adhesion on the Nanostructure of Electrodeposited ZnO Films*” was reused with permission from American Chemical Society (ACS) Appl. Nano Mater. 2019, 2, 831-843. Copyright 2019 American Chemical Society.

<https://pubs.acs.org/doi/10.1021/acsanm.8b02091>

Zinc oxide nanostructures have reached a high level of interest due to their broad field of applications like photochemistry^{82,83}, gas sensors⁶⁸ and adhesion promoting properties³⁴ as already discussed in the introduction of this PhD thesis. However, the molecular mechanisms of nanostructured ZnO films causes behind these adhesion promoting properties are still an open question. Based on the enhancement of the macroscopic adhesion of poly(acrylic acid) shown in the **3. publication** below, the following **1. publication** combined the adhesion properties of both the zinc oxide nanostructures and poly(acrylic acid) to quantify the real molecular adhesion mechanisms by means of single molecule force spectroscopy (SMFS) based on atomic force microscopy (AFM). Gold cantilevers were modified with PEG via thiol-gold chemistry to first covalently bind an inert polymer chain as a distance holder between the tip of the cantilever and the end of the chain. Then, the distal amine groups in the PEG chains were used for the subsequent amide condensation with carboxylate groups present in the PAA chains, which remain thus attached to the gold-coated AFM tip. The dependence of the ratio of nonpolar sidewalls and polar topper parts of the ZnO wurtzite nanocrystals on the molecular adhesion with different dwell times was investigated. The results clearly demonstrated the increased interfacial molecular adhesion via coordinative and chelate bonds by having a higher amount of more accessible Zn^{+II} atoms in the outer part of the nonpolar sidewalls realized by ZnO nanorods. In comparison to that the platelet-like ZnO films showed lower molecular adhesion forces visible as rupture events in the corresponding force distance curves and plateau events occurred with increasing dwell time caused by lower molecular adhesion mechanisms based on electrostatic interactions and hydrogen bridging. This **1. publication** underlines that the adhesion promoting of ZnO nanostructures is not only affected by the mechanical interlocking but also based on the interfacial chemistry controlled by deposition methodology.

The input of the total work corresponding to the different Co-authors is summarized in the following Table 2. The first results were collected in the master thesis of S.E. We could reproduce

the results and use his work as a starting point for this publication. All produced results and figures are based on new work and ideas from D.M.

Table 2. Summary of the author contributions involved in the publication “*Dependence of Poly(acrylic acid) Interfacial Adhesion on the Nanostructure of Electrodeposited ZnO Films*”.

author contributions	involved persons
validation, writing, coordination, investigation, conceptualization, original draft, visualization, sample preparation, experimental executions, analytical measurements, evaluations, data curation, formal analysis, scientific discussion, review & editing	D.M
scientific discussion, support, mentoring, interpretation of data revisions of the manuscript, review & editing	A.G.O.
conceptualization, investigation, scientific discussion, content checking, review & editing	S.E., I.G.
project administration, funding acquisition, resources, conceptualization, scientific discussion, supervision, mentoring, interpretation of data, revisions of the manuscript, review & editing	G.G.

Dependence of Poly(acrylic acid) Interfacial Adhesion on the Nanostructure of Electrodeposited ZnO Films

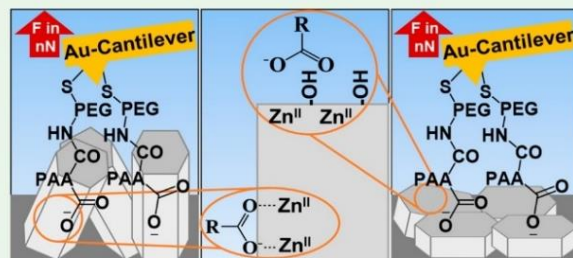
Dennis Meinderink,[✉] Alejandro Gonzalez Orive, Simon Ewertowski,[†] Ignacio Giner, and Guido Grundmeier*

Technical and Macromolecular Chemistry, University of Paderborn, Warburger Strasse 100, 33098 Paderborn, Germany

S Supporting Information

ABSTRACT: Understanding the impact of the intricate morphology and surface chemistry of ZnO nanorod arrays on their interactions with polyelectrolyte polymers is crucial for the development of nascent ZnO-based adhesion-promoting materials. AFM-based single molecule force spectroscopy was applied for the analysis of the adsorption of poly(acrylic acid) (PAA) on zinc oxide (ZnO) film covered stainless steel substrates in aqueous electrolytes at pH 7. Based on the electrodeposition process, the morphology of zinc oxide films could be varied ranging from platelet-like crystals to nanorods. This approach allowed for the morphology dependent analysis of macromolecular adsorption processes on complex ZnO nanostructures which have diverse applications in the field of adhesion-promoting thin films. The surface chemical composition, as determined by X-ray photoelectron spectroscopy, could be correlated to the AFM-based desorption studies. Only equilibrium desorption events (plateaus), centered at 42 pN, were observed on mirror polished, preconditioned stainless steel. However, for platelet-like ZnO films, the poly(acrylic acid) desorption showed a mixture of rupture events (mean rupture forces of about 350 pN) and equilibrium desorption, while ZnO nanorod structures showed solely rupture events with mean rupture forces of about 1300 pN. These results indicate that simultaneous multiple ruptures of carboxylate–zinc bonds occur due to the macromolecular coordination of poly(acrylic acid) to the ZnO nanorods. The analysis of the interfacial adhesion processes is further supported by the dwell time dependence of desorption processes.

KEYWORDS: electrochemical deposition, zinc oxide (ZnO), stainless steel, single molecule force spectroscopy (SMFS), molecular adhesion, poly(acrylic acid), adsorption free energy, worm-like chain (WLC) model



1. INTRODUCTION

Fundamental and applied studies on both the optical, physicochemical, and electronic features and also the interfacial adhesion properties to polymers and macromolecules exhibited by crystalline zinc oxide-based surfaces (ZnO) have received considerable attention from the research community. ZnO nanostructures have been studied intensively in recent years. They find application in many fields, such as photodiodes, photocatalysts, light emitting diodes, photodetectors, solar cells, varistors, and gas sensors.^{1–4} The wide application range of ZnO nanostructures can be attributed to the inherent characteristics of ZnO and its ability to create diverse morphological structures both in solution and at solid substrates. In addition, their physicochemical surface area reactivity can be monitored by varying their aspect ratio.⁵

Both the crystal structure of ZnO surfaces and their growth mechanisms have been thoroughly investigated over the past few years.⁶ Recent reviews provide a comprehensive overview over the different deposition methodologies aimed at the controlled growth of ZnO nanostructures.^{5,7,8} In this regard, deposition methods based on aqueous solutions have been proved to be an efficient and low-cost methodology to grow one-dimensional ZnO nanostructures even on substrates with a

large surface area under mild conditions. Deposition parameters such as temperature, concentration of the precursor molecules, deposition time, and the addition of growth-affecting organic⁹ or inorganic additives, strongly influence the growth behavior of the as-obtained structures and the parameters of the synthesis were optimized over the most recent decades.^{10–12} The deposition of ZnO nanorod structures on conductive materials can be easily achieved by electrodeposition from aqueous precursor solutions. In this procedure the application of a potential across the interface allows for an accurate control of the deposition process as shown in a recent review by Skomska and Zarebska.⁵ As an example, Liu et al. and Wong et al. used this methodology to precipitate ZnO nanorods onto gold substrates and polycrystalline Zn foils, respectively.^{13,14}

The design of nascent polymer–metal oxide interfaces based on nanostructured crystalline ZnO surfaces is of great interest for many different applications.^{15,16} In particular, the modification of substrates with ZnO nanorods would offer

Received: November 19, 2018

Accepted: January 16, 2019

Published: January 16, 2019

significant advances related to their inherent adhesion-promoting capabilities.¹⁵ Ozcan et al. have proved that significant adhesion enhancement between a metal substrate and an adhesive polymer can be achieved by modifying the substrate with ZnO nanorod films most likely due to the enhanced interfacial surface area together with the differential surface energy at ZnO adsorption sites.¹⁵ However, the fundamental mechanisms leading to such macroscopically very stable interfaces have not been reported yet. Here we will explore the enhancement in the interfacial adhesion to a model polyelectrolyte, namely, poly(acrylic acid) (PAA), experienced by stainless steel substrates modified with ZnO nanorod films by means of AFM-based single molecule force spectroscopy (SMFS). SMFS allows one to quantify interfacial binding properties of single molecules and macromolecules (covalently attached to an AFM tip) to a specific surface.¹⁷ In a typical SMFS experiment, the force experienced by a molecular interaction with a specific site on the substrate increases gradually as the AFM tip is withdrawn from the sample until its subsequent rupture. These adhesion forces can be straightforwardly estimated from the peaks/plateaus arising in the force–distance curve. Extensive reviews of this measurement technique was published by Butt et al.,¹⁸ Kim et al.,¹⁹ and Anselmetti et al.²⁰ The crystalline surfaces present in individual nanorods are the ZnO(0001)–Zn oriented top surface and ZnO(10 $\bar{1}$ 0)–Zn facets parallel to the *c*-axis arranged in hexagonal prisms. Under atmospheric conditions, the Zn-terminated polar ZnO(0001) surfaces are stabilized via adsorption of hydroxyl groups, which cancel the intrinsic dipole moment present at the Zn atoms.^{16,21,22} The sidewall surfaces, where Zn and O atoms are exposed, exhibit higher chemical reactivity to form coordinative bonds with various functional groups such as carboxylic and phosphonic acids. In this regard, fundamental adsorption studies carried out by Valtiner and Grundmeier on single-crystalline ZnO(0001)–Zn surfaces by means of SMFS clearly demonstrated that carboxylic acid functionalities present in PAA molecules adsorb weakly to hydroxyl-stabilized polar ZnO(0001)–Zn surfaces (equilibrium peel-off plateau forces), whereas they strongly bind to the separating step edges, namely, at nonpolar ZnO(10 $\bar{1}$ 0)–Zn domains, between the polar terraces, most probably via coordinative bonds (nonlinear non-equilibrium rupture forces).¹⁶

Based on the latter results primarily obtained by Valtiner and Grundmeier¹⁶ and Ozcan et al.,¹⁵ and in order to elucidate some important issues regarding the mechanisms for the interfacial adsorption of polyelectrolyte polymers, namely, PAA, onto ZnO nanorods, but both at a single-molecule level and on the nanoscale, SMFS measurements have been carried out within this work. PAA polyelectrolyte (macro)molecules are used here as a suitable sensor for characterizing the adhesive properties of surfaces of interest in the nanoscopic level.^{16,23–27} SMFS not only represents an outstanding tool for probing these local interfacial adhesion interactions on zinc oxide crystalline surfaces, but also allows for the unveiling and quantification of (possible) unfolding, shear, and interlocking events²⁸ occurring on randomly oriented and densely packed electrodeposited ZnO nanorod arrays. Presumably, an enhanced proportion of nonpolar sidewall surfaces exposed to the interface in these ZnO nanorod films should lead to enhanced unbinding values for the detachment of PAA molecules. In order to clearly demonstrate (and quantify) this assumption, ZnO nanostructured films exhibiting different

aspect ratios were consequently prepared on stainless steel substrates: ZnO nanorod and platelet-like ZnO films. Thus, the dependence between the shape/profile and the magnitude of rupture force and plateaus present in the force–distance curves obtained for cycles of adsorption/desorption of PAA (macro)molecules onto ZnO nanorod films with the specific morphology of the samples and the dwell time are investigated. To further illustrate the enhanced adhesion promotion exerted by these two ZnO surfaces, the SMFS results were compared to those exhibited by preconditioned bare stainless steel samples. To the best of our knowledge, very few reports have dealt so far with the characterization of the adhesive capabilities exhibited by nanostructured or nanoroughened metal oxide crystalline surfaces such as those exhibited by ZnO nanorods of high aspect ratio.²⁹ Finally, here we show that PAA adsorption can be dramatically favored by the precise control of ZnO-film morphology.

2. EXPERIMENTAL SECTION

2.1. Materials and Chemicals. **2.1.1. Preconditioning of Stainless Steel Samples for SMFS Measurements.** Mirror polished stainless steel foil (type 1.4301, X5CrNi18-10) was cut into 2 × 2 cm² pieces. The samples were consecutively rinsed for 15 min in tetrahydrofuran (THF; p.a. grade, stabilized), isopropanol (p.a. grade), and ethanol (p.a. grade) in an ultrasonic bath. Afterward, the samples were dried in a nitrogen stream. In addition, a plasma cleaning step (Plasma Surface Technology, Diener electronic GmbH, Germany) was carried out by treating the samples in a pure oxygen plasma (*p* < 0.4 mbar, >40 l/h) for 1 min to remove any organic contamination. Finally, the cleaned stainless steel substrates were exposed to the aqueous electrolyte (2 mM NaClO₄, pH adjusted to 7 by adding drops of 0.1 M NaOH) for 72 h to create a hydroxyl-rich surface according to the work of Landoulsi and Dupres.³⁰

2.1.2. ZnO-Film Deposition. ZnO nanorod films were deposited by cathodic electrodeposition on the mirror polished stainless steel after the solvent cleaning steps mentioned before. The cathodic electrodeposition was performed in equimolar 0.01 M hexamethylenetetramine (HMTA) and 0.1 M/0.01 M Zn(NO₃)₂·6H₂O-containing aqueous solution at 80 °C for 900 s, using a three-electrode setup. By using a Reference 600 potentiostat (Gamry Instruments), a constant current density of −0.5 mA/cm² was applied to the steel samples. The surface area of the working electrode (WE) was confined by isolating the sample with aid of an inert adhesive tape to have a final surface area of 2 × 2 cm². A potassium chloride-saturated Ag/AgCl electrode was used as reference electrode (RE). This was connected to the heated solution (*T* = 80 ± 3 °C) by means of a salt bridge (filled with 0.1 M NaNO₃ aqueous solution) in order to avoid potential differences due to the thermal treatment. A cylindrical tube made of stainless steel, which allows one to obtain a homogeneous electrical field distribution, was chosen as counter electrode (CE). After each deposition time, the samples were rinsed with ultrapure water (0.055 μS/cm, Ultra Clear TWF, SG water, Hamburg, Germany) and a successive drying step with a gentle nitrogen flux was carried out as described above.

2.2. AFM-Tip Preparation. Gold-coated Si cantilevers (HQ-CSC17/Cr-Au, MikroMash, 10–17 kHz, 0.2 N/m) were used as delivered without further cleaning. The functionalization of the cantilevers was done via thiol–gold chemistry. PAA functionalization was carried out with help of an amide coupling of PAA chains to the previously modified NH₂–PEG-functionalized cantilevers according to Valtiner and Grundmeier.¹⁶ First, the cantilevers were immersed for 5.25 h in an aqueous solution of α -mercapto- ω -amino PEG hydrochloride (HS-PEG-NH₂ × HCl, 0.025 g, 0.05 mmol; PEG MW: 10 000 Da; Rapp Polymere GmbH) in purified milli-Q water (50 mL). *N*-Hydroxysulfonosuccinimide sodium salt (S-NHS; 28 mg, 26 mmol; Sigma-Aldrich) and *N*-(3-(dimethylamino)propyl)-*N*'-ethylcarbodiimide hydrochloride (EDC hydrochloride; ≥98%, 75 mg, 96 mmol; Sigma-Aldrich) were solved in 5 mL of an aqueous solution of

4-(2-hydroxyethyl)-1-piperazineethanesulfonic acid buffer (HEPES, high-purity grade, Amresco, USA; 10 mM; pH tuned to 7.1 with NaOH solution). A 100 μL aliquot of that stock solution was added to 10 mL of a solution of PAA (5 g/L; MW: 450 000; Sigma-Aldrich) in 10 mM HEPES buffer solution. The as-prepared solution was shaken shortly, and the NH_2 -PEG-functionalized cantilevers were immersed into the latter for 90 min. Afterward, the resulting PAA-modified cantilevers were stored in 1 mM EDTA-containing aqueous solution for 12 h and then for an additional 6 h in pure milli-Q water. The storage of the loaded cantilevers was performed in 100 mM EDTA solution. The cantilevers were used directly in order to avoid a condensation of the PAA chains after dipping three times in ultrapure water.

Together with the preparation of the cantilevers, 200 nm of PVD gold-coated Si wafers were added to the solutions at each step of the functionalization process with the aim to monitor the chemical surface structure modification of the as-prepared cantilevers. The confirmation of a successful modification of the cantilevers with PAA was performed by means of PM-IRRAS and XPS experiments. Details of these measurements are thoroughly explained in the Supporting Information (SI).

2.3. Analytical Methods. **2.3.1. Electron Microscopy.** The morphological characterization of the produced ZnO nanorod and platelet-like ZnO films was carried out with the help of a field-emission scanning electron microscope (FE-SEM). A NEON 40 FE-SEM (Carl Zeiss SMT AG) was used to acquire high-resolution SEM images.

2.3.2. Analysis of the Chemical Surface Composition. Chemical analysis of the prepared cantilevers was performed by means of polarization modulation infrared reflection absorption spectroscopy (PM-IRRAS) using a Bruker Vertex 70 (Bruker Optics, Germany). The samples were analyzed with a resolution of 4 cm^{-1} at an angle of 80° . A ZnSe photo-elastic modulator (PMA50, Bruker, Germany) was used to apply a 50 kHz modulation to an aluminum wire grid in order to receive p-polarized light. The light reflected by the sample was focused by a ZnSe lens on the entrance of a liquid nitrogen cooled mercury cadmium telluride (LN-MCT) detector.

Furthermore, angle resolved X-ray photoemission spectroscopy (AR-XPS) measurements were done in an ESCA+ setup (Omicron NanoTechnology, Germany) at a base pressure better than 5.0×10^{-10} mbar. Monochromatic Al-K α irradiation (1486.7 eV) was used under an angle of 60° with respect to the surface plane in the cases of the ZnO films and the gold samples for the cantilever modification as well. Angles of 20° and 80° with respect to the surface plane were used in the case of the polished and preconditioned stainless steel. A multichannel plate detector (Omicron Argus, Germany) was used to collect the photoelectrons. No neutralization was applied. The resulting spectra were calibrated according to the C 1s peak position at 285.0 eV as an internal reference. CASA-XPS software was used for peak fitting and data analysis. Peaks were integrated with respect to the corresponding relative sensitivity factor (RSF) values. A Gauss–Lorentzian peak shape and a Shirley type background correction were used.

2.3.3. Single Molecule Force Spectroscopy. The force–distance measurements were performed with a JPK Nano-Wizard III AFM (JPK Instruments, Germany) in the force-mapping contact mode. An electrochemistry cell (JPK Instruments) was used to measure within an aqueous electrolyte solution under reproducible experimental conditions. The electrolyte consisted of an aqueous solution of 2 mM NaClO_4 (98+%, Sigma-Aldrich). NaClO_4 was used as electrolyte since it can be considered an inert salt which does not adsorb specifically on metal oxide surfaces as stated by Gerischer and Sorg.³¹ A NaOH solution (0.1 M, ultrapure, Sigma-Aldrich) was used to tune the pH of all electrolytes to a value around 7.0. All force measurements were carried out at 298 K. Under these conditions, ZnO nanorod surfaces should remain stable during the typical SMFS measurement time, as shown for ZnO(0001)–Zn single-crystal substrates by Valtiner and Grundmeier.¹⁶ Small ionic concentrations were applied to avoid a screening effect toward the polymeric chains. In addition to that, the ionic strength and pH were kept constant so that the Debye length

and the electrostatic double layer of the corresponding interfaces should be nearly the same. To avoid concentration changes caused by evaporation of the electrolyte, a constant flow of around 0.52 mL/min was chosen. The initial filling of the cell before a measurement was done by a flow rate of 2.24 mL/min.

The approaching and retracting speed of the cantilever was set to a constant value of $0.5\text{ }\mu\text{m/s}$ in the z -direction. The primary deflection set point during the first cantilever approach in dry conditions was set to 100 mV (around 2.0 nN after calibration). Then the cantilever was retracted again 100 μm from the surface and approached with a set point of 200 mV (around 4.0 nN after calibration). Prior to every measurement, the deflection of the cantilever was converted from a voltage into a force by using the deflection sensitivity of the cantilever, given by the slope of the deflection (unit V)–piezo height displacement curve in the contact regime. Furthermore, the required spring constant k_c of the cantilever was determined by the thermal contact-free method in water at 28°C with the specific parameters of the cantilever (HQ; CSC17/Cr-Au). Afterward, the deflection set point was fixed to a constant value of 4 nN in all map measurements.

In every measurement 256 force–distance curves were recorded using a $2 \times 2\text{ }\mu\text{m}^2$ area on a patterned grid with 16×16 pixels on three different positions from distinct but equivalent samples. JPK data-processing software was used to analyze the recorded force–distance curves after baseline correction and to determine the rupture and plateau forces curve by curve.

3. RESULTS AND DISCUSSION

A graphical scheme that summarizes the key steps involved in the present work is shown in Figure 1.

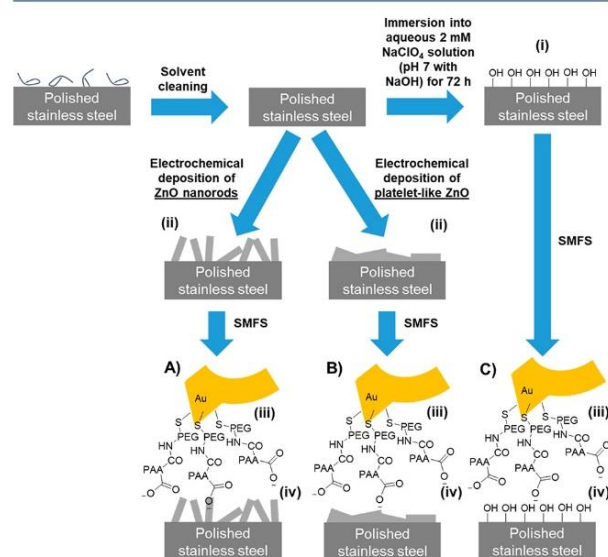


Figure 1. Schematic illustration of the step by step fabrication of the three different surfaces. Single molecule force spectroscopy (SMFS) was performed with deprotonated poly(acrylic acid) functionalities (PAA) connected to a gold cantilever with a poly(ethylene glycol) (PEG) chain on (A) ZnO nanorods, (B) platelet-like ZnO, and (C) preconditioned, polished stainless steel substrates.

The latter includes the following: preconditioning bare stainless steel samples (i), the fabrication of ZnO-based nanostructured films exhibiting different aspect ratios onto stainless steel substrates, namely, platelet-like ZnO and ZnO nanorod films (ii), the modification of gold-coated AFM tips via thiol chemistry for the covalent attachment of PAA chains (iii), and the subsequent characterization of the adhesion-

promoting properties of the as-prepared ZnO-based surfaces to a model polyelectrolyte such as PAA by means of SMFS (iv).

3.1. Electrochemical Deposition of Platelet-like ZnO and ZnO Nanorod Films on Mirror Polished Stainless Steel. Two different ZnO morphologies (platelet-like ZnO and ZnO nanorod films) with different aspect ratios, were prepared by cathodic electrodeposition from zinc nitrate precursor-containing solutions onto mirror polished stainless steel substrates such as those described above.

Typical potential versus time curves for the deposition of ZnO nanorods and platelet-like ZnO films on the stainless steel samples are illustrated in Figure S1 of the [Supporting Information](#). The chronopotentiometric curves exhibit a characteristic profile, consisting of a potential minimum at low deposition times followed by a monotonic shift to more negative potentials for higher deposition times. As can be observed in Figure S1, the registered potential values are larger for the higher $\text{Zn}(\text{NO}_3)_2/\text{HMTA}$ ratio, i.e., platelet-like ZnO film. The measured values were in the same range as the potentials described in literature for the deposition of ZnO nanorods.³² Regarding the constant slope of both curves, the deposition seems to be very stable although it was carried out upon thermal convection at 80 °C bath temperature. The FE-SEM images of the polished preconditioned stainless steel, the ZnO nanorods, and platelet-like ZnO films are depicted in Figure 2.

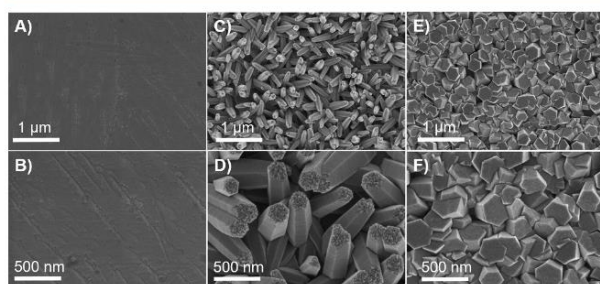


Figure 2. FE-SEM images of (A, B) mirror polished stainless steel substrate after cleaning steps; (C–F) mirror polished stainless steel after cathodic electrodeposition ($i = -0.5 \text{ mA}/\text{cm}^2$, $t = 900 \text{ s}$, $T = 80 \text{ °C}$ without stirring) of ZnO nanorods with (C, D) 10 mM $\text{Zn}(\text{NO}_3)_2 \cdot 6\text{H}_2\text{O}/10 \text{ mM}$ HMTA and of platelet-like ZnO (E, F) 100 mM $\text{Zn}(\text{NO}_3)_2 \cdot 6\text{H}_2\text{O}/10 \text{ mM}$ HMTA.

The FE-SEM images indicated in Figure 2C,D show hexagonal rods with comparable sizes exhibiting diameters in the regime of 100 nm. Their length was estimated to be around 500 nm. The rods are narrower when approaching their end faces, which exhibit a certain roughness. Furthermore, the rod orientation is not homogeneous. Indeed, some of them are oriented perpendicular to the substrate, while others grow in a wide range of tilt angles with respect to the substrate normal. This inhomogeneity ensures a good accessibility for the PAA molecules bound to the tip of the AFM cantilever. In general, the mechanical interlocking and/or the mechanical adhesion of these surfaces should be higher than in the case of polished stainless steel and platelet-like ZnO surfaces.

The influence of different parameters on the growth morphology such as the concentration of precursors (specially Zn^{2+} and OH^-), the pH, and structural modifiers are well-known and discussed in further detail in the reviewed literature.⁵ Typically, precursors such as zinc nitrate offer the

advantage of being very soluble in water. The proposed mechanisms and chemical reactions under reductive electrochemical conditions are reported elsewhere.⁵ Especially the effect of using additives to control the morphology is a nice tool to create well-defined ZnO films on different substrates.⁵ In general, the modifiers should specifically block the nonpolar wall sides, as stated in the literature for Cl^- ions.^{5,33} Nicholas et al. had figured out that the use of citrate and ethylenediamine are also possible options to control the aspect ratio of ZnO crystals.³⁴ In this context, HMT (for hexamine), also named HMTA (for hexamethylenetetramine), has been suggested as a OH^- source³⁵ and, additionally, it has been proposed by Sugunan et al. that these HMTA molecules might act as a chelating agent which could specifically block the nonpolar areas, i.e., (10 $\bar{1}$ 0) and (10 $\bar{1}$ 1), as well.^{5,10} Then, the transport of Zn^{2+} ions for the crystal structure growth is consequently hindered and the platelet-like ZnO films, shown in the FE-SEM images in Figure 2E,F, were subsequently obtained. In this case, the top hexagonal facets show a larger size than in the case of the nanorods. Consequently, the polar/nonpolar crystalline face ratio is higher than that obtained for the ZnO nanorods. We have used HMTA for both deposition processes since HMTA is unquestionably a good OH^- source, but interestingly only with the change in the ratio of zinc nitrate precursor to HMTA, i.e., from 1:1 (for ZnO nanorods) to 10:1 (for platelet-like ZnO), is enough to monitor the proposed growth mechanism, as suggested in the literature.⁵

A scheme with the crystallographic facet distribution, valid for the two different ZnO films, is shown in Figure S2 of the [Supporting Information](#) according to the widely discussed data obtained from the bibliography.⁵ The difference in the aspect ratios becomes thus clear and would imply an enhanced proportion of nonpolar sidewall surfaces exposed to the interface for the case of ZnO nanorod films. The description of ZnO single crystals was used to explain the surface chemistry and crystalline structure of ZnO nanorods, which is subsequently extrapolated to platelet-like ZnO films. The polar (001)-planes should be OH^- stabilized, as previously stated by Valtiner et al., while the lateral wall sides are essentially nonpolar.²¹ Accordingly, by increasing the nonpolar area ratio, it should be possible to obtain more coordinative binding sites for ions and adhesion-promoting molecules such as PAA.

3.1.1. XPS Results of the Electrodeposited ZnO Films. As expected, the XPS survey spectra of the electrodeposited ZnO nanorod films and platelet-like ZnO films show the presence of Zn, O, and C. These spectra were measured at an angle of 60° with respect to the surface and are displayed in the Figure S3 of the [Supporting Information](#). By evaluating the core level spectra, surface concentrations of 40.9 at. % for oxygen, 36.1 at. % for zinc, and 23.0 at. % for carbon are obtained in the case of ZnO nanorods, as can be seen in Table 1.

Table 1. XPS Data of the ZnO Nanorod and Platelet-like ZnO Surfaces

	ZnO nanorods		platelet-like ZnO	
	binding energy/eV	at. %	binding energy/eV	at. %
O 1s	530.3	40.9	530.3	42.2
Zn 2p _{3/2}	1021.5	36.1	1021.6	31.6
C 1s	285.0	23.0	285.0	26.2

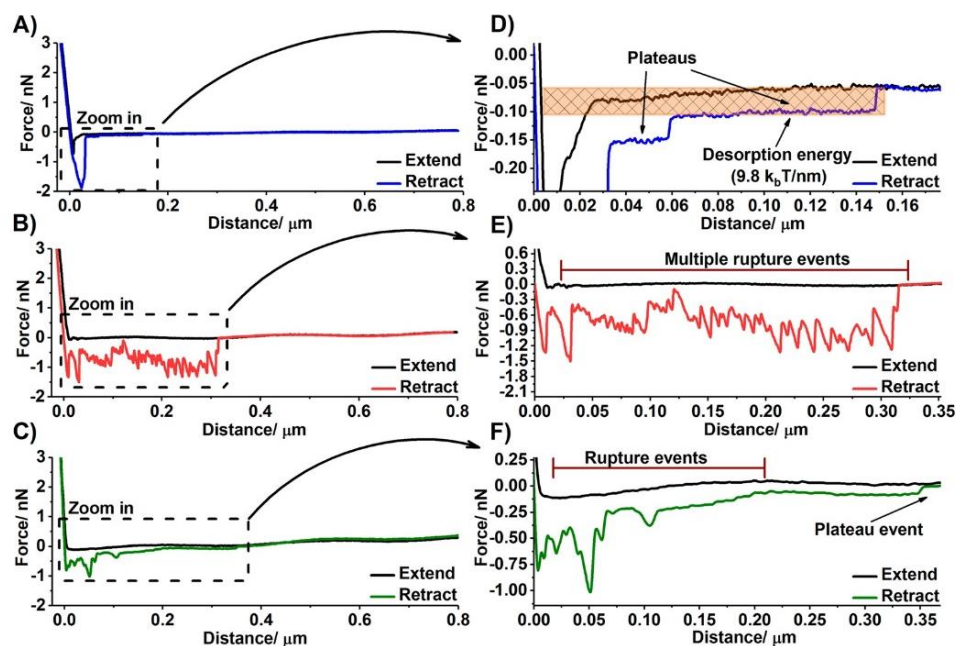


Figure 3. Characteristic force–distance curves obtained for the three different surfaces with a dwell time of 5.0 s: (A) preconditioned polished stainless steel, (B) ZnO nanorods, and (C) platelet-like ZnO; (D–F) corresponding zoom-ins. Plateaus and rupture events are marked.

The ratio of oxygen to zinc in the case of the ZnO nanorod films is about 1.1:1, while for the platelet-like ZnO films, it is about 1.3:1. Pure ZnO without any stabilization with hydroxyl groups should lead to a ratio of 1:1. However, taking into account the adsorbed water for the stabilization mechanism of the polar planes and the adsorbed carbon contaminations, the measured ratio is in a reasonable range. It is indeed in a very good agreement with the current literature for ZnO films.^{36,37} For example, Mutel et al. found a ratio of 1.1–1.2 and explained it in terms of a small excess of oxygen as OH groups at the surface.³⁷ In our measurements, the carbon contamination is around 10–15% higher. This can be attributed to the enhanced total surface area in comparison to smooth pure crystalline ZnO films. Furthermore, our results show that a high amount of oxygen is present at the surface, which could be due to specific oxygen species such as surface hydroxyl groups in the form of $\text{Zn}(\text{OH})_2$, adsorbed water and oxygen, and/or carbonates.^{38–40} In addition, it was also shown by Valtiner et al. and other authors that the $\text{Zn}(0001)$ -plane is strongly stabilized by hydroxyl species, as mentioned before.^{21,41–43} Regarding the identification of the different components, a tentative peak fitting is provided in Figure S4 in the Supporting Information for the high-resolution XPS spectra of O 1s, C 1s, and Zn $2p_{3/2}$ for the ZnO nanorod films and for the platelet-like ZnO films. The peak positions and concentrations are summarized in Table S1. No nitrogen contributions could be detected in the XPS measurements of the platelet-like ZnO and ZnO nanorod films. Consequently, no molecules bearing N-containing functional groups such as HMTA remain adsorbed on the ZnO-based surfaces after the ZnO synthesis and the subsequent rinsing processes of the ZnO-modified stainless steel substrates. All further results are discussed and quoted in the SI.

3.2. SMFS of Poly(acrylic acid) on Preconditioned Stainless Steel Surfaces, ZnO Nanorod, and Platelet-like ZnO Films. 3.2.1. Qualitative Comparison of Desorption

Curves. As previously stated, SMFS has been proven to be a valuable tool to unveil and quantify interfacial adhesion forces occurring between molecules or macromolecules covalently attached to an AFM tip and specific sites in metal oxide surfaces and, in particular, on ZnO crystalline substrates.¹⁶

AFM tips were functionalized by gold–thiol chemistry and were characterized by PM-IRRAS and XPS (Figure S5, Table S2, and Figure S6 in the Supporting Information). The infrared data show the characteristic peaks expected for the PEG chain such as the vibration mode for the aliphatic part C–H at around 2870 cm^{-1} and the carbonyl (C=O) stretching mode at around 1738 cm^{-1} . Further detailed discussion can be found in the Supporting Information.

After an equilibration time of 15 min with a pumping speed of 0.5 mL/min , force–distance curves were collected. For all measurements considered, equivalent cantilevers prepared in similar conditions were used. Within this work, we have only considered unbinding events corresponding to both plateau and rupture forces, those which exhibit desorption values higher than 10 pN (versus the corrected baseline at 0 pN). Additionally, different spots from distinct but equivalent samples were analyzed by means of SMFS at neutral pH. Sonnenberg et al. had discussed the influence of the pH on the PAA conformation and the charging effects.²⁴ Regarding the conformation of the PAA chains, the proposed experimental conditions should provide a good compromise between shrinking of the coils and the completely unfolded polyelectrolyte chains situations, as previously discussed by Kunze et al.⁴⁴ The carboxylic functionalities of the poly(acrylic acid) chains at neutral pH in a 2 mM NaClO_4 aqueous solution should be negatively charged since the pK_a of acrylic acid monomers has been mentioned to be around 5.5 by Sonnenberg et al. ($\text{pH} < \text{pK}_a$) and 6.0 for PAA chains, as reported by Valtiner et al.^{16,24} In this regard, Palacio et al. provided a pK_a value for PAA of 4.7 and showed SMFS measurements of negatively charged PAA chains present on

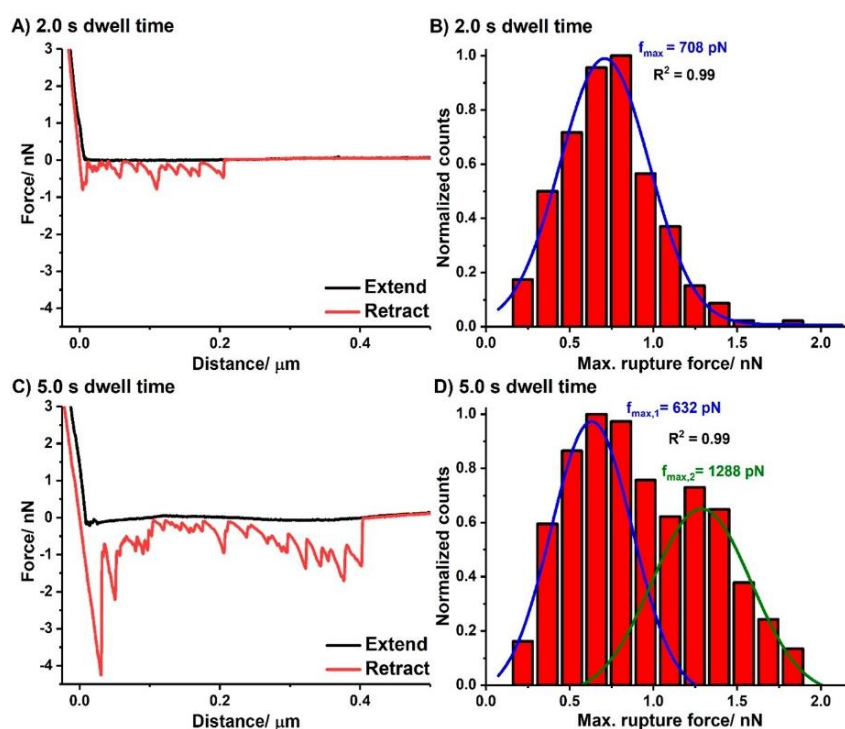


Figure 4. (A, C) Force–distance curves for the two different dwell times, 2.0 and 5.0 s, with corresponding normalized histograms obtained from statistic results of the maximum rupture force registered for ZnO nanorods deposited on stainless steel for (B) 2.0 and (D) 5.0 s dwell times.

polymers by using protein-functionalized AFM tips at pH 7.4 and pH 6.2.⁴⁵

Such negatively charged PAA functionalities are used in our approach to probe the molecular adhesion capabilities of the three substrates: mirror polished and preconditioned stainless steel, ZnO nanorod, and platelet-like ZnO films deposited on stainless steel. Typical force–distance curves obtained for the three investigated surfaces are shown in Figure 3.

The plots displayed in Figure 3A,D show typical force–distance curves measured for stainless steel; curves B and E have been obtained for ZnO nanorods and curves C and F for stainless steel covered with platelet-like ZnO films. By comparing the three different force–distance profiles shown in Figure 3A–C, it can be observed that surface morphology and surface chemistry have a strong influence on the desorption curve profiles which reflect the adsorbed macromolecules. Some little deviations from perfect linearity can be identified in the baseline of the *F*–*D* profiles displayed in Figure 3. The latter can be attributed to some optical interferences getting to the photodiode coming from light scattering (stray light) originated in the sample surface (especially when the substrates are also highly reflective as in our case) or in the different interfaces appearing when the system is operating in the liquid cell fulfilled with electrolyte.⁴⁶ Nevertheless, for the quantification of the magnitude of both rupture and plateau forces, a careful selection of the suitable sections and subsequent correction of the baseline slope have been carried out with the aim of avoiding any misinterpretation of the as-registered desorption data.

For passive film covered stainless steel, solely equilibrium desorption curves with step heights of about 40 pN, typically observed for physisorbed macromolecules at electrolyte/oxide interfaces, were observed (Figure 3A,D). The detailed

evaluation of the XPS data of the polished, preconditioned stainless steel is illustrated in Figure S7 (XPS surveys measured at 80° and 20° with respect to the surface), and Figure S8 (high-resolution XPS spectra of O 1s and C 1s). The quantifications of the corresponding components are displayed in Tables S3–S5. The histograms for the dwell times of 2.0 and 5.0 s are plotted in Figure S9, while their quantifications are presented in Table S6 of the Supporting Information. Nanorod films showed solely non-equilibrium rupture events as shown in Figure 3B,E. However, both equilibrium and non-equilibrium events were observed for the platelet-like ZnO films with rupture forces (see Figure 3C,F) exhibiting an average value of 370 pN as deduced from statistic evaluation (see below). Such results are in agreement with recent studies of macromolecular desorption of a spider silk protein and poly(allylamine)⁴⁷ on stainless steel and PAA on ZnO single-crystal surfaces.¹⁶

Nonlinear force–extension profiles resembling non-equilibrium desorption events, most probably due to PAA irreversibly bound Zn atoms present in nonpolar crystalline side facets of nanorod ZnO films, are observed, as displayed in Figure 3B,E. In the case of the platelet-like ZnO structure, which is rather dominated by the polar crystal orientation, such coordinative bonds are less likely. Second, plateau desorption forces are indicative of equilibrium desorption processes related to weaker interactions via reversible hydrogen bridging and electrostatic interactions of PAA at polar hydroxyl-stabilized top surfaces. The latter has already been shown for ZnO single crystals by Valtiner and Grundmeier.¹⁶ However, the following considerations should be taken into account before discussing SMFS experimental data. The first peak appearing in the withdrawal/retract regime of the force–distance curves, which represents the unspecific interactions of

the gold tip with the surface, is neglected. Occasionally, it slightly overlaps with the beginning of the PAA chains interactions, as can be seen in Figure 3C,F. In order to exclude possible interactions from the uncovered tips, additional experiments were carried out using non-PAA-modified cantilevers. Such bare tips showed only the aforementioned unspecific interaction of the AFM tip with the surface. To avoid a strong interaction and overlapping of the adhesion forces in the force–distance curves of the pure tip interaction with the surfaces, the mentioned PEG chain is linked between the tip and the PAA chain, as thoroughly explained by Geisler et al.⁴⁷ The latter was found for all three different surfaces. Conversely, the characteristic force–distance curves depicted in Figure 3 were observed only when modified cantilevers were used. The rupture event starts initially close to the baseline level. During the detachment of the cantilever away from the surface, the force rises until the interacting bond between the PAA chain and the surface breaks. The successive force drop would ideally end at the baseline level of force at 0 pN. However, for the ZnO-coated substrates, the cantilever is not able to bend back to its starting position. Either another segment of the same PAA chain or another PAA molecule is detached from the surface and leads to a subsequent rebinding of the cantilever. Thus, the rupture events tend to overlap and sometimes cannot be effectively separated. The characteristic profile exhibited by these *F–D* curves, namely, overlapping multiple rupture force events, could be originating from the simultaneous desorption of different carboxylate moieties present in the same PAA molecule but also from the concomitant rupturing bonds from different PAA chains attached to the same AFM tip.²⁸ The corresponding effect was considered in the evaluation of the data. Therefore, strongly overlapping events are not evaluated within this work but should be kept in mind in further discussion.

3.2.2. Evaluation of SMFS Data on ZnO Nanorod Films. SMFS performed on the ZnO nanorod films showed mainly only rupture events, as can be seen in Figure 3 and in Figure 4A,C. The form of multiple rupture events is typical for multimolecular adhesion modes and parallel interactions thoroughly described by Li et al.²³ A characteristic rupture event has a curved increasing of the force until a maximum is reached. This mechanical extension is mentioned elsewhere in the literature.¹⁶ After that point, the force drops to the baseline and the binding is ruptured. Our results show only multiple rupture events in most of the curves. Therefore, the evaluation of the data with the often used freely jointed chain (FJC) model²³ or the worm-like chain (WLC) model^{16,48} is rather complicated due to the overlapping of events. However, some selected curves could be fitted to the latter model with the JPK Data Processing Software (JPK Instruments AG in Berlin, Germany), but it is clear that a collection of sensible statistic data is challenging. The WLC model in the software is based on the work from Bustamante et al.,⁴⁹ where the estimated maximum error is around 10%. We chose a temperature of 298 K and corrected the contact position and baseline offset for the selected curves, if necessary. Some tentative examples for the fitting of force–distance curves are shown in Figure S10 in the Supporting Information for the two different dwell times (2.0 and 5.0 s) on the ZnO nanorod films. Although the creation of a representative statistic could not be done, the maximum distance where rupture events occurred has been taken into account and is presented in Figure S11 in the Supporting Information. The calculated parameters based on the WLC

model embedded in the JPK software, for example the contour lengths and the persistence lengths, are summarized in Table 2.

Table 2. Summary of the Fitting Results with the WLC Model for the ZnO Nanorods for the Two Dwell Times

	2.0 s dwell time	5.0 s dwell time
L/nm^a	100 ± 10	312 ± 31
l_p/pm^b	189 ± 18	212 ± 21

^a L = contour length. ^b l_p = persistence length.

The contour length increases by a factor of around 3.1 as can be seen from Table 2. This result is in a very good agreement with the diffusion of the PAA chains into the pores (ZnO nanorod interspace). Further coordination with the accessible Zn^{2+} atoms in the nonpolar surfaces of the wurtzite structure can be assumed. The overall decrease of the surface energy is proposed as the driving force for the increased contour length with increasing dwell time. As expected, the persistence length is consistently constant for increasing dwell times since it resembles the length of each segment/monomer in the polymer.

Panels B and D of Figure 4 show the histograms corresponding to the normalized distribution obtained for the maximum of the registered rupture forces for every force–distance curve for the two investigated dwell times, 2.0 and 5.0 s.

The PZC of the ZnO(10 $\bar{1}$ 0) planes, which are chemically equal to other nonpolar surfaces of the wurtzite structure, has been measured under comparable conditions by Kunze et al. and resulting in a pH of 10.2 ± 0.2 .⁴⁴ Accordingly, at pH 7 the nonpolar side walls should be positively charged, while the PAA chains are mainly negatively charged. Consequently, the PAA chains are preferably coordinated to the nonpolar side walls of the ZnO crystalline structures. In this case, nonequilibrium rupture forces related to PAA molecules irreversibly bound are detected in the retract force–distance curve, as can be seen in Figure 4A,C. Kunze et al.⁴⁴ were able to show that PAA molecules/carboxylate groups are specifically adsorbed at the edges of the accessible Zn atoms present at nonpolar side walls, via coordinative bonds, under nearly the same experimental conditions (pH = 7.4 in aqueous $\text{NaClO}_4/\text{NaOH}$). Furthermore, they concluded that these strong interactions induced the unfolding and specific PAA adsorption at sides/steps of the ZnO structures which are also favorable from the point of view of the binding enthalpy to optimize the overall interface energy. It is worth noting that our results indicate that the dwell time has a strong influence on the maximum rupture force distribution. Figure 4 illustrates that an increased dwell time is also accompanied by a boost in the average rupture force. Indeed, a second Gaussian fit is possible in the case of 5.0 s dwell time. Hence, the system, i.e., PAA chains, had enough time to diffuse into the gaps of the ZnO nanorods interspace and give thus rise to the coordinative binding with the Zn atoms present at nonpolar sides as described by Kunze et al.⁴⁴ The simultaneous rupture event of multiple coordinative bindings is well-known in SMFS. For example, Wong et al. explained this peak separation for breaking of two biotin–streptavidin pairs at the same moment in their carbon nanotube AFM studies.⁵⁰ In our case, more than one functionality of the PAA chains are detached at the same time. Indeed, the second fitting (1288 pN) is two times higher than the first one (632 pN) (summarized in Table S7 in

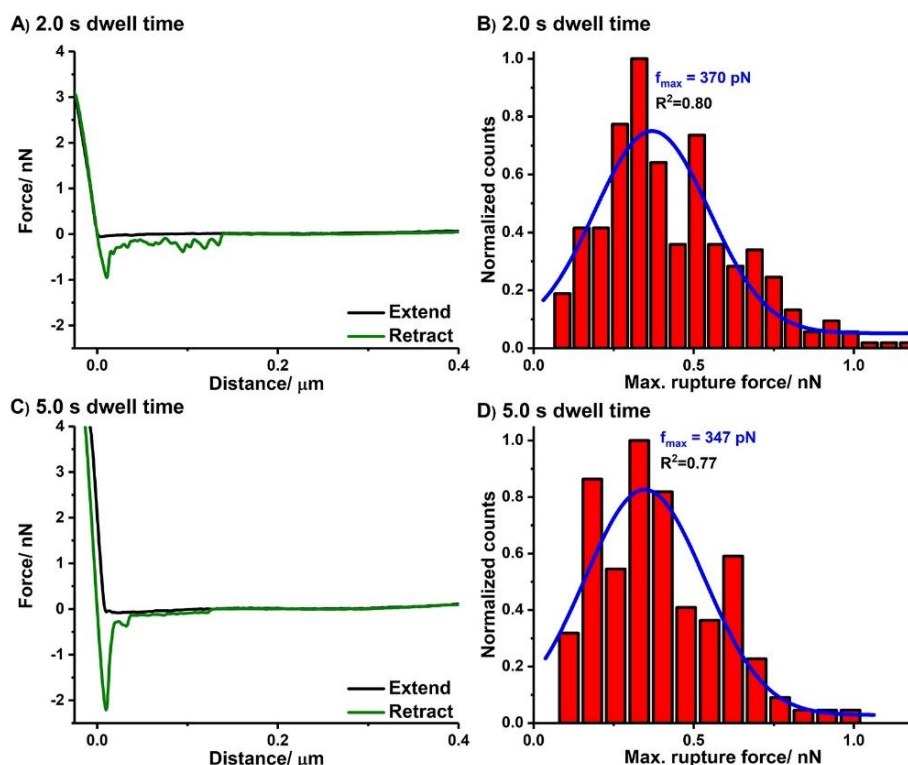


Figure 5. Force–distance curves on the platelet-like ZnO films for two different dwell times, (A) 2.0 and (C) 5.0 s, with the corresponding normalized SMFS statistics of the maxima rupture forces, (B) 2.0 and (D) 5.0 s.

the Supporting Information). We measured more multiple rupture events at 5.0 s dwell time (35.9% of all measured curves), and simultaneous binding breaks might occur because of the higher amount of coordinative binding at steps edges. The latter is in perfect agreement with the ex situ results shown by Kunze et al.⁴⁴ In addition, Li et al. could also show a similar behavior for their system of catechol–iron coordination bonds.⁵¹ The values of the maximum of the Gaussian fittings and the percentage of the curves exhibiting plateaus and rupture events are summarized in Table S7 in the Supporting Information.

In a seminal contribution, Hugel and co-workers elegantly demonstrated that multiple rupture force profiles exhibiting enhanced adhesion values can be obtained when either a single (multi)branched polyelectrolyte chain or several polymer molecules attached to the AFM tips are used in SMFS measurements.²⁸ Indeed, more multiple rupture events were detected for the ZnO nanorods when the dwell time was increased to 5.0 s, i.e., when the (relatively coiled) PAA chain(s) were provided with enough time to diffuse through the interspace between adjacent ZnO nanorods. Consequently, more coordinative PAA–Zn^{II} bonds are expected to be formed at the nonpolar side walls, which can be further detached, more or less simultaneously, when the PAA-modified tip is pulled off from the surface. Additionally, conformational (unfolding) changes in PAA chains related to shear and geometrical interlock events occurring when the polyelectrolyte is desorbed from the ZnO nanorod films might also play a role. The intricate nanostructured/nanocrystalline morphology exhibited mostly by the tightly packed ZnO nanorods (randomly tilted versus the surface normal), leaving nanosized gaps in between, might account for shear and interlock-based breakages

occurring when the polymer is detached and disentangled from the ZnO nanorod matrix. These effects might be also increased for growing dwell times which allowed PAA chains to diffuse through the ZnO nanorod mesh.⁵² These related two facts would be most likely responsible for the arising of this second adhesion distribution value peak centered at 1288 pN (nearly a 2-fold increase in adhesion force regarding the first one). Finally, the as-obtained values are, in any case, lower than those belonging to the covalent regime. For instance, Si–C, C–C, or Au–S bonds would be in the range of 1.7–2.3, 2.0–13, and 1.5–2.2 nN, respectively.^{16,53–55}

The occurrence of only some equilibria plateau peel-off force events is attributed to the presence of some spots of pristine steel, which were not properly modified with ZnO nanorods or to PAA molecules reversibly bound to the polar OH[−]-stabilized upper facets of ZnO nanorods as well. Although for the ZnO nanorods and according to FE-SEM images displayed in Figure 2, the latter upper facets appear not to be very well terminated and defined, the reversible PAA adsorption via van der Waals interactions, hydrogen bonding, or electrostatic interactions cannot be completely ruled out. Especially on those tightly packed ZnO nanorods areas where the diffusion of PAA chains toward the Zn atoms at the nonpolar side walls is highly hindered. The statistical results of the force–distance curves on ZnO nanorod films presented in Table S7 indicate that both the number of curves exhibiting rupture events and the magnitude of the rupture strength is increasing when the dwell time is risen. This effect is schematically shown in the Figure 7. The longer the dwell time, the more possible coordinative bindings can be formed. Consequently, a lot of multiple rupture events could be observed in the case of 5.0 s dwell time.

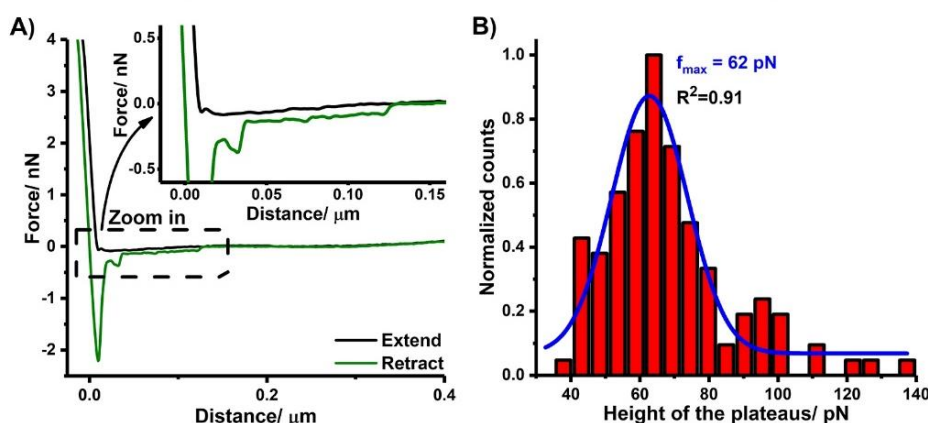


Figure 6. Force–distance curves on the platelet-like ZnO films for 5.0 s dwell time in (A) and the normalized SMFS statistic results of plateaus for the dwell time of 2.0 s in (B).

XPS characterization of the ZnO nanorod samples (spectra shown in Figures S3 and S4 and Table S1) shows the presence of organic components rich in carboxylate groups, probably adsorbed adventitious carbon. This is typical for ZnO films, because the organic components could easily remain adsorbed in pores and at the nonpolar sides of the ZnO. The same organic contaminations could be found in studies where ZnO films were also characterized by means of XPS.^{38,40} Consequently, these organic species already block the active adsorption sites at ZnO surfaces of the nanostructures. Then, a significant decrease in the overall amount of the events takes place in any case. Although the measurements were done in an electrolyte medium, the adsorption of these organic molecules cannot be completely excluded as it would definitely occur in ultrahigh-vacuum (UHV) conditions.

3.2.3. Evaluation of SMFS on Platelet-like ZnO Films. Both rupture events and plateaus could be detected in the case of platelet-like ZnO films deposited on stainless steel samples (see Figure 3, Figure 5, and the magnification in Figure 6). The characteristic plots of the normalized counts versus the maximal rupture forces in nN are shown as histograms for the two different dwell times in Figure 5B,D. In the case of a dwell time of 5.0 s, a higher number of equilibrium plateaus could be evaluated in comparison to ZnO nanorods. Here, the Gaussian fittings are broader than in the other cases. This means that the maximum rupture force is not centered on a specific value such as in the other cases. Additionally, the heights of the maximum rupture forces are lower in comparison to the ZnO nanorods on stainless steel. Regarding the morphology, the ratio of the polar to nonpolar surface areas of the hexagonal structure is higher than in the case of the ZnO nanorods, as can be seen in Figure 2 and in Figure S2 in the Supporting Information. As a consequence, the accessibility of PAA molecules to free surface Zn atoms of the side walls is noticeably reduced and, consequently, the number of coordination bonds should drop drastically. This can be seen in Figure 5, where the height of the rupture events is much lower in the case of the platelet-like ZnO films than in the case of the ZnO nanorods, also shown in Figure 6. This is in good agreement with the maximum of the rupture events of all events from the Gaussian fits summarized in the Table S6 in the Supporting Information.

It could be estimated from the FE-SEM images that the overall content of the ZnO(0001)–Zn plane is much higher

than the nonpolar surfaces such as the ZnO(10 $\bar{1}$ 0) surface (see Figure 2 and Figure S2 for comparison purposes). Based on this, we propose a PZC of 9.3¹⁶ calculated by Valtiner et al. under mainly the same experimental conditions while the literature cited a PZC value of 8.7 ± 0.2 ²² for the case of ZnO(0001)–Zn surfaces, which should be rather similar to our platelet-like ZnO films. Thus, the nanostructured surface is positively charged in this case while the PAA chains are essentially negatively charged, as already discussed before.

The plateaus are the result of electrostatic interactions and hydrogen bridges of the hydroxyl-stabilized ZnO(0001)–Zn surfaces which are the larger parts in the case of the platelet-like ZnO films. Nevertheless, the FE-SEM images show also some edges which are equal to the nonpolar sides. Here, the PAA molecules could coordinate, as explained before for the case of the ZnO nanorods.

The two nanostructure possibilities are the reason for the measurement of both, plateaus and rupture events in the case of the platelet-like ZnO films. In other words, it is a combination of the chemical state of the hydroxyl-rich stainless steel surface and the nonpolar side walls in the case of the ZnO nanorods regarding the state of the hydroxyl groups. Additionally, we calculated adsorption free energies of the plateaus of $17 \pm 4 k_B T / \text{nm}$ for the platelet-like ZnO films. This clarifies the increasing of chemical adhesion as a consequence of the presence of the nanostructured film of platelet-like ZnO, since this energy value is around 1.7 times higher than the measured adsorption free energy for the case of the bare preconditioned stainless steel. As a matter of comparison, and in order to illustrate the increase in the interfacial adhesion after the modification with ZnO-based thin films, the analysis of SMFS force–distance curves, histograms of plateaus measured at dwell times of $t = 2.0$ and 5.0 s, and the calculus of adsorption free energies registered for preconditioned bare stainless steel substrates are displayed in the Supporting Information.

It is worth noting that our SMFS results (see Tables S7 and S8) indicate that, even when a significantly enhanced proportion of ZnO(0001)–Zn facets is prepared, i.e., in platelet-like ZnO films, surprisingly, only a reduced ratio of equilibrium peel-off plateau forces ($\sim 15\%$) can be obtained. The results obtained by Kunze et al. for the adsorption of PAA molecules onto single-crystalline ZnO(0001)–Zn substrates would support the idea that some/most of those PAA

molecules, or at least some parts/sections of them, initially adsorbed (weakly) on the highly preponderant polar hydroxyl-stabilized $c(0001)$ facets, might subsequently diffuse to the borders in order to acquire the advantageous coordination state with the minimized energy at (short) nonpolar crystalline sidewalls.

The observed slight changes in the maximum rupture forces for the ZnO platelet-like films for $t = 2.0$ and 5.0 s dwell time can be considered as statistically insignificant, i.e., no noticeable dependence with the dwell time can be observed. However, this slight increase of the maximum rupture force could then be attributed to the occurrence of more coordinative PAA-Zn^{II} bonds expected to be formed at the nonpolar side walls when PAA chain are provided with more time to diffuse between close ZnO platelets. The interfacial adhesion figures displayed in Figures 5 and 6 are in very good agreement with the desorption values registered for rupture forces and plateaus on ZnO(0001)-Zn single-crystalline substrates with PAA chains under nearly the same experimental conditions by Valtiner and Grundmeier.¹⁶ Here, the terraces are approximately between 150 and 300 nm in diameter, so that edge effects are expected to play a larger role than in the case of the larger 1 μm big terraces reported in the publication of Valtiner and Grundmeier.¹⁶ Especially the binding enthalpy effect on the coordination of PAA chains at the nonpolar sides mentioned by Kunze et al. takes place here.⁴⁴ Additionally, the same blockage of the ZnO surface could happen like in the ZnO nanorod film case because of the organic contaminations shown by XPS analysis in Table S1 and in Figure S4 in the Supporting Information.

Our results indicate that the polished and preconditioned stainless steel shows an averaged desorption force of around 42 pN (see the Supporting Information). For platelet-like ZnO substrates, the plateau forces are in the same order of magnitude, although they show higher values (average desorption force of about 62 pN). The molecular adhesion mechanism on both surfaces is based on van der Waals forces, electrostatic interactions, and hydrogen bonding.

The lower surface coverage of nonpolar side walls in the interphase of the platelet-like ZnO films in comparison to ZnO nanorods leads to occasional rupture events. However, the measured rupture forces were observed to be a factor of 1.9 lower than those observed for the ZnO nanorods.

Moreover, force histograms for ZnO nanorods show a second peak at around 1288 pN when the dwell time is increased. The mechanistic understanding of PAA macromolecular adsorption for both ZnO nanostructures is illustrated in Figure 7. Based on the observed dwell time dependence of both systems, we propose three different explanations of the interfacial bond formation in agreement with the work of Lu et al.:⁵⁶

1. multidentate and/or chelate bindings^{57–59} to more accessible Zn^{II} atoms present in nonpolar side walls as suggested by Valtiner and Grundmeier;¹⁶
2. differential coordination of edge atoms versus those present in terraces of the nonpolar ZnO crystalline side walls (see below—part of the platelet-like ZnO surfaces);
3. diffusion through the interspace between nanorods, allowing for multiple coordinative binding of PAA chains to several adjacent nanorods which would also imply changes in their conformation.^{28,52}

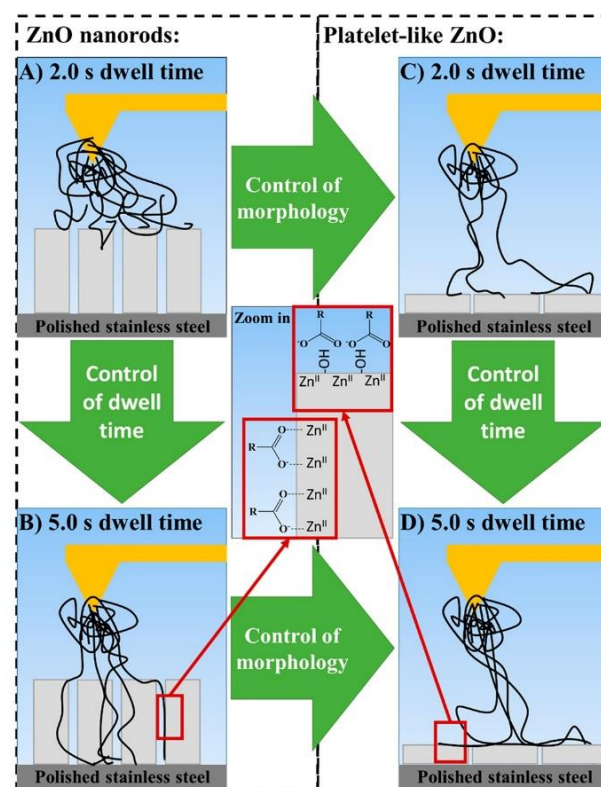


Figure 7. Schematic illustration of the correlation of the ZnO nanorods morphology, dwell time, and the adsorption/coordination of poly(acrylic acid) molecules connected to an AFM gold tip on the ZnO nanorods coated stainless steel in aqueous 2 mM NaClO₄. ZnO nanorods with (A) 2.0 s dwell time and (B) 5.0 s dwell time; platelet-like ZnO with (C) 2.0 s dwell time and (D) 5.0 s dwell time.

During the first few seconds the PAA chains coordinate to the Zn atoms present at the nonpolar side walls, but not to the same extent as for ZnO nanorods based on the increased nonpolar surface area of ZnO nanorods. The second peak at 1288 pN observed for ZnO nanorods can be attributed to the diffusion of the PAA chains in the space between the ZnO nanorod structures (mechanical adhesion). The latter would significantly enhance the number of coordinative bonds (from one-single or several PAA chains) which are simultaneously unbound.

4. CONCLUSIONS

The morphology-dependent SMFS analysis of poly(acrylic acid) desorption at electrolyte/ZnO interfaces in combination with the surface analysis of such films allowed for the analysis of the contributions of acid–base interactions at Zn sites and macromolecular coordination leading to multiple rupture events. While passive film covered stainless steel substrates show solely equilibrium desorption as expected for a hydroxyl-rich smooth oxide surface, ZnO films induced, however, non-equilibrium desorption events with high rupture forces. As supported by SMFS and XPS analysis, we concluded that carboxylic acid groups form strong acid–base interactions with Zn surface atoms at nonpolar ZnO surfaces, while the hydroxyl surface coverage of polar surfaces rather prevents the strong binding of carboxylic acid groups. Observed multiple rupture events could be assigned to the macromolecular coordination

on ZnO nanorods characterized by a high fraction of adsorbed monomers. However, force histograms display a broad distribution of rupture forces, which is explained by the complex ZnO nanorod film structure, comprised of polar and nonpolar surfaces and rods of different tilting angles and interspace distances. The time-dependent process of diffusion and adsorption of PAA within the ZnO nanorod layers is characterized by the dwell time dependence of the observed force histograms. This time dependence was specifically observed for the nanorod films, however, not for platelet-like ZnO films which did not show multiple rupture events. The here presented results indicate that the macromolecular adsorption of PAA and resulting adhesion on ZnO nanostructures can be tuned by the control of thin film morphology.

■ ASSOCIATED CONTENT

Supporting Information

The Supporting Information is available free of charge on the ACS Publications website at DOI: 10.1021/acsanm.8b02091.

Additional results, i.e., current-density curves of the ZnO deposition, illustration of the ZnO nanostructure, AR-XPS survey and high-resolution spectra of preconditioned stainless steel with quantifications, XPS survey and high-resolution spectra of the ZnO films on stainless steel, PM-IRRAS, XPS data after the cantilever modification steps, and SMFS with examples of fitted curves with the WLC model (PDF)

■ AUTHOR INFORMATION

Corresponding Author

*E-mail: g.grundmeier@tc.uni-paderborn.de.

ORCID

Dennis Meinderink: 0000-0002-2755-6514

Present Address

[†]Institute of Physical Chemistry, University of Cologne, Luxemburger Str. 116, 50939 Cologne, Germany.

Notes

The authors declare no competing financial interest.

■ ACKNOWLEDGMENTS

We thank the German Research Foundation for financial support within the project “Comparative Molecular Adhesion Studies of Polyacrylic Acids on ZnO Single Crystal Surfaces and ZnO Nanocrystalline Films” (Project No. 320414069; GR 1709/22-1). We also thank Teresa de los Arcos and Adrian Keller for helpful discussions and Nadine Buitkamp for FE-SEM measurements and assistance.

■ ABBREVIATIONS

AFM, atomic force microscopy
AR-XPS, angle resolved X-ray photoemission spectroscopy
EDTA, ethylenediaminetetraacetic acid
F–D curves, force–distance curves
FE-SEM, field-emission scanning electron microscopy
HMTA, hexamethylenetetramine
PAA, poly(acrylic acid)
PBS, phosphate-buffered saline
PEG, poly(ethylene glycol)
PM-IRRAS, photoelastic modulated infrared reflection absorption spectroscopy.

PZC, point of zero charge

PZC_{SS}, point of zero charge of stainless steel

SMFS, single molecule force spectroscopy

SS, stainless steel

■ REFERENCES

- (1) Baxter, J. B.; Walker, A. M.; van Ommering, K.; Aydil, E. S. Synthesis and characterization of ZnO nanowires and their integration into dye-sensitized solar cells. *Nanotechnology* **2006**, *17*, S304–S312.
- (2) Müller, J.; Schöpe, G.; Kluth, O.; Rech, B.; Sittlinger, V.; Szyszka, B.; Geyer, R.; Lechner, P.; Schade, H.; Ruske, M.; Dittmar, G.; Bochem, H.-P. State-of-the-art mid-frequency sputtered ZnO films for thin film silicon solar cells and modules. *Thin Solid Films* **2003**, *442*, 158–162.
- (3) Lee, J. Y.; Choi, Y. S.; Kim, J. H.; Park, M. O.; Im, S. Optimizing n-ZnO/p-Si heterojunctions for photodiode applications. *Thin Solid Films* **2002**, *403–404*, 553–557.
- (4) Lin, Y.; Zhang, Z.; Tang, Z.; Yuan, F.; Li, J. Characterisation of ZnO-based varistors prepared from nanometre Precursor powders. *Adv. Mater. Opt. Electron.* **1999**, *9*, 205–209.
- (5) Skompska, M.; Zarębska, K. Electrodeposition of ZnO Nanorod Arrays on Transparent Conducting Substrates—a Review. *Electrochim. Acta* **2014**, *127*, 467–488.
- (6) Sun, Y.; Riley, D. J.; Ashfold, M. N. R. Mechanism of ZnO Nanotube Growth by Hydrothermal Methods on ZnO Film-Coated Si Substrates. *J. Phys. Chem. B* **2006**, *110*, 15186–15192.
- (7) Ahmad, M.; Zhu, J. ZnO based advanced functional nanostructures: Synthesis, properties and applications. *J. Mater. Chem.* **2011**, *21*, 599–614.
- (8) Xu, S.; Wang, Z. L. One-dimensional ZnO nanostructures: Solution growth and functional properties. *Nano Res.* **2011**, *4*, 1013–1098.
- (9) Garcia, S. P.; Semancik, S. Controlling the Morphology of Zinc Oxide Nanorods Crystallized from Aqueous Solutions: The Effect of Crystal Growth Modifiers on Aspect Ratio. *Chem. Mater.* **2007**, *19*, 4016–4022.
- (10) Sugunan, A.; Warad, H. C.; Boman, M.; Dutta, J. Zinc oxide nanowires in chemical bath on seeded substrates: Role of hexamine. *J. Sol-Gel Sci. Technol.* **2006**, *39*, 49–56.
- (11) Govender, K.; Boyle, D. S.; Kenway, P. B.; O'Brien, P. Understanding the factors that govern the deposition and morphology of thin films of ZnO from aqueous solution. *J. Mater. Chem.* **2004**, *14*, 2575–2591.
- (12) Izaki, M.; Omi, T. Electrolyte Optimization for Cathodic Growth of Zinc Oxide Films. *J. Electrochem. Soc.* **1996**, *143*, L53–L55.
- (13) Liu, R.; Vertegel, A. A.; Bohannon, E. W.; Sorenson, T. A.; Switzer, J. A. Epitaxial Electrodeposition of Zinc Oxide Nanopillars on Single-Crystal Gold. *Chem. Mater.* **2001**, *13*, 508–512.
- (14) Wong, M. H.; Berenov, A.; Qi, X.; Kappers, M. J.; Barber, Z. H.; Illy, B.; Lockman, Z.; Ryan, M. P.; MacManus-Driscoll, J. L. Electrochemical growth of ZnO nano-rods on polycrystalline Zn foil. *Nanotechnology* **2003**, *14*, 968–973.
- (15) Ozcan, O.; Pohl, K.; Ozkaya, B.; Grundmeier, G. Molecular Studies of Adhesion and De-Adhesion on ZnO Nanorod Film-Covered Metals. *J. Adhes.* **2013**, *89*, 128–139.
- (16) Valtiner, M.; Grundmeier, G. Single Molecules as Sensors for Local Molecular Adhesion Studies. *Langmuir* **2010**, *26*, 815–820.
- (17) Ritzefeld, M.; Walhorn, V.; Anselmetti, D.; Sewald, N. Analysis of DNA interactions using single-molecule force spectroscopy. *Amino Acids* **2013**, *44*, 1457–1475.
- (18) Butt, H.-J.; Cappella, B.; Kappl, M. Force measurements with the atomic force microscope: Technique, interpretation and applications. *Surf. Sci. Rep.* **2005**, *59*, 1–152.
- (19) Kim, Y.; Kim, W.; Park, J. W. Principles and Applications of Force Spectroscopy Using Atomic Force Microscopy. *Bull. Korean Chem. Soc.* **2016**, *37*, 1895–1907.
- (20) Walhorn, V.; Dierks, T.; Mattay, J.; Sewald, N.; Andselmetti, D. Single-Molecule Mechanics and Force Spectroscopy. In *Functional*

Soft Matter, Vol. 94; Wallhorn, V., Dierks, T., Mattay, J., Sewald, N., Anselmetti, D., Eds.; Forschungszentrum Jülich: Jülich, Germany, 2015.

(21) Valtiner, M.; Borodin, S.; Grundmeier, G. Preparation and characterisation of hydroxide stabilised ZnO(0001)-Zn-OH surfaces. *Phys. Chem. Chem. Phys.* **2007**, *9*, 2406–2412.

(22) Valtiner, M.; Borodin, S.; Grundmeier, G. Stabilization and Acidic Dissolution Mechanism of Single-Crystalline ZnO(0001) Surfaces in Electrolytes Studied by In-Situ AFM Imaging and Ex-Situ LEED. *Langmuir* **2008**, *24*, 5350–5358.

(23) Li, H.; Liu, B.; Zhang, X.; Gao, C.; Shen, J.; Zou, G. Single-Molecule Force Spectroscopy on Poly(acrylic acid) by AFM. *Langmuir* **1999**, *15*, 2120–2124.

(24) Sonnenberg, L.; Parvole, J.; Borisov, O.; Billon, L.; Gaub, H. E.; Seitz, M. AFM-Based Single Molecule Force Spectroscopy of End-Grafted Poly(acrylic acid) Monolayers. *Macromolecules* **2006**, *39*, 281–288.

(25) Friedsam, C.; Bécères, A. D. C.; Jonas, U.; Seitz, M.; Gaub, H. E. Adsorption of polyacrylic acid on self-assembled monolayers investigated by single-molecule force spectroscopy. *New J. Phys.* **2004**, *6*, 9–25.

(26) Bauer, A.; Meinderink, D.; Giner, I.; Steger, H.; Weitz, J.; Grundmeier, G. Electropolymerization of acrylic acid on carbon fibers for improved epoxy/fiber adhesion. *Surf. Coat. Technol.* **2017**, *321*, 128–135.

(27) Meinderink, D.; Orive, A. G.; Grundmeier, G. Electrodeposition of poly(acrylic acid) on stainless steel with enhanced adhesion properties. *Surf. Interface Anal.* **2018**, *50*, 1224–1229.

(28) Kienle, S.; Gallei, M.; Yu, H.; Zhang, B.; Krysiak, S.; Balzer, B. N.; Rehahn, M.; Schlüter, A. D.; Hugel, T. Effect of Molecular Architecture on Single Polymer Adhesion. *Langmuir* **2014**, *30*, 4351–4357.

(29) Geisler, M.; Horinek, D.; Hugel, T. Single Molecule Adhesion Mechanics on Rough Surfaces. *Macromolecules* **2009**, *42*, 9338–9343.

(30) Landoulsi, J.; Dupres, V. Probing Peptide–Inorganic Surface Interaction at the Single Molecule Level Using Force Spectroscopy. *ChemPhysChem* **2011**, *12*, 1310–1316.

(31) Gerischer, H.; Sorg, N. Chemical dissolution of zinc oxide crystals in aqueous electrolytes—An analysis of the kinetics. *Electrochim. Acta* **1992**, *37*, 827–835.

(32) Seipel, B.; Nadarajah, A.; Wutzke, B.; Könenkamp, R. Electrodeposition of ZnO nanorods in the presence of metal ions. *Mater. Lett.* **2009**, *63*, 736–738.

(33) Jiao, S.; Zhang, K.; Bai, S.; Li, H.; Gao, S.; Li, H.; Wang, J.; Yu, Q.; Guo, F.; Zhao, L. Controlled morphology evolution of ZnO nanostructures in the electrochemical deposition: From the point of view of chloride ions. *Electrochim. Acta* **2013**, *111*, 64–70.

(34) Nicholas, N. J.; Franks, G. V.; Ducker, W. A. Selective Adsorption to Particular Crystal Faces of ZnO. *Langmuir* **2012**, *28*, 7189–7196.

(35) Vyssieres, L.; Keis, K.; Lindquist, S.-E.; Hagfeldt, A. Purpose-Built Anisotropic Metal Oxide Material: 3D Highly Oriented Microrod Array of ZnO. *J. Phys. Chem. B* **2001**, *105*, 3350–3352.

(36) Amor, S. B.; Jacquet, M.; Fioux, P.; Nardin, M. XPS characterisation of plasma treated and zinc oxide coated PET. *Appl. Surf. Sci.* **2009**, *255*, S052–S061.

(37) Mutel, B.; Taleb, A. B.; Dessaux, O.; Goudmand, P.; Gengembre, L.; Grimblot, J. Characterization of mixed zinc-oxidized zinc thin films deposited by a cold remote nitrogen plasma. *Thin Solid Films* **1995**, *266*, 119–128.

(38) Al-Kuhaili, M. F.; Durrani, S. M. A.; Bakhtiari, I. A. Influence of oxygen flow rate on the surface chemistry and morphology of radio frequency (RF) magnetron sputtered zinc oxide thin films. *Surf. Interface Anal.* **2013**, *45*, 1353–1357.

(39) Majumder, S. B.; Jain, M.; Dobal, P. S.; Katiyar, R. S. Investigations on solution derived aluminium doped zinc oxide thin films. *Mater. Sci. Eng., B* **2003**, *103*, 16–25.

(40) Chen, M.; Wang, X.; Yu, Y. H.; Pei, Z. L.; Bai, X. D.; Sun, C.; Huang, R. F.; Wen, L. S. X-ray photoelectron spectroscopy and auger

electron spectroscopy studies of Al-doped ZnO films. *Appl. Surf. Sci.* **2000**, *158*, 134–140.

(41) Lauritsen, J. V.; Porsgaard, S.; Rasmussen, M. K.; Jensen, M. C. R.; Bechstein, R.; Meinander, K.; Clausen, B. S.; Helveg, S.; Wahl, R.; Kresse, G.; Besenbacher, F. Stabilization Principles for Polar Surfaces of ZnO. *ACS Nano* **2011**, *5*, S987–S994.

(42) Wander, A.; Harrison, N. M. The stability of polar oxide surfaces: The interaction of H₂O with ZnO(0001) and ZnO(000 $\bar{1}$). *J. Chem. Phys.* **2001**, *115*, 2312–2316.

(43) Dulub, O.; Diebold, U.; Kresse, G. Novel Stabilization Mechanism on Polar Surfaces: ZnO(0001)-Zn. *Phys. Rev. Lett.* **2003**, *90*, 016102.

(44) Kunze, C.; Valtiner, M.; Michels, R.; Huber, K.; Grundmeier, G. Self-localization of polyacrylic acid molecules on polar ZnO(0001)-Zn surfaces. *Phys. Chem. Chem. Phys.* **2011**, *13*, 12959–12967.

(45) Palacio, M. L. B.; Schrick, S. R.; Bhushan, B. Bioadhesion of various proteins on random, diblock and triblock copolymer surfaces and the effect of pH conditions. *J. R. Soc., Interface* **2011**, *8*, 630–640.

(46) Kassies, R.; van der Werf, K. O.; Bennink, M. L.; Otto, C. Removing interference and optical feedback artifacts in atomic force microscopy measurements by application of high frequency laser current modulation. *Rev. Sci. Instrum.* **2004**, *75*, 689–693.

(47) Geisler, M.; Balzer, B. N.; Hugel, T. Polymer Adhesion at the Solid–Liquid Interface Probed by a Single–Molecule Force Sensor. *Small* **2009**, *5*, 2864–2869.

(48) Mosebach, B.; Ozkaya, B.; Giner, I.; Keller, A.; Grundmeier, G. Analysis of acid-base interactions at Al₂O₃ (11–20) interfaces by means of single molecule force spectroscopy. *Appl. Surf. Sci.* **2017**, *420*, 296–302.

(49) Bustamante, C.; Marko, J. F.; Siggia, E. D.; Smith, S. Entropic elasticity of lambda-phage DNA. *Science* **1994**, *265*, 1599–1600.

(50) Wong, S. S.; Joselevich, E.; Woolley, A. T.; Cheung, C. L.; Lieber, C. M. Covalently functionalized nanotubes as nanometer-sized probes in chemistry and biology. *Nature* **1998**, *394*, 52–55.

(51) Li, Y.; Wen, J.; Qin, M.; Cao, Y.; Ma, H.; Wang, W. Single-Molecule Mechanics of Catechol-Iron Coordination Bonds. *ACS Biomater. Sci. Eng.* **2017**, *3*, 979–989.

(52) Balzer, B. N.; Micciulla, S.; Dodoo, S.; Zerboll, M.; Gallei, M.; Rehahn, M.; Klitzing, R. v.; Hugel, T. Adhesion Property Profiles of Supported Thin Polymer Films. *ACS Appl. Mater. Interfaces* **2013**, *5*, 6300–6306.

(53) Grandbois, M.; Beyer, M.; Rief, M.; Clausen-Schaumann, H.; Gaub, H. E. How Strong Is a Covalent Bond? *Science (Washington, DC, U. S.)* **1999**, *283*, 1727–1730.

(54) Liu, N.; Zhang, W. Feeling Inter- or Intramolecular Interactions with the Polymer Chain as Probe: Recent Progress in SMFS Studies on Macromolecular Interactions. *ChemPhysChem* **2012**, *13*, 2238–2256.

(55) Xue, Y.; Li, X.; Li, H.; Zhang, W. Quantifying thiol–gold interactions towards the efficient strength control. *Nat. Commun.* **2014**, *5*, 4348–4357.

(56) Taratula, O.; Galoppini, E.; Wang, D.; Chu, D.; Zhang, Z.; Chen, H.; Saraf, G.; Lu, Y. Binding Studies of Molecular Linkers to ZnO and MgZnO Nanotip Films. *J. Phys. Chem. B* **2006**, *110*, 6506–6515.

(57) Bauer, T.; Schmaltz, T.; Lenz, T.; Halik, M.; Meyer, B.; Clark, T. Phosphonate- and Carboxylate-Based Self-Assembled Monolayers for Organic Devices: A Theoretical Study of Surface Binding on Aluminum Oxide with Experimental Support. *ACS Appl. Mater. Interfaces* **2013**, *5*, 6073–6080.

(58) Bishop, L. M.; Yeager, J. C.; Chen, X.; Wheeler, J. N.; Torelli, M. D.; Benson, M. C.; Burke, S. D.; Pedersen, J. A.; Hamers, R. J. A Citric Acid-Derived Ligand for Modular Functionalization of Metal Oxide Surfaces via “Click” Chemistry. *Langmuir* **2012**, *28*, 1322–1329.

(59) Cebula, I.; Lu, H.; Zharnikov, M.; Buck, M. Monolayers of trimelic and isophthalic acid on Cu and Ag: The influence of

coordination strength on adsorption geometry. *Chem. Sci.* **2013**, *4*, 4455–4464.

Reprinted with permission from American Chemical Society (ACS) Appl. Nano Mater. 2019, 2, 831–843, authors: D. Meinderink, A. G. Orive, S. Ewertowski, I. Giner and G. Grundmeier, title: “Dependence of Poly(acrylic acid) Interfacial Adhesion on the Nanostructure of Electrodeposited ZnO Films”. Copyright 2019 American Chemical Society.

Supporting Information

Dependence of Poly(acrylic acid) Interfacial Adhesion on the Nanostructure of Electrodeposited ZnO Films

Dennis Meinderink¹, Alejandro Gonzalez Orive¹, Simon Ewertowski², Ignacio Giner¹ and Guido Grundmeier^{1}*

¹Technical and Macromolecular Chemistry, University of Paderborn, Warburger Str. 100, 33098 Paderborn, Germany

²Current Address: Institute of Physical Chemistry, University of Cologne, Luxemburger Str. 116, 50939 Cologne, Germany

*Corresponding author: g.grundmeier@tc.uni-paderborn.de

S-1

Reprinted with permission from American Chemical Society (ACS) Appl. Nano Mater. 2019, 2, 831-843, authors: D. Meinderink, A. G. Orive, S. Ewertowski, I. Giner and G. Grundmeier, title: "Dependence of Poly(acrylic acid) Interfacial Adhesion on the Nanostructure of Electrodeposited ZnO Films". Copyright 2019 American Chemical Society.

1 Electrochemical deposition of ZnO nanostructures on stainless steel samples

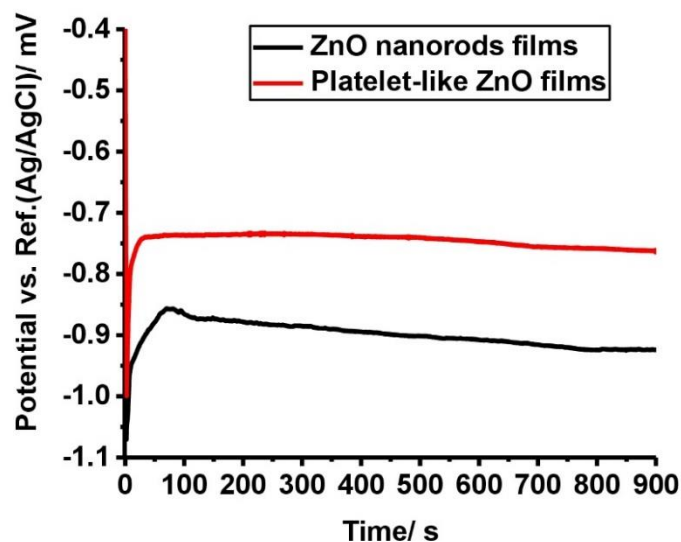


Figure S1. Potential versus time curves at constant current densities (-0.5 mA/cm^2) for the two different deposition parameters: black line for ZnO nanorods films with 10 mM $\text{Zn}(\text{NO}_3)_2$, 10 mM HMTA and red line for platelet-like ZnO films with 100 mM $\text{Zn}(\text{NO}_3)_2$, 10 mM HMTA.

Typical deposition parameters such as a temperature of around 80°C , a precursor concentration of 5 mM zinc nitrate and a potential range of -0.8 V till -1.0 V vs. Ag/AgCl were used according to Seipel et al. and Sheini et al.^{1,2}

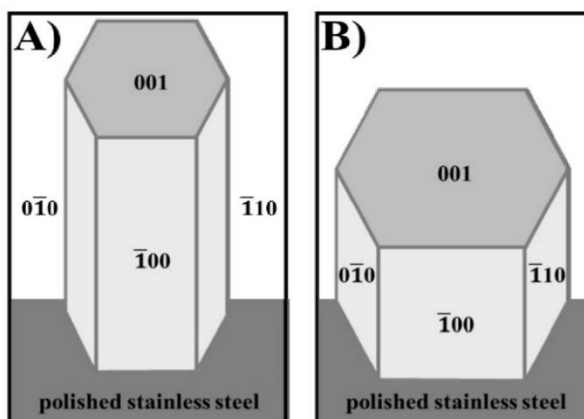


Figure S2. Schematic illustration of the ZnO crystalline wurtzite architecture in the case of A) ZnO nanorods and B) platelet-like ZnO.

2 Characterization of electrodeposited ZnO films with XPS

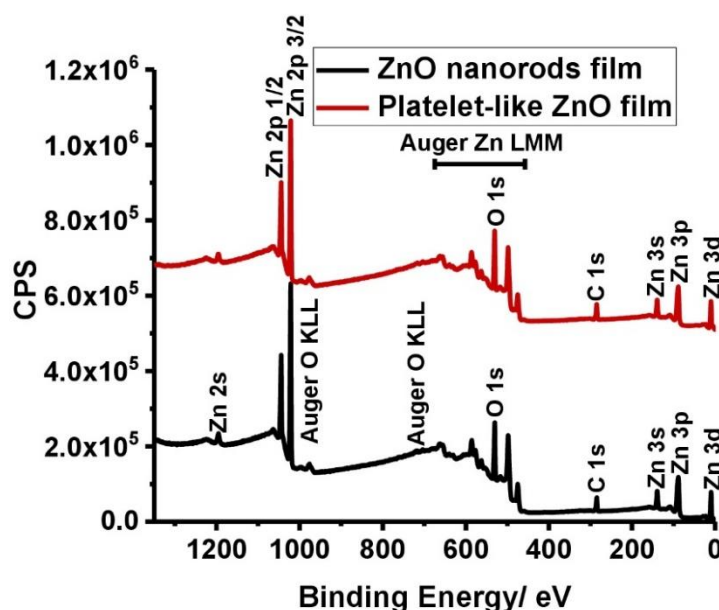


Figure S3. XPS surveys of ZnO nanorod films deposited on stainless steel with cathodic electrodeposition (900 s with -0.5 mA/cm^2): black) 10 mM $\text{Zn}(\text{NO}_3)_2$ and 10 mM HMTA, red) 100 mM $\text{Zn}(\text{NO}_3)_2$ and 10 mM HMTA.

Both survey spectra in Figure S3 show the core level peaks of different atoms as well as the Auger peaks. The black line corresponds to the ZnO film deposited for 900 s in 10 mM aqueous $\text{Zn}(\text{NO}_3)_2$ and 10 mM HMTA for 900 s with -0.5 mA/cm^2 at 80°C and the red line to the one obtained under the same conditions but with 100 mM $\text{Zn}(\text{NO}_3)_2$ in the electrolyte. As can be seen, only peaks corresponding to zinc oxide species are present. The C 1s peak at 285.0 eV is associated to adventitious carbon. No iron signal is observed, indicating a dense layer of ZnO nanorods on the substrate which is in agreement with the FE-SEM images in the main text.

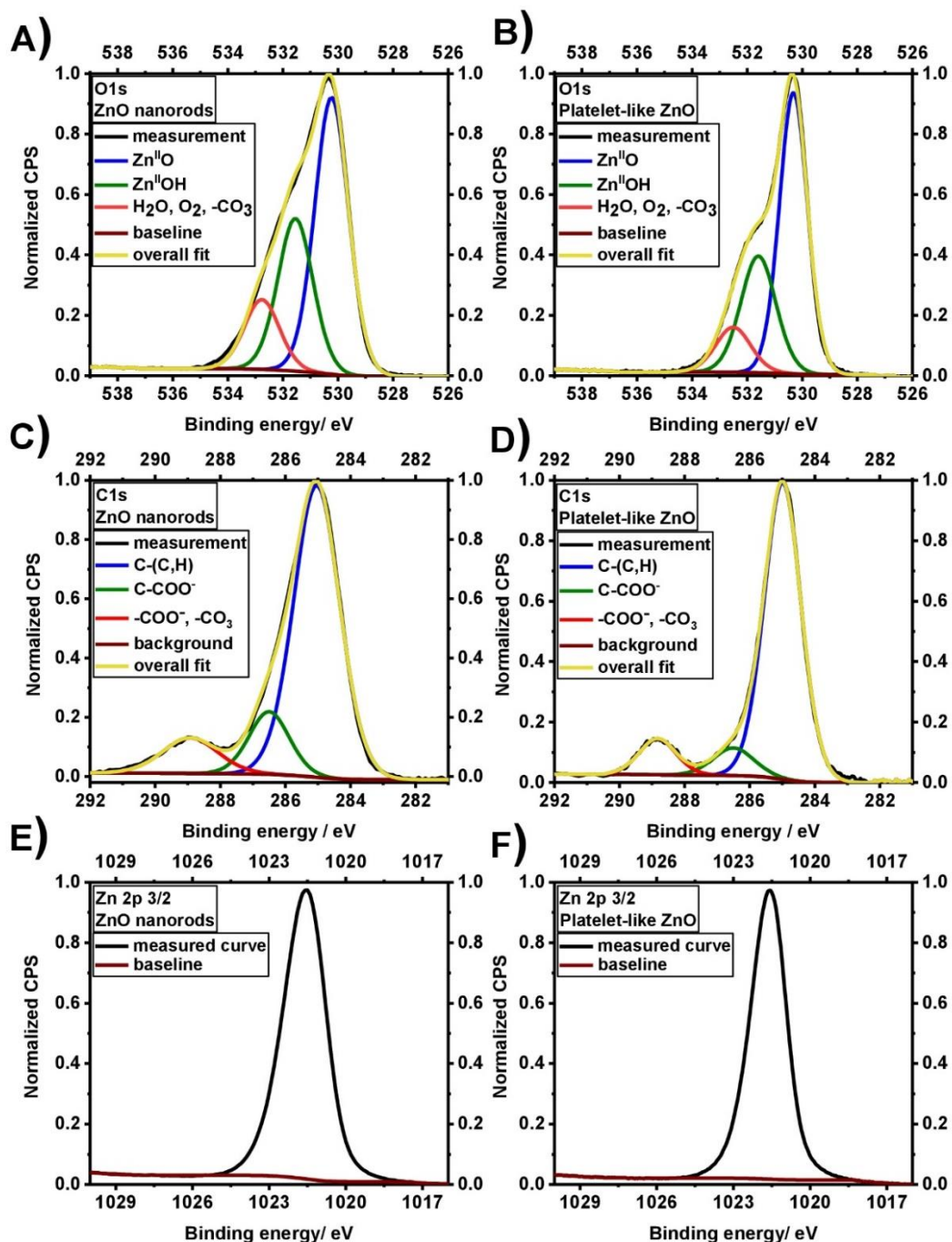


Figure S4. XPS core level peak of O 1s for A) ZnO nanorods and B) platelet-like ZnO, of C 1s for C) ZnO nanorods and D) platelet-like ZnO and of Zn 2p 3/2 for E) ZnO nanorods and F) platelet-like ZnO.

S-5

Reprinted with permission from American Chemical Society (ACS) Appl. Nano Mater. 2019, 2, 831-843, authors: D. Meinderink, A. G. Orive, S. Ewertowski, I. Giner and G. Grundmeier, title: "Dependence of Poly(acrylic acid) Interfacial Adhesion on the Nanostructure of Electrodeposited ZnO Films". Copyright 2019 American Chemical Society.

The O 1s peak showed three components in Figure S4. The first one at around 530.2 eV is attributed to inorganic oxygen O²⁻ like in the wurtzite structure for ZnO as stated elsewhere.³⁻⁶ The second peak is attributed to OH⁻ groups present on the surface of ZnO, as mentioned in the main text.³⁻⁶ A third peak around 532.8 eV is associated to adsorbed water, oxygen and carbonates which is typical for ZnO surfaces, mentioned by various authors like Majumder et al. and Al-Kuhaili et al.^{3,4,6}

The component of the C 1s peak at a binding energy of 285.0 eV is attributed to aliphatic carbon species, while the component at 286.5 eV could be functional groups like C-COO⁻ linked to Zn^{II} atoms of the wurtzite structure, which correlates with the 532.8 eV component in the O 1s peak. The third component in the C 1s peak, at 288.9 eV, is interpreted as carboxylate groups adsorbed to the Zn^{II} atoms and as adsorbed carbonates -CO₃ from the air.^{3,4,6}

The Zn 2p 3/2 peak appeared at a binding energy of 1021.5 eV for the ZnO nanorods and 1021.6 eV for the platelet-like ZnO films. Al-Kuhaili et al. mentioned a range for ZnO films of 1021.5-1022.4 eV for ZnO.³

Table S1. Summary of the component fittings of the O 1s, C 1s and Zn 2p 3/2 high resolution XPS peaks of the ZnO nanorod and ZnO platelet-like films.

O 1s	ZnO nanorod film		Platelet-like ZnO film	
	binding energy / eV	at.-%	binding energy / eV	at.-%
O ²⁻	530.2	54.4	530.3	58.2
Zn ^{II} OH	531.5	31.3	531.6	30.2
-COO ⁻ , -CO ₃ , O ₂ , H ₂ O(ads)	532.8	14.3	532.5	11.6
C 1s				
C-(C,H)	285.0	74.9	285.0	81.6
C-COO ⁻ Zn ^{II}	286.5	14.1	286.5	8.4
-C-COO ⁻ Zn ^{II} , -CO ₃	288.9	11.0	288.8	10.0
Zn 2p 3/2				
Δ(Zn 2p 1/2)-(Zn 2p 3/2)	23.0 eV		23.0 eV	

3 Characterisation of the prepared cantilevers by means of PM-IRRAS and XPS

Gold-coated Si wafers were prepared in the same solutions than the SMFS cantilevers with the aim to obtain larger samples for the PM-IRRAS analysis.

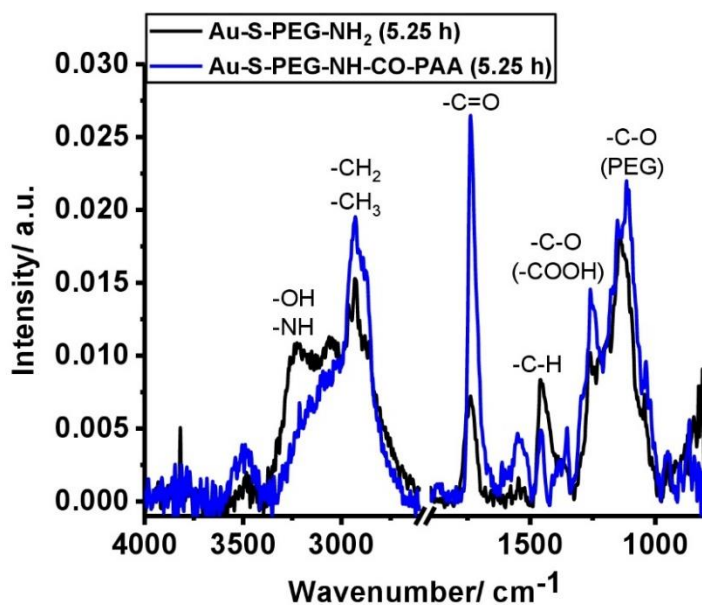


Figure S5. PM-IRRAS spectra of PVD gold coated silicon wafers: black) after Au-S-PEG-NH₂ functionalizing and blue) after Au-S-PEG-NH-CO-PAA functionalizing.

Figure S5 shows the PM-IRRAS spectra after two different modification steps: the black line after the functionalization with only without the PEG coupling SAM and the blue line after the final functionalization with PAA. Intense signals in the CH_n-stretching (2870 cm⁻¹) and the C-O-stretching (1121 cm⁻¹) regions indicate the presence of the PEG-chains. Furthermore, the signals in the region between 1200 and 1550 cm⁻¹ are attributed to the methylene oxide chain of the PEG. An intense peak at 1665 cm⁻¹ is attributed to amide groups and water-bridged carboxylates. The

signals at 1738 cm^{-1} and 1250 cm^{-1} are assigned to COOH vibrations of the carboxylic acid groups.

⁷⁻⁹ The band positions and assignments are summarized in Table S2.

Table S2. Summary of PM-IRRAS results with wavenumbers in cm^{-1} .

	Literature	PEG-PAA
OH-stretch/ NH-stretch	3200-3600 ⁷	3305
CH_n-stretch (PEG)	2800-3000 ⁷	2870
C=O stretch (COOH)	1680-1750 ⁸	1738
C=O (amid) and water bridged COO⁻	1660-1680 ⁹	1665
C-H-def. (PEG + Impurities)	1240-1480 ⁸	1240-1545
C-O stretch (COOH)	1240 ⁸ / 1248 ⁹	1250
C-O-stretch (PEG)	1119 ⁸	1121

The cantilever modification steps were also characterized by XPS, as illustrated in Figure S6.

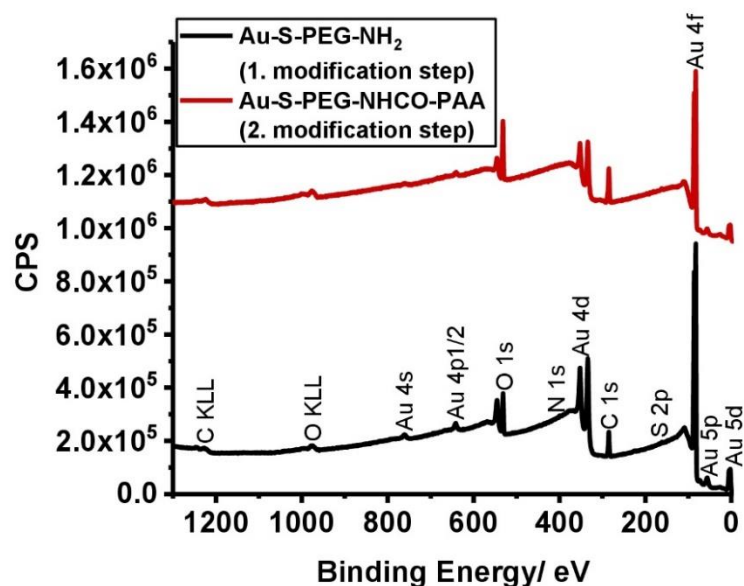


Figure S6. XPS spectra after the two modification steps on PVD gold coated silicon wafers measured at take-off angle of 60° with respect to the surface plane.

The results match the conclusions obtained from the PM-IRRAS analysis. Only gold from the substrate and elements present within the PEG chains and the PAA chains (namely nitrogen, carbon, and oxygen) were detected. After the first modification step, it could also be observed around 1.1 % nitrogen of the amine group of the thiol poly(ethylene glycol) amine chains. 0.7 % of sulfur from the thiol binding to the gold is measured after the coupling with the poly(acrylic acid) molecules. The percentage values for gold decreased from 28.0 at% to 13.5 at% after the two modification steps. The latter is associated with the increasing surface coverage of PAA.

4 Characterization of preconditioned stainless steel with angle-resolved X-ray photoelectron spectroscopy (AR-XPS)

The polished stainless steel after the mentioned preconditioning step was characterized by XPS at two different take-off angles. The following Figure S7 shows the two survey spectra at an angle of 80° and 20° with respect to the surface plane.

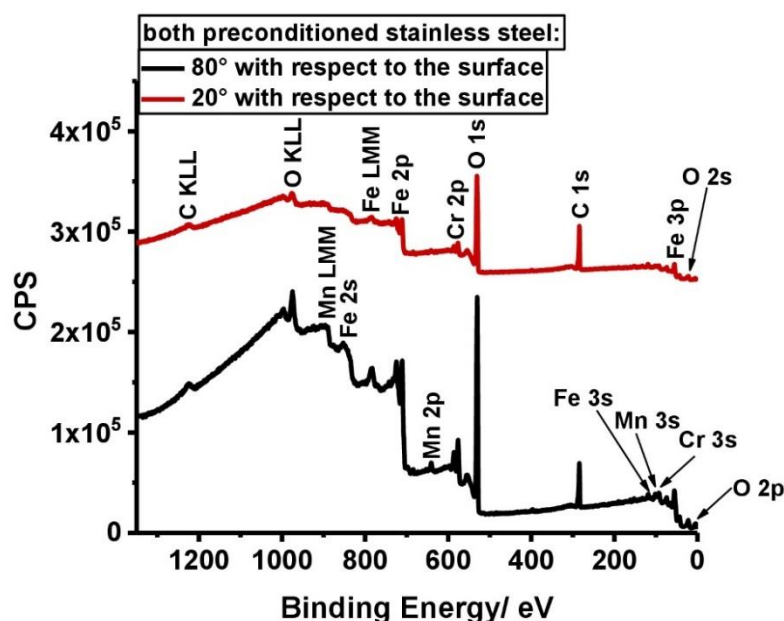


Figure S7. XPS surveys of mirror polished stainless steel after solvent and oxygen plasma cleaning at two different take-off angles.

The corresponding core level peaks of O 1s and C 1s are shown in the Figure S8.

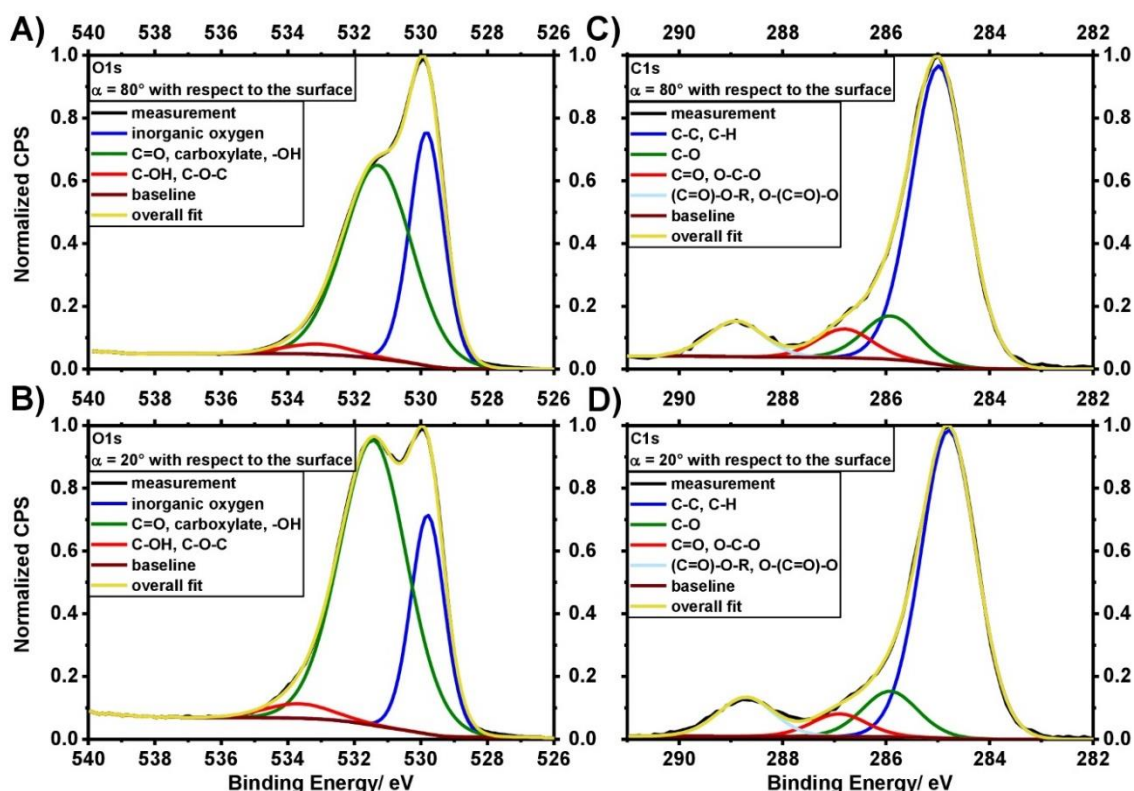


Figure S8. High resolution XPS spectra of O 1s and C 1s for preconditioned stainless steel at two different angles with respect to the surface: A) O 1s 80° B) O 1s 20° and C) C 1s 80° D) C 1s 20°.

A typical three peak fitting in the case of the O 1s peak and a four peak fitting in the case of the C 1s peak were done like mentioned by Landoulsi et al.¹⁰ for the two different measuring angles. The ratios of these fittings and the corresponding chemical functionalities are illustrated in Table S3 and Table S4 and are in a good agreement with the peak positions of Landoulsi et al.¹⁰

Table S3. XPS O 1s data of the polished preconditioned stainless steel measured at 20 ° and 80° with respect to the surface.

O 1s	O 1s – 20°		O 1s – 80°	
	binding energy/ eV	at.-%	binding energy / eV	at.-%
inorganic oxygen	530.0	27.1	530.0	37.2
C=O, carboxylate,-OH	531.6	69.5	531.5	58.4
C-OH, C-O-C	533.7	3.4	533.2	4.4

Table S4. XPS C 1s data of the polished preconditioned stainless steel measured at 20 ° and 80° with respect to the surface.

C 1s	C 1s – 20°		C 1s – 80°	
	binding energy / eV	at.-%	binding energy / eV	at.-%
C-(C,H)	285.0	74.8	285.0	73.0
C-O	286.2	10.7	285.9	11.0
C=O, O-C-O	287.2	5.1	286.8	7.2
(C=O)-O-R, O-(C=O)-O	288.9	9.4	288.9	8.8

The survey XPS spectra and the O 1s and C 1s core level peaks of the preconditioned stainless steel surfaces measured at two different angles are illustrated in the Figure S8. The peaks show that a hydroxyl group-rich surface was reached. The evaluation of the XPS data was done in a similar way to that proposed by Landoulsi et al. due to the similarities between the employed stainless steel substrates and surface modification procedures.¹⁰ The overall atomic composition, summarized in Table S5, is typical of a stainless steel surface.^{10–12}

Table S5. XPS data of the high-resolution spectra of the polished, preconditioned stainless steel surfaces at two different measuring angles with respect to the surface.

	20° with respect to the surface		80° with respect to the surface	
	binding energy /eV	at.-%	binding energy /eV	at.-%
O 1s	530.2	48.8	530.1	58.5
C 1s	285.0	42.9	285.0	26.3
Fe 2p_{3/2}	711.0	5.5	710.7	9.5
Cr 2p_{3/2}	576.6	2.5	576.8	4.9
Mn 2p_{3/2}	640.7	0.3	640.5	0.8

After intensive cleaning and a preconditioning process consisting of 72 h-immersion in 2 mM NaClO₄, analogue to the process proposed by Landoulsi et al.¹⁰, only a contamination of carbon species could be found (compare the results illustrated in the Figure S7 and Table S5).^{10,13} As can be seen, the compositions of the carbon species do not change at all.

More hydroxyl functionalities can be found in the outer sphere (20° with respect to the surface) of the preconditioned stainless steel than in the inner sphere (80° with respect to the surface), which is in a good agreement with the mentioned results by Landoulsi et al.¹⁰ Indeed, they concluded that the passive film after an immersion time of 72 h, under similar conditions, consists mostly of iron oxyhydroxides (FeOOH) species and that a steady state may be reached, as monitored via open circuit potential (OCP) measurements and XPS.^{10,13}

5 Evaluation of SMFS data for passive film covered stainless steel

Many applications demand significant covalent and/or noncovalent bonding of polymers or (macro) molecules to metal oxide substrates¹⁴ and in particular to steel.¹³ However, to the best of our knowledge, only few reports have been devoted to the study of the adhesive properties exerted by iron-based surfaces to adhesion-promoting molecules or biomolecules. For instance, Francius and co-workers thoroughly studied the adhesive properties exhibited by the combination of iron-containing green rust nanoparticles and bacteria exopolymeric substances (EPS) by means of Chemical Force Microscopy (CFM) and SMFS measurements.^{15–18} For the latter, AFM tips modified with 11-mercaptopundecanoic acid were employed. Regarding stainless steel (SS), in particular SS 316 L, Geisler et al. published a seminal contribution showing the bonding capabilities exhibited by the latter to a mimic spider silk-like polymer covalently grafted to the AFM tip.¹⁹ More recently, Dupres and co-workers have reported SMFS experiences carried out with peptide chains grafted to the AFM tip onto passivated SS 316 L surfaces.¹³

The survey spectra showed the expected chemical composition consisting of mainly iron, chromium and manganese. Also, some little contaminations from adsorbed organic components (adventitious carbon) cannot be avoided as mentioned elsewhere.^{10–12} Evaluation of the O1s core level peak shows three components at binding energy of 530.0 eV (associated to metal oxide), 531.6 eV (associated to C=O, carboxylates, and/or -OH) and 533.7 eV (C-OH, C-O-C). Measurements carried out at different take-off angles (see Figure S8 and Table S5) show an enrichment of the carboxylate component at the near-surface region. Consequently, it should be expected that the interactions between the mostly deprotonated PAA chains (R-COO^-), as explained before ($\text{pK}_a = 6.0^{20} < \text{pH} = 7.0$), and the FeOOH -terminated steel surface will be essentially based either on short range electrostatic interactions or van-der-Waals interactions and

hydrogen bridging. In the dilute electrolyte concentrations used in this work, namely 2 mM NaClO₄, the Debye length of the dilute background electrolyte should be high, so that the electrostatic double layer is expected to have a strong influence on the electrostatic interactions in the liquid medium.

Our experiments showed that in the case of the hydroxyl-rich stainless steel surface, terraces of constant peel-off force are obtained. Examples of the latter were displayed in Figure 3 A) and D) in the main text. Dupres et al. have mentioned a point of zero charge of 8.0 for iron hydroxide and iron oxyhydroxide.¹³ Consequently, the carboxylate groups are negatively charged while the stainless steel surface is positively charged in our experimental conditions, i.e. pH 7 (pH < PZC_{SS}). Thus, the reversible adsorption of PAA molecules, via van der Waals, hydrogen bridging or electrostatic interactions, lead to weak interactions at the hydroxyl-rich steel surface, giving rise thus to equilibrium peel-off force plateaus during the desorption process. Because of the slight positively charged surface and the presence of negatively charged carboxylate moieties in the PAA chains, electrostatic interactions might be mostly favored.

Geisler et al.¹⁹ calculated the adsorption free energies for plateaus, similar to the events found in our experiments (Figure 3 D in the main text). The averaged values for stainless steel are typically given in k_BT/nm. For the case of 2.0 s of dwell time on stainless steel, we have approximately 11 ± 2 k_BT/nm, and 10 ± 3 k_BT/nm for 5.0 s dwell time. These values underline that the equilibrium desorption events are mostly independent of the dwell time since a steady state is reached in the both cases. In addition to that, the magnitude of this values are also in a good agreement with the adsorption free energies reported by Geisler et al.¹⁹ For example, these authors could find a value of 7.8 k_BT for the case of polished steel 316L with poly(allylamine) functionalized AFM cantilevers in PBS at 36.5 °C.

The magnitude of the observed plateau forces for two different dwell times, namely 2.0 s and 5.0 s, is presented as histograms in Figure S9.

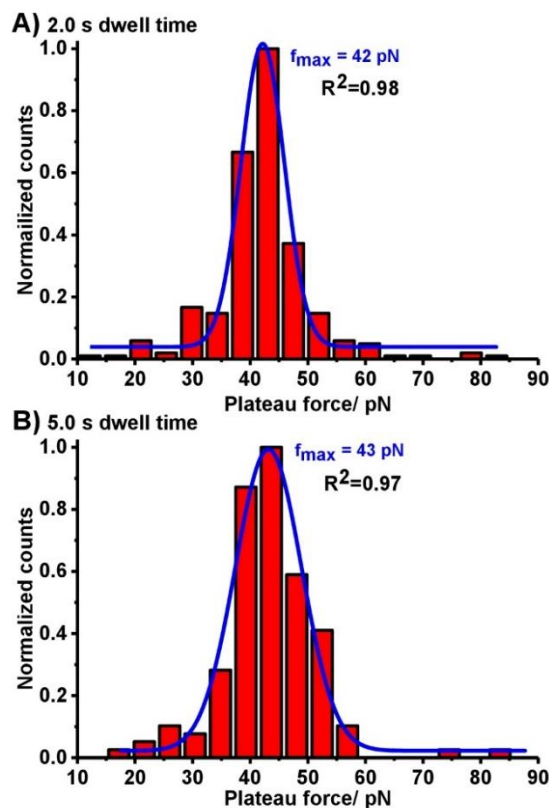


Figure S9. Normalized SMFS statistic results of the heights of the plateau forces on polished, preconditioned stainless steel for different dwell times: 2.0 s (A) and 5.0 s (B).

The blue lines displayed in Figure S9 correspond to the Gaussian fittings of the plateau force distributions and are accompanied by the correspondent errors by means of the typical R^2 . The distributions in both cases are quite narrow, indicating neither overlapping nor other molecular adhesion forces. The averaged peel-off forces are summarized in Table S6. It can be easily concluded from the latter that many curves show no events, even at high dwell times, while some curves exhibit measurement artifacts or little rupture forces (4.2 % till 7.6 %).

As previously stated, Table S6 underlines that a dwell time of 2.0 s is already enough to provide the system with enough time to reach the equilibration state. Mosebach et al. used basically the same cantilever modification chemistry and showed that only a small percentage of the registered curves exhibit desorption events.²¹ The latter statement is indeed in a good agreement with our results. In addition to that, the magnitude of the desorption forces obtained by plateaus is in the same order than that found by Valtiner et al. for the ZnO single crystal surfaces²⁰ or for other substrates.^{22,23} In this context, Geisler et al. also explored in a seminal contribution the adhesion properties exhibited by some peptide units (the amino acids units are expected to be responsible for the bonding processes) of a mimic spider-silk-like polymer covalently attached to an AFM tip with a stainless steel 316 L surface, at neutral pH in a dilute electrolyte solution, by means of SMFS. The magnitude of the plateau forces shown by them perfectly matches with our results depicted in Table S6.

Table S6. Summary of the peel-off forces and ratios of the amount of different events on stainless steel of the two different dwell times.

	2.0 s dwell time	5.0 s dwell time
Maximum of the peel-off force of all plateaus/ pN	42	43
Percentage of curves without any event/ %	66.8	76.2
Percentage of curves with plateaus/ %	29.0	18.2
Percentage of curves with rupture events/ %	4.2	5.6

The presented values are in the same order than those obtained by Dupres et al. for the SMFS of a peptide-based chain-modified AFM tip, namely a D-Ala-D-Ala-terminated tip, on a similarly preconditioned stainless steel in a buffer solution at pH 8.¹³ They could find adhesion plateau forces of around $72 \text{ pN} \pm 12 \text{ pN}$.¹³ In addition to that, they could also find only a 18 % of all measured curves showing molecular adhesion events¹³, which matches our results.

6 Evaluation examples of the SMFS on the ZnO coated stainless steel

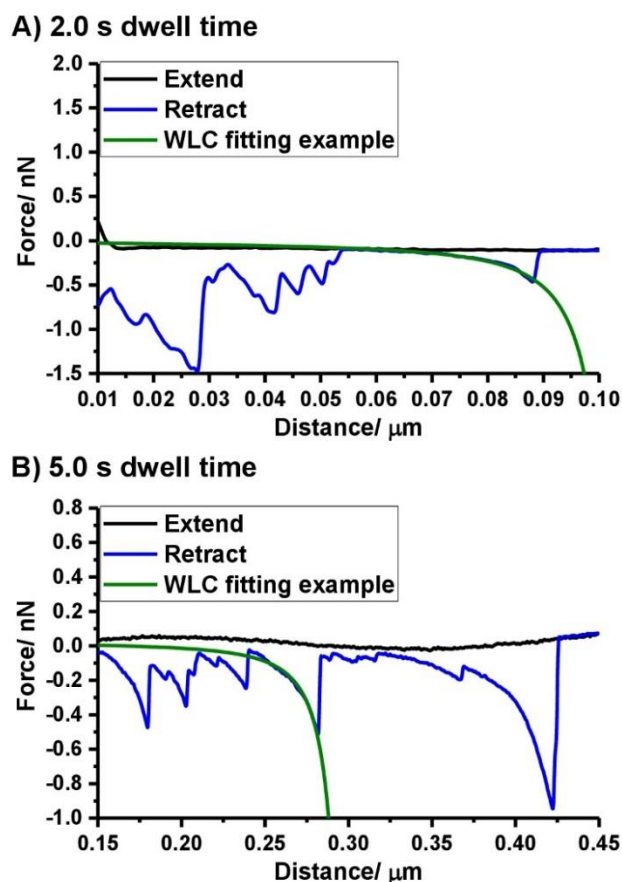


Figure S10. Force-distance curves for PAA on the ZnO nanorod coated stainless steel tentatively fitted to WLC model (green) for A) a dwell time of 2.0 s and B) for a dwell time of 5.0 s.

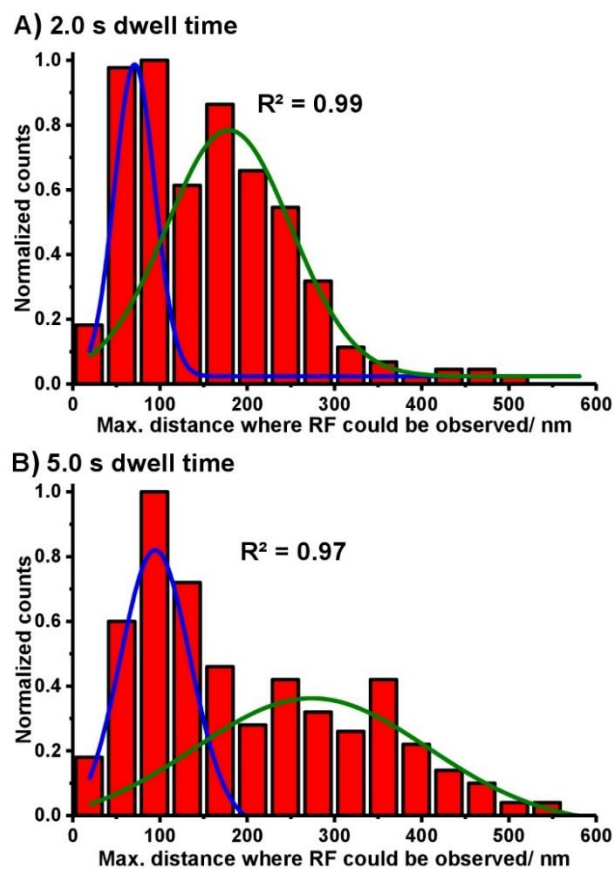


Figure S11. Histograms obtained for the measured maxima distance, where rupture events could be observed for the ZnO nanorod films on stainless steel for different dwell times: A) 2.0 s and B) 5.0 s. The data based on three different measurements with a size of 16 x 16 points per map which means 768 measured F-D-curves.

Table S7. Summary of the peel-off forces and ratios of the number of different events on ZnO nanorod coated stainless steel of the two different dwell times.

	2.0 s dwell time	5.0 s dwell time
Max. of the rupture event of all events/ pN	708	632 (blue fit) 1288 (green fit)
Percentage of curves without any event/ %	67.0	62.0
Percentage of curves with plateaus/ %	1.6	2.1
Percentage of curves with rupture events/ %	31.4	35.9

Table S8. Summary of the desorption forces and ratios of the number of different events on platelet-like ZnO films for the two different dwell times.

	2.0 s dwell time	5.0 s dwell time
Max. of the rupture event of all events/ pN	347	370
Max. of the plateaus of all events/ pN	-	62
Percentage of curves without any event/ %	57.6	71.2
Percentage of curves with plateaus/ %	0.0	13.4
Percentage of curves with rupture events/ %	42.4	15.4

7 References

- (1) Seipel, B.; Nadarajah, A.; Wutzke, B.; Könenkamp, R. Electrodeposition of ZnO nanorods in the presence of metal ions. *Materials Letters* **2009**, *63*, 736–738.
- (2) Sheini, F. J.; Mulla, I. S.; Joag, D. S.; More, M. A. Influence of process variables on growth of ZnO nanowires by cathodic electrodeposition on zinc substrate. *Thin Solid Films* **2009**, *517*, 6605–6611.
- (3) Al-Kuhaili, M. F.; Durrani, S. M. A.; Bakhtiari, I. A. Influence of oxygen flow rate on the surface chemistry and morphology of radio frequency (RF) magnetron sputtered zinc oxide thin films. *Surf. Interface Anal.* **2013**, *45*, 1353–1357.
- (4) Majumder, S.B.; Jain, M.; Dobal, P.S.; Katiyar, R.S. Investigations on solution derived aluminium doped zinc oxide thin films. *Materials Science and Engineering: B* **2003**, *103*, 16–25.
- (5) Meng, L.-J.; Moreira de Sá, C. P.; dos Santos, M. P. Study of the structural properties of ZnO thin films by x-ray photoelectron spectroscopy. *Applied Surface Science* **1994**, *78*, 57–61.
- (6) Chen, M.; Wang, X.; Yu, Y.H.; Pei, Z.L.; Bai, X.D.; Sun, C.; Huang, R.F.; Wen, L.S. X-ray photoelectron spectroscopy and auger electron spectroscopy studies of Al-doped ZnO films. *Applied Surface Science* **2000**, *158*, 134–140.
- (7) Dong, J.; Ozaki, Y.; Nakashima, K. Infrared, Raman, and Near-Infrared Spectroscopic Evidence for the Coexistence of Various Hydrogen-Bond Forms in Poly(acrylic acid). *Macromolecules* **1997**, *30*, 1111–1117.
- (8) Miyazawa, T.; Fukushima, K.; Ideguchi, Y. Molecular Vibrations and Structure of High Polymers. III. Polarized Infrared Spectra, Normal Vibrations, and Helical Conformation of Polyethylene Glycol. *The Journal of Chemical Physics* **1962**, *37*, 2764–2776.
- (9) Stuart, B. H. *Infrared spectroscopy: Fundamentals and applications*; Analytical techniques in the sciences; Wiley: Chichester, West Sussex, 2008.
- (10) Landoulsi, J.; Genet, M. J.; Richard, C.; El Kirat, K.; Pulvin, S.; Rouxhet, P. G. Evolution of the passive film and organic constituents at the surface of stainless steel immersed in fresh water. *Journal of colloid and interface science* **2008**, *318*, 278–289.
- (11) Lin, T.-C.; Seshadri, G.; Kelber, J. A. A consistent method for quantitative XPS peak analysis of thin oxide films on clean polycrystalline iron surfaces. *Applied Surface Science* **1997**, *119*, 83–92.

- (12) Fredriksson, W.; Malmgren, S.; Gustafsson, T.; Gorgoi, M.; Edström, K. Full depth profile of passive films on 316L stainless steel based on high resolution HAXPES in combination with ARXPS. *Applied Surface Science* **2012**, 258, 5790–5797.
- (13) Landoulsi, J.; Dupres, V. Probing Peptide–Inorganic Surface Interaction at the Single Molecule Level Using Force Spectroscopy. *Chemphyschem : a European journal of chemical physics and physical chemistry*, 12, 1310–1316.
- (14) González-Orive, A.; Giner, I.; los Arcos, T. de; Keller, A.; Grundmeier, G. Analysis of polymer/oxide interfaces under ambient conditions – An experimental perspective. *Applied Surface Science* **2018**, 442, 581–594.
- (15) Zegeye, A.; Etique, M.; Carteret, C.; Ruby, C.; Schaaf, P.; Francius, G. Origin of the Differential Nanoscale Reactivity of Biologically and Chemically Formed Green Rust Crystals Investigated by Chemical Force Spectroscopy. *J. Phys. Chem. C* **2014**, 118, 5978–5987.
- (16) Beaussart, A.; Ngo, T. C.; Derclaye, S.; Kalinova, R.; Mincheva, R.; Dubois, P.; Leclère, P.; Dufrêne, Y. F. Chemical force microscopy of stimuli-responsive adhesive copolymers. *Nanoscale* **2014**, 6, 565–571.
- (17) Li, Y.; Liu, H.; Wang, T.; Qin, M.; Cao, Y.; Wang, W. Single-Molecule Force Spectroscopy Reveals Multiple Binding Modes between DOPA and Different Rutile Surfaces. *Chemphyschem* **2017**, 18, 1466–1469.
- (18) Li, Y.; Wang, T.; Xia, L.; Wang, L.; Qin, M.; Li, Y.; Wang, W.; Cao, Y. Single-molecule study of the synergistic effects of positive charges and Dopa for wet adhesion. *J. Mater. Chem. B* **2017**, 5, 4416–4420.
- (19) Geisler, M.; Balzer Bizan, N.; Hugel, T. Polymer Adhesion at the Solid–Liquid Interface Probed by a Single–Molecule Force Sensor. *Small* **2009**, 5, 2864–2869.
- (20) Valtiner, M.; Grundmeier, G. Single Molecules as Sensors for Local Molecular Adhesion Studies. *Langmuir* **2010**, 26, 815–820.
- (21) Mosebach, B.; Ozkaya, B.; Giner, I.; Keller, A.; Grundmeier, G. Analysis of acid-base interactions at Al₂O₃ (11-20) interfaces by means of single molecule force spectroscopy. *Applied Surface Science* **2017**, 420, 296–302.
- (22) Kienle, S.; Gallei, M.; Yu, H.; Zhang, B.; Krysiak, S.; Balzer, B. N.; Rehahn, M.; Schlüter, A. D.; Hugel, T. Effect of Molecular Architecture on Single Polymer Adhesion. *Langmuir* **2014**, 30, 4351–4357.

(23) Balzer, B. N.; Micciulla, S.; Dodoo, S.; Zerball, M.; Gallei, M.; Rehahn, M.; V Klitzing, R.; Hugel, T. Adhesion Property Profiles of Supported Thin Polymer Films. *ACS Appl. Mater. Interfaces* **2013**, 5, 6300–6306.

3.2 Effect of PAA-induced surface etching on the adhesion properties of ZnO nanostructured films

The following publication (**2. publication** of this PhD thesis) was reused from:

D. Meinderink, C. Kielar, O. Sobol, L. Ruhm, F. Rieker, K. Nolkemper, A. G. Orive, O. Ozcan, Guido Grundmeier, International Journal of Adhesion and Adhesives 106 (**2021**) 102812 (Copyright Elsevier 2021) with permission from Elsevier for reuse and embedding the article in this PhD thesis.

<https://doi.org/10.1016/j.ijadhadh.2021.102812>

The molecular adhesion properties of ZnO nanostructures and PAA was investigated by means of SMFS in the **1. publication**. However, the macroscopic adhesion performance and the influence of PAA pre-treatment by immersion into water-based solution containing dilute PAA concentrations had still been an open question at this point. This **2. publication** investigated the macroscopic adhesion properties of i) ZnO nanostructures including nanorods and nanocrystalline films where the latter ones are comparable to the previous platelet-like ZnO films on stainless steel and ii) the influence of the immersion of the ZnO nanostructures into an aqueous 3.64 μM PAA (250.000 g/mol) solution at pH 7 on the peel-off forces of an epoxy-amine model adhesive similar to the used in the **3. publication** below. Hot-dipped galvanized steel (HDG) was used as an industrially relevant substrate for the deposition of hydrothermal grown ZnO nanostructures. Indeed, the immersion into a dilute PAA solution for 10 min confirmed an increase in the adhesion measured by peel-tests. The comparison with the immersion into ultra-pure water showed that the presence of PAA is needed to reach a significant enhancement in the adhesion performance. Furthermore, additional immersion experiments at higher PAA concentrations indicate a nanoetching effect of the ZnO crystals leading to a higher mechanical interlocking. A molecular-microscopic adhesion and nanoetching process could be developed and proposed. In fact, these results could be correlated with the investigations performed by SMFS and open the door for the usage of PAA in industrial applications like following within the next **publications 3. and 4.**

The following Table 3 sums up the involved persons with their work inputs.

Table 3. Summary of the author contributions involved in the publication “*Effect of PAA-induced surface etching on the adhesion properties of ZnO nanostructured films*”.

author contributions	involved persons
validation, writing, coordination, investigation, conceptualization, original draft, visualization, sample preparation, experimental executions, analytical measurements, evaluations, data curation, formal analysis, scientific discussion, review & editing	D.M
conceptualization based on bachelor thesis, content checking, review & editing	C.K.
ToF-SIMS measurements, content checking	O.S.
support for: sample preparation, peel-tests, DRITFS, review & editing	L.R., F.R., K.N.
scientific discussion, support, mentoring, interpretation of data, content checking, revisions of the manuscript, review & editing	A.G.O.
conceptualization, interpretation of data, content checking, review & editing	O.O.
project administration, funding acquisition, resources, conceptualization, scientific discussion, supervision, mentoring, interpretation of data, content checking, revisions of the manuscript, review & editing	G.G.



Contents lists available at ScienceDirect

International Journal of Adhesion and Adhesives

journal homepage: <http://www.elsevier.com/locate/ijadhadh>

Effect of PAA-induced surface etching on the adhesion properties of ZnO nanostructured films

D. Meinderink, C. Kielar¹, O. Sobol², L. Ruhm, F. Rieker, K. Nolkemper, A.G. Orive, O. Ozcan², G. Grundmeier^{*}

Technical and Macromolecular Chemistry, University of Paderborn, Warburgerstr. 100, 33098, Paderborn, Germany

ARTICLE INFO

Keywords:

ZnO nanorods
Nanocrystalline ZnO films
Adhesion by mechanical interlocking
Poly(acrylic acid)
Morphology control
Interfacial stability

ABSTRACT

Zinc oxide - polymer interfaces are known to exhibit interesting properties regarding molecular adhesion. This work is aimed at the investigation of the effect of the morphology and surface chemistry on the macroscopic adhesion of a model epoxy-based adhesive to nanorod (ZnO NR) and nanocrystalline (ZnO NC) ZnO-modified surfaces. Both ZnO films have been prepared using hydrothermal synthesis on hot-dip galvanized steel (HDG) surfaces by varying the precursor chemistry in order to control the film morphology. Poly (acrylic acid) (PAA) was used to improve the interfacial adhesion by modifying the morphology and surface chemistry of ZnO nanostructured films. The strong interaction of PAA from a dilute and neutral aqueous solution with the ZnO nanocrystallites was shown to significantly improve the interfacial adhesion by means of a nanoetching process. It was shown that the wet peel-forces correlate well with the considered morphology and surface chemistry.

1. Introduction

In the last decades, adhesive bonding of similar or dissimilar materials has gained scientific and technical significance, especially in automotive and aircraft assembly as well as in microelectronics and construction industry [1–3]. Adhesive joining of metal structures presents numerous advantages including the reduction of weight and an improved crash resistance [4]. From the perspective of light-weight construction, adhesive joining is applied to join metallic parts, such as steel, alloy coated steel, aluminium and magnesium alloys, with other metallic, polymeric or composite materials [5,6]. In all cases, the overall joint performance is dictated by the strength of the adhesive – metal/metal oxide interface, where the knowledge of the surface chemistry of metal/metal oxides of industrial relevance, such as hot dipped galvanized steel (HDG), plays a crucial role for the latter [5,7–9].

A lot of publications about adhesive bonding with epoxy adhesive formulations with different amines and the corresponding analysis of the adhesion mechanisms and failure modes on HDG can be found in the literature [10–15]. For example, Calvez et al. studied the interfacial degradation of epoxy adhesive on galvanized steel focusing on the durability of the joints [10]. In this context, the strong interactions of

amines with the HDG/zinc surfaces have been reported by Gaillard et al. [16]. The created interface of epoxy-amine adhesives exhibiting different chemical and physical properties and metal oxide substrates, depending on their surface chemistry and morphology, is probably the most important and critical point in joined metal-polymer systems [1, 10,15].

Moreover, while a technically acceptable initial adhesion strength is rather easy to achieve, the long-term stability of adhesive joints under exposure to various environmental conditions still presents a challenge to be overcome via an interdisciplinary approach [17]. Consequently, the synthesis of ZnO films as coating hybrid materials with different morphologies has attracted the scientific interest [18–20]. For example, Trino et al. showed an enhanced corrosion resistance of titanium implants after the surface functionalisation with zinc oxide [21]. In addition, Jin et al. demonstrated that the presence of 3-dimensional ZnO tetrapods promoted an enhanced adhesion between two polymeric films, namely poly (tetrafluoroethylene) (PTFE) and poly (dimethylsilane) (PDMS) [22].

ZnO deposition methods such as electrodeposition, hydrothermal synthesis, sol-gel chemistry or for example from vapour phase on silicon and glass substrates are well-known and published elsewhere [19,20,

^{*} Corresponding author.

E-mail address: g.grundmeier@tc.uni-paderborn.de (G. Grundmeier).

¹ Institute of Resource Ecology, Helmholtz-Zentrum Dresden-Rossendorf, Bautzner Landstraße 400, 01328, Dresden, Germany.

² Bundesanstalt für Materialforschung und -prüfung (BAM), Unter den Eichen 87, 12205 Berlin, Germany.

<https://doi.org/10.1016/j.ijadhadh.2021.102812>

Received 5 May 2020; Accepted 9 January 2021

Available online 15 January 2021

0143-7496/© 2021 Elsevier Ltd. All rights reserved.

This article was published in: “International Journal of Adhesives and Adhesion” Vol. 106, D. Meinderink, C. Kielar, O. Sobol, L. Ruhm, F. Rieker, K. Nolkemper, A. G. Orive, O. Ozcan, Guido Grundmeier, “Effect of PAA-induced surface etching on the adhesion properties of ZnO nanostructured films”, 102812, Copyright Elsevier 2021, reused with permission from Elsevier.

23–32]. Indeed, it is possible to prepare anisotropic ZnO crystalline films [19,20,30–35]. For instance, the hydrothermal synthesis of nanocrystalline ZnO films results in the deposition of densely packed columnar crystallites with a hexagonal cross-section [19,20,32,33,36,37]. The top and side surfaces of the individual ZnO nanorods exhibit the (0001) and (10-10) crystalline orientations, respectively [38]. The potential beneficial effect of these unique morphologies on the interfacial adhesion strength was only recently shown [36,39–41]. For instance, Ehlert et al. showed that the deposition of ZnO nanowires on carbon fibers leads to hybrid composites with strong adhesion properties [40].

Furthermore, it has already been published that carboxylate groups could induce nanoetching processes of ZnO nanostructures [42,43]. Ryu et al. demonstrated that isotropic nanoetching of ZnO nanorods leads to nanocactus structures after a thermochemical reaction [43]. In addition to that, Han et al. reported a selective wet-chemical etching of ZnO nanostructures like ZnO nanorods [42]. Their work clearly exhibits the possible etching with carboxylate groups (here based on oleic acid) at the nonpolar sidewalls of ZnO nanorods [42]. Moreover, the dissolution of ZnO nanocrystalline surfaces with octadecylphosphonic acid (ODPA) has been demonstrated by Pomorska et al. [44]. This effect could be prevented by the control of Zn^{2+} ions in the solution [44].

With regards to the understanding of the adhesion-promoting properties of ZnO and PAA, molecular adhesion studies by means of single molecule force spectroscopy (SMFS) have demonstrated the role of the crystalline orientation on the adhesion of PAA molecules on single crystalline ZnO surfaces [45] and ZnO nanorod and nanocrystalline films [29]. Valtiner et al. have reported that PAA molecules can form coordination bonds at the non-polar step edges of the hydroxyl covered polar ZnO (0001)-Zn surfaces [45], while Meinderink et al. have shown the dependence on the molecular adhesion forces with the nano-architecture of electrodeposited ZnO films exhibiting different aspect ratios [29]. Formation of strong coordinative bonds to the nonpolar sidewalls were observed in the form of multiple rupture events [29]. Furthermore, the surface diffusion of PAA molecules to non-polar steps in ZnO (0001)-Zn single crystalline surfaces reported by Kunze et al. [46] is in good agreement with the mentioned SMFS studies. On top of that, thin PAA films deposited by electropolymerisation on stainless steel were shown to exhibit enhanced adhesion promoting properties [47].

To the best of our knowledge, no publication is showing the macroscopic adhesion promoting properties of ZnO structures with the prior treatment with dilute PAA solution for the interfacial adhesion control on technically relevant HDG substrates. Accordingly, the aim of this work is to investigate the effect of the ZnO film morphology on the adhesion to a polymeric film as well as to study the adhesion promotion effect of PAA as a function of the ZnO nanocrystal aspect ratio. The formation of highly stable coordinative bonds between PAA molecules in solution and Zn^{II} atoms coming from ZnO crystalline surfaces [29] promotes a selective etching/dissolution of these structures, with the subsequent modification of their morphology and the arising of new active anchoring sites for the bonding of polymeric layers. This process is consequently translated in an enhanced interfacial adhesion to a model epoxy-amine resin.

2. Materials and methods

2.1. Sample preparation and chemicals

Skin passed hot-dip galvanized steel substrates (supplied by Chemetall GmbH, Frankfurt, Germany) were cut to 2.0 cm × 4.5 cm size and subsequently cleaned in tetrahydrofuran (THF) (Merck, Darmstadt, Germany), isopropanol (IsOH) (Merck, Darmstadt, Germany) and ethanol (EtOH) (UN 1170 ethanol provided by Martin und Werner Mundo oHG, Mainz-Kostheim, Germany) for 15 min in an ultrasonic bath to remove the protective oil. The solvent cleaned samples (SC) were then immersed in an alkaline cleaning solution (30 g/l Gardoclean

S5176 and 5 g/l Additive H7376/1; provided by Chemetall GmbH, Frankfurt, Germany) under stirring at 55 °C for 1 min. For all experiments in this work, de-ionized water (<0.075 µS/cm conductivity, Ultra Clear TWF, SG Water, Hamburg, Germany) was used.

ZnO nanorod (ZnO NR) growth was performed by immersing the substrates in an aqueous solution of 25 mM zinc nitrate, $\text{Zn}(\text{NO}_3)_2 \cdot 6\text{H}_2\text{O}$ (zinc nitrate hexahydrate, 98% extra pure, ACROS Organics) and 25 mM hexamethylenetetramine $\text{C}_6\text{H}_{12}\text{N}_4$ (HMTA, AnaLaR NORMAPUR®, VWR Chemicals) for 30 min at 90 °C (± 5 °C) followed by directly rinsing with de-ionized water. The continuous ZnO nanocrystalline morphology (ZnO NC) was achieved by addition of 0.12 mM sodium citrate (sodium citrate dehydrate, ACS, 99.0%, ABCR GmbH & Co. KG, Karlsruhe, Germany) to an aqueous deposition bath consisting of 50 mM Zn (NO_3)₂·6H₂O and 43 mM HMTA in this case. The deposition time was also 30 min at 90 °C (± 5 °C).

PAA adsorption was carried out by immersion of the substrates for 10 min in an aqueous 2.6 g/l PAA solution (poly (acrylic acid); $M_w \sim 250,000$, 35 wt % in H₂O, Sigma Aldrich, Germany) with a final concentration of 3.64 µM PAA solution at 23 °C (± 2 °C) with a pH 7 (adjusted with solid NaOH) without stirring, followed by rinsing with milli-pure water and drying in a stream of nitrogen. At this pH value the PAA chains should be deprotonated ($\text{pK}_a = 4.7$) [29,45,48] in the solution and mainly carboxylate groups ($-\text{COO}^-$) of the weak acid are present.

2.2. 90°-peel-tests

A hot-curing two component epoxy-amine resin (11.19 g epoxy resin, a diglycidyl ether of bisphenol A (D.E.R 331, DOW Chemicals, USA) and 6.78 g amine hardener (poly (propylene glycol) bis(2-aminopropyl ether), Sigma-Aldrich)) was employed as model adhesive and applied on the substrates after mixing and degassing as described elsewhere [47]. To control the thickness of the adhesive films the samples were coated with 4 commercial adhesive tapes (1 layer of Scotch Magic™ Tape, supplied by 3 M, Germany, and 3 layers of Tesafilm, supplied by tesaafilm®, Germany). An aluminium foil was used to form the sandwich geometry, which was removed after the hardening step to obtain an open polymer film. Before the application of the liquid adhesive the samples were stored in a glove box (filled with a mixture of dry air and nitrogen) with controlled relative humidity ($6.0\% \pm 3.0\%$) at room temperature (21.5 ± 1.0 °C) for 15 min (± 5 min) to remove the most adsorbed water layers from the atmosphere. The completed sandwich geometry was kept under these conditions for 15 min (± 5 min) to be sure that all pores are filled with liquid adhesive before curing step (120 °C for 75 min). To investigate the wet de-adhesion process the samples were exposed to humid atmosphere (>95% r.h.) at 40 °C for 24 h (± 1 h) before the peel-test measurements [47,49].

Peel-tests have been performed at a constant perpendicular angle to the sample surface with 1 mm/min velocity using a force gauge (model ZP-5, Imada, Tokyo, Japan) and a motorized peel-tester (MV-220 Motorized Test Stand, Imada, Tokyo, Japan) at 95% relative humidity at room temperature (21.5 ± 2.0 °C) [39,47,49]. At least 3 different samples prepared under equal experimental conditions with 3–4 released adhesive stripes per sample gives a sufficient statistic accuracy with at least 11 stripes under each condition used for the evaluation of the adhesion properties after the different surface treatments.

The film thicknesses of the applied model adhesives were measured with a DUALSCOPE® FMP20 (magnetoinductive and eddy current method, Helmut Fischer GmbH, Germany) at five different positions on five different coated samples. Before the measurements the equipment was calibrated with defined foils provided by the supplier of the measurement equipment. The resulted mean averaged value of the total epoxy-amine adhesive films is 150 µm (± 19 µm).

2.3. Field-emission scanning electron microscopy (FE-SEM)

Morphological characterization of ZnO films and peeled adhesive surfaces was performed by means of a field-emission scanning electron microscope (NEON® 40 FE-SEM, Carl Zeiss SMT AG, Germany) using an InLens detector. Some samples were milled with a focused ion beam (FIB) system (NEON® 40 FE-SEM, Carl Zeiss SMT AG, Germany) with a Ga liquid ion source (LMIS). In all FIB procedures a current of 50 pA and a beam of 30 keV were used. Prior to the measurements of polymeric films, 3 nm Au/Pd (80 wt% Au, 20 wt% Pd) thick sputter coatings were deposited [39].

2.4. Diffuse reflection infrared fourier transform spectroscopy (DRIFTS)

For the identification of adsorbed PAA on SC, ZnO NR and ZnO NC films DRIFT measurements were done with a Vertex 70 spectrometer (Bruker Optics, Germany). A gold sample (300 nm gold deposited via PVD on silicon wafer (100)) was measured as a reference. A resolution of 4 cm^{-1} , 512 scans for each sample, and a LN-MCT detector were used.

2.5. X-ray photoelectron spectroscopy (XPS)

X-ray photoemission spectroscopy (XPS) was performed in an ESCA+ setup (Omicron NanoTechnology, Germany). A monochromatic Al-K α irradiation source (1486.7 eV) and an angle of 30° with respect to the surface plane were used for all measurements. The base pressure was lower than 3.0×10^{-10} mbar and neutralization in the case of the polymer films after peel-tests was used. For the detection, a multi-channel plate detector (Omicron Argus, Germany) was used. A convolution of a Gauss (30%) and Lorentzian (70%) shape was chosen (Shirley background) in the CASA-XPS software (Casa Software Ltd., Teignmouth, UK) for peak fittings and the C 1s peak at position 285.0 eV was set as internal calibration [39].

2.6. Time-of-flight secondary ion mass spectrometry (ToF-SIMS)

Time-of-Flight secondary ion mass spectrometry (ToF-SIMS) measurements were performed using a ToF-SIMS IV (IONTOF GmbH, Münster, Germany) equipped with a 25 keV BiMn liquid metal ion gun (LMIG). Due to a better contribution with a negative polarity for the identification of PAA [50], spectra were acquired in the negative polarity. All measurements were performed using the spectrometry mode (high current bunched mode - HCBU) to enable good mass resolution, on a region of $100\text{ }\mu\text{m} \times 100\text{ }\mu\text{m}$. Analyses were conducted in the interlaced mode, allowing to couple the analysis process with a sputter process within the acquisition cycle. Sputtering was done using a 1 kV Ar beam and a sputtered area of $300\text{ }\mu\text{m} \times 300\text{ }\mu\text{m}$ (where the analyzed area is in the centre of the sputtered area). Ar was selected as a sputter species to remove surface contaminations without obtaining a significant influence on the secondary ion yield.

As control, SC and ZnO NC samples were spray-coated with the same PAA solution (3.64 μM PAA (250.000 g/mol) in water at pH 7 adjusted with solid NaOH) and analyzed via ToF-SIMS. The spray coating process of aqueous PAA solutions has been described elsewhere [39]. A commercial spray coater (ND-SP 11/4 Precision Spray Coater, Nadetech Innovations S.L., Spain) with an installed hot-plate was used. The motor speed was fixed at 1200 mm/min. A volume speed of 200 ml/h, a nozzle distance to the substrate surface of 12 cm, an operating temperature of 75 °C and 4.0 bar pressure of nitrogen were selected in the equipment.

3. Results and discussion

3.1. Characterization of zinc oxide morphologies synthesised via hydrothermal growth

The growth of ZnO nanorods (ZnO NR) and nanocrystalline ZnO

films (ZnO NC) was carried out by a hydrothermal methodology on alkaline cleaned HDG substrates. The latter resulted in homogeneously and densely packed films as can be deduced from the FE-SEM images displayed in Fig. 1.

The FE-SEM images of the solvent cleaned (SC) substrate, taken as a reference (without any treatment) and displayed in Fig. 1a) and b), show relatively smooth areas disrupted by scratches and grain boundaries. The thickness of the zinc layer could be estimated between 200 nm and 600 nm from the FIB cross-section shown in Fig. 1 c).

The hydrothermal synthesis of the two different ZnO morphologies, i.e. ZnO nanorods (ZnO NR) and nanocrystalline ZnO films (ZnO NC), gives rise to the expected well-defined hexagonal crystallites which can be observed in Fig. 1d)–i). Ozcan et al. could already show the hydrothermal growth of ZnO NR on polished zinc sheets with the use of zinc nitrate hexahydrate as the precursor salt and hexamethylenetetramine (HMTA) [20,36]. HMTA and citrate anions are commonly used in most of the deposition methods of ZnO films and particles described in the literature [29,51,52], and it has been proposed that HMTA controls the growth mechanisms by blocking the nonpolar side walls of the ZnO crystallites via chelating mechanisms [29,52]. Here, we could deposit ZnO NC by adding a low concentration of citrate anions as mentioned by Baruah et al. Ozcan, and Engelkemeier et al. [20,25,51] which leads to well-defined ZnO NC films as those observed in Fig. 1. On top of that, it is important to have a seed layer of passivated zinc which acts as nucleation points for the following growth step [36,51]. In this regard, HDG steel surfaces possess a thick zinc oxide surface which leads to a successful deposition of crystalline zinc oxide structures (see XPS section). These ZnO films are homogeneously deposited on the zinc layer of the HDG samples and no defects or pinholes allowing identification of the bare substrate underneath could be found. As deduced from the FE-SEM images, the crystallites are randomly oriented. The diameters measured for ZnO NR and the ZnO NC are around 150 nm and 250 nm, respectively. Furthermore, FE-SEM imaging of FIB cross-sections of these films have been performed to analyse the length of the as-prepared ZnO crystallites, see Fig. 1 f), i). Here, the ZnO NR have a total length of around 400 nm, while the ZnO NC exhibit estimated length of 150 nm.

The characterization of the chemical composition of the surfaces (SC, ZnO NR and ZnO NC) with XPS will be discussed later on.

3.2. Peel-test results and surface analysis

For the characterization of the adhesion promoting properties of the as-modified surfaces vs. a model epoxy-amine resin [47,49], peel-tests were carried out on the three HDG substrates without and with immersion into PAA containing solution. The results are displayed in Fig. 2.

A representative peel-off force vs. distance curve is provided in Fig. S1 in the Supporting Information (SI). All curves are showing characteristic plateaus which were used to evaluate the peel-off forces without the influence of the elastic behavior of the used model adhesive [47,49]. For a clear demonstration of the (etching)effect of PAA on adhesion enhancement, all three samples (SC, ZnO NR, ZnO NC) were immersed into ultra-pure water for the same time of 10 min and rinsed with ultra-pure water.

The SC samples show peel-off forces in the same range than those already published by Knust et al. [7] for similar samples. All the water and PAA-immersed samples show a significant improvement in the macroscopic adhesion as illustrated in Fig. 2. The peel-off force for the ZnO NR is in a good agreement with the results for similarly prepared ZnO NR on zinc substrates reported by Ozcan et al. [36]. Both deposited nanostructures confirm a significant enhancement in the adhesion caused by the highly increased mechanical interlocking (see Fig. 1). In this regard, an enhancement of the adhesion by a factor of (at least) 1.3 could be reached after the deposition of ZnO NR on HDG in comparison to the SC samples without further treatments. Here, the maximum and minimum values extracted from the dispersion of the measured data are taken into account. For instance, the highest peel-off force for the SC is

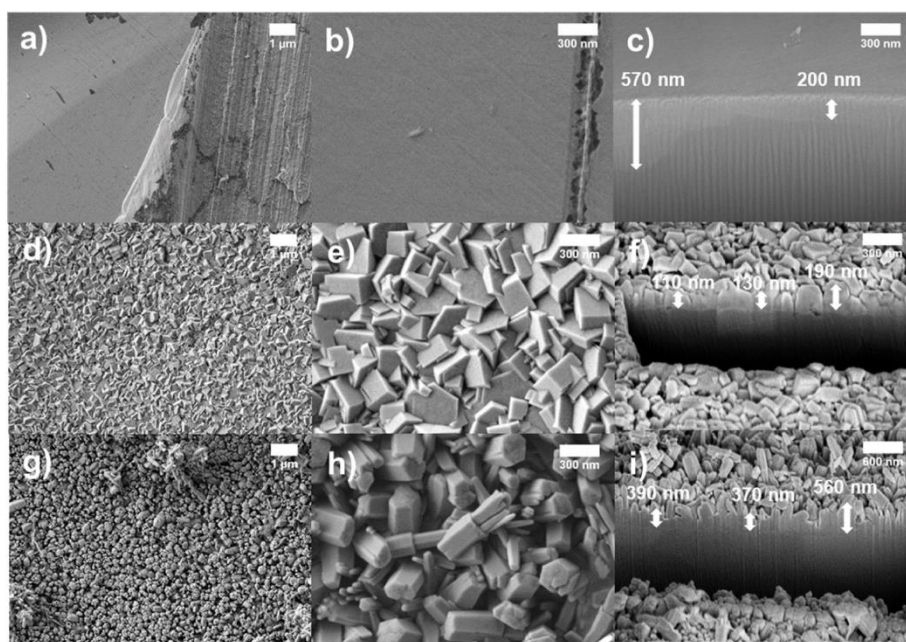


Fig. 1. FE-SEM images at different magnifications of HDG steel after ZnO synthesis with FE-SEM images of cross sections. FE-SEM images a)-c) show the solvent cleaned (SC), d)-f) ZnO nanocrystalline film (NC) and g)-i) ZnO nanorods (NR) samples.

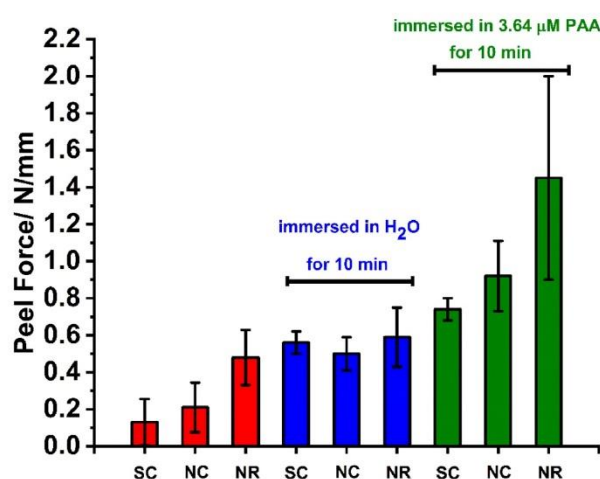


Fig. 2. Measured peel-off forces of the epoxy-amine resin from SC, ZnO NR and ZnO NC surfaces after exposure to high humidity for one day: no surface treatment (on the left in red), surfaces immersed into milli-pure water for 10 min (in the middle in blue); surfaces immersed into aqueous 3.64 μM PAA solution (pH 7 adjusted with NaOH) (on the right in green). (For interpretation of the references to colour in this figure legend, the reader is referred to the Web version of this article.)

0.26 N/mm, while the minimum peel-off force registered for the ZnO NR reaches 0.33 N/mm.

Strong interactions between ZnO and amines (here from the epoxy-amine resin) are already known and mentioned in literature [53]. Bach et al. proposed covalent bonds between ZnO surfaces and amines [53] while Ballerini et al. suggested Lewis acid/base interactions between zinc cations and 1,2-diaminoethane under UHV conditions [54]. Stable chelating complexes of zinc oxides with bidentate

ligand-ethylenediamine could also be found in the literature [55]. In our case, the non-reacted amine ($-\text{NH}_2$) functionalities from poly(propylene glycol) bis(2-aminopropyl ether), could interact with these ZnO surfaces via the already mentioned binding mechanisms.

The samples immersed into ultra-pure water show an adhesion enhancement by a factor of (at least) 1.9 by considering the peel-off force corresponding to the maximum of the error bars of SC before (0.26 N/mm) and the minimum value measured after immersion into ultra-pure water. This can be explained by a possible hydroxylation of the surfaces due to a stronger interaction behavior between the latter and adhesive film based on epoxy and amine groups. This interaction has been reported in the literature for different substrates. Especially, the amine groups could strongly interact with the hydroxylate groups of the metal oxide surfaces shown by several publications [53–55].

The peel forces of the ZnO NR and the ZnO NR after immersion into PAA containing solutions are increased by a factor of (at least) 1.4 (0.9 N/mm as the minimum of the error bar of ZnO NR after immersion into dilute PAA and 0.63 N/mm as the maximum of the error bar of the ZnO NR) which is indicative of a highly interfacial adhesion promotion between the ZnO NR and the adhesive film. In fact, the high adhesion forces of PAA to ZnO measured with SMFS by Valtiner et al. and Meinderink et al. [29,45] are supporting these macroscopic peel-off measurements. Interestingly, even in the case of the ZnO NC, after immersion in PAA solution, high adhesion promoting properties could be reached. This higher enhancement factor of around 2.1 in comparison to the ZnO NR films before and after PAA immersions (1.4) can be explained by the overall increased mechanical interlocking due to the PAA treatment. In the case of ZnO NC even slightly nanoetching effects results in a significant improvement in the adhesion peel-off force. However, in the case of ZnO NR the high surface area due to the high-aspect ratio of the nanorods can be only slightly improved through the PAA treatment, but not in such a significant way like for the ZnO NC which exhibit lower mechanical interlocking sites for the 2 component adhesive (compare Fig. 1 e) and h)). Here, a slight nanoetching effect increases the overall mechanical interlocking much more effectively when compared to the ZnO NR. The coordinative binding mechanism to

the nonpolar sidewalls and/or nanoetching could be proposed as a reasonable explanation for this phenomenon. By introducing accessible nonpolar sidewalls with the deposition of ZnO NC and, especially, in the case of ZnO NR, the carboxylate groups of PAA chains could give rise to strong interactions with the crystalline ZnO nanostructures [29]. Strong acid-base interactions of the carboxylate groups with the acidic ZnO, chelating or coordinative binding mechanisms are also proposed in the literature [29,47,49,56] which could explain the highly improved adhesion by adding PAA molecules to the zinc oxide surfaces and/or a nanoetching process. The high peel-off forces are indicating strong interfacial interactions between the cured epoxy-amine resin [6,16], the nanoetched ZnO nanostructures, and the eventually adsorbed PAA molecules. The typical curing reaction of epoxy-amine resins are published elsewhere [6,57]. A possible adhesion mechanism would include carboxylate groups from the deprotonated PAA layer linked to ZnO surface strongly interacting with the applied epoxy-amine resin. It could be proposed that diamine groups, in excess in the epoxy resin, could bind to these carboxylate groups, giving rise to different possible reaction products, for example via ring opening reaction or polycondensation [57–61]. The zinc carboxylate and/or the amine could probably act as catalysts as reported by Blank et al. for different epoxy resins and catalysts combinations [58]. Finally, there exists the possibility of a cross-linking process to create a dense interfacial network by the classical curing epoxy-amine reaction [10,57].

However, the adhesion promoting effect due to adsorbed PAA and/or nanoetching is a still open question which will be clarified in the following section by means of analytical surface investigations such as DRIFTS, XPS and ToF-SIMS.

3.3. Characterization of adsorbed PAA on the modified zinc coated steel after immersion in aqueous 3.64 μM PAA solutions (pH = 7)

The substantial enhancement in the adhesion leads to the question whether the PAA molecules are in between the ZnO films and the epoxy-amine adhesive films as adhesion promoting molecules or if the carboxylate groups from the PAA are responsible for the well-known nanoetching process at the ZnO crystallites [42,43]. In addition, Dang et al. showed for sodium poly (acrylic acid) in contact with ZnO particles in a suspension at pH 7 that the PAA form complexes with dissolved zinc ions [62].

For that reason, DRIFT spectroscopy measurements were carried out to confirm the adsorption of PAA on the three different substrates, namely, solvent cleaned sample (SC), zinc oxide nanorod film (ZnO NR) and nanocrystalline ZnO film (ZnO NC) with PAA molecules. The collected spectra (after atmospheric and baseline subtraction) are depicted in Fig. 3.

A broad band of the O–H vibration between 3700 and 3100 cm^{-1} and centered at 3381 cm^{-1} were interpreted as adsorbed or embedded water molecules from the water-based adsorption process [47,63–65]. Vibration modes of carbonates could be found in the range from 1200 cm^{-1} to 1700 cm^{-1} published by Hlaing Oo et al. via infrared spectroscopy on ZnO particles [66]. The characteristic peaks attributed to carboxylate groups, adventitious carbon species and oxidized ones could be detected. Obviously, the peaks for adsorbed carbonates from the atmosphere and impurities would consequently overlap with most of the bands attributed to PAA. For example, the vibration modes of the C–H stretching of the backbone from the PAA and adventitious carbon are visible at $\sim 2965 \text{ cm}^{-1}$, $\sim 2928 \text{ cm}^{-1}$ and $\sim 2856 \text{ cm}^{-1}$ [29,47,63,67,68]. A broad band of the carboxylate groups at a centered position at $\sim 1582 \text{ cm}^{-1}$ [47,68,69] which could be assigned to the deprotonated groups from the used PAA or oxidized species from the atmosphere. The latter is followed by a small peak accounting for the carbonyl vibration mode (C=O) at $\sim 1711 \text{ cm}^{-1}$ [63,64], while deformation vibration modes from C–H and C–O (from carboxylate ion COO^-) appear at $\sim 1474 \text{ cm}^{-1}$ and $\sim 1404 \text{ cm}^{-1}$ [29,47,63,64,68–70]. A shoulder at $\sim 1620\text{--}1640 \text{ cm}^{-1}$ could result from adsorbed water layers [71] and the

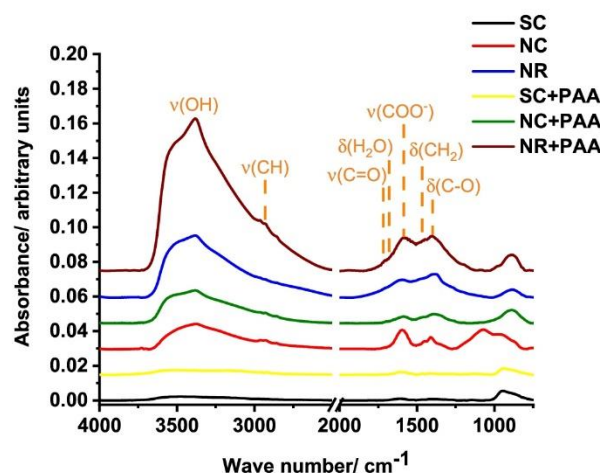


Fig. 3. DRIFT spectra from the solvent cleaned HDG substrate (SC; black), the ZnO nanorod (NR; blue) and the ZnO nanocrystalline (NC; red) films after the adsorption of PAA from water-based solutions. The spectra were shifted by a constant factor of 0.15 arb. Units. (For interpretation of the references to colour in this figure legend, the reader is referred to the Web version of this article.)

peak at $\sim 1240\text{--}1260 \text{ cm}^{-1}$ could be related to the C–O stretching mode [63,64,69,72]. However, it is difficult to clearly distinguish between carbonates adsorbed from the atmosphere exhibiting analogue vibration modes like deprotonated PAA molecules. For instance, Noei et al. showed by the fundamental analysis with infrared studies of ZnO single crystals that the adsorption of CO_2 leads to tridentate carbonate species at a maximum peak at 1581 cm^{-1} with two adjacent peaks at 1621 cm^{-1} and 1543 cm^{-1} [73]. Especially the nonpolar sidewalls with the orientation ZnO (10 $\bar{1}$ 0) are showing highly reactive properties regarding the adsorption of CO_2 [73]. Furthermore, the presented DRIFT spectra analysis shows that the adsorption of adsorbed species (carbonate contaminations and/or PAA) is reduced in the case of the ZnO NC films even in comparison to the solvent cleaned ones. This could be explained by the mentioned bonding mechanisms where the non-polar sidewalls are the preferred sites to have strong interactions, i.e. coordinative binding, of the carboxylate groups with the (more accessible) zinc atoms, while mainly electrostatic interactions and hydrogen bringing is occurring at polar facets of the ZnO hexagonal crystals. Additionally, nanostructured surfaces have a higher amount of adsorption positions for molecules. Furthermore, Gao, Teplyakov et al. showed the highly selective adsorption of carboxylate groups to sidewalls by studying the formation of bidentate carboxylate linkages to ZnO nanorods from propionic acid molecules adsorbed from the gas phase [74]. The trend of the OH-peak is also reasonable: in the case of the ZnO NR, the pores and gaps in between adjacent rods open the door for the increased adsorption of water molecules from the immersion bath during the PAA adsorption step which are probably partly embedded in the PAA films or adsorbed at the highly rough surface of the zinc oxide.

The (possible) adsorption of PAA on the SC, ZnO NC and ZnO NR surfaces is also investigated by means of XPS measurements by comparing the chemical surface composition before and after the PAA adsorption step. The quantitative analysis of the high-resolution spectra from the XPS measurements is summarized in Table 1.

The XPS data show the deposition of a dense layer of ZnO hexagonal crystals in all cases (compare Table 1). The total surface concentration of zinc in at.-% from the zinc $2p_{3/2}$ peak could be increased from around 7 at.-% (SC sample) to ~ 29 at.-% in the case of the ZnO NR. In addition to that, the Al 2p signal contribution, coming from the bare substrate, could not be detected at all in the case of the ZnO NC films. However, a very low surface concentration of Al remains barely distinguishable in

Table 1

Quantitative evaluation of the XPS data from high-resolution spectra of solvent cleaned (SC), ZnO nanorod (ZnO NR) film, ZnO nanocrystalline (ZnO NC) film and all three samples after immersion in 3.64 μM PAA for 10 min.

At.-% from HR-XPS	Solvent cleaned (SC)	SC/3.64 μM PAA	Nanocrystalline films (NC)	NC/3.64 μM PAA	Nanorod films (NR)	NR/3.64 μM PAA
C 1s	40.2	41.2	32.0	35.4	27.2	28.9
O 1s	36.6	35.4	40.5	37.9	41.7	40.7
Na 1s	–	0.6	–	0.4	–	0.4
Zn 2p _{3/2}	6.9	5.7	27.5	26.4	29.3	30.1
Al 2p	15.4	17.2	–	–	1.8	–
Ca 2p	0.9	–	–	–	–	–

the case of the ZnO NR. In this last case probably the gaps between the ZnO NR still allows to detect the pristine surface of the hot dipped galvanized steel underneath.

On top of that, the XPS results are in a good agreement with the DRIFTS. The minor differences registered in the at.-% of the C 1s peaks (shown in Fig. S2 and Table S1 in the SI) and the Na 1s peak (from neutralization of the polymeric acid with NaOH) before and after immersion in PAA could be assigned to the adsorption of the deprotonated acrylic acid polymer. But it is even possible that these little differences (<3.4 at.-%) in the C 1s could be attributed to minor differences in the amount of adsorbed species for impurities of the atmosphere mentioned for ZnO films analyzed by XPS (no sputtering was executed before the XPS measurements) [75–80]. The shape and peak positions of the C 1s peaks are similar before and after the immersion into PAA solution (compare Fig. S2 in the SI). Consequently, in our case it is not possible to distinguish between adventitious carbon covered zinc carbonate containing surfaces which is typical for crystalline ZnO films and particles [29,39,75–79] and PAA molecules from the immersion step [81,82] by XPS. For instance, Al-Kuhaili et al. mentioned on magnetron sputtered ZnO films a contamination of carbonates detected with XPS [76]. Adsorbed $-\text{CO}_3$, water and molecular oxygen were even found for ZnO films in the contribution published by Chen et al. [77].

In order to validate and identify the absorbance of PAA molecules, four types of samples were analyzed by ToF-SIMS, namely the solvent cleaned (SC) sample, SC samples after immersion into aqueous 3.64 μM PAA solution (pH 7, adjusted with NaOH), ZnO nanocrystalline (NC) films-coated samples and NC samples after immersion under similar conditions. The ZnO nanorod (NR) films-coated sample was not analyzed by ToF-SIMS due to the strong influence of the topography on the secondary ionization yield (i.e. matrix/topography effects) as it was shown by Seah [83]. ToF-SIMS results for the SC samples before and after the immersion into aqueous PAA solution are displayed in Fig. 4. The spectra show no significant differences at fragments with higher m/z .

In this context, López et al. have measured spin-casted PAA films on clean glass disks with ToF-SIMS [50]. The authors mentioned prominent peaks in the negative mode for PAA at m/z 111, 125, 143, and 171. Shi et al. have analyzed polymerized acrylic acid films on ZnO particles by ToF-SIMS [84]. The authors were able to detect differences at higher m/z values which were attributed to the dimers of acrylic acid like at position m/z 143 (acrylic acid dimer), m/z 185 acrylic acid dimer + C_2H_4 and m/z 199 acrylic acid dimer + C_4H_8 [84]. These peaks were not detected in all samples immersed into the aqueous PAA solution in the present case. Unlike the given literature for PAA films [50,83–86], no significant differences before and after the immersion into the PAA containing solution were obtained. It can be assumed that only a small portion of the PAA was attached to the surface and was fragmented by the bismuth primary ions leading to an intensive fragmentation during the analysis. Therefore, higher m/z were not detected.

In addition to the SC and ZnO NC sample before and after immersion into PAA solution, spray coated samples (i.e. “reference samples” with PAA) were analyzed via ToF-SIMS. All ToF-SIMS spectra for the SC and ZnO NC cases (before and after immersion into PAA solution and spray coated samples) are displayed in Fig. S3 and Fig. S4, respectively, in the Supporting Information. The results indicate that there are major

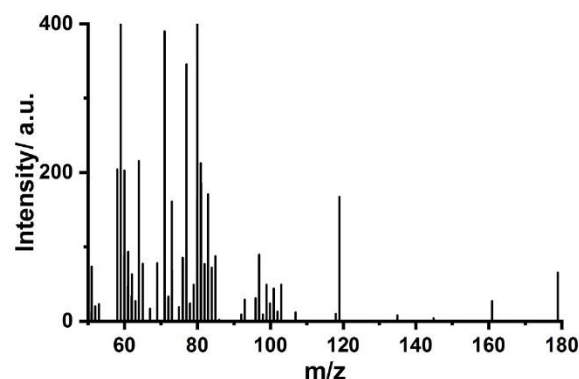
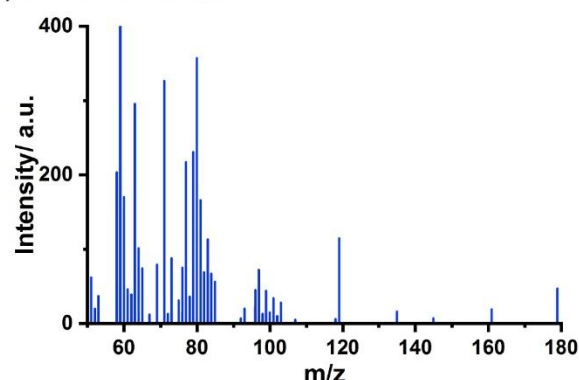
a) SC**b) SC+PAA immersed**

Fig. 4. ToF-SIMS spectra acquired in the negative mode of a) solvent cleaned substrate (SC), b) SC after immersion in aqueous 3.64 μM PAA solution (pH 7). Both spectra are given in the range from 50 m/z to 180 m/z for a better clearance in the regions of higher m/z .

differences between the spray coated samples and the immersed samples. Since the lower m/z values (< m/z 60) show minor differences, it is difficult to distinguish between the mentioned adsorbed species and contaminations such as carbonates or carboxylates with short chain lengths. Consequently, only the higher m/z values (> m/z 130) give a clear indication of PAA chains. Moreover, in the reference spectra mentioned before as the most useful one, reported by Alexander et al. [85], similar typical high fragments for PAA mentioned by López et al. [50], O'Toole et al. [86] and Alexander et al. [85] could be detected as well. Especially the higher dimer fragments were obtained as published by Shi et al. (m/z 143, m/z 185 and m/z 199) [84]. Finally, it can be concluded that no PAA was deposited after the immersion into water-based PAA solution (3.64 μM at pH 7) in the case of SC and ZnO NC films as observed by ToF-SIMS.

With regards to the adhesion promoting properties and the proof of no adsorption of PAA, a possible nanoetching of the adsorbed films of PAA is an advantage, since it would still allow for mechanical interlocking of ZnO NR, while it would avoid problems related to further PAA cohesive failure like shown by Meinderink et al. for thick electro-deposited PAA films on stainless steel [47]. The works of Ryu et al. [43] and of Han et al. [42] regarding nanoetching of ZnO NR by carboxylate groups could be the explanation for the adhesion enhancement after the immersion into the PAA containing solution. No significant differences in the morphology of the ZnO films could be observed in the FE-SEM images for the ZnO NC and ZnO NR after being exposed to the 3.64 μM PAA-based aqueous solutions when compared to the base substrates. The latter is in very good agreement with the data extracted from XPS measurements which indicated no major increases in the C/Zn ratio of the ZnO surfaces after modification with PAA. It is clear that this nanoetching effect must necessarily be less significant than, for instance, the nanoetching carried out by means of a thermochemical reaction applying high temperatures and higher concentrations [42,43]. For that reason, at this point, significant changes in the morphology are not clearly detectable via FE-SEM under the mentioned immersion parameters (3.64 μM PAA (250.000 g/mol) for 10 min at room temperature). However, the occurrence of a nanoetching/dissolution process due to PAA molecules was confirmed by FE-SEM with the images displayed in Fig. S5 in the SI registered at a higher immersion time of 60 min in a 0.085 mM PAA solution (pH 7 adjusted with NaOH) under similar experimental conditions to those used before. Blue arrows in Fig. S7 show some positions as examples of nanoetching/dissolution points which could be found especially at the nonpolar sidewalls in Figure S5 c)-f) for the ZnO nanostructured films.

Some conclusions could be drawn from the FE-SEM and XPS results: (i) these anisotropic ZnO nanostructures exhibit great stability, since no significant dissolution/pitting could be detected by FE-SEM (or significant alterations in the XPS spectra) after immersion for $t = 10$ min in the aqueous 3.64 μM PAA-containing solution, and (ii) the nanoetching effect of the as-obtained ZnO films are consequently nanometer sized (not clearly detectable in the FE-SEM images displayed in Fig. 6 and Fig. 7 after peel-test [after immersion in 3.64 μM PAA solution for 10 min]). Moreover, the high-resolution FE-SEM images displayed in Fig. S5 in the SI, registered after exposure to a more concentrated PAA solution, unveiled noticeable changes in the morphology of ZnO nanostructures. These can be summarized in a significant increase in the distance in between adjacent nanorods, together with the arising of defects and pinholes on the formerly smooth nonpolar sidewalls (blue arrows in the FE-SEM images displayed in Fig. S5). While the former increases the occurrence of mechanical interlocking, the latter would quantitatively raise the effective surface area of anchoring sites for a polymeric layer. These two effects combined, both of them resulting as a consequence of the described nanoetching process, are proposed to be responsible for the significant enhancement of the interfacial adhesion registered in the peel-off tests with the model epoxy-amine resin showed in Fig. 2. However, a compromise between the occurrence of these two related phenomena, i.e. the increase in the distance between adjacent nanorods and the occurrence of defects in the polar sidewalls, due to the nanoetching reaction induced by the strong interaction of PAA with Zn^{II} in the crystalline facets, and a massive dissolution of the unmodified as-prepared ZnO nanostructures (occurring for higher PAA concentrations) had to be achieved in order to reach the optimum bonding experimental conditions.

A similar nanoetching process mentioned by Han et al. [42] and Ryu et al. [43] can be proposed for the ZnO nanostructures in this work by considering the SMFS results of Valtiner et al. [45] and Meinderink et al. [29]. These works could demonstrate that the coordinative binding processes of deprotonated PAA chains occur especially at stepped single-crystals [45] and the nonpolar sidewalls of ZnO crystals [29]. We can then propose the following nanoetching mechanism, including the strong interaction between zinc atoms and the deprotonated carboxylic

acid groups, as displayed in Fig. 5.

The dashed lines in Fig. 5 between the carboxylate groups and the zinc atoms (Zn^{II}) which are more accessible in the nonpolar sidewalls caused by the stabilization mechanisms of the polar surface (0001)-planes via hydroxyl groups [29,87] are illustrating the strong adsorption and interaction between the Zn^{II} atoms at the surfaces of the ZnO crystals. After the rinsing step with ultra-pure water, the zinc-carboxylate complexes could be removed and the ZnO crystallites show dissolved edges, especially at the nonpolar sidewalls and crystal edges, as illustrated by blue arrows in Fig. S5 in the SI. This nanoetching effect probably leads to a higher surface coverage of anchoring sites for the used epoxy-amine resin, producing thus higher peel-off force values as shown in Fig. 2.

With the aim to confirm the proposed mechanism, a detailed analysis and identification of the failure mechanism in the detachment process have been carried out. The metallic substrates were measured with FE-SEM after the peel-tests. The corresponding FE-SEM images are illustrated in Fig. 6.

Here, the FE-SEM images detected by the InLens detector show mainly the same morphology registered before the peel-tests (see Fig. 2) for the cases of the SC + PAA and ZnO NC + PAA substrates. The SC samples (Fig. 6 a)-c)) show the presence of some randomly distributed patches from organic components (identified by blue arrows in the corresponding FE-SEM images). It is reasonable that some polymeric residues from the adhesive films could be left on the metallic parts. This could be assigned to an interfacial near breakage of the adhesive film caused by low interaction forces between the different materials (Zn/Al, adhesive). In comparison to that, the ZnO NC morphology is completely intact and the surface show no transfer of components such as organic molecules or defects/pinholes in the nanocrystalline film. In the case of the ZnO NR shown in Fig. 6g) and h), many more darker parts, indicative of the presence of organic molecule deposits, could be found. Additionally, it could be detected that some ZnO NR were detached from the metallic counterpart (Fig. 6 f)), which is further confirmed by measuring the peeled epoxy strips via FE-SEM. These images, displayed in Fig. 7d)-f), show that the interfacial failure is most likely occurring at the interphase Zinc/ZnO coating-steel in the cases of the ZnO NR and the ZnO NC films.

It is clear that the negative images of the topography of the ZnO substrates are visible in all the three cases (SC, ZnO NR and ZnO NC). However, some transfer of zinc oxide to the polymeric (epoxy) counterpart in the case of ZnO NC could be seen in Fig. 7d)-f), identified by blue arrows in the FE-SEM images. The interfacial breakage of the zinc coating from the steel substrate is barely taking place in this case. In comparison, the FE-SEM analysis of the samples without immersion into PAA containing water-based solution (displayed in Fig. S6 and Fig. S7 in the Supporting Information (SI)), i.e. ZnO NC without PAA, show no transfer of zinc. This indicates that the nanoetching with PAA molecules increases the adhesion between the ZnO NC and the adhesive in some defined positions. In the case of the ZnO NR with and without immersion step in PAA solution, see Fig. 6 g)/h) and Figure S6 g)-i), respectively, the transfer of organic components is increased when the PAA film is present (see blue arrows in the corresponding FE-SEM images in Fig. 6). According to that, it could be assumed that the intensity of the bonding process between the adhesive-nanoetched-ZnO NR is noticeably higher.

The characterizations of the chemical compositions of the surfaces of the peeled-off adhesive film strips by means XPS is provided in Table 2.

A high surface concentration of carbon and oxidized species (for example, ether groups and hydroxyl groups) can be found in all polymeric strips after the peel-tests identified by C 1s and O 1s from XPS survey spectra. According to the estimated chemical composition extracted from the bulk phase of the epoxy-amine resin (compare experimental part), an averaged concentration of around 2 at.-% of nitrogen has been detected. Indeed, this could be explained by the amine functionalities and the cross-linked polymer consisting of new C-N bonds from the polycondensation reaction at the curing step [57].

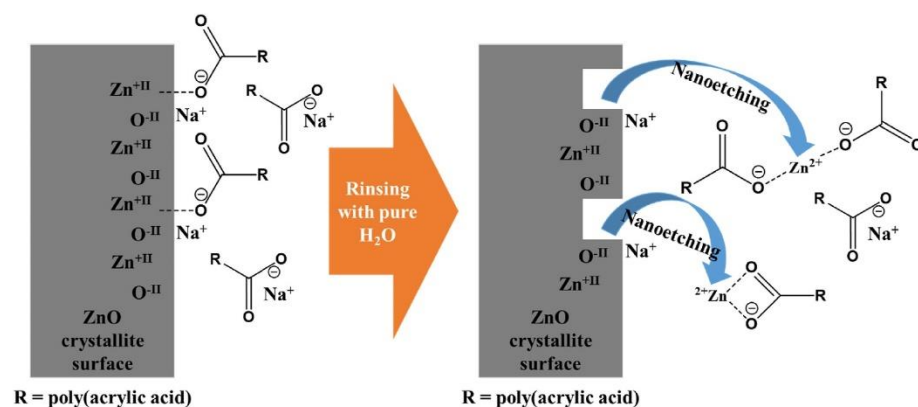


Fig. 5. Schematic summary of the possible nanoetching process. Left: ZnO crystallite immersed in an aqueous 3.64 μM PAA (250,000 g/mol) solution at pH 7 (adjusted with NaOH). Carboxylate groups of PAA could coordinately bind to the Zn atoms (Zn^{II}). Right: the rinsing with water leads to the removal of zinc carboxylate from the ZnO crystallites based on the strong interactions between the carboxylate groups and Zn^{II} and the high solubility of PAA in water (based on the publications from Ryu et al. [43] and Han et al. [42]).

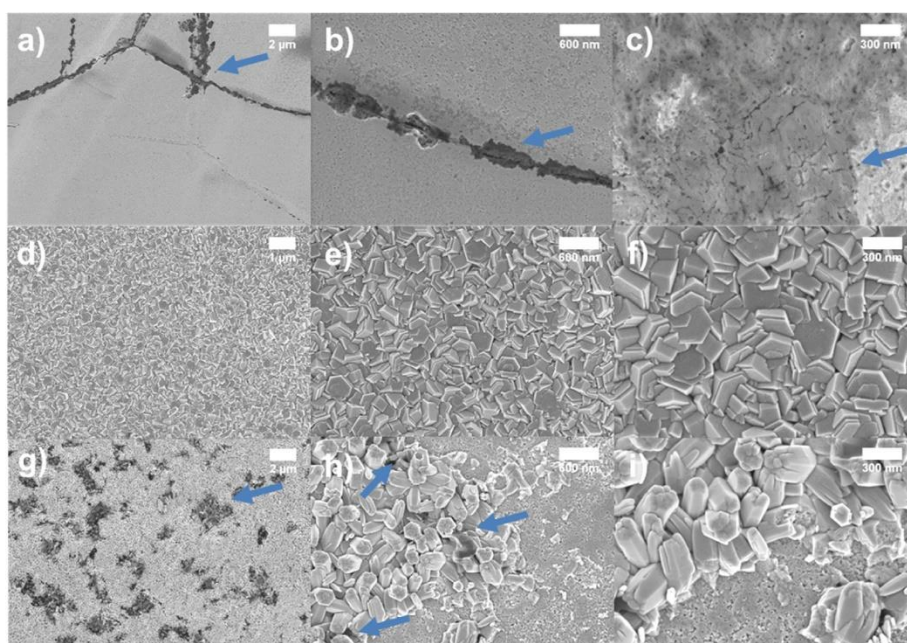


Fig. 6. FE-SEM images of the metallic substrates prior modified with 3.64 μM PAA solution for 10 min after peel-test measurements. The FE-SEM images show a)-c) SC sample, d)-f) ZnO NC and g)-i) ZnO NR all at three different magnifications. Blue arrows point to organic breaks. (For interpretation of the references to colour in this figure legend, the reader is referred to the Web version of this article.)

Furthermore, the XPS results after peel-tests support the FE-SEM images in Fig. 7, Fig. S6 and Fig. S7. The transfer of zinc could be detected in all measured polymer films after the peel-tests. Some metallic parts could be seen in the mentioned FE-SEM images, for example in Fig. 7 g-j for the case of the ZnO NR and in low concentrations in the case of ZnO NC (Fig. 7 j)). Interestingly, even in the case of the SC sample the transfer of zinc from the metallic part to the polymer film strip could be found by XPS, even when they could not be detected in the measured FE-SEM images. The overall transferred zinc amount in the case of the ZnO NC is much lower (0.2 at.-%) than in the case of the ZnO NR (0.8 at.-%) which can be translated into a higher mechanical and chemical adhesion in the interfacial zones as already explained before in the section of the peel-test results. The influence of the nanoetching with PAA as adhesion enhancing step between the ZnO and the epoxy-amine resin is also observable in the XPS data. Here, an increase of the total transferred zinc concentration to the polymeric film strips is indicating a highly

improved interaction between the ZnO as already shown by the peel-test results in Fig. 2 and the FE-SEM images in Fig. 7, Fig. S6 and Fig. S7. Moreover, in all cases of samples after the immersion step in aqueous PAA solution, a transfer of sodium from the metallic part to the polymeric counterpart can be found too (as can be deduced from the comparison with the XPS results after immersion step in aqueous PAA solution presented in Table 1). As already mentioned before, the sodium ions are originated in the step of the adjustment of the pH-value of the aqueous PAA solution (see experimental section). As expected, the sodium ions are adsorbed on the ZnO surfaces. Consequently, they could be accessible for the epoxy-amine molecules and be adsorbed/-transferred to the polymeric strips. In addition, a minor transfer of aluminum from the metallic parts of the SC sample without and with the immersion step in aqueous PAA solution could be identified by XPS which is indicating a strong interaction between the aluminum species of the HDG and the polymeric moieties. The results are in a good

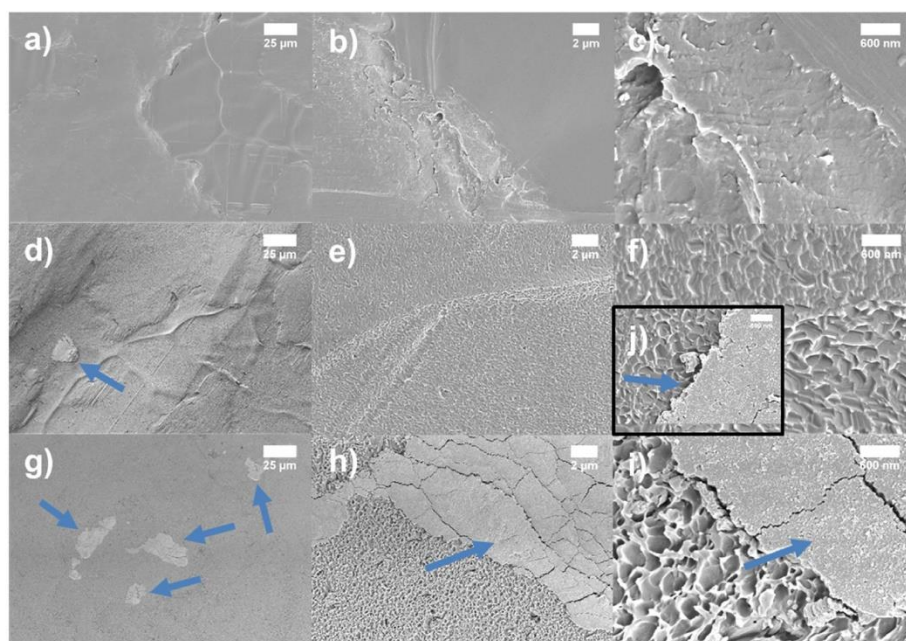


Fig. 7. FE-SEM images of the resin strips in contact with PAA-modified (with 3.64 μM PAA solution for 10 min) substrates after peel-test measurement. The FE-SEM images show a)-c) SC sample, d)-f) ZnO NC and g)-i) ZnO NR all at three different magnifications. Blue arrows point to transferred zinc oxide. (For interpretation of the references to colour in this figure legend, the reader is referred to the Web version of this article.)

Table 2

XPS analysis of the polymeric strips after the peel-test.

At.-% from surveys	Solvent cleaned (SC)	SC/ 3.64 μM PAA	Nanocrystalline films (NC)	NC/ 3.64 μM PAA	Nanorod films (NR)	NR/ 3.64 μM PAA
C 1s	78.5	76.7	78.8	77.2	77.8	75.7
O 1s	18.9	20.1	18.5	19.8	19.3	20.8
Na 1s	–	0.3	–	0.2	–	0.1
Zn 2p _{3/2}	0.1	0.5	0.2	0.5	0.8	1.5
Al 2p	0.2	0.3	–	–	–	–
Cl 2p	0.2	–	0.1	0.1	–	–
N 1s	2.1	2.1	2.4	2.2	2.1	1.9

agreement with the XPS results before the peel-tests in Table 1. Here, aluminum could already be detected in high amount from the surfaces of the SC samples and a minor Al concentration (1.8 at.-% - from Table 1) in the case of ZnO NR after the hydrothermal synthesis of the ZnO films.

4. Conclusions

The growth of well-defined hexagonal ZnO structures like ZnO nanorods (ZnO NR) and nanocrystalline ZnO (ZnO NC) films was carried out by means of a hydrothermal growth methodology, while the surface characterization was performed by FE-SEM and XPS. The peel-off forces registered for these ZnO-based surfaces versus a model adhesive, based on an epoxy-amine resin, showed a significant improvement in adhesion in comparison to the solvent-cleaned HDG substrate. The usage of a nanoetching step promoted by strongly interacting PAA molecules, in combination with the zinc oxide nanorod morphology, increased the peel-off force by a factor of around 9. Indeed, the immersion into an aqueous 3.64 mM PAA solution led, in all cases (solvent cleaned, ZnO NC and ZnO NR), to an increasing interfacial adhesion. The identification of deprotonated PAA chains was performed with DRIFT spectroscopy, XPS

and ToF-SIMS measurements. The infrared and XPS data showed typical peaks for carbonate groups and aliphatic hydrocarbon from adsorbed molecules from the atmosphere which is typical for zinc oxide surfaces [76,78] or the PAA molecules [81,82]. However, it is not possible to distinguish between adventitious carbon species on all samples with DRIFTS and XPS. Therefore, ToF-SIMS measurements on the SC and ZnO NC were carried out and compared with a PAA spray coated reference sample. Here, it could be unambiguously demonstrated that no irreversible PAA adsorption is taking place during the immersion step. FE-SEM images showed the nanoetching of ZnO nanostructures after the immersion into PAA containing water-based solution. This procedure slightly increased the distance between adjacent nanorods and increased the effective surface area of anchoring sites for the epoxy adhesive, resulting thus in the rise of the interfacial adhesion due to the promotion of mechanical interlocking and polymer-surface binding interaction, respectively. An interfacial failure of the zinc coating on the steel substrates of the ZnO NR/PAA and ZnO NC/PAA systems could be shown. This is supporting the strong interactions between the epoxy-amine resin and the ZnO NC and especially the ZnO NR with probably increased mechanical interlocking performed with previous nanoetching step with mostly deprotonated PAA molecules.

Acknowledgements

The authors would like to acknowledge the German Research Foundation (Deutsche Forschungsgemeinschaft, DFG) for the financial support (Project No. 320414069; GR 1709/22–1). Furthermore, we are thankful for the help of Nadine Buitkamp from the Department of Coating Materials & Polymers (University of Paderborn, Paderborn, Germany) for the FE-SEM and FIB measurements.

In addition, we also thank the Chemetall GmbH especially Stefan Birkenheuer for supplying the chemicals for the Gardocleaning and the hot dipped galvanized steel substrates.

Appendix A. Supplementary data

Supplementary data to this article can be found online at <https://doi.org/10.1016/j.ijadhadh.2021.102812>.

References

- [1] Kinloch AJ. Adhesion and adhesives: science and technology. Dordrecht: Springer Netherlands; 1987.
- [2] Xu S, Dillard DA, Dillard JG. Environmental aging effects on the durability of electrically conductive adhesive joints. *Int J Adhesion Adhes* 2003;23(3):235–50. [https://doi.org/10.1016/S0143-7496\(03\)00027-7](https://doi.org/10.1016/S0143-7496(03)00027-7).
- [3] Machado JJM, Marques EAS, da Silva LFM. Adhesives and adhesive joints under impact loadings: an overview. *J Adhes* 2018;94(6):421–52. <https://doi.org/10.1080/00218464.2017.1282349>.
- [4] Hornung M, Hajj M. Structural bonding for lightweight construction. *MS* 2009; 618–619:49–56. <https://doi.org/10.4028/www.scientific.net/MSF.618-619.49>.
- [5] Maeda S. Surface chemistry of galvanized steel sheets relevant to adhesion performance. *Prog Org Coating* 1996;28(4):227–38. [https://doi.org/10.1016/0300-9440\(95\)00610-9](https://doi.org/10.1016/0300-9440(95)00610-9).
- [6] Ellis B. Chemistry and technology of epoxy resins. Springer; 1993.
- [7] Knust S, Kuhlmann A, Arcos Tdl, Grundmeier G. Surface modification of ZnMgAl-coated steel by dielectric-barrier discharge plasma. *RSC Adv* 2019;9(60): 35077–88. <https://doi.org/10.1039/C9RA07378G>.
- [8] Brewis DM, Critchlow GW. Adhesion and surface analysis. *J Adhes* 1995;54(1–4): 175–99. <https://doi.org/10.1080/00218469508014390>.
- [9] Pletinckx S, Fockaert LLI, Mol JMC, Hauffman T, Terryn H. Probing the formation and degradation of chemical interactions from model molecule/metal oxide to buried polymer/metal oxide interfaces. *npj Mater Degrad* 2019;3(1):17. <https://doi.org/10.1038/s41529-019-0085-2>.
- [10] Calvez P, Bistac S, Brogly M, Richard J, Verchère D. Mechanisms of interfacial degradation of epoxy adhesive/galvanized steel assemblies: relevance to durability. *J Adhes* 2012;88(2):145–70. <https://doi.org/10.1080/00218464.2012.648067>.
- [11] Barthès-Labrousse MG. Adhesion mechanisms at amine-cured epoxy/aluminium interfaces. *J Adhes* 1996;57(1–4):65–75. <https://doi.org/10.1080/00218469608013644>.
- [12] Fitzpatrick MF, Watts JF. Adhesive bonding of hot-dipped galvanized steel: use of ToF-SIMS for forensic analysis of failed joints. *Surf Interface Anal* 1999;27(8): 705–15. [https://doi.org/10.1002/\(SICI\)1096-9918\(199908\)27:8<705::AID-SIA564>3.0.CO;2-Y](https://doi.org/10.1002/(SICI)1096-9918(199908)27:8<705::AID-SIA564>3.0.CO;2-Y).
- [13] Foister RT. Adhesive bonding to galvanized steel: II. Substrate chemistry, morphology and bond failure analysis. *J Adhes* 1987;24(2–4):279–313. <https://doi.org/10.1080/00218468708075433>.
- [14] Maeda S, Asai T, Fuj S, Nomura Y, Nomoto A. Mechanism of adhesion failure of epoxy-bonded galvanized steel sheets exposed to a wet atmosphere. *J Adhes Sci Technol* 1988;2(1):271–86. <https://doi.org/10.1163/156856188X00273>.
- [15] Aufray M, André Roche A. Epoxy-amine/metal interphases: influences from sharp needle-like crystal formation. *Int J Adhesion Adhes* 2007;27(5):387–93. <https://doi.org/10.1016/j.ijadhadh.2006.09.009>.
- [16] Gaillard F, Romand M, Verchère D, Hocquaux H. Zinc coated steel/epoxy adhesive systems: investigation of the interfacial zone by FTIR spectroscopy. *J Adhes* 1994; 46(1–4):227–41. <https://doi.org/10.1080/00218469408026662>.
- [17] González-Orive A, Giner I, los Arcos T de, Keller A, Grundmeier G. Analysis of polymer/oxide interfaces under ambient conditions – an experimental perspective. *Appl Surf Sci* 2018;442:581–94. <https://doi.org/10.1016/j.apsusc.2018.02.155>.
- [18] Özcan Ö, Grundmeier G, Schubach P. Method for coating metallic surfaces with nanocrystalline zinc oxide layers, aqueous compositions thereof and use of the surfaces coated in this way(WO2014/076105A3). Available from, <https://patentimages.storage.googleapis.com/c4/cb/34/03d5e796bc6242/WO2014076105A3.pdf>; 2014.
- [19] Lee S-Y, Umar A, Suh D-I, Park J-E, Hahn Y-B, Ahn J-Y, et al. The synthesis of ZnO nanowires and their subsequent use in high-current field-effect transistors formed by dielectrophoresis alignment. *Phys E Low-dimens Syst Nanostruct* 2008;40(4): 866–72. <https://doi.org/10.1016/j.physe.2007.10.094>.
- [20] Özcan O. Synthesis, characterisation and functionalisation of ZnO nanorods on metals. Ph.D. Dissertation. Bochum: Ruhr-University Bochum; 2011.
- [21] Trino LD, Dias LFG, Albano LGS, Bronze-Uhle ES, Rangel EC, Graeff CFO, et al. Zinc oxide surface functionalization and related effects on corrosion resistance of titanium implants. *Ceram Int* 2018;44(4):4000–8. <https://doi.org/10.1016/j.ceramint.2017.11.195>.
- [22] Jin X, Struelsen J, Heepe L, Kovalev A, Mishra YK, Adelung R, et al. Joining the unjoinable: adhesion between low surface energy polymers using tetrapodal ZnO linkers. *Adv Mater Weinheim* 2012;24(42):5676–80. <https://doi.org/10.1002/adma.201201780>.
- [23] Wang Z, Li HL. Highly ordered zinc oxide nanotubes synthesized within the anodic aluminum oxide template. *Appl Phys A* 2002;74(2):201–3. <https://doi.org/10.1007/s003390100856>.
- [24] Ait Ahmed N, Eyraud M, Hammache H, Vacandio F, Sam S, Gabouze N, et al. New insight into the mechanism of cathodic electrodeposition of zinc oxide thin films onto vitreous carbon. *Electrochim Acta* 2013;94:238–44. <https://doi.org/10.1016/j.electacta.2013.01.103>.
- [25] Engelkemier K, Lindner JKN, Bürger J, Vaupel K, Hartmann M, Tiemann M, et al. Nano-architectural complexity of zinc oxide nanowall hollow microspheres and their structural properties. *Nanotechnology* 2019;31(9):95701. <https://doi.org/10.1088/1361-6528/ab55bc>.
- [26] Jung M-H, Chu M-J. Synthesis of hexagonal ZnO nanodisks, nanosheets and nanowires by the ionic effect during the growth of hexagonal ZnO crystals. *J Mater Chem C* 2014;2(32):6675–82. <https://doi.org/10.1039/C4TC01132E>.
- [27] Sugunan A, Warad HC, Boman M, Dutta J. Zinc oxide nanowires in chemical bath on seeded substrates: role of hexamine. *J Sol Gel Sci Technol* 2006;39(1):49–56. <https://doi.org/10.1007/s10971-006-6969-y>.
- [28] Miao L, Ieda Y, Tanemura S, Cao YG, Tanemura M, Hayashi Y, et al. Synthesis, microstructure and photoluminescence of well-aligned ZnO nanorods on Si substrate. *Sci Technol Adv Mater* 2007;8(6):443–7. <https://doi.org/10.1016/j.stam.2007.02.012>.
- [29] Meinderink D, Orive AG, Ewertowski S, Giner I, Grundmeier G. Dependence of poly (acrylic acid) interfacial adhesion on the nanostructure of electrodeposited ZnO films. *ACS Appl. Nano Mater.* 2019;2(2):831–43. <https://doi.org/10.1021/acsnm.8b02091>.
- [30] Meagley KL, Garcia SP. Chemical control of crystal growth with multidentate carboxylate ligands: effect of ligand denticity on zinc oxide crystal shape. *Cryst Growth Des* 2012;12(2):707–13. <https://doi.org/10.1021/cg200992z>.
- [31] Liu H, Piret G, Sieber B, Laureys J, Roussel P, Xu W, et al. Electrochemical impedance spectroscopy of ZnO nanostructures. *Electrochim Commun* 2009;11(5): 945–9. <https://doi.org/10.1016/j.elecom.2009.02.019>.
- [32] Greene LE, Law M, Tan DH, Montano M, Goldberger J, Somorjai G, et al. General route to vertical ZnO nanowire arrays using textured ZnO seeds. *Nano Lett* 2005;5 (7):1231–6. <https://doi.org/10.1021/nl050788g>.
- [33] Vayssieres L. Growth of arrayed nanorods and nanowires of ZnO from aqueous solutions. *Adv Mater* 2003;15(5):464–6. <https://doi.org/10.1002/adma.200390108>.
- [34] Tena-Zaera R, Elias J, Lévy-Clément C, Mora-Seró I, Luo Y, Bisquert J. Electrodeposition and impedance spectroscopy characterization of ZnO nanowire arrays. *phys. stat. sol. (a)* 2008;205(10):2345–50. <https://doi.org/10.1002/pssa.200779426>.
- [35] Auld J, Houlton DJ, Jones AC, Rushworth SA, Malik MA, O'Brien P, et al. Growth of ZnO by MOCVD using alkylzinc alkoxides as single-source precursors. *J Mater Chem* 1994;4(8):1249. <https://doi.org/10.1039/jm9940401249>.
- [36] Özcan O, Pohl K, Ozkaya B, Grundmeier G. Molecular studies of adhesion and de-adhesion on ZnO nanorod film-covered metals. *J Adhes* 2013;89(2):128–39. <https://doi.org/10.1080/00218464.2012.731928>.
- [37] Garcia SP, Semancik S. Controlling the morphology of zinc oxide nanorods crystallized from aqueous solutions: the effect of crystal growth modifiers on aspect ratio. *Chem Mater* 2007;19(16):4016–22. <https://doi.org/10.1021/cm061977r>.
- [38] Elias J, Tena-Zaera R, Wang G-Y, Lévy-Clément C. Conversion of ZnO nanowires into nanotubes with tailored dimensions. *Chem Mater* 2008;20(21):6633–7. <https://doi.org/10.1021/cm801131t>.
- [39] Meinderink Dennis, Karlo J, Nolkemper R, Bürger Julius, Orive Alejandro G, Lindner Jörg KN, Guido Grundmeier. Spray coating of poly(acrylic acid)/ZnO tetrapod adhesion promoting nanocomposite films for polymer laminates. *Surf Coating Technol* 2019;375:112–22. <https://doi.org/10.1016/j.surfcoat.2019.06.083>.
- [40] Ehler GJ, Galan U, Sodano HA. Role of surface chemistry in adhesion between ZnO nanowires and carbon fibers in hybrid composites. *ACS Appl Mater Interfaces* 2013;5(3):635–45. <https://doi.org/10.1021/am302060v>.
- [41] Zhu X, Zhang Z, Men X, Yang J, Xu X. Fabrication of an intelligent superhydrophobic surface based on ZnO nanorod arrays with switchable adhesion property. *Appl Surf Sci* 2010;256(24):7619–22. <https://doi.org/10.1016/j.apsusc.2010.06.014>.
- [42] Han X-G, Jiang Y-Q, Xie S-F, Kuang Q, Zhou X, Cai D-P, et al. Control of the surface of ZnO nanostructures by selective wet-chemical etching. *J Phys Chem C* 2010;114 (22):10114–8. <https://doi.org/10.1021/jp101284p>.
- [43] Ryu SR, Ram SDG, Cho H-D, Lee DJ, Kang TW, Woo Y. Single ZnO nanocactus gas sensor formed by etching of ZnO nanorod. *Nanoscale* 2015;7(25):11115–22. <https://doi.org/10.1039/c5nr02387d>.
- [44] Pomorska A, Grundmeier G, Özcan O. Effect of Zn²⁺ concentration on the adsorption of organophosphonic acids on nanocrystalline ZnO surfaces. *Colloids and Interface Science Communications* 2014;2:11–4. <https://doi.org/10.1016/j.colcom.2014.08.004>.
- [45] Valtiner M, Grundmeier G. Single molecules as sensors for local molecular adhesion studies. *Langmuir* 2010;26(2):815–20. <https://doi.org/10.1021/la902232z>.
- [46] Kunze C, Valtiner M, Michels R, Huber K, Grundmeier G. Self-localization of polyacrylic acid molecules on polar ZnO(0001)-Zn surfaces. *Phys Chem Chem Phys* 2011;13(28):12959–67. <https://doi.org/10.1039/c1cp20913b>.
- [47] Meinderink D, Orive AG, Grundmeier G. Electrodeposition of poly(acrylic acid) on stainless steel with enhanced adhesion properties. *Surf Interface Anal* 2018;50(11): 1224–9. <https://doi.org/10.1002/sia.6440>.
- [48] Palacio MLB, Schriker SR, Bhushan B. Bioadhesion of various proteins on random, diblock and triblock copolymer surfaces and the effect of pH conditions. *J R Soc Interface* 2011;8(58):630–40. <https://doi.org/10.1098/rsif.2010.0557>.
- [49] Bauer A, Meinderink D, Giner I, Steger H, Weill, Johann, Grundmeier, Guido. Electropolymerization of acrylic acid on carbon fibers for improved epoxy/fiber adhesion. *Surf Coating Technol* 2017;321:128–35. <https://doi.org/10.1016/j.surfcoat.2017.04.039>.
- [50] López GP, Chilkoti A, Briggs D, Ratner BD. Substrate temperature effects on film chemistry in plasma deposition of organics. III. Analysis by static secondary ion mass spectrometry. *J Polym Sci A Polym Chem* 1992;30(11):2427–41. <https://doi.org/10.1002/pola.1992.080301117>.

- [51] Baruah S, Dutta J. Hydrothermal growth of ZnO nanostructures. *Sci Technol Adv Mater* 2009;10(1):13001. <https://doi.org/10.1088/1468-6996/10/1/013001>.
- [52] Skompska M, Zarębska K. Electrodeposition of ZnO nanorod arrays on transparent conducting substrates—a review. *Electrochim Acta* 2014;127:467–88. <https://doi.org/10.1016/j.electacta.2014.02.049>.
- [53] Bach RD, Andrés JL, Winter JE, Bernhard Schlegel H, Ball JC, Holubka JW. A model for adhesion-producing interactions of zinc oxide surfaces with alcohols, amines, and alkenes. *J Adhes Sci Technol* 1994;8(3):249–59. <https://doi.org/10.1163/156856194X01095>.
- [54] Ballerini G, Ogle K, Barthès-Labrousse M-G. The acid–base properties of the surface of native zinc oxide layers: an XPS study of adsorption of 1,2-diaminoethane. *Appl Surf Sci* 2007;253(16):6860–7. <https://doi.org/10.1016/j.apsusc.2007.01.126>.
- [55] Nazarov A, Thierry D, Volovitch P, Ogle K. An SKP and EIS investigation of amine adsorption on zinc oxide surfaces. *Surf Interface Anal* 2011;43(10):1286–98. <https://doi.org/10.1002/sia.3710>.
- [56] Gaillard F, Peilleux E, Romand M, Verchère D, Hocquaux H. Influence of surface treatments of hot-dip galvanized steels on their acid-base properties and on their reactions with some organic compounds. *Surf Interface Anal* 1995;23(5):307–12. <https://doi.org/10.1002/sia.740230506>.
- [57] Shechter L, Wynstra J, Kurkij RP. Glycidyl ether reactions with amines. *Ind Eng Chem* 1956;48(1):94–7. <https://doi.org/10.1021/ie50553a029>.
- [58] Blank WJ, He ZA, Picci M. Catalysis of the epoxy-carboxyl reaction. *J Coating Technol* 2002;74(926):33–41. <https://doi.org/10.1007/BF02720158>.
- [59] Allen RA, LeRoy WS. Curable epoxy-carboxylic acid adducts(US4119609A). 1978.
- [60] Fellers J. Kinetics of a polyacid-epoxy condensation reaction. *Macromolecules* 1970;3(2):202–6. <https://doi.org/10.1021/ma60014a016>.
- [61] Tillet G, Boutevin B, Ameduri B. Chemical reactions of polymer crosslinking and post-crosslinking at room and medium temperature. *Prog Polym Sci* 2011;36(2):191–217. <https://doi.org/10.1016/j.progpolymsci.2010.08.003>.
- [62] Dange C, Phan TNT, André V, Rieger J, Persello J, Foissy A. Adsorption mechanism and dispersion efficiency of three anionic additives [poly(acrylic acid), poly(styrene sulfonate) and HEDP] on zinc oxide. *J Colloid Interface Sci* 2007;315(1):107–15. <https://doi.org/10.1016/j.jcis.2007.03.068>.
- [63] Ricciardi S, Castagna R, Severino SM, Ferrante I, Frascella F, Celasco E, et al. Surface functionalization by poly-acrylic acid plasma-polymerized films for microarray DNA diagnostics. *Surf Coating Technol* 2012;207:389–99. <https://doi.org/10.1016/j.surfcoat.2012.07.026>.
- [64] Dong J, Ozaki Y, Nakashima K. Infrared, Raman, and near-infrared spectroscopic evidence for the coexistence of various hydrogen-bond forms in poly(acrylic acid). *Macromolecules* 1997;30(4):1111–7. <https://doi.org/10.1021/ma960693x>.
- [65] Chen S, Wu G, Liu Y, Long D. Preparation of poly(acrylic acid) grafted multiwalled carbon nanotubes by a two-step irradiation technique. *Macromolecules* 2006;39(1):330–4. <https://doi.org/10.1021/ma0520500>.
- [66] Hlaing Oo WM, McCluskey MD, Lalonde AD, Norton MG. Infrared spectroscopy of ZnO nanoparticles containing CO impurities. *Appl Phys Lett* 2005;86(7):73111. <https://doi.org/10.1063/1.1866511>.
- [67] Ying JY. Surface structure of nanocrystalline oxides. In: Hadjipanayis GC, Siegel RW, editors. *Nanophase materials: synthesis — properties — applications*. Dordrecht: Springer Netherlands; 1994. p. 197–204.
- [68] van den Brand J, Blajiev O, Beentjes PCJ, Terryn H, Wit JHW de. Interaction of anhydride and carboxylic acid compounds with aluminum oxide surfaces studied using infrared reflection absorption spectroscopy. *Langmuir* 2004;20(15):6308–17. <https://doi.org/10.1021/la0496845>.
- [69] Kirwan LJ, Fawell PD, van Bronswijk W. In situ FTIR-ATR examination of poly(acrylic acid) adsorbed onto hematite at low pH. *Langmuir* 2003;19(14):5802–7. <https://doi.org/10.1021/la027012d>.
- [70] Hung K-B, Li J, Fan Q, Chen Z-H. The enhancement of carbon fiber modified with electropolymer coating to the mechanical properties of epoxy resin composites. *Compos Appl Sci Manuf* 2008;39(7):1133–40. <https://doi.org/10.1016/j.compositesa.2008.04.004>.
- [71] Bechambi O, Touati A, Sayadi S, Najjar W. Effect of cerium doping on the textural, structural and optical properties of zinc oxide: role of cerium and hydrogen peroxide to enhance the photocatalytic degradation of endocrine disrupting compounds. *Mater Sci Semicond Process* 2015;39:807–16. <https://doi.org/10.1016/j.mssp.2015.05.052>.
- [72] Ward LJ, Schofield WCE, Badyal JPS, Goodwin AJ, Merlin PJ. Atmospheric pressure plasma deposition of structurally well-defined polyacrylic acid films. *Chem Mater* 2003;15(7):1466–9. <https://doi.org/10.1021/cm020289e>.
- [73] Noei H, Jin L, Qiu H, Xu M, Gao Y, Zhao J, et al. Vibrational spectroscopic studies on pure and metal-covered metal oxide surfaces. *Phys Status Solidi* 2013;250(6):1204–21. <https://doi.org/10.1002/pssb.201248534>.
- [74] Gao F, Aminane S, Bai S, Teplyakov AV. Chemical protection of material morphology: robust and gentle gas-phase surface functionalization of ZnO with propionic acid. *Chem Mater* 2017;29(9):4063–71. <https://doi.org/10.1021/acs.chemmater.7b00747>.
- [75] Al-Gaashani R, Radiman S, Daud AR, Tabet N, Al-Douri Y. XPS and optical studies of different morphologies of ZnO nanostructures prepared by microwave methods. *Ceram Int* 2013;39(3):2283–92. <https://doi.org/10.1016/j.ceramint.2012.08.075>.
- [76] Al-Kuhaili MF, Durrani SMA, Bakhtiari IA. Influence of oxygen flow rate on the surface chemistry and morphology of radio frequency (RF) magnetron sputtered zinc oxide thin films. *Surf Interface Anal* 2013;45(9):1353–7. <https://doi.org/10.1002/sia.5289>.
- [77] Chen M, Wang X, Yu YH, Pei ZL, Bai XD, Sun C, et al. X-ray photoelectron spectroscopy and auger electron spectroscopy studies of Al-doped ZnO films. *Appl Surf Sci* 2000;158(1):134–40. [https://doi.org/10.1016/S0169-4332\(99\)00601-7](https://doi.org/10.1016/S0169-4332(99)00601-7).
- [78] Cimino A, Minelli G, Angelis BA de. Investigation of the surface composition of MgO/ZnO solid solutions by X-ray photoelectron spectroscopy. *J Electron Spectrosc Relat Phenom* 1978;13(3):291–303. [https://doi.org/10.1016/0368-2048\(78\)85035-X](https://doi.org/10.1016/0368-2048(78)85035-X).
- [79] Lai L-W, Lee C-T. Investigation of optical and electrical properties of ZnO thin films. *Mater Chem Phys* 2008;110(2):393–6. <https://doi.org/10.1016/j.materchemphys.2008.02.029>.
- [80] Jeong SH, Kho S, Jung D, Lee SB, Boo J-H. Deposition of aluminum-doped zinc oxide films by RF magnetron sputtering and study of their surface characteristics. *Surf Coating Technol* 2003;174–175. [https://doi.org/10.1016/S0257-8972\(03\)00600-5](https://doi.org/10.1016/S0257-8972(03)00600-5).
- [81] Yan R, He W, Zhai T, Ma H. Anticorrosion organic–inorganic hybrid films constructed on iron substrates using self-assembled polyacrylic acid as a functional bottom layer. *Electrochim Acta* 2019;295:942–55. <https://doi.org/10.1016/j.electacta.2018.11.117>.
- [82] Dietrich PM, Hennig A, Holzweber M, Thiele T, Borcherdig H, Lippitz A, et al. Surface analytical study of poly(acrylic acid)-grafted microparticles (beads): characterization, chemical derivatization, and quantification of surface carboxyl groups. *J Phys Chem C* 2014;118(35):20393–404. <https://doi.org/10.1021/jp505519g>.
- [83] Seah MP. Topography effects and monatomic ion sputtering of undulating surfaces, particles and large nanoparticles: sputtering yields, effective sputter rates and topography evolution. *Surf Interface Anal* 2012;44(2):208–18. <https://doi.org/10.1002/sia.3798>.
- [84] Shi D, He P, Lian J, Wang L, van Ooij WJ. Plasma deposition and characterization of acrylic acid thin film on ZnO nanoparticles. *J Mater Res* 2002;17(10):2555–60. <https://doi.org/10.1557/JMR.2002.0371>.
- [85] Alex eMR, Duc TM. The chemistry of deposits formed from acrylic acid plasmas. *J Mater Chem* 1998;8(4):937–43. <https://doi.org/10.1039/a708064f>.
- [86] O'Toole L, Beck AJ, Short RD. Characterization of plasma polymers of acrylic acid and propanoic acid. *Macromolecules* 1996;29(15):5172–7. <https://doi.org/10.1021/ma9518417>.
- [87] Valtiner M, Borodin S, Grundmeier G. Stabilization and acidic dissolution mechanism of single-crystalline ZnO(0001) surfaces in electrolytes studied by in-situ AFM imaging and ex-situ LEED. *Langmuir* 2008;24(10):5350–8. <https://doi.org/10.1021/la7037697>.

Supporting Information

Effect of PAA induced surface etching on the adhesion properties of ZnO nanostructured films

D. Meinderink^a, C. Kielar^{a,b}, O. Sobol^c, L. Ruhm^a, F. Rieker^a, K. Nolkemper^a, A. G. Orive^a,
O. Ozcan^c, G. Grundmeier^{a*}

^a Technical and Macromolecular Chemistry, University of Paderborn, Warburgerstr. 100,
33098 Paderborn, Germany

^b Present address: Institute of Resource Ecology, Helmholtz-Zentrum Dresden-Rossendorf,
Bautzner Landstraße 400, 01328 Dresden, Germany

^c Present address: Bundesanstalt für Materialforschung und –prüfung (BAM), Unter den
Eichen 87, 12205 Berlin, Germany

*Corresponding author: Guido Grundmeier (e-mail: g.grundmeier@tc.uni-paderborn.de)

1 90°-Peel-Tests – detailed results

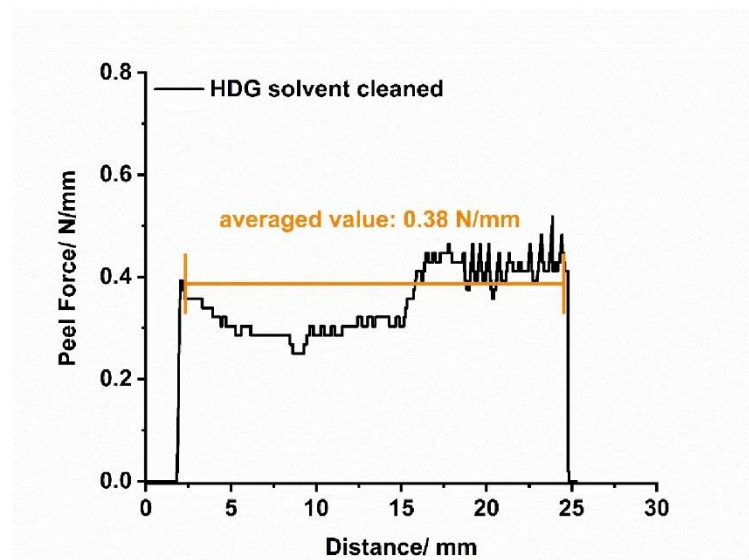


Figure S1. Example of the peel-force versus distance generate from the peel-test of one stripe from the solvent cleaned (SC) sample.

2 XPS results of SC, ZnO NR and ZnO NC films before and after immersion into PAA containing solution

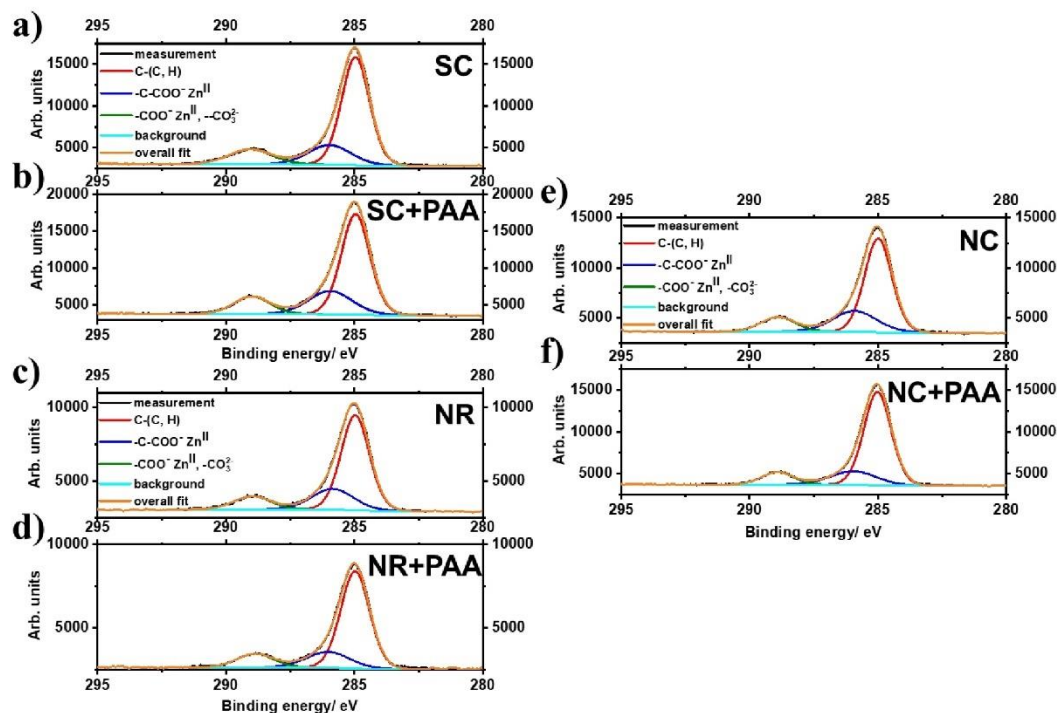


Figure S2. High-resolution C 1s spectra of a) SC, b) SC with PAA, c) ZnO NR, d) ZnO NR with PAA, e) ZnO NC and f) ZnO NC with PAA.

2

Table S1. Quantitative evaluation of the C 1s HR-XPS spectra of solvent cleaned (SC), ZnO nanorod (ZnO NR) film, ZnO nanocrystalline (ZnO NC) film and all three samples after immersion in 3.64 μ M PAA for 10 min.

Total at.-% from C 1s HR-spectra	Solvent cleaned	SC/ 3.64 μM PAA	Nanocrystalline films (NC)	NC/ 3.64 μM PAA	Nanorod films (NR)	NR/ 3.64 μM PAA
C-C, C-H	26.8	26.1	20.4	25.1	18.1	20.2
C-O	7.5	9.2	7.5	6.3	5.9	5.0
C=O	5.9	5.9	4.1	4.0	3.2	3.7
Sum	40.2	41.2	32.0	35.4	27.2	28.9

3 Additional ToF-SIMS results of SC and ZnO NC films before and after immersion into aqueous 3.64 μM PAA

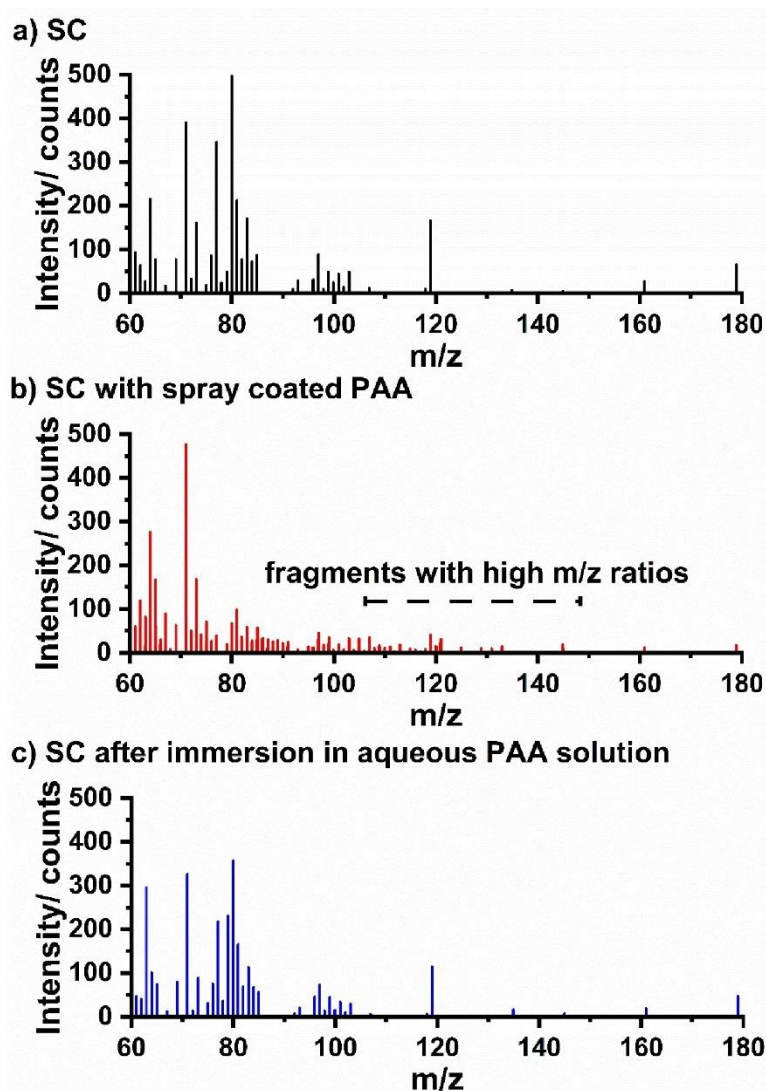


Figure S3. Negative ToF-SIMS spectra of a) solvent cleaned sample (SC), b) SC with spray coated PAA and c) SC after immersion in aqueous 3.64 μM PAA solution (pH 7) for 10 min.

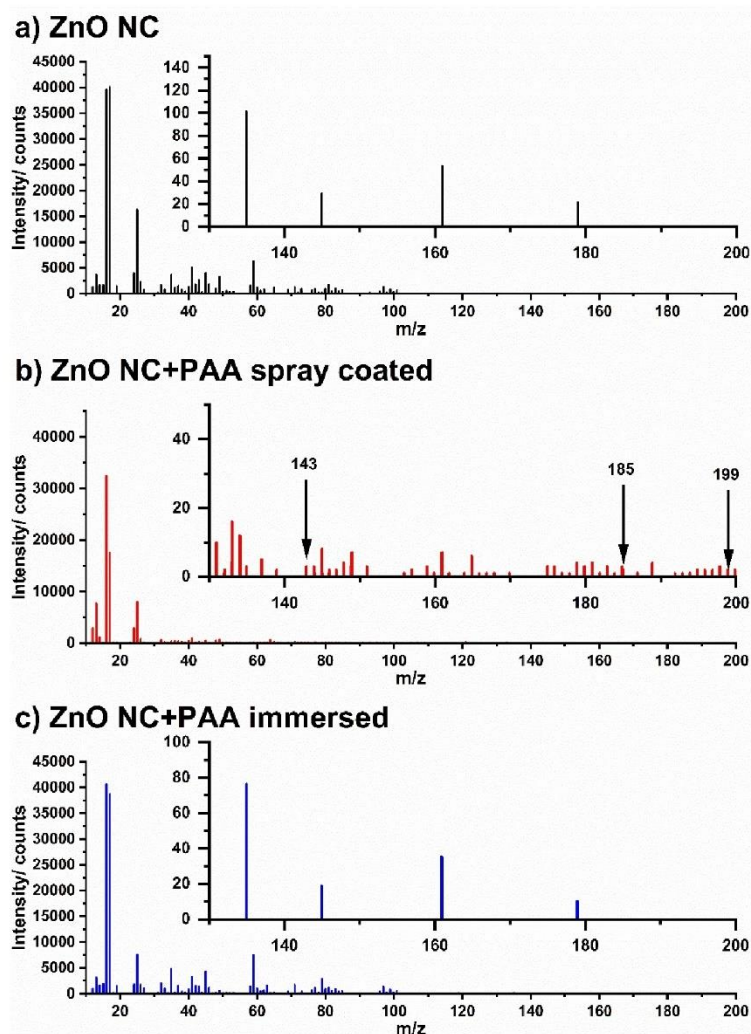


Figure S4. Negative ToF-SIMS spectra of a) nanocrystalline ZnO films (NC), b) NC with spray coated PAA and c) NC after immersion in aqueous 3.64 μM PAA solution (pH 7) for 10 min.

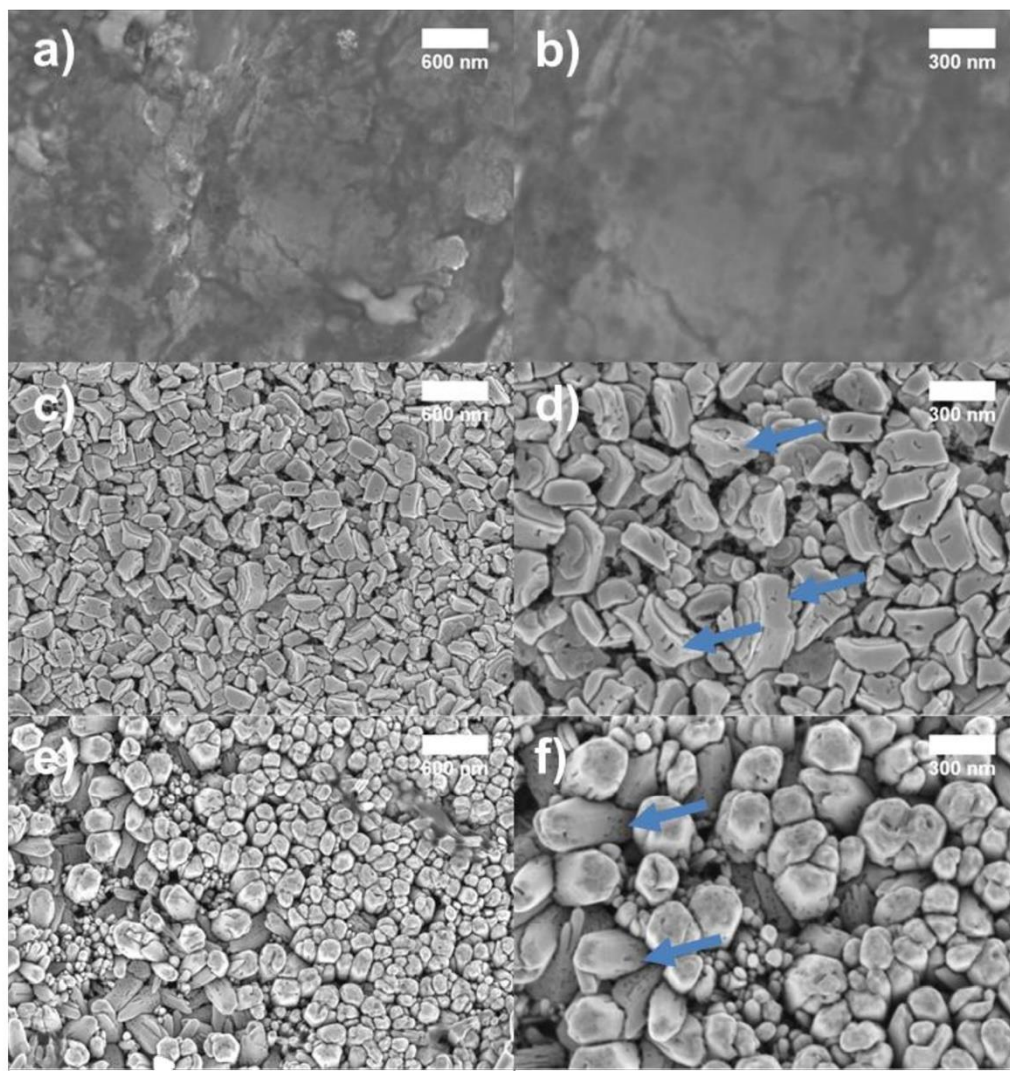


Figure S5. FE-SEM images of all samples after immersion in aqueous 0.085 mM PAA (250.000 g/mol) solution for 60 min. The FE-SEM images show a)-b) SC sample, c)-d) ZnO NC and e)-f) ZnO NR all at two different magnifications.

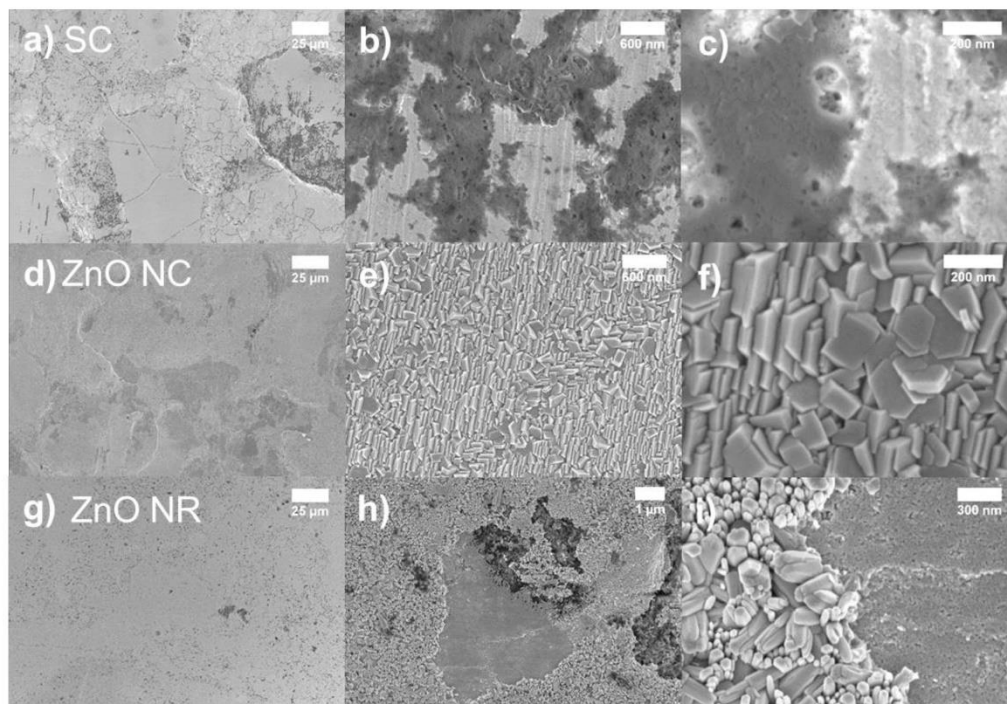


Figure S6. FE-SEM images of the metallic substrates without immersion in aqueous PAA solution after peel-tests. The FE-SEM images show a)-c) SC sample, d)-f) ZnO NC and g)-i) ZnO NR all at three different magnifications.

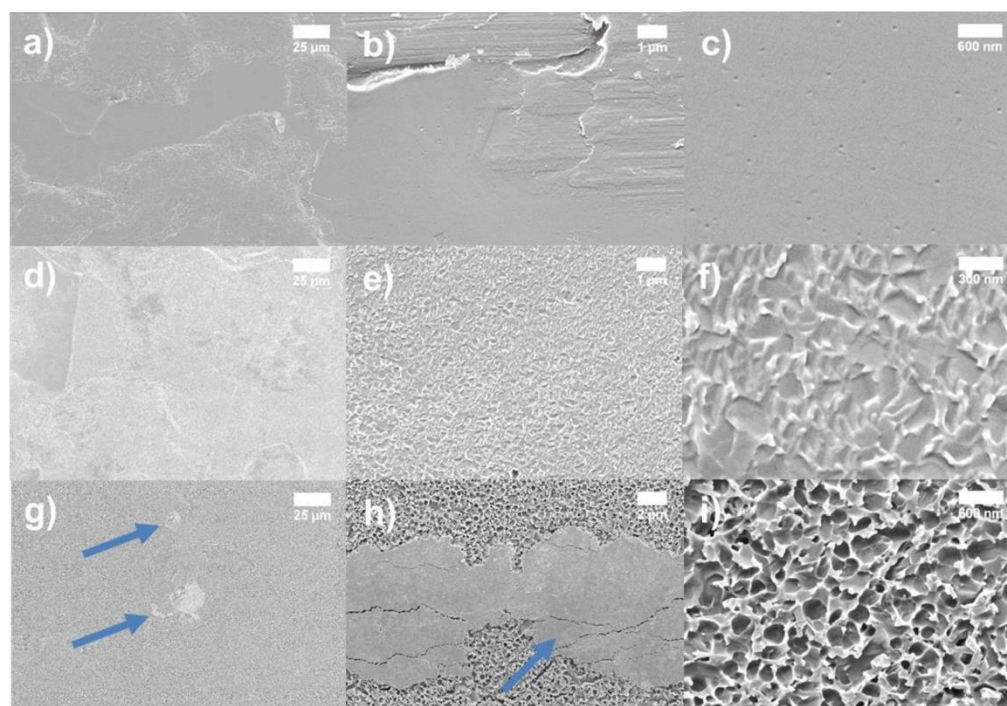


Figure S7. FE-SEM images of the polymeric parts without immersion in aqueous PAA solution after peel-tests. The FE-SEM images show a)-c) SC sample, d)-f) ZnO NC and g)-i) ZnO NR all at three different magnifications.

7

3.3 Electrodeposition of poly(acrylic acid) on stainless steel with enhanced adhesion properties

The following publication (**3. publication** of this PhD thesis) from D. Meinderink, A. G. Orive, G. Grundmeier was reused from “*Surface and Interface Analysis*”, Volume 50, pages 1224-1229 (Copyright Wiley & Sons, Ltd. 2018) with permission from Wiley & Sons, Ltd. (License Numbers 4731840123016, 4987720158233).

<https://doi.org/10.1002/sia.6440>

The deposition of polymers on metal oxide surfaces like technically relevant iron and iron-based alloys is a key application in surface treatments for corrosion protection and adhesion promoting. Thus, the modification of stainless steel with adhesion promoting polymers such as poly(acrylic acid) steel indicated by SMFS in the **1. publication** is an interesting and necessary investment for long-term stable joining in automotive and aerospace business. In the work below, an investigation of the adhesion promoting properties of poly(acrylic acid) dependent on the deposition time of the electrochemically initiated polymerization of acrylic acid was performed. The obtained results led to the prediction of an interfacial failure in the PAA layer influenced by the layer thickness and opened the door for the application of PAA coatings as adhesion promoting thin films for joining. The input of the total work corresponding to the different Co-authors is summarized in the following Table 4.

Table 4. Summary of the author contributions involved in the publication “*Electrodeposition of poly(acrylic acid) on stainless steel with enhanced adhesion properties*”.

author contributions	involved persons
validation, writing, coordination, investigation, conceptualization, original draft, visualization, sample preparation, experimental executions, evaluations, data curation, formal analysis, scientific discussion, review & editing	D.M
AFM measurements including evaluations, scientific discussion, support, mentoring, interpretation of data revisions of the manuscript, review & editing	A.G.O.
project administration, funding acquisition, resources, conceptualization, scientific discussion, supervision, mentoring, interpretation of data, revisions of the manuscript, review & editing	G.G.

Electrodeposition of poly(acrylic acid) on stainless steel with enhanced adhesion properties

D. Meinderink  | A. G. Orive | G. Grundmeier

Department of Technical and Macromolecular Chemistry, University of Paderborn, Warburger Str. 100, 33098 Paderborn, Germany

Correspondence

Grundmeier G., Department of Technical and Macromolecular Chemistry, University of Paderborn, Warburger Str. 100, 33098 Paderborn, Germany.
Email: guido.grundmeier@uni-paderborn.de

Funding information

German Research Foundation, Grant/Award Number: GR 1709/22-1

A facile electrochemical methodology to prepare poly(acrylic acid) (PAA) thin films in mildly acid aqueous solutions onto stainless steel is presented. Together with the PAA, the codeposition of Zn species is observed. The latter can be further removed by rinsing with dilute HCl aqueous solutions. These PAA-modified steel samples have been characterized by infrared reflection absorption spectroscopy and atomic force microscopy and exhibit good adhesion-promoting capabilities.

1 | INTRODUCTION

The modification of surfaces with polymer films has been reported to have promising applications in areas such as corrosion protection, adhesion promoting, and nanocomposite bioadhesion.¹ Permanently adhering organic coatings onto inorganic surfaces is long-last challenging.² Many strategies such plasma coating technologies, polymer grafting, and polymer adsorption have been developed.³ Among the high research activity in the area of surface modification, electrografting technique is a powerful coating method which has received comparatively little attention.⁴ This approach leads to the formation of a covalent bond between the surface and the polymer. However, promising results were obtained only in limited conditions, ie, water and air-free solutions, highly potentials, and pure monomers. Therefore, the introduction of an electrochemical initiator allows working in milder environments opening thus the door to a wide range of demanding technological applications.⁵

Iron and iron-based alloys are most widely used in the industry. Prior to its application, they need to be modified by organic coatings to improve their adhesion properties and to reduce their corrosion attack.^{6,7} Consequently, acrylic polymer derivatives have gained much attention as adhesion promoter and corrosion inhibitors of engineering metal.⁸ The coating polymer act as a bridge between engineering metals end resins, where the bonding formation between the —COOH functionality and epoxy resin groups enhances the strength stability of the metal/polymer interface. The molecular adsorption of the carboxylic moiety onto the metal surface inhibits the metal dissolution

forming a compact barrier film.⁹ The control of the polymer architecture plays a key role on the tuning of the final polymer properties.¹⁰

Electropolymerization of acrylic acid (AA) results a promising alternative for coating iron-based alloys with improved properties regarding the adhesion strength and the development of a barrier film. Over the plasma treatment, electropolymerization has the advantage to allow the precise control of the chemical composition of the polymer film. A high adhesion between metal and polymer occurs because the monomers wet the metal surface easily than polymers do and can thus induce polymerization within the edges and corners. Because the difficulty to reduce/oxidize the AA monomer itself in aqueous solutions, water-based catalysts were introduced to facilitate the polymerization reaction. In this sense, persulfate salts and zinc ions have been used as electroinitiators for these reactions.^{5,11} The polymerization reaction is driven by the reduction of the electroinitiator at the surface, and then, the electron excess is transferred to an acrylic monomer.¹¹ This kind of electroinitiator requires that the monomer is situated in the vicinity of the metal/electrolyte interface initiating the electropolymerization.¹¹

To provide a good control of the polymer growth, a simple electrochemical deposition process is applied within this paper. The electropolymerization of AA on stainless steel is performed by cathodic deposition at pH 6 from an aqueous solution containing Zn²⁺ ions as electroinitiators and bisacrylamide as cross-linker.¹² This process leads to reproducible deposition of thin films the coating of steel surfaces in a controlled way with improved properties regarding the adhesion strength as adhesion promoting interfacial layers.

2 | EXPERIMENTAL

2.1 | Materials and chemicals

Polished stainless steel substrates (ASIS 316L, Goodfellow GmbH) of 3.0×4.5 cm size for all experiments were used as working materials. To remove all organic contaminations, 3 successive cleaning steps with tetrahydrofurane, isopropyl alcohol, and ethanol for 15 minutes of each solvent in an ultrasonic bath were carried out. Afterwards, the substrates were dried in a nitrogen stream.

The chemicals and solvents used in this work were of p.a. grade quality. Deionized water for the electrolyte preparation ($0.055 \mu\text{S cm}^{-1}$, Ultra Clear TWF, SG water, Hamburg, Germany) was used.

2.2 | Electrochemical deposition and cleaning steps

A typical 3-electrode setup with a potassium chloride saturated silver/silver chloride as reference electrode, the stainless steel substrates as working electrode (6.0 cm^2 front side, backside was taped), and a closely coiled platinum wire (219.9 cm^2) in a lugging filled with an aqueous $0.025 \text{ M H}_2\text{SO}_4$ solution, was used. The 75 mL water-based electrolyte for each deposition experiment consisted of 2.0 M acrylic acid (monomer) with methoxyphenone (inhibitor) (Sigma-Aldrich), 0.2 M zinc chloride (initiator) (Merck KGaA), and 0.04 M N,N' -methylenebisacrylamide (cross-linker) (Sigma-Aldrich). The pH of the resulting solution is raised to 6.0 by adding solid NaOH. Before every deposition, the electrolyte was purged with nitrogen for 15 minutes to create oxygen-free conditions. Otherwise, the reaction will be stopped as a consequence of the biradical character of oxygen because it reacts with the radical AA breaking off the electropolymerization. The atmosphere was purged during the reaction time.

A potentiostat Reference 600™ (Gamry Instruments) was used to reach a constant potential of -1.15 V vs Ag/AgCl. In this regard, chronocoulometry measurements were performed to apply a well-defined bias voltage at the working electrode for 75, 100, 150, 225, and 300 seconds at room temperature.

After the electrodeposition, samples were cleaned for 4 minutes in 100 mL of pure water and analyzed with Fourier transformed infrared reflection absorption spectroscopy (FT-IRRAS) and atomic force microscopy (AFM). To remove all zinc species embedded in the polymer, the modified stainless steel substrates were dipped in 100 mL of an aqueous 0.1 M HCl solution for 4 minutes. This step was followed by the characterization with PM-IRRAS and AFM measurements.

2.3 | Analytical methods

2.3.1 | Characterization with IRRAS

To identify and characterize the chemical composition of the deposited poly(acrylic acid) films after rinsing with water, FT-IRRAS was performed with an FT-IR microscope of type Hyperion 1000 connected to a Vertex 70 spectrometer (both Bruker Optics, Germany). The thin poly(acrylic acid) (PAA) films after the rinsing step with 0.1 M HCl were analyzed with PM-IRRAS using a Vertex 70 (Bruker Optics, Germany) and a ZnSe photoelastic modulator for the p-polarization (Bruker,

Germany). LN-MCT detectors were used in both measurement devices. Five hundred twelve scans per spectrum were detected, and a gold mirror was measured as the reference in the case of FT-IRRAS. The resolutions were 4 cm^{-1} .

2.3.2 | AFM

Atomic force microscopy imaging was carried out using a MFP-3D-SA (Asylum Research) equipped with an antivibration table and an acoustic enclosure in intermittent contact mode operating in ambient air conditions at a scan rate of 0.5 to 1.2 Hz. To this end, HQ:NSC15/AIBS (325 kHz and 40 N m^{-1} , nominal radius of 8 nm) and HQ:NSC18/AIBS tips (75 kHz and 2.8 N m^{-1} , nominal radius of 8 nm), purchased from Mikromasch, were used. Root mean square (RMS) roughness measurements, R_q , from at least $3 \times 10 \times 10 \mu\text{m}^2$ AFM images taken from different but equivalent sample areas for every deposition time have been collected and averaged.

2.3.3 | Application of a model adhesive and peel test experiments

A 2-component epoxy amine adhesive consists of 11.19 g epoxy resin (D.E.R. 331, DOW Chemicals, Midland/USA) and 6.78 g of the amine (poly(propylene glycol)bis(2-aminopropyl ether), Sigma-Aldrich). After mixing the 2 components, the polymer mix was degassed in vacuum ($<1.0 \times 10^{-2} \text{ mbar}$) for 1 hour. To remove all bubbles, the mixture was treated in ultrasonic bath for 15 minutes followed by another hour in vacuum for additional degassing. The poly(acrylic acid)-coated samples and untreated stainless steel samples taken as references were covered with 6 commercial adhesive tapes of around $300\text{-}\mu\text{m}$ thickness to create well-defined spacers for the application of the epoxy amine mix between the tapes. The coating step was carried out in a dry nitrogen atmosphere ($7.0\% \pm 2.0\% \text{ r.h.}$) at $19^\circ\text{C} \pm 1^\circ\text{C}$. The samples were put on Polytetrafluoroethylene blocks coated with aluminum foil and fixed with a constant pressure with clamps. This was followed by the hardening step at 120°C for 75 minutes in the oven. Then, the samples were subsequently exposed for 72 hours at 40°C to humid air ($>95\% \text{ RH}$). The free-standing model adhesive films were cut into stripes, and the 90° pull-off forces (force gauge of type Model ZP-5, Imada) were recorded from each stripe. To maintain the peel-off angle, a motorized peel tester (MV-220 Motorized Test Stand, Imada) with a constant haul-off speed of 1 mm second^{-1} was used.

3 | RESULTS AND DISCUSSION

3.1 | Synthesis of PAA films on stainless steel

Figure 1A shows the chronocoulometric curves obtained for the different deposition times. The charge density exhibits a characteristic linear behavior indicating a constant polymerization rate. The registered charge density results from the reduction of the initiator onto the stainless steel surface. It has been stated that the electropolymerization of AA implies the formation in solution of a complex Zn^{2+} -acrylate.⁵ A cathodic potential of -1.15 V vs Ag/AgCl was set for the reduction of Zn^{2+} to Zn^0 because this value exhibited

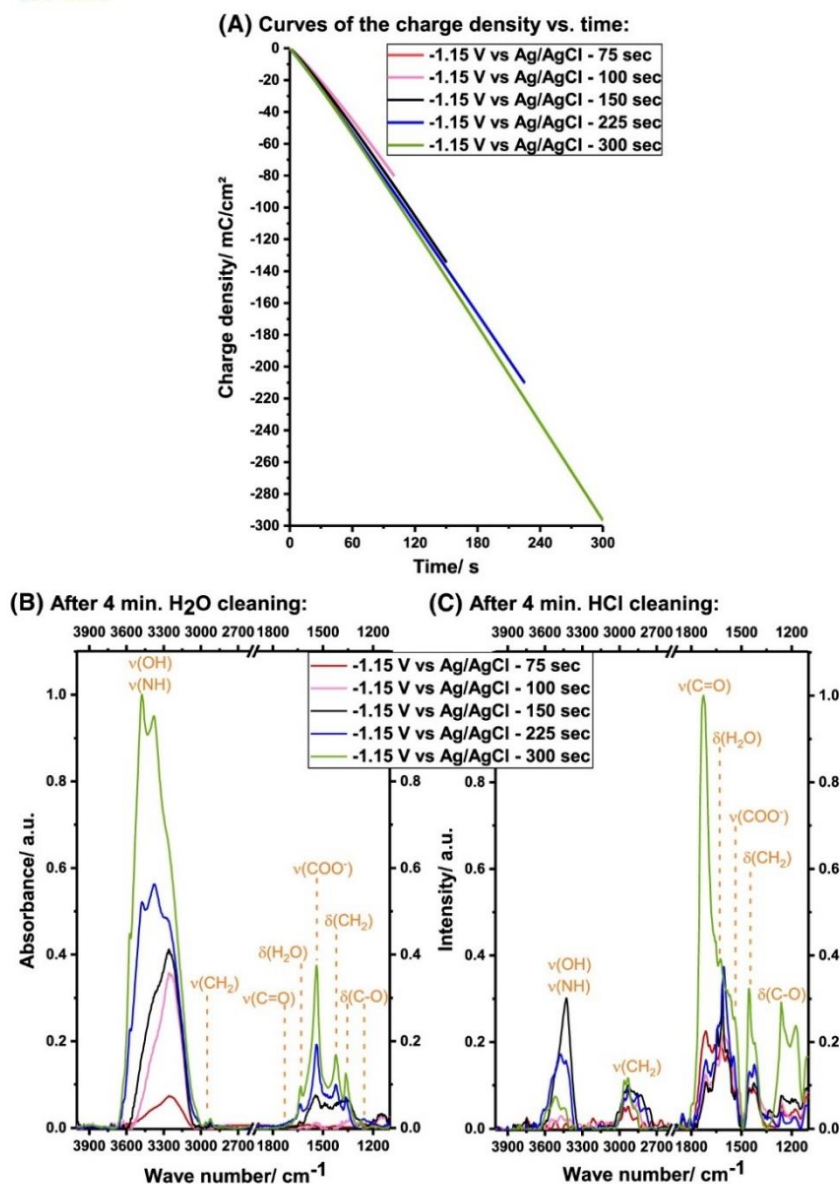


FIGURE 1 (A) Charge density curves vs time registered for stainless steel substrates for different deposition times. (B) FT-IRRAS spectra of different PAA films on polished stainless steel electrodeposited at -1.15 V (vs Ag/AgCl) for deposition times after cleaning in pure water. (C) Subsequent cleaning in 0.1 M aqueous HCl

the best performance within a complete set of previous experiences. Briefly, more positive values produced negligible reduction of Zn^{2+} to Zn^0 , being the essential step for initiating the PAA deposition. Consequently, no trace of AA polymerization was detected either by AFM or FT-IRRAS. On the other hand, getting into more negative values gave rise to massive Zn deposition (difficult to completely dissolve by rinsing in 0.1 M HCl or by applying positive potentials) together with certain degree of overlapping with the hydrogen evolution reaction. These facts have been frequently related to the formation of cracks and porous and highly defective PAA films, which could have a negative impact on the adhesion properties of the as-prepared polymer. In this context, Katz et al reported analog potential deposition values for a similar pH window range and electrolyte composition.⁵ In any case,

at this cathodic potential, the Zn^{2+} complexed ions are reduced on the stainless steel surface, and subsequently, some electrons are transferred to the vinyl monomers, generating a radical and starting thus the polymerization reaction. In parallel, the reduction of Zn^{2+} ions also takes place giving rise to Zn-based deposits embedded into the polymer.^{12,13} The mechanism for which the electrons are transferred to the vinyl monomers is not well understood but tentatively proposed in literature.^{8,11}

Figure 1B shows the FT-IRRAS spectra of the corresponding stainless steel samples after the different deposition times and after the cleaning with pure water for 4 minutes and Figure 1C after the cleaning with aqueous 0.1 M HCl for 4 minutes. The spectra were normalized to the most intense peak. Typical characteristic bands

arising from the electrodeposited PAA films are observed. The broad band between 3600 and 3000 cm^{-1} is attributed to the hydroxide stretching mode and the —NH stretching mode, whereas the peaks located between 3000 and 2800 cm^{-1} are attributed to the stretching mode of the C—H hydrocarbon bone.³ The peak located at 1740 and 1720 cm^{-1} is associated to the carbonyl group.¹⁴ The peak at 1540 cm^{-1} is attributed to the presence of carboxylate groups which are created by the reaction with zinc species and other metallic cations.¹⁴ The peaks at 1457 , 1420 , and 1250 cm^{-1} are associated to the deformation band of the polymer backbone and stretching modes of the C—O bond, respectively.¹⁵ The trend of the increasing of the

characteristic vibration modes like the —OH peaks and the $\text{—COO}^-/\text{C=O}$ peaks in dependence on the deposition time is in a good agreement with the literature.¹¹ It could be shown that the deposition time has to be higher than around 150 seconds to show a linear polymer growth.¹¹

In the absence of Zn^{2+} , after rinsing in diluted HCl , only the bands resulting from the organic part are observed (Figure 1C). Consequently, those peaks attributed to the $\text{—COO}^- \text{—Zn}^{2+}$ species are significantly decreased. All intensities are lower after the second cleaning step which is a direct consequence of the good solubility of poly(acrylic acid) in the water.

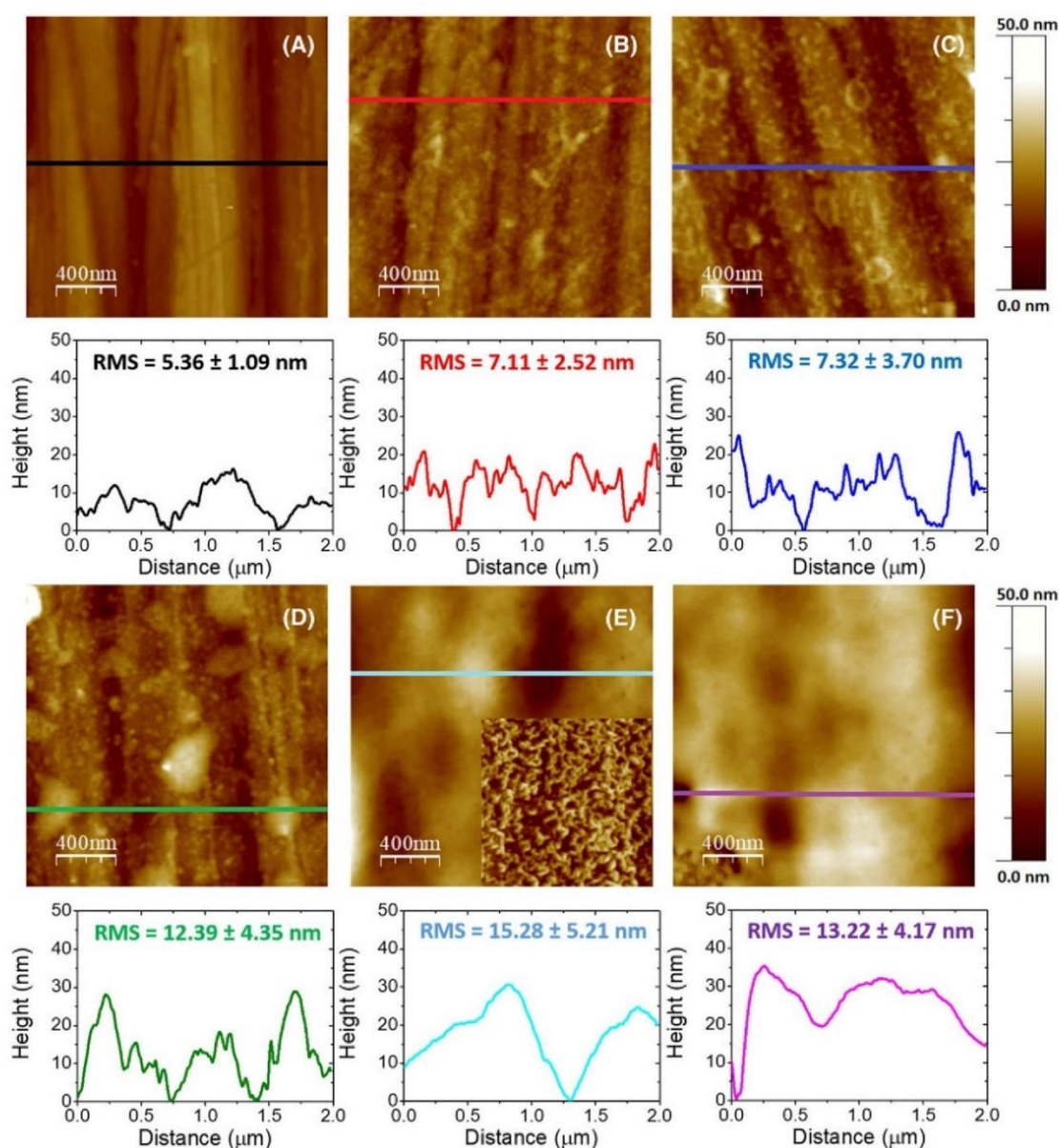


FIGURE 2 AFM images ($2.0 \times 2.0\text{ }\mu\text{m}^2$) registered for the stainless steel substrate before (A) and after the electrochemical modification with ZnO/PAA for 75 seconds (B), 100 seconds (C), 150 seconds (D), 225 seconds (E), and 300 seconds (F), after rinsing with 0.01 M HCl , upper panels. Representative cross-sectional profiles showing the dimensions of the corresponding PAA deposits and RMS roughness values are depicted in the lower panels. The inset in Figure 2E ($10 \times 10\text{ }\mu\text{m}^2$) shows the presence of Zn/ZnO particles before rinsing in 0.1 M HCl

3.2 | AFM

Atomic force microscopy measurements were carried out to characterize the topography of the stainless steel samples before and after applying a pulse of -1.15 V (vs Ag/AgCl) in the Zn^{2+} /AA containing solution for growing deposition times and subsequent cleaning in a dilute HCl aqueous solution. Thus, Figure 2A shows the characteristic topographic features of a bare stainless steel where parallel polishing lines and scratches can be distinguished.

Atomic force microscopy images show for lower deposition times the formation of a PAA-based granular electrodeposit consisting of small particles, ie, 3 to 8 nm high and 18 to 35 nm wide (after correction by the tip convolution), which gradually covers the steel substrate; see Figure 2A to C. Accordingly, the RMS roughness increased from 5.4 nm (bare steel) to 7.3 nm. Then, these grain particles start to aggregate progressively giving rise to the growth of PAA pancake-like structures as can be observed in Figure 2C, D, around 7 to 10 nm high. From $t = 150$ seconds and later, these PAA islands finally collapse forming smooth globular-like polymer structures (~ 20 – 30 nm thick) which nearly cover the whole substrate (Figure 2E, F) but still leaving some polymer-free steel areas in between. The latter can be tentatively attributed to the dissolution of previously deposited Zn/ZnO particles when the electrodeposited ZnO/PAA composite film is exposed to a dilute HCl aqueous solution. In this regard, the inset in Figure 2E shows the presence of Zn/ZnO crystalline structures (~ 300 nm high) before the sample was thoroughly rinsed in 0.1 M HCl. As a consequence, the RMS value still increased up to $t = 225$ seconds, namely 15.3 nm, reaching then a steady value for higher deposition times, ie, 13.2 nm for $t = 300$ seconds.

3.3 | Peel test

The influence of the deposition time on the wet adhesion has been assessed, and these results are presented in Figure 3. The PAA films

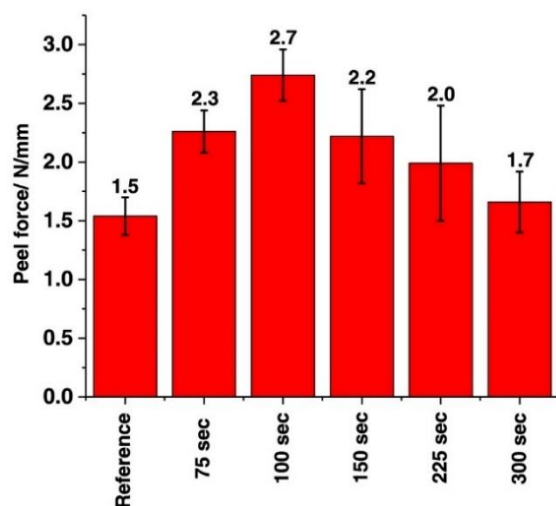


FIGURE 3 Peel forces: polished stainless steel after solvent cleaning and stainless steel after applying -1.15 V (vs Ag/AgCl) for 75, 100, 150, 225, and 300 seconds after rinsing with 0.1 M HCl aqueous solution

are expected to promote the adhesion between the stainless steel substrate and the epoxy-amine adhesive film.¹¹ Peel-off forces of 1.54 and 2.74 N mm⁻¹ were registered for the reference and 100-second PAA-coated samples, respectively.

Our results show that the adhesion is improved, ie, by a factor of nearly 1.8, in the case of 100 seconds. However, for 300 seconds, the adhesion experiences show no significant enhancement in comparison to that exhibited by the bare stainless steel surface. Interestingly, rather, a decrease of peel forces could be observed for deposition times higher than 100 seconds. This finding could be correlated with the morphology of the PAA films. Briefly, when PAA grain particles (see Figure 2B, C), start to aggregate to form 3D pancake-like structures (see Figure 2D–F), the macroscopic adhesion values decrease. This observation can be tentatively attributed to a cohesive failure of the as-prepared PAA layer at a critical film thickness. It can be concluded that a PAA thin film of only some few nanometer thickness is beneficial for interfacial adhesion promotion. In this regard, coordinative bond formation between the iron oxide containing passive film and the carboxylic acid groups of the PAA and/or are likely.¹¹

4 | CONCLUSIONS

Poly(acrylic acid) thin films can be prepared onto stainless steel by electrochemical polarization at cathodic potentials in a Zn^{2+} /AA containing aqueous solution at slightly acidic pH. Zn species can be removed from the as-obtained Zn-PAA-based composite by rinsing with a dilute HCl solution. The resulting surfaces have been thoroughly characterized by AFM and FT-IRRAS confirming the successful modification of the steel samples with the polymer. These PAA-modified steel samples exhibit enhanced adhesion properties to a model epoxy/amine resin in comparison to that exhibited by the bare stainless steel surface.

ACKNOWLEDGEMENT

The authors acknowledge the partial funding of the project by the German Research Foundation (GR 1709/22-1).

ORCID

D. Meinderink  <http://orcid.org/0000-0002-2755-6514>

REFERENCES

- Li C, Bai H, Shi G. Conducting polymer nanomaterials: Electrosynthesis and applications. *Chem Soc Rev*. 2009;38(8):2397–2409.
- Pujari SP, Scheres L, Marcelis ATM, Zuilhof H. Covalent surface modification of oxide surfaces. *Angew Chem Int Ed*. 2014;53(25):6322–6356.
- Ward LJ, Schofield WCE, Badyal JPS, Goodwin AJ, Merlin PJ. Atmospheric pressure plasma deposition of structurally well-defined Polyacrylic acid films. *Chem Mater*. 2003;15(7):1466–1469.
- Belanger D, Pinson J. Electrografting: A powerful method for surface modification. *Chem Soc Rev*. 2011;40(7):3995–4048.
- Katz E, de Lacey AL, Fernandez VM. Covalent binding of viologen to electrode surfaces coated with poly(acrylic acid) prepared by electropolymerization of acrylate ions: II. Effect of the ionization state of the polymeric coating on the formal potential of viologen. *J Electroanal Chem*. 1993;358(1–2):261–272.

6. Wu L-K, Hu J-M, Zhang J-Q. Electrodeposition of zinc-doped silane films for corrosion protection of mild steels. *Corros Sci.* 2012;59: 348-351.
7. Liu Y-H, Jin X-H, Hu J-M. Electrodeposited silica films post-treated with organosilane coupling agent as the pretreatment layers of organic coating system. *Corros Sci.* 2016;106:127-136.
8. Gabriel S, Jérôme R, Jérôme C. Cathodic electrografting of acrylics: From fundamentals to functional coatings. *Prog Polym Sci.* 2010; 35(1-2):113-140.
9. Umoren SA, Li Y, Wang FH. Influence of iron microstructure on the performance of polyacrylic acid as corrosion inhibitor in sulfuric acid solution. *Corros Sci.* 2011;53(5):1778-1785.
10. Charlot A, Gabriel S, Detrembleur C, Jerome R, Jerome C. Combination of electrografting and layer-by-layer deposition: An efficient way to tailor polymer coatings of (semi)-conductors. *Chem Commun.* 2007; (44):4656-4658.
11. Bauer A, Meinderink D, Giner I, Steger H, Weitz J, Grundmeier G. Electropolymerization of acrylic acid on carbon fibers for improved epoxy/fiber adhesion. *Surf Coat Technol.* 2017;321:128-135.
12. Chegel VI, Raitman OA, Lioubashevski O, Shirshov Y, Katz E, Willner I. Redox-switching of Electrorefractive, electrochromic, and conductivity functions of Cu²⁺/Polyacrylic acid films associated with electrodes. *Adv Mater.* 2002;14(21):1549-1553.
13. Wang X, Bohn PW. Anisotropic in-plane gradients of poly(acrylic acid) formed by electropolymerization with spatiotemporal control of the electrochemical potential. *J Am Chem Soc.* 2004;126(21):6825-6832.
14. Le XT, Viel P, Sorin A, Jegou P, Palacin S. Electrochemical behaviour of polyacrylic acid coated gold electrodes: An application to remove heavy metal ions from wastewater. *Electrochim Acta.* 2009;54(25): 6089-6093.
15. Ricciardi S, Castagna R, Severino SM, et al. Surface functionalization by poly-acrylic acid plasma-polymerized films for microarray DNA diagnostics. *Surf Coat Technol.* 2012;207:389-399.

How to cite this article: Meinderink D, Orive AG, Grundmeier G. Electrodeposition of poly(acrylic acid) on stainless steel with enhanced adhesion properties. *Surf Interface Anal.* 2018;50:1224-1229. <https://doi.org/10.1002/sia.6440>

3.4 Spray coating of poly(acrylic acid)/ZnO tetrapod adhesion promoting nanocomposite films for polymer laminates

The following **4. publication** was reused from the publication:

Dennis Meinderink, Karlo J.R. Nolkemper, Julius Bürger, Alejandro G. Orive, Jörg K.N. Lindner, Guido Grundmeier, Surface and Coatings Technology 375 (2019) 112-122. (Copyright Elsevier 2019) with permission from Elsevier for reuse and embedding the article in this PhD thesis.

<https://doi.org/10.1016/j.surfcoat.2019.06.083>

The joining of nonpolar polymers like poly(propylene) foils to laminates is limited by the van der Waals forces in the interfacial region of the system. The publications before already showed the molecular and macroscopic adhesion properties of ZnO nanostructures and poly(acrylic acid). Within this **4. publication** of this PhD thesis, a novel ultrathin hybrid film containing of ZnO tetrapods and poly(acrylic acid) was developed to transfer the knowledge of the fundamental adhesion properties of PAA/ZnO materials to a technical relevant and easy application tool. Spray coating as a highly industrial relevant application method was chosen to deposit the aqueous dispersion on nonpolar poly(propylene) foils to increase their interfacial adhesion mechanisms. Indeed, the shear strength tests showed that the shear strengths increase with increasing ZnO tetrapod surface concentration. Furthermore, the results demonstrated the cohesive adhesion failure mainly in the centers of the ZnO tetrapod crystals.

The following Table 5 sums up the involved persons with their work inputs.

Table 5. Summary of the author contributions involved in the publication “*Spray coating of poly(acrylic acid)/ZnO tetrapod adhesion promoting nanocomposite films for polymer laminates*”.

author contributions	involved persons
validation, writing, coordination, investigation, conceptualization, original draft, visualization, sample preparation, experimental executions, analytical measurements, evaluations, data curation, formal analysis, scientific discussion, review & editing	D.M
support for: sample preparation, plasma pre-treatments, contact angle measurements and shear tests, review & editing	K.N.
TEM measurements, resources, data interpretation, review & editing	J.B., J.K.N.L.
scientific discussion, support, mentoring, interpretation of data, revisions of the manuscript, review & editing	A.G.O.
project administration, funding acquisition, resources, conceptualization, scientific discussion, supervision, mentoring, interpretation of data, revisions of the manuscript	G.G.



Contents lists available at ScienceDirect

Surface & Coatings Technology

journal homepage: www.elsevier.com/locate/surfcoat

Spray coating of poly(acrylic acid)/ZnO tetrapod adhesion promoting nanocomposite films for polymer laminates

Dennis Meinderink^a, Karlo J.R. Nolkemper^a, Julius Bürger^b, Alejandro G. Orive^a, Jörg K.N. Lindner^b, Guido Grundmeier^{a,*}

^a Technical and Macromolecular Chemistry, University of Paderborn, Warburger Str. 100, 33098 Paderborn, Germany

^b Department of Physics, University of Paderborn, Warburger Str. 100, 33098 Paderborn, Germany

ARTICLE INFO

Keywords:

ZnO tetrapods (ZnO TP)

Spray coating

Dispersions

Poly(acrylic acid) (PAA)

Nanocomposite

Adhesion promoting films

ABSTRACT

Zinc oxide tetrapods (ZnO TP) have reached a high level of interest in the last years due to their broad fields of applications. Here, the combination of the adhesion promoting properties of both ZnO TP and poly(acrylic acid) (PAA) is demonstrated. A very rapid spray coating of water-based dispersions has been used to deposit homogenous thin nanocomposite films on poly(propylene) (PP) foils considered as model system. The characterization of ZnO TPs has been carried out by field-emission scanning electron microscopy (FE-SEM), high-resolution X-ray photoelectron spectroscopy (XPS) and transmission electron microscopy (TEM). The increased shear strength values exhibited by PP/PP laminates with interfacial ZnO TP/PAA films could be attributed to mechanical interlocking of ZnO TP and the macromolecular adhesion promotion by PAA. FE-SEM imaging after shear tests indicated a failure in the core of the ZnO TP. The fast application method via plasma activation of the PP foils and spray coating of the composite films with low concentrations of 0.085 mM PAA and 8 mg/ml ZnO TP makes this technique rather interesting for industrial applications.

1. Introduction

The application of ZnO tetrapods (ZnO TP) in different fields such as gas sensing [1,2], humidity sensing [3], UV sensing [4], electron [5] or photoluminescence devices [6], photocatalytic properties [7], for self-reporting materials with stress sensitive photoluminescence like in ZnO tetrapods/poly(dimethylsiloxane) (PDMS) composites [8] or for thermally and electrically conductive epoxy composites with graphene-coated ZnO TP [9], coated with gold particles for surface-enhanced Raman spectroscopy (SERS) [10] and adhesion promoting [11] has been considered in the last years. For example, the optical and dielectric properties of ZnO TP were thoroughly studied by Han et al. [12]. ZnO TP also show a high potential for dye-sensitized solar cells as published by Hsu et al. [13]. The reviews of Newton and Warburton [14], Modi [15], Mishra [16,17] and Yan et al. [18] provide a good overview about the synthesis, characterizations, and applications of ZnO TP. The use of ZnO TP as template materials for composites was recently shown by Yang et al. [19]. A good summary about the different synthesis procedures is given in the seminal contribution by Mishra et al. [16]. Fabrication methods of ZnO TP are well established. Mishra et al. developed a simple flame transport approach for obtaining different ZnO

morphologies [20,21]. A muffle oven-based synthesis with poly(vinylbutyral) (PVB), zinc microparticles and ethanol has been employed for this purpose. Another possibility to fabricate ZnO TP is the thermal evaporation in a tube oven [2]. Zinc powder or even zinc plates can be used as precursors with the inlet of nitrogen as transport gas and oxygen for the oxidation of vaporous zinc. The impact of the experimental conditions has been thoroughly explored in the last years [2,22–29]. For example, the feed rates, the temperature, the amount of zinc and the relative position in the tube are important parameters to be controlled during the synthesis [30].

Different deposition processes of ZnO TP have been considered over the last few years. For example, homogenous films with dispersions of ZnO TP were achieved by means of spin coating onto indium tin oxide (ITO) glasses [13]. A coating from liquid polymer by directly spreading onto the substrates was demonstrated by Hölken et al. [31]. Another way to produce coatings with ZnO TP using an automatic film coating apparatus for the deposition of ultrasonicated ZnO TP/poly(urethane acrylate) (PUA) composites on glass plates followed by UV curing was shown by Kim et al. [32].

Spray coating is a well-known tool based on ultrasonic spraying useful to create thin films of metal oxides by means of pyrolysis from a

* Corresponding author.

E-mail address: g.grundmeier@tc.uni-paderborn.de (G. Grundmeier).

<https://doi.org/10.1016/j.surfcoat.2019.06.083>

Received 17 May 2019; Received in revised form 27 June 2019; Accepted 28 June 2019

Available online 29 June 2019

0257-8972/ © 2019 Elsevier B.V. All rights reserved.

sprayed aerosol [33–35]. Metal oxides like SnO_2 or ZnO were synthesized by using their organometallic or mineral salts as precursors [33,34]. Another way to deposit metal oxides onto surfaces is the direct use of dispersions or suspensions of oxide particles. A homogenous and stable dispersion is the basis of metal oxide source materials for the spray coating process [36,37]. In this regard, the electrostatic and steric stabilization in the chosen dispersant play an important role [37]. Process development has to consider the control of the liquid jet via pumps or pneumatic systems, the droplet size, the nozzle, the distance to the substrate surface, pressure of the carrier gas and the substrate temperature [34,37]. Arca et al. showed the dependence of the precursors on the properties of the deposited ZnO coatings [34], while Pawlowski summed up all details regarding the spray coating process [37]. To the best of our knowledge, ZnO TP have not been dispersed in water-based polymer solution and spray coated with a polymer component like PAA so far [17]. PAA has been typically casted by spray coating for preparing layer-by-layer (LbL) films [38]. Li et al. have carried out the spraying of aqueous PAA solutions with additional polymers to generate superhydrophobic coatings [39].

The optimized dispersion of metal oxide nanoparticles is still a challenge and has to be optimized for every individual case [37,40]. For the generation of a stable particle dispersion without sedimentation, the repulsive electrostatic interactions play an important role [41,42]. ZnO particles can be dispersed in different suspensions based on methanol [12,23,43], dichloromethane with *n*-hexyltrichlorosilane [6], isopropanol [2] or ethanol [5]. The adsorption of poly(ethylene glycol) (PEG) on zinc oxide nanoparticle surfaces was analyzed by Liufu et al. [44]. However, for a wider industrial application of ZnO particle-based dispersions and a “green chemistry” approach, an ethylene glycol-water [45,46] stable suspension, or even dispersions in pure water [47] should be considered [48]. ZnO TP could be mixed in a 0.25 M zinc acetate/ethanol solution as demonstrated by Hsu et al. [13] or in aqueous AgNO_3 /PEG solutions as published by Wang et al. [25]. The high potential of the adhesion promoting properties of ZnO TP was shown by Adelung and his working group for the joining of poly(tetrafluorethylene) (PTFE) and PDMS [11]. They could demonstrate that ZnO TP are increasing the mechanical interlocking between the cured PTFE and PDMS polymer films via ZnO TP deposited with a sieve. However, the interface preparation was quite complex and not suitable for technical processes.

In the present work, we show the spray coating of a novel composite film in combination with plasma activation of substrates for a time-efficient surface processing. Poly(propylene) is used as a model polymer which is difficult to laminate. Plasma activation of PP foils was carried out as proposed by Gross et al. [49], Morent et al. [50] and Occhiello et al. [51] in oxygen containing atmosphere. Plasma activated poly(propylene) foils were then spray coated with different water-based PAA dispersions containing ZnO TP and homogenous spray coated films of PAA and ZnO TP/PAA composites could be achieved. To quantify the adhesion promoting capabilities of ZnO TP and PAA films, two joined PP foils were subjected to shear tests under high humidity. The optimized performance of the nascent ZnO TP/PAA composite films is here attributed to mechanical interlocking by ZnO TP combined with the adhesion-promoting properties exhibited by PAA films, which has been largely stated in several studies [38,52–57]. Furthermore, PAA was chosen to slow down the sedimentation of the ZnO TP in the dispersion.

2. Experimental

The ZnO TP synthesis was addressed according to a well-known procedure commonly known as “vapor phase growth processes” [1,2,23]. A schematic illustration of the tube oven setup can be found in the work of Calestani et al. [2]. Briefly, ZnO TP were synthesized in a quartz tube of 1200 mm length with an outer diameter of 34 mm. In our synthesis, no extra tubes for the inlet of the gases (N_2 and O_2) were used. The principal setup is displayed in Fig. S1 in the Supporting

information (SI). For an easy collection of the ZnO TP, a conical SiO_2 tube (28 mm and 5 mm inner diameters) marked as area 3 and 4 in Fig. S1 was inserted with a second smaller quartz tube in the tube oven, according to the publication of Wang et al. [28] and Delaunay et al. [26]. Before starting the synthesis, the tube oven was heated up to 900 °C and purged for 10 min with pure nitrogen (volume speed 16 l/h) to avoid any water contaminations. Zinc powder (1.6 g, Riedel-de Haën, fine powder, for analysis) in an aluminum oxide vessel was positioned in the middle of the tube oven under nitrogen flow. Then the oxygen flow was set to 1.6 l/h (± 0.5 l/h) while the nitrogen flow was decreased to 6.0 l/h (± 0.5 l/h). After a reaction time of 30 min, the oxygen/nitrogen flow and the heating of the oven were stopped. The cooling down to room temperature was done overnight under nitrogen atmosphere. ZnO TP as colorless fluffy powder in area 4 (Fig. S1) were collected from the inserted short quartz tube by picking up with a spatula from the inner walls.

Poly(propylene) foil (PP) (thickness 0.1 mm, homopolymer, Goodfellow, England) was cut into 1 cm \times 4 cm pieces with a scalpel and used as substrate. In order to remove all pollutants from laboratory atmosphere the films were cleaned with ethanol in an ultrasonic bath and dried under nitrogen steam. To reach higher hydrophilicity, a plasma activation for poly(propylene) films (PP) was done in a Plasma Cleaner Setup (Plasma Surface Technology, Diener electronic GmbH, Germany) under pure oxygen with constant pressure controlled by the volume flux of oxygen. The oxygen pressure was set to 0.34 mbar. A deviation of ± 0.04 mbar caused by flux instabilities has been estimated. All plasma activations were carried out for 1 min and the samples were directly used for spray coating followed by the analytical steps.

For the spray coating process, a conventional spray coater (ND-SP 11/4 Precision Spray Coater, Nadetech Innovations S.L., Spain) with vertical configuration and integrated hotplate was used. A mixture of nitrogen and the water-based dispersion was sprayed with a high viscosity liquid atomization spray nozzle (mini-atomized nozzle MMAE/MMA type, Nadetech Innovations S.L., Spain) made of 316 L stainless steel. Here, the following parameters were chosen at the spray coater: a hotplate temperature of 75 °C (± 3 °C), a volume speed of 100 ml/min, a distance between the nozzle and the substrate surface of 12 cm, a movement speed of the nozzle of 1200 mm/min (i.e. 1 s for spray coating time on 1 cm² PP foil), a system pressure higher than 6.0 bar of pure nitrogen and a pressure at the nozzle of 3.50 bar. Before each spray coating experiment, the whole system was cleaned with at least 20 ml of ultrapure water (0.055 $\mu\text{S}/\text{cm}$, Ultra Clear TWF, SG water, Hamburg, Germany). Additionally, a stabilization time of 2 s to create a stable spray coating mist was set in the software (Nadetech Innovations S.L., Spain).

In all experiments aqueous dispersions with a pH value of 7 (± 0.1) adjusted with solid NaOH pellets (Merck Millipore, Germany) were used. For a stable dispersion for around 20 min (± 10 min), a 0.085 mM poly(acrylic acid) (PAA) (250.000 g/mol, 35 wt% in H_2O , Sigma Aldrich) solution in ultrapure water (0.055 $\mu\text{S}/\text{cm}$, Ultra Clear TWF, SG water, Hamburg, Germany) was used. The dependence of the ZnO tetrapod (ZnO TP) concentration on the spray coating homogeneity and adhesion was checked for different ZnO TP concentrations. For this purpose, ZnO TP were added to the previously prepared 0.085 mM PAA aqueous solution (pH 7) to get concentrations of 8 mg/ml and 16 mg/ml. The new measured pH values are 8.8 (± 0.2) for the 8 mg/ml ZnO TP dispersion and 8.6 (± 0.2) for the 16 mg/ml ZnO TP dispersion with 0.085 mM PAA (pH 7). To reach a high homogeneity, the dispersions (a volume of 50 ml) were stirred at 150 rpm for 10 min. After homogenization the dispersions were loaded in the syringes of the spray coater and were shaken softly before the spray coating process. Some photographic images of the spray coated PP foils can be found in the Fig. S2 in the SI.

All spray coated samples were stored for at least 24 h in a desiccator filled with silica particles at a pressure of 30 mbar. The joining of two

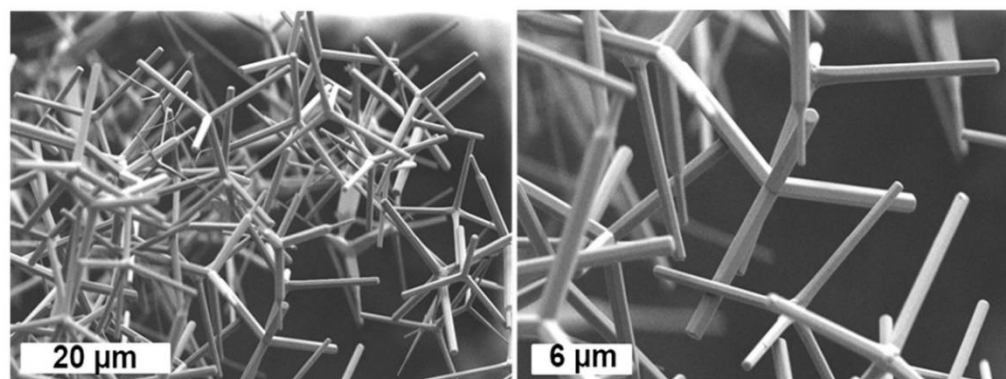


Fig. 1. FE-SEM images of the ZnO tetrapod powder supported on a carbon pad.

overlapping PP foils with 1.0 cm^2 joining area was carried out by using a laboratory hydraulic press (CY-PCH-600D) with two heating plates (CYKY, China). A schematic illustration of the setup is shown in Fig. S3 in the SI. The temperature of the hotplates was set to 65°C ($\pm 0.5^\circ\text{C}$) and a constant hydraulic pressure of 0.5 MPa (with an estimated variation of $\pm 0.4 \text{ MPa}$) was applied for 30 s with 7 samples (total overlapping area is then 7 cm^2). Mirror polished stainless steel coated with poly(tetrafluorethene) (PTFE) foils (0.1 mm thickness) were used to achieve flat surfaces and to get an easy removal of the jointed foils. Two jointed samples illustrated via photographic images can be seen in the Fig. S2 in the SI.

A field-emission scanning electron microscope (NEON® 40 FE-SEM, Carl Zeiss SMT AG, Germany) with a SE2 and an InLens detector was used for the generation of high-resolution SEM images of the ZnO TP and PP surfaces. A focused ion beam (FIB) system (NEON® 40 FIB, Carl Zeiss SMT AG, Germany) with a Ga liquid metal ion source (LMIS) was used for milling some of the samples. A beam of 30 keV Ga^+ ions was used for all FIB processes at currents of 50 pA and 5 nA . The samples were sputter coated with 3 nm Au/Pd ($80 \text{ wt}\% \text{ Au}$, $20 \text{ wt}\% \text{ Pd}$) prior to all FIB measurements.

Investigations on the joining parts of the ZnO TP branches were performed on a probe-side C_s -corrected JEOL JEM-ARM200F at an acceleration voltage of 200 kV . For TEM analysis a droplet of ZnO TP dispersed in isopropyl alcohol was placed on a carbon coated grid and dried. To analyze cracking behavior, a ZnO TP holding grid was first covered by a second grid (carbon side on top of carbon side). In a second step ZnO TP were ground by displacing the covering grid which leads to cracking of TPs (as shown in Fig. S4 in SI).

The surface chemical composition of ZnO TP and spray coatings was studied by X-ray photoelectron spectroscopy (XPS) using an Omicron ESCA+ equipment (Omicron NanoTechnology, Germany) at a pressure of $< 5 \cdot 10^{-10} \text{ mbar}$. For all measurements monochromatic Al-K α X-ray radiation (1486.7 eV), a spot diameter of $600 \mu\text{m}$, a take-off angle of 30° and a hemispheric analyzer were used. The C 1s peak at 285.0 eV was set as internal energy reference and no neutralization was applied in all measurements. The software CasaXPS (Casa Software Ltd., Teignmouth, UK) was used for peak fitting with the corresponding relative sensitivity factors (RSF) for the peak integration. Here, a convolution of a Gauss (30%) and Lorentzian (70%) shape and a Shirley background was selected.

Raman Spectroscopy was used for the additional chemical and morphological characterization of the synthesized ZnO tetrapods. For this, an InVia Renishaw Raman microscope (Renishaw, Germany) with a CCD detector, two lasers (532 nm and 785 nm) with corresponding gratings and filter and mirror systems was employed. A YAG-Laser (532 nm , 55 mW max. power) and a $50\times$ objective were used for all measurements. The precise power with this configuration was

measured with a calibrated USB photodiode (DIN EN ISO 9001, THORLABS, Germany) and was 6.16 mW . A silicon wafer was used for internal calibration of the position of wave number 520.0 cm^{-1} ($\pm 0.5 \text{ cm}^{-1}$).

Static water contact angle measurements via sessile drop method were done for the characterization of the wettability properties before and after plasma treatments on the PP foils. A contact angle system (OCA 15 plus, DataPhysics, Filderstadt, Germany) with the SCA20 Software (DataPhysics Instruments GmbH, Filderstadt, Germany) was used to evaluate the drops and calculate the contact angles by the Young-Laplace method.

After the joining step, the samples were exposed to 40°C ($\pm 2^\circ\text{C}$) at high humidities (r.H. is higher than 95%) in a closed box for 48 h to reach a water saturation of the polymers. For the analysis of the adhesion at high r.H., shear tests of the jointed PP foils were done in a box with constantly humid atmosphere (r.H. $> 95\%$, $24^\circ\text{C} \pm 2^\circ\text{C}$). The recording of the force vs. time was performed with a ZP recorder (force gauge of type Model ZP-5, Imada) with a movement speed of 1 mm/s . For the evaluation of the force-time curves the maximum shear strength values were selected.

3. Results and discussion

3.1. Characterization of ZnO tetrapods synthesized in a tube oven

The morphology and geometry assessment was carried out by FE-SEM. Some particles of the cotton-like and colorless ZnO TP product were carefully spread onto carbon pads. FE-SEM images in Fig. 1 show ZnO tetrapods exhibiting their characteristic four arms. These ZnO arms (nanorods) have an estimated length of $8\text{--}10 \mu\text{m}$. A diameter of around $600\text{--}800 \text{ nm}$ could be deduced from FE-SEM images at higher magnifications (data not shown).

In general, ZnO TP belonging to different synthesis batches showed different sizes. It can be concluded from the analysis of FE-SEM images that the length of nanorod-shaped arms ranges from $1 \mu\text{m}$ up to $15 \mu\text{m}$ and their diameter varies between 200 nm and $1 \mu\text{m}$.

To form a tetrapod, the joining part has a high number of planar defects (mainly twin boundaries), as already reported by Fujii et al. [58]. However, the discussion regarding the formation mechanisms of ZnO TP is still going on [14,18,59]. In Fig. 2a) the center of the four joining arms of a ZnO TP is displayed in a TEM bright-field image.

Due to high specimen thickness of 380 nm , electron transparency is low and defects have little contrast. However, TEM dark-field (Fig. 2b)) images show planar defects at coinciding planes of two arms. In addition, a structure of the inner core, driving the ZnO TP formation can be observed, exhibiting rough interfaces towards the ZnO arms. This core structure is not visible in all of the TPs. High-resolution imaging was

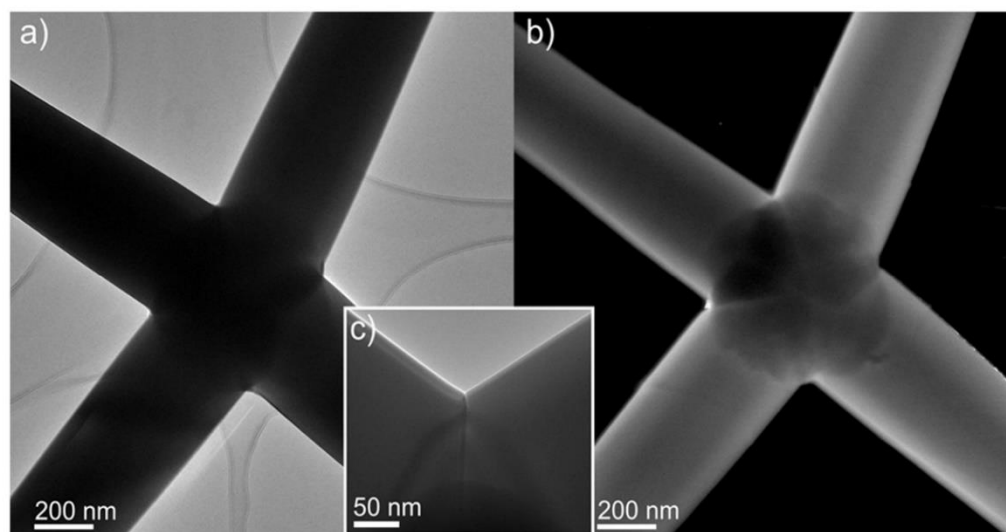


Fig. 2. a) TEM bright-field image of the center of a ZnO TP. b) TEM dark-field image of the same TP, revealing planar defects and the inner structure of the TP core. Inset c) shows characteristic fringe contrast of two-dimensional defects at the interface of two tetrapod arms.

not possible due to high specimen thickness, though a TEM bright-field image at higher magnification (Fig. 2c)) showed fringes typical for planar defects.

The chemical characterization was addressed via Raman spectroscopy as shown in Fig. S5. A detailed analysis of all the expected peaks for ZnO TP is provided by Lupan et al. [60]. The most intense peak at 437 cm^{-1} (E_2 mode) indicates the Wurtzite structure [4,21,61]. For example, the peaks measured at 380 cm^{-1} and 409 cm^{-1} are in good agreement with the positions of the A_1 and E_1 mode of ZnO TP [4,21,60,62]. The microscopic image displayed in Fig. S5B) underlines the 3D bundles of the ZnO TP and is in agreement with the FE-SEM and TEM images.

In addition to that, XPS measurements of ZnO TP supported on carbon pads were carried out and shown in Fig. 3. To the best of our knowledge, very few publications dealing with a detailed XPS analysis of ZnO TP are available [60], namely with the quantification of the core-level spectra of C 1s and O 1s. The quantification of the high-resolution spectra of the peaks of zinc, oxygen and adventitious carbon showed the typical peak positions and overall composition expected for ZnO nanostructures [62,63].

No silicon signal could be found. Consequently, the carbon pad, which typically shows silicon in the surface (data not shown), is not influencing the measurement. The quantitative summary of the evaluation of the XPS survey spectra of ZnO tetrapod powder shows a content of Zn 2p_{3/2} with 27.2 at.-%, O 1s with 37.5 at.-% and 35.3 at.-% of C 1s. The latter, i.e. the adsorption of different oxidized carbon species from the atmosphere, is characteristic of such ZnO nanostructures with high surface area as it has been previously discussed in the literature for the case of ZnO nanorods deposited on stainless steel [63].

A tentative peak fitting was carried out and displayed in Fig. 3B) and C) for high-resolution XPS spectra of C 1s and O 1s. The contribution in the case of the C 1s shows an intense peak at the position of 285.0 eV with 70.1 at.-% assigned to C–C and C–H, a second peak at 285.6 eV with 22.6 at.-% and a third peak at 288.9 eV with 7.3 at.-%. The latter two peaks could be interpreted as adsorbed oxidized carbon species like carboxylates/ COO^- and carbonates/ CO_3^{2-} [63]. The O1s peak can be separated in two components: the most intense one attributed to zinc oxide at 530.3 eV with 59.3 at.-% and the second one at 531.9 eV with 40.7 at.-%. The last one is assigned to adsorbed species

containing oxygen like the mentioned oxidized carbon species, molecular oxygen, hydroxyl groups, or adsorbed water [63]. The XPS results underline the successful synthesis of ZnO TP already shown by FE-SEM and TEM measurements.

3.2. Characterization of poly(propylene) foils before and after plasma activation

Water contact angle and high-resolution XPS measurements were done to prove the increase in hydrophilicity and the subsequent enrichment of oxidized carbon groups on the surface of the PP foil as a consequence of the plasma treatment in oxygen atmosphere. The results before and after the plasma activation are illustrated in Fig. 4.

The solvent cleaned PP foils show a water contact angle of $97.8^\circ (\pm 1.0^\circ)$ (Fig. 4A)) and exhibit a 99.4 at.-% C 1s and a 0.6 at.-% O 1s peak (from survey, see Fig. S6 in the Supporting information). This is in very good agreement with other XPS and contact angle measurements reported for untreated PP foils in the literature [49–51,64]. Plasma activation resulted in an average water contact angle of $16.4^\circ (\pm 4.3^\circ)$ (Fig. 4C)). For more meaningful statistics of the contact angle assessment, 78 measurements were done to avoid the effect of the unstable oxygen flow mentioned in the experimental part on the plasma activation. Although the peak fitting of plasma activated polymer films is challenging [65], four peaks were chosen for a reasonable fitting (Fig. 4D)), as published elsewhere [49,50,66]. Table 1 sums up the total surface composition according to the XPS survey analysis of the untreated and plasma activated PP foils.

The increase of the oxygen content in the surface after plasma activation by a factor of around 40 is explainable and the goal of this treatment. The XPS results of plasma modified PP foils as shown in Fig. 4 reveal the incorporation of polar C–O, C=O and O–C=O groups in concentrations which are typical for such plasma treatments [49–51,67]. The reported functional groups lead to increased Keesom interactions and specifically strong hydrogen bonds with the aqueous phase [67]. As a consequence, the wettability is strongly increased after plasma treatment. The peak fitting of the C 1s depicted in Fig. 4D) and the corresponding quantifications show clearly the growth of oxygen groups bound to carbon atoms like C–O groups (14.1 at.-%), carbonyl functionalities/C=O (12.4 at.-%) and 16.3 at.-% of carboxylic groups/O–C=O on the PP surface. All values from XPS quantifications

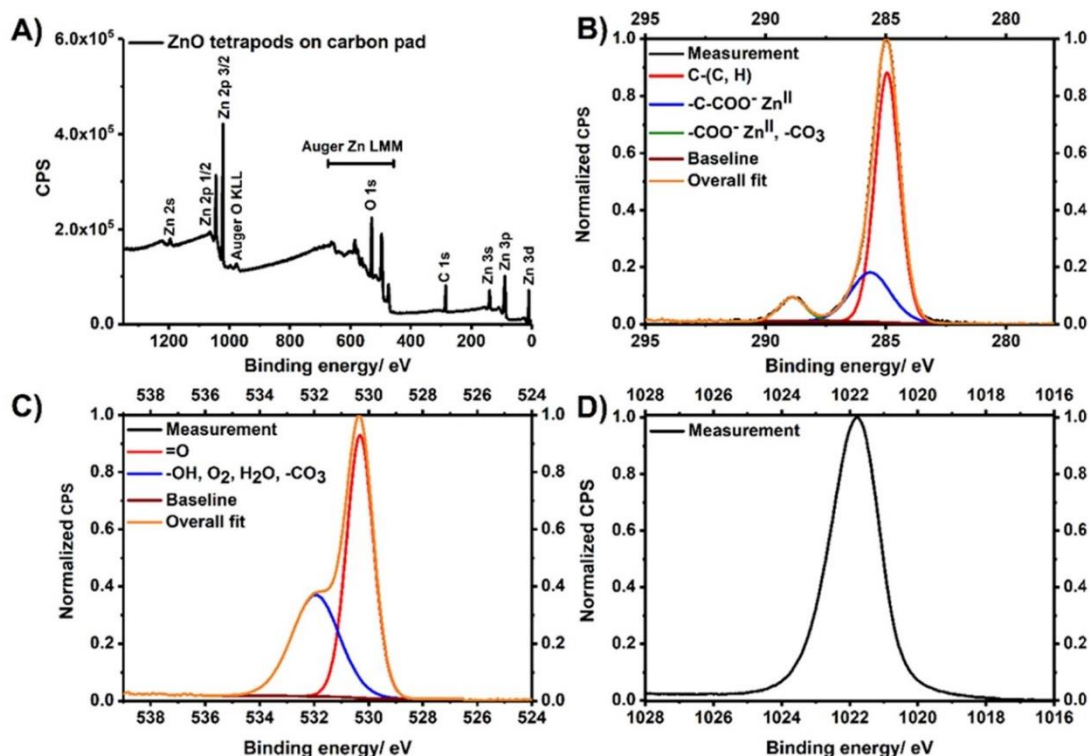


Fig. 3. XPS measurement results of the ZnO tetrapod powder supported on a carbon pad. A) survey spectrum and corresponding high-resolution spectrum of C 1s in B), O 1s in C) and Zn 2p_{3/2} in D).

are in a good agreement with other plasma activations of PP foils [49–51,67,68]. The thereby improved wettability is a prerequisite for the following spray coating step. Without this plasma activation step, the spray coatings showed droplets on the PP surface even for water with only 0.085 mM PAA (pH 7) (data not shown). Minor contaminations like Si (1.2 at.-%) and N (0.4 at.-%) are probably coming from the environment. In addition, Gross et al. could also find such impurities in a similar plasma process [49], while Morent et al. detected nitrogen after the plasma treatment of PP foils with air as well [50]. Both authors found similar compositions via high-resolution XPS spectra of the C 1s peak.

3.3. Characterization of spray coatings

FE-SEM images displayed in Fig. S7A) in the SI showed the surface features expected for ethanol cleaned PP foils after plasma activation. After the spray coating step with aqueous 0.085 mM PAA (pH 7), the surface is homogeneously coated (thickness is around 100–200 nm, see below), and the natural scratches of the PP foil are filled with PAA (Fig. S7B) in the SI). This is similar to what has been observed for PAA coatings via Electrohydrodynamic Atomization (EHDA) on poly(ethylene) foils by Tatoulian et al. [54].

By adding the as-prepared ZnO TP to the 0.085 mM PAA aqueous solutions and spray coating with the same parameters on PP foils, the FE-SEM images displayed in Fig. 5 were analyzed. Two different concentrations of ZnO TP in the aqueous PAA solution were tested: 8 mg/ml and 16 mg/ml.

The FE-SEM images showed still intact ZnO TP deposited on the PP foil. In most of the cases the ZnO TP are standing with three nanorod shaped arms leaning on the PAA coating/PP substrate while the fourth arm is oriented parallel to the substrate surface normal (see Fig. 5C) and D)). Furthermore, some ZnO TP nanorods show a mainly complete

coating with PAA, even on the ZnO nanorods oriented perpendicularly to the surface (Fig. 5D)). Meinderink et al. already showed by means of Single Molecule Force Spectroscopy (SMFS) the specific adsorption of carboxylate groups of PAA chains on the nonpolar sidewalls of ZnO nanorods [63].

By doubling the concentration, higher ZnO TP surface coverages could be achieved as shown by the comparison of images A) and B) depicted in Fig. 5.

3.4. Characterization of spray coatings after shear tests

To quantify the interfacial adhesion properties of the PAA/ZnO TP spray coated PP surfaces, foils with different surface chemistry were joined to purely plasma activated PP foils in a hydraulic press with hotplates. Our hypothesis, consisting of the increase in the interfacial adhesion due to mechanical interlocking, is based on the results previously published by Adelung and co-workers for the joining between PTFE and PDMS films [11]. They could show a significant improvement of the adhesion by adding ZnO TP between the cured polymeric phases.

The incorporation of the ZnO TP in the interphases of the PP foil/PAA films should then lead to a significant interlocking between the joined PP foils, increasing thus the shear strength required to separate the specimens during a shear test. A photographic image of the shear test with two joined PP foils is given in Fig. S8. Based on Hook's law the shear test also probes the elastic behaviour of the specimens. For this reason, we chose the maxima of the force-time/force-distance curves (some representative ones are displayed in Fig. S9 in the SI). The as-obtained averaged values are presented in Fig. 6.

An enhancement of the interfacial adhesion via different spray coatings could be achieved. The solvent cleaned samples showed a mean averaged shear strength of 8.8 N/cm² while the spray coating with 16 mg/ml ZnO TP in 0.085 mM PAA dispersion shows a value of

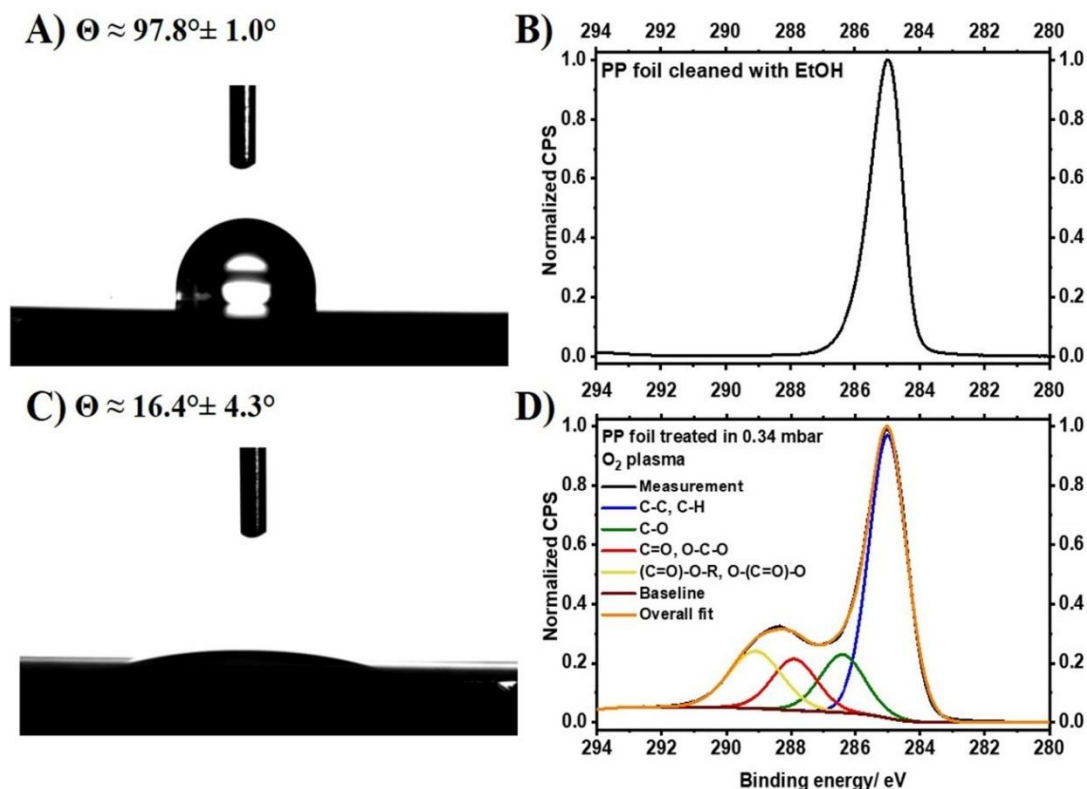


Fig. 4. Water contact angle measurements and high-resolution XPS C 1s spectra of: A), B) ethanol- cleaned poly(propylene) foil and C), D) poly(propylene) foil after plasma activation for 1 min in oxygen atmosphere at a chamber pressure of 0.34 mbar.

Table 1

Summary of the quantitative analysis of XPS survey spectra of the untreated and plasma treated PP foils.

Surface state	At.-% C 1s	At.-% O 1s	At.-% Si 2p	At.-% N 1s
Plasma activated PP	74.7	23.7	1.2	0.4
Untreated PP	99.4	0.6	0.0	0.0

19.0 N/cm². The pure PAA coating with 0.085 mM PAA already led to a 1.6-fold increase in shear strength by considering the mean averaged values depicted in Fig. 6. Indeed, PAA has shown interesting adhesion-promoting properties on different surfaces, prepared, for example, via electropolymerisation [52,53,63,69]. The high shear strength registered for the PAA spray coating films without ZnO TP indicates strong interactions due to carboxylate groups present in the deprotonated PAA at pH 7. PAA has been shown to exhibit coordinative bindings to ZnO nanorod surfaces as demonstrated in [53] via Single Molecule Spectroscopy (SMFS). Thus, a strong interaction between the deprotonated PAA functionalities and the ZnO TP can be expected. In addition to that, PAA should form hydrogen bonds or even covalent bonds with the oxidized functional groups present in the surface of plasma activated PP foils. Wettmarshausen et al. reported ester bond formation between PAA and plasma-oxidized carbon fibers, which would further explain the increase in the interfacial shear strength tests registered for PAA coatings [56,69]. The surface concentration of reactive groups could be increased with plasma activation (compare XPS results in Fig. 4 and Table 1). Consequently, PAA could react with these groups to form interfacial covalent bonds as proposed by Tatoulian et al. [54]. The interfacial adhesion strength of specimens with interfacial ZnO TP/PAA composite films seems to be even higher than the cohesive strength of

the pure PP foil (compare Fig. S9 in SI). To sum up, noticeable adhesion-promoting properties to plasma-activated PP foils due to mechanical interlocking (mechanical adhesion) and surface chemistry (chemical adhesion) related to ZnO TP and PAA, respectively, present in the as-prepared spray coated films, are demonstrated.

The hypothesis for the adhesion promoting capabilities of ZnO TP in this case is confirmed by the FE-SEM and FIB images of tested foils as shown in Figs. 7 and 8. In general, the images show ZnO TP embedded in the polymeric phases of PAA and PP, which provides interfacial interlocking and the bridging between the two polymer foils. Moreover, a transfer of tetrapods from the spray coated PP foil to the plasma activated PP foil could be observed (Fig. 7).

The FE-SEM image in Fig. 7A) showed cavities and delaminated composite films on the PP foil. The cavities are partly filled with parts of ZnO TP (Fig. 7B)–E)) or present imprints of the ZnO TP (Fig. 7F)). Furthermore, it is possible to detect a significant number of spots at which the perpendicular nanorod of the ZnO TP from the coated PP foil has been transferred to the plasma activated side (Fig. 7G)). The FIB cuts in Fig. 7D) and H) confirm the embedding the ZnO TP into the polymeric phases of the PAA and PP. The temperature and the high pressure in the joining process increases the mobility of the poly(propylene) chains. Thus, the ZnO TP particles could be easily pressed into the polymeric phases. No significant differences between the two concentrations of the ZnO TP could be observed. However, in the case of the lower concentration of 8 mg/ml ZnO TP, the number of holes, transferred ZnO TP, and the contribution of ZnO particles is lower, as expected.

Fig. 8 shows selected FE-SEM images and FIB cross sections of the spray coated PP foils after shear test. The FE-SEM images showed also some holes from the transferred ZnO TP (A) and E) in Fig. 8), broken

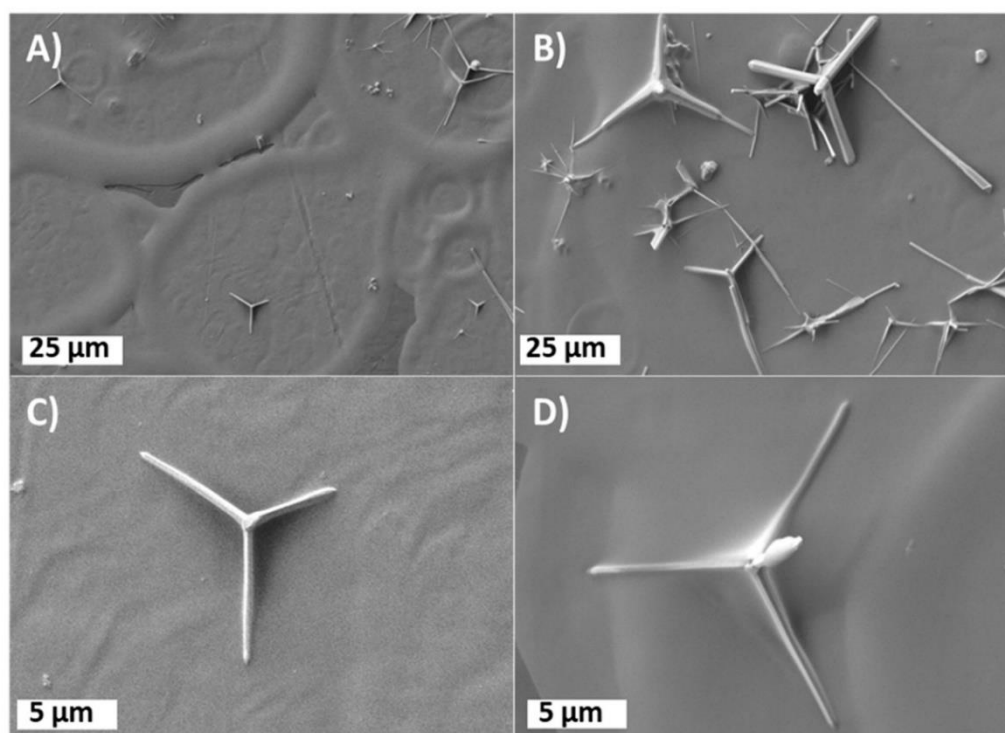


Fig. 5. FE-SEM images of PP foils coated with two different concentrations of ZnO tetrapods in an aqueous 0.085 mM PAA dispersion at pH7 at two different magnifications: A), C) 8 mg/ml ZnO tetrapods and B), D) 16 mg/ml ZnO tetrapods. The spray coating parameters were the same for the two cases: 75 °C, 12 cm nozzle distance, 100 ml/min volume speed and 1200 mm/min motor speed.

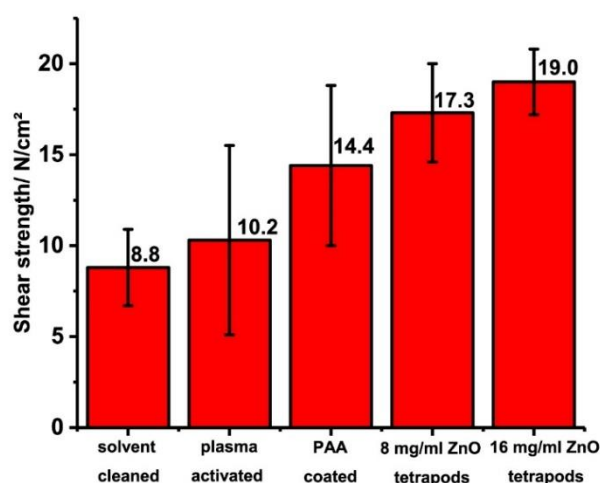


Fig. 6. Averaged shear test results of the PP foils with different spray coatings. For the solvent cleaned samples, the counter PP foil was also only solvent cleaned. The counter PP foil in all other cases was a purely plasma activated PP foil.

ZnO TP (Fig. 8B), C), G)), delamination of PP/PAA films (A), B), E) and F) in Fig. 8) and areas without PAA coating (dark areas in A) and E) in Fig. 8 for example). Interestingly, most ZnO TP break at the core of connection of the four nanorod arms (compare Fig. 8B), C) and G)).

FIB FE-SEM cross sections displayed in Fig. 8D) and H) showed an average PAA film thickness of around 40 nm on the ZnO TP while the film thickness on the PP foil was typically 100–200 nm (see Fig. S10).

For a better comparison, and especially for the interpretation of the transfer of PAA films and interfacial fracture modes, the FE-SEM images of the uncoated samples and those modified with only PAA, collected after shear tests, are displayed in Figs. S11 and S12. The FE-SEM images of the solvent cleaned and joined PP foils after shear test in Fig. S11A)–C) indicate no significant fracture of the PP films. Obviously, the joining process at elevated temperatures did not cause melting of the polymeric phases. Thus, the presented tests characterize the stability of the formed interface. The same behavior was observed for plasma activated and PAA coated PP foils depicted in Figs. S11D)–F) and S12A)–F). The FE-SEM image in Fig. S12 indicates that a PAA layer is located in between the ZnO TP and the PP because of the differences in the material contrasts (InLens detector used in this case).

A TEM analysis of fractured ZnO TP is shown in Fig. 9.

As shown in Fig. 9, ZnO TP tend to fracture along planar defects. This finding supports the FE-SEM investigations after shear testing. The cracked TPs in Fig. 9a) and b) have two arms left. In Fig. 9a) smooth cleaving edges are visible, while in Fig. 9b) a rough three-dimensional fracture morphology can be observed. This difference may be due to different load directions during the fracture experiments. In both cases, however, the fracture has occurred at those positions where planar defects could be observed in non-fractured TPs. The cleavage planes are inclined to the polar (0001) planes perpendicular to the [0001] arm axis. It is therefore likely that cleavage planes are non-polar, facilitating fracture.

The combined information of shear testing and electron microscopy shows that both the macromolecular adhesion promotion and the mechanical interlocking influence the overall interface stability.

XPS analysis was carried out on the PP foils spray coated with 8 mg/ml ZnO TP and 16 mg/ml ZnO TP in aqueous 0.085 mM PAA (Table S1). The spray coatings showed the expected chemical major composition of

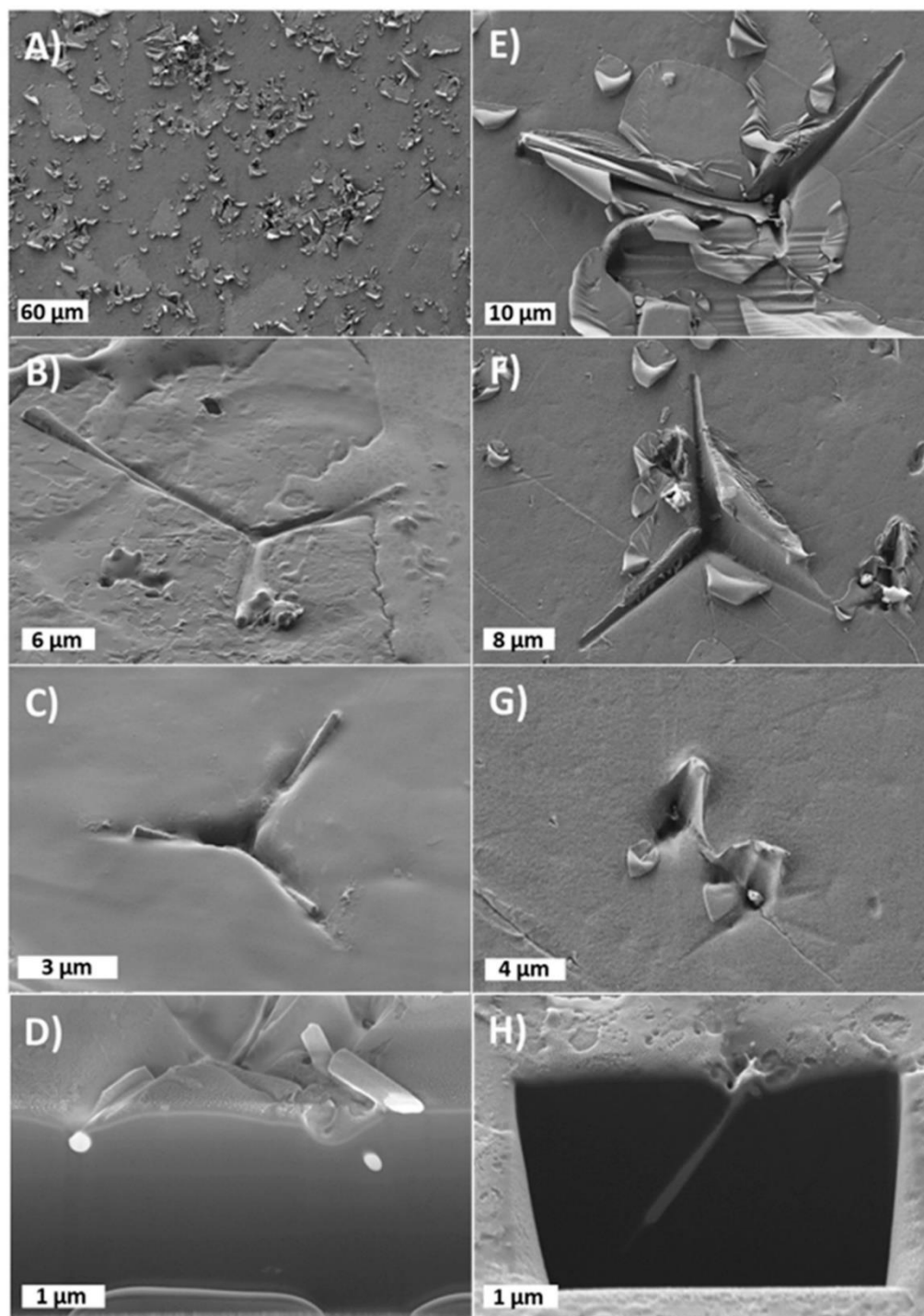


Fig. 7. A)–C), E)–G) Selected FE-SEM images of plasma activated PP foils after shear test. The samples were joined with ZnO TP/PAA spray coated PP foils. D), H) SEM images after FIB cut with embedded ZnO TP arms in PP/transferred PAA material.

C, O, Zn and Na (coming from the pH neutralization with NaOH). In the case of 8 mg/ml ZnO TP only 1.2 at.-% Zn (0.7 at.-% in the case of 16 mg/ml ZnO TP) could be quantified from the Zn $2p_{3/2}$ high-resolution peak. Only some parts of the ZnO TP seems to be uncoated

(polymer free), so that only small zinc contributions could be detected. Consequently, these XPS results confirm that ZnO TP are mostly coated with PAA, corroborating the FE-SEM images depicted in Fig. S10 which showed a 20–60 nm thick PAA coating on the ZnO TP.

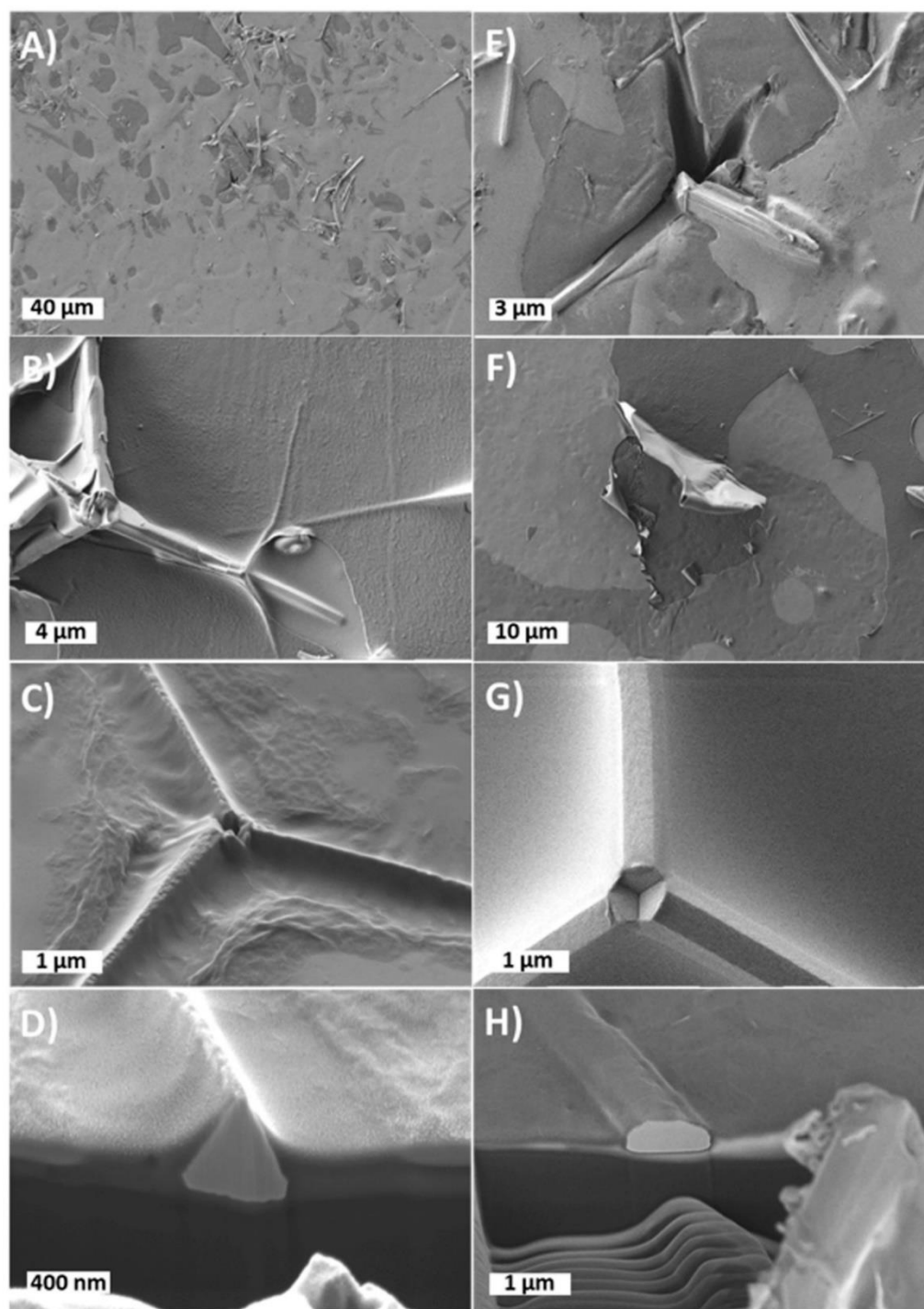


Fig. 8. A)–C), E)–G) Selected FE-SEM images of PP foils spray coated with ZnO TP/PAA after shear test. D), H) SEM images after FIB profiles with embedded ZnO TP arms in PP/transferred PAA material. The FE-SEM images taken after FIB cross-sectioning D) and H) with measurement of the PAA layers can be found in the Supporting information (SI) (Fig. S10).

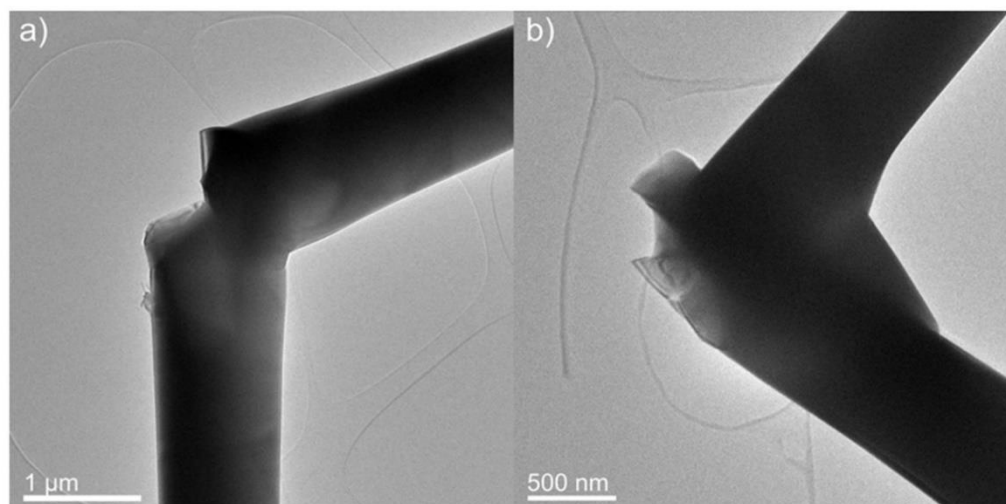


Fig. 9. TEM bright-field images (a, b) of two intentionally cracked tetrapods. The position as well as the sharp edges of cleavage planes lead to the assumption that cracking of the TP is preferred at the planar defects in the TP core.

4. Conclusions

Well-defined and regularly shaped ZnO TP were synthesized via vapor phase growth and characterized by FE-SEM, XPS, Raman and TEM measurements for further usage in a spray coating process. FE-SEM images of the spray coatings based on aqueous dispersions of PAA/ZnO TP indicated the formation of homogenous films incorporating ZnO TP on plasma activated poly(propylene) (PP) foils. The tetrapods are typically orientated in the deposited composite film. The XPS and FE-SEM results confirmed that ZnO TP surfaces are mainly fully covered with PAA. FIB FE-SEM cross sections showed the embedding of such PAA-modified arms into the PP material after the lamination at elevated temperature. Mechanical testing of laminated foils showed a significant improvement of the interfacial adhesion due to mechanical interlocking and chemical functionalization of the ZnO TP/PAA coatings. The crack surfaces displayed ZnO TP fractured in the center of the four connected nanorod-shaped arms as demonstrated by FE-SEM and TEM images. The TEM analysis showed that the mechanical stability of the ZnO TP is limited by planar defects at the TP joints.

Acknowledgement

The authors gratefully acknowledge the German Research Foundation/Deutsche Forschungsgemeinschaft (DFG) (Grant Award No: 320414069; GR 1709/22-1) and the NRW-Forschungskolleg “Leicht-Effizient-Mobil” for the financial support for this work.

The authors are thankful for the FE-SEM and FIB measurements by Nadine Buitkamp. In addition, we thank Professor Wolfgang Bremser for the access to the hydraulic pressure setup which allowed the joining of foils by lamination.

Appendix A. Supplementary data

Supplementary data to this article can be found online at <https://doi.org/10.1016/j.surfcoat.2019.06.083>.

References

- [1] C. Xiangfeng, J. Dongli, A.B. Djurišić, Y.H. Leung, *Chem. Phys. Lett.* 401 (2005) 426–429.
- [2] D. Calestani, M. Zha, R. Mosca, A. Zappettini, M.C. Carotta, V. Di Natale, L. Zanotti, *Sens. and Actuators B: Chemical* 144 (2010) 472–478.
- [3] Y. Qiu, S. Yang, *Adv. Funct. Mater.* 17 (2007) 1345–1352.
- [4] D. Gedamu, I. Paulowicz, S. Kaps, O. Lupan, S. Wille, G. Haidarschin, Y.K. Mishra, R. Adelung, *Adv. Mater.* (Deerfield Beach, Fla.) 26 (2014) 1541–1550.
- [5] Q. Wan, K. Yu, T.H. Wang, C.L. Lin, *Appl. Phys. Lett.* 83 (2003) 2253–2255.
- [6] A.B. Djurišić, Y.H. Leung, W.C.H. Choy, K.W. Cheah, W.K. Chan, *Appl. Phys. Lett.* 84 (2004) 2635–2637.
- [7] M.Y. Guo, A.M.C. Ng, F. Liu, A.B. Djurišić, W.K. Chan, H. Su, K.S. Wong, *J. Phys. Chem. C* 115 (2011) 11095–11101.
- [8] X. Jin, M. Götz, S. Wille, Y.K. Mishra, R. Adelung, C. Zollfrank, *Adv. Mater.* (Deerfield Beach, Fla.) 25 (2013) 1342–1347.
- [9] Y. Jiang, R. Sun, H.-B. Zhang, P. Min, D. Yang, Z.-Z. Yu, *Compos. A: Appl. Sci. Manuf.* 94 (2017) 104–112.
- [10] S. Piccolini, N. Castagnetti, R. Vanna, D. Mehn, M. Bedoni, F. Gramatica, M. Villani, D. Calestani, M. Pavesi, L. Lazzarini, A. Zappettini, C. Morasso, *RSC Adv.* 5 (2015) 93644–93651.
- [11] X. Jin, J. Strueben, L. Heepe, A. Kovalev, Y.K. Mishra, R. Adelung, S.N. Gorb, A. Staubitz, *Adv. Mater.* (Deerfield Beach, Fla.) 24 (2012) 5676–5680.
- [12] J. Han, Z. Zhu, S. Ray, A.K. Azad, W. Zhang, M. He, S. Li, Y. Zhao, *Appl. Phys. Lett.* 89 (2006) 31107.
- [13] Y.F. Hsu, Y.Y. Xi, C.T. Yip, A.B. Djurišić, W.K. Chan, *J. Appl. Phys.* 103 (2008) 83114.
- [14] M.C. Newton, P.A. Warburton, *Mater. Today* 10 (2007) 50–54.
- [15] G. Modi, *Adv. Nat. Sci. Nanosci. Nanotechnol.* 6 (2015) 33002.
- [16] Y.K. Mishra, S. Kaps, A. Schuchardt, I. Paulowicz, X. Jin, D. Gedamu, S. Wille, O. Lupan, R. Adelung, *KONA* 31 (2014) 92–110.
- [17] Y.K. Mishra, R. Adelung, *Mater. Today* 21 (2018) 631–651.
- [18] L. Yan, A. Uddin, H. Wang, *Nanomater. and Nanotechnol.* 5 (2015) 19.
- [19] R. Yang, H. Du, Z. Lin, L. Yang, H. Zhu, H. Zhang, Z. Tang, X. Gui, *Carbon* 141 (2019) 258–265.
- [20] Y.K. Mishra, S. Kaps, A. Schuchardt, I. Paulowicz, X. Jin, D. Gedamu, S. Freitag, M. Claus, S. Wille, A. Kovalev, S.N. Gorb, R. Adelung, *Part. Part. Syst. Charact.* 30 (2013) 775–783.
- [21] Y.K. Mishra, G. Modi, V. Cretu, V. Postica, O. Lupan, T. Reimer, I. Paulowicz, V. Hrkac, W. Benecke, L. Kienle, R. Adelung, *ACS Appl. Mater. & Interfaces* 7 (2015) 14303–14316.
- [22] J.S. Tawale, K.K. Dey, R. Pasricha, K.N. Sood, A.K. Srivastava, *Thin Solid Films* 519 (2010) 1244–1247.
- [23] J.P. Mondia, R. Sharma, J. Schäfer, W. Smith, Y.P. Zhao, Z.H. Lu, L.J. Wang, *Appl. Phys. Lett.* 93 (2008) 121102.
- [24] L.A. Ma, T.L. Guo, *Ceram. Int.* 39 (2013) 6923–6929.
- [25] J. Wang, X.M. Fan, K. Tian, Z.W. Zhou, Y. Wang, *Appl. Surf. Sci.* 257 (2011) 7763–7770.
- [26] J.-J. Delaunay, N. Kakoiyama, I. Yamada, *Mater. Chem. and Phys.* 104 (2007) 141–145.
- [27] Y.G. Wang, M. Sakurai, M. Aono, *Nanotechnology* 19 (2008) 245610.
- [28] F.Z. Wang, Z.Z. Ye, D.W. Ma, L.P. Zhu, F. Zhuge, *Mater. Lett.* 59 (2005) 560–563.
- [29] M. Zha, D. Calestani, A. Zappettini, R. Mosca, M. Mazzera, L. Lazzarini, L. Zanotti, *Nanotechnology* 19 (2008) 325603.
- [30] S. Rackauskas, K. Mustonen, T. Järvinen, M. Mattila, O. Klimova, H. Jiang, O. Tolochko, H. Lipsanen, E.I. Kauppinen, A.G. Nasibulin, *Nanotechnology* 23 (2012) 95502.
- [31] I. Hölken, M. Hoppe, Y.K. Mishra, S.N. Gorb, R. Adelung, M.J. Baum, *PCCP* 18 (2016) 7114–7123.
- [32] D. Kim, M. Jang, J. Seo, K.-H. Nam, H. Han, S.B. Khan, *Compos. Sci. Technol.* 75

- (2013) 84–92.
- [33] G. Blandenet, M. Court, Y. Lagarde, *Thin Solid Films* 77 (1981) 81–90.
- [34] E. Arca, K. Fleischer, I.v. Shvets, *J. Phys. Chem. C* 113 (2009) 21074–21081.
- [35] X. Yu, T.J. Marks, A. Facchetti, *Nat. Mater.* 15 (2016) (383 EP -).
- [36] A. Steele, I. Bayer, E. Loth, *Nano Lett.* 9 (2009) 501–505.
- [37] L. Pawlowski, *Surf. and Coat. Technol.* 203 (2009) 2807–2829.
- [38] P.J. Rivero, A. Urrutia, J. Goicoechea, F.J. Arregui, I.R. Matias, *Fifth International Conference on Sensing Technology (ICST)*, 2011: Nov. 28 2011–Dec. 1 2011, Palmerston North, New Zealand, IEEE, Piscataway, NJ, 2011, pp. 376–379.
- [39] Y. Li, S. Chen, M. Wu, J. Sun, *Adv. Mater. (Deerfield Beach, Fla.)* 26 (2014) 3344–3348.
- [40] P. Bihari, M. Vippola, S. Schultes, M. Praetner, A.G. Khandoga, C.A. Reichel, C. Coester, T. Tuomi, M. Rehberg, F. Krombach, *Particle and Fibre Toxicology* 5 (2008) 14.
- [41] A. Degen, M. Kosec, *J. Eur. Ceram. Soc.* 20 (2000) 667–673.
- [42] C.-p. Tso, C.-m. Zhung, Y.-h. Shih, Y.-M. Tseng, S.-c. Wu, R.-a. Doong, *Water science and technology a journal of the International Association on Water Pollution Research* 61 (2010) 127–133.
- [43] R. Rhodes, M. Horie, H. Chen, Z. Wang, M.L. Turner, B.R. Saunders, *J. Colloid Interface Sci.* 344 (2010) 261–271.
- [44] S. Liufu, H. Xiao, Y. Li, *Powder Technol.* 145 (2004) 20–24.
- [45] O. Mahian, A. Kianifar, S. Wongwises, *J. Clust. Sci.* 24 (2013) 1103–1114.
- [46] J. Lee, D. Bhattacharyya, A.J. Easteal, J.B. Metson, *Current Appl. Phys.* 8 (2008) 42–47.
- [47] K. Ghule, A.V. Ghule, B.-J. Chen, Y.-C. Ling, *Green Chem.* 8 (2006) 1034.
- [48] Carole Allyson Maria Tapley, Philip Laurence Lyth, Iain Michael Harper, *Zinc Oxide Dispersions*, (accessed 10 October 2018).
- [49] T. Gross, G. Kühn, W.E.S. Unger, *Surf. Interface Anal.* 41 (2009) 445–448.
- [50] R. Morent, N. de Geyter, C. Leys, L. Gengembre, E. Payen, *Surf. Interface Anal.* 40 (2008) 597–600.
- [51] E. Occhiello, M. Morra, G. Morini, F. Garbassi, P. Humphrey, *J. Appl. Polym. Sci.* 42 (1991) 551–559.
- [52] A. Bauer, D. Meinderink, I. Giner, H. Steger, J. Weitzl, G. Grundmeier, *Surf. and Coat. Technol.* 321 (2017) 128–135.
- [53] D. Meinderink, A.G. Orive, G. Grundmeier, *Surf. Interface Anal.* 50 (2018) 1224–1229.
- [54] M. Tatoulian, F. Arefi-Khonsari, L. Tatoulian, J. Amouroux, J.P. Borra, *Chem. Mater.* 18 (2006) 5860–5863.
- [55] M.E. Abd El-Aziz, S.M.M. Morsi, D.M. Salama, M.S. Abdel-Aziz, M.S. Abd Elwahed, E.A. Shaaban, A.M. Youssef, *Intern. J. Biol. Macromol.* 123 (2019) 856–865.
- [56] J. Friedrich, K. Altmann, S. Wettmarshausen, G. Hidde, *Plasma Process. Polym.* 14 (2017) 1600074.
- [57] Y.-C. Nho, J.-S. Park, Y.-M. Lim, *Polymers* 6 (2014) 890–898.
- [58] M. Fujii, H. Iwanaga, M. Ichihara, S. Takeuchi, *J. Cryst. Growth* 128 (1993) 1095–1098.
- [59] B. Ludi, M. Niederberger, *Dalton Transactions (Cambridge, England)* 2003 (2013) 12554–12568.
- [60] O. Lupan, L. Chow, G. Chai, B. Roldan, A. Naitabdi, A. Schulte, H. Heinrich, *Mater. Sci. and Eng.: B* 145 (2007) 57–66.
- [61] O. Ozcan, K. Pohl, B. Ozkaya, G. Grundmeier, *J. Adhes.* 89 (2013) 128–139.
- [62] M.C. Newton, S. Firth, T. Matsuura, P.A. Warburton, *J. Phys.: Conference Series* 26 (2006) 251–255.
- [63] D. Meinderink, A.G. Orive, S. Ewertowski, I. Giner, G. Grundmeier, *ACS Appl. Nano Mater.* 2 (2019) 831–843.
- [64] J. Kurdi, H. Ardelean, P. Marcus, P. Jonnard, F. Arefi-Khonsari, *Appl. Surf. Sci.* 189 (2002) 119–128.
- [65] B. Nisolf, F. Reniers, *J. Electron Spectrosc. Relat. Phenom.* 200 (2015) 311–331.
- [66] S. Zanini, C. Riccardi, E. Grimaldi, C. Colombo, A.M. Villa, A. Natalello, P. Gatti-Lafraconi, M. Lotti, S.M. Doglia, *J. Colloid Interface Sci.* 341 (2010) 53–58.
- [67] N.-Y. Cui, N.M.D. Brown, *Appl. Surf. Sci.* 189 (2002) 31–38.
- [68] B. Jaleh, P. Parvin, P. Wanichapichart, A.P. Saffar, A. Reyhani, *Appl. Surf. Sci.* 257 (2010) 1655–1659.
- [69] S. Wettmarshausen, J.F. Friedrich, A. Meyer-Plath, G. Kalinka, G. Hidde, S. Weidner, *J. Adhes. Sci. and Technol.* 29 (2015) 1628–1650.

Supporting Information

Spray Coating of Poly(acrylic Acid)/ZnO Tetrapod Adhesion Promoting Nanocomposite Films for Polymer Laminates

Dennis Meinderink¹, Karlo J.R. Nolkemper¹, Julius Bürger², Alejandro G. Orive¹,
Jörg K.N. Lindner², Guido Grundmeier^{1*}

¹Technical and Macromolecular Chemistry, University of Paderborn, Warburger Str. 100,
33098 Paderborn, Germany

²Department of Physics, University of Paderborn, Warburger Str. 100, 33098 Paderborn,
Germany.

*Corresponding author: g.grundmeier@tc.uni-paderborn.de

Phone +49 525160-5700

Fax +49 525160-3244

1 Synthesis and characterisation of ZnO tetrapods and poly(propylene) foils

The vapour growth of the ZnO TP was done in a commercial tube oven. The main setup is shown in the Figure S1.

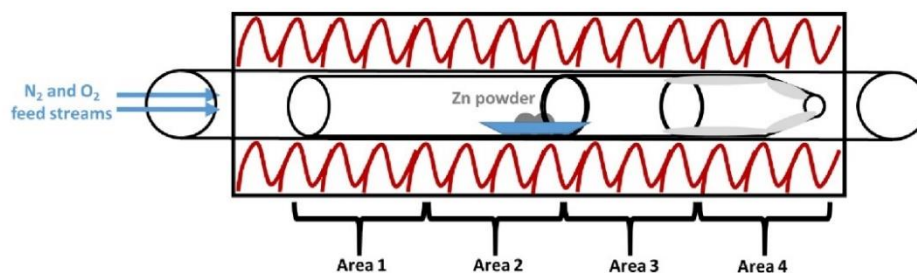


Figure S1. Schematic illustration of the configuration of the tube oven for the gas phase synthesis of ZnO tetrapods with metallic zinc as precursor and oxygen and nitrogen gas streams.

2 Joining tool for the poly(propylene) foils after spray coating processes

The spray coatings gave rise to homogenous composite films on poly(propylene) foils as illustrated in Figure S2.

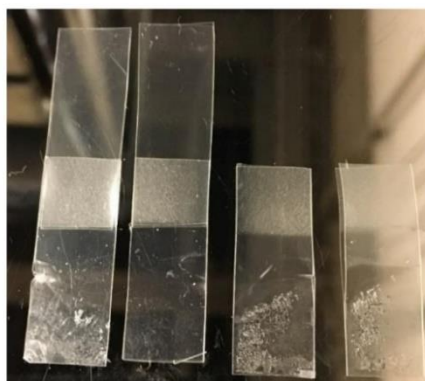


Figure S2. Photographical images of some joined specimens (the ones on the left) and only spray coated samples (the ones on the right) with 16 mg/ml ZnO TP in aqueous 0.085 mM PAA.

The joining was carried out by using a hydraulic pressure equipment with two hotplates. The foils were overlapped an area of 1.0 cm². A schematic image of the joining process is shown in Figure S3.

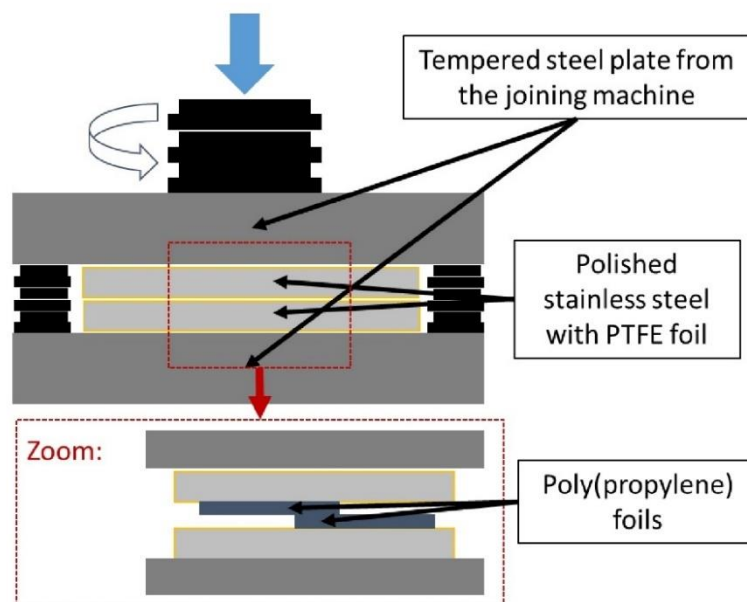


Figure S3. Schematic illustration of the hydraulic pressure equipment with hotplates and substrate positions.

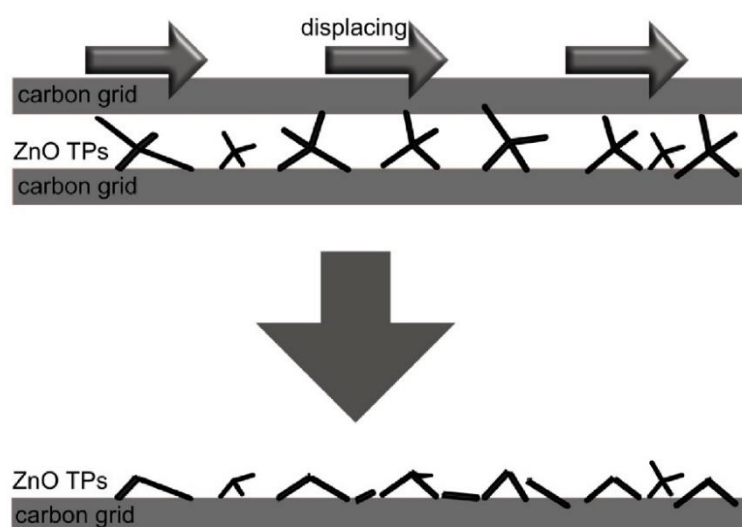


Figure S4. Schematic depiction of intentional cracking of zinc oxide tetrapods. ZnO TPs dispersed on a carbon grid are cracked by placing another carbon grid on top (carbon side on carbon side) and displacing the top grid with tweezers.

3 Characterisation of ZnO tetrapods and poly(propylene) foils

Additional characterization of ZnO TP was performed with Raman measurements. The details and results of the measurement are depicted in Figure S5.

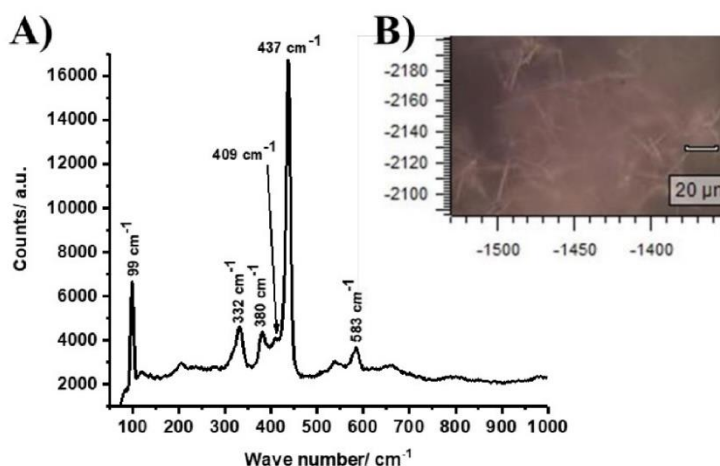


Figure S5. Raman measurement of ZnO tetrapod powder on gold coated silicon wafer. A) The Raman measurement was done with a green 532 nm laser (50 % power, 6.16 mW), 1800 l/mm grid and 6x10 s acquisition. B) The microscope image was done with an 50x objective.

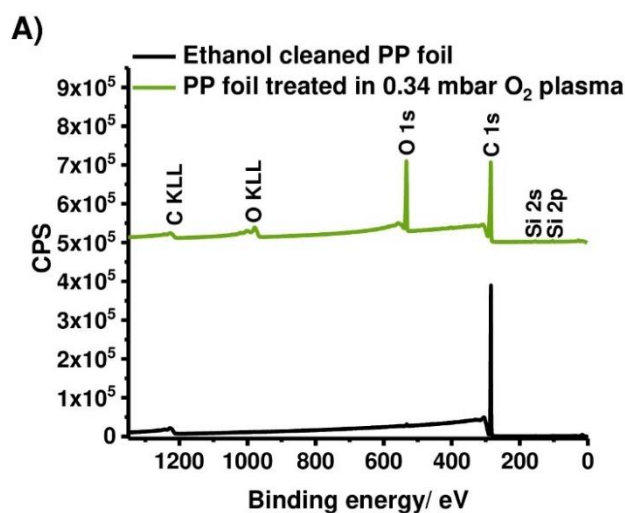


Figure S6. XPS survey spectra of poly(propylene) foil (black line) and poly(propylene) foil after oxygen plasma treatment at 0.34 mbar. Both samples were ethanol cleaned.

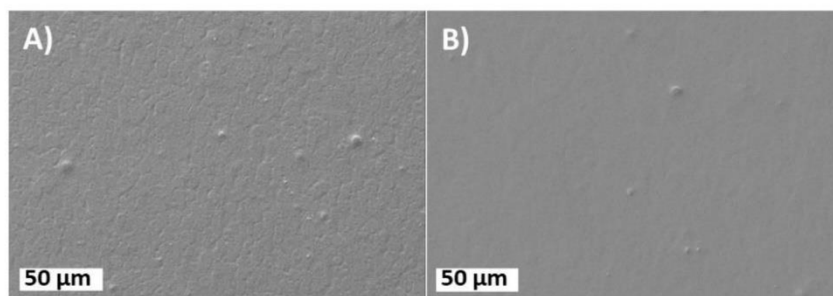


Figure S7. FE-SEM images of A) ethanol cleaned poly(propylene) foil and B) of ethanol cleaned poly(propylene) foil after spray coating of PAA film (aqueous 0.085 mM poly(acrylic acid), pH 7).

Table S1. XPS quantification results from surveys of spray coated PP foils with 0.085 mM PAA added with 8 mg/ml and 16 mg/ml ZnO TPs.

	8 mg/ml ZnO TP with 0.085 mM PAA/ At.-%	16 mg/ml ZnO TP with 0.085 mM PAA/ At.-%
C 1s	56.8	62.4
O 1s	31.2	24.5
Na 1s	10.8	5.0
Zn 2p 3/2	1.2	0.7
Si 2p	-	4.3
F 1s	-	2.7
N 1s	-	0.4

4 Shear test of jointed poly(propylene) foils without and with spray coatings

The shear tests were carried out in a modified peel test approach. Here, we fixed the plate under the clamp for the adjustment of the second PP foil. This is illustrated in Figure S8.

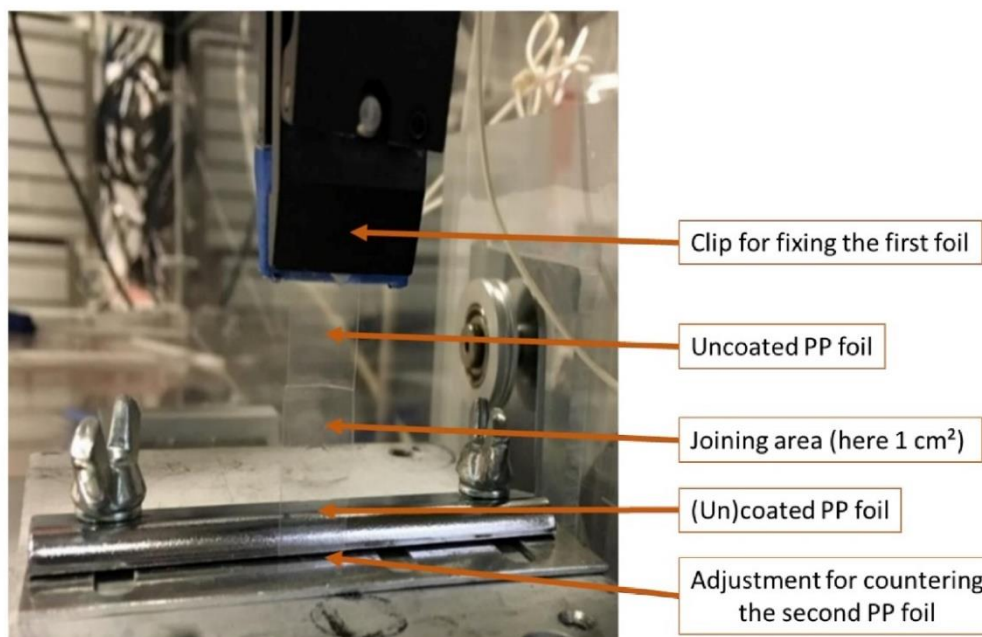


Figure S8. Experimental setup of the shear tests with solvent cleaned and jointed PP foils.

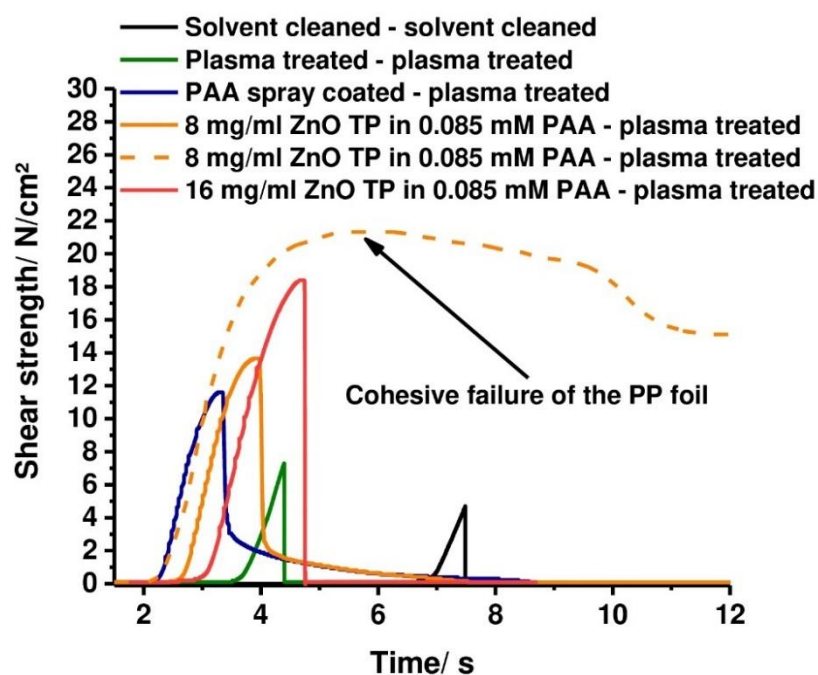


Figure S9. Tentative curves of the force-time/ force-distance plots of the shear tests.

All measurements were taken into account although some samples show some cohesive breaks in the PP foils like in the cases of the 8 mg/ml and 16 mg/ml ZnO TP in 0.085 mM PAA which underlines the high adhesion enhancement of the laminates with spray coatings. One example of these cohesive failures has been plotted in Figure S8.

5 Additional SEM images of the poly(propylene) foils after shear tests

Additional FIB profiles of the nanorods of the ZnO TP which are directly on the PP foil after spray coating were carried out. The corresponding FE-SEM images at two different positions are shown in Figure S10.

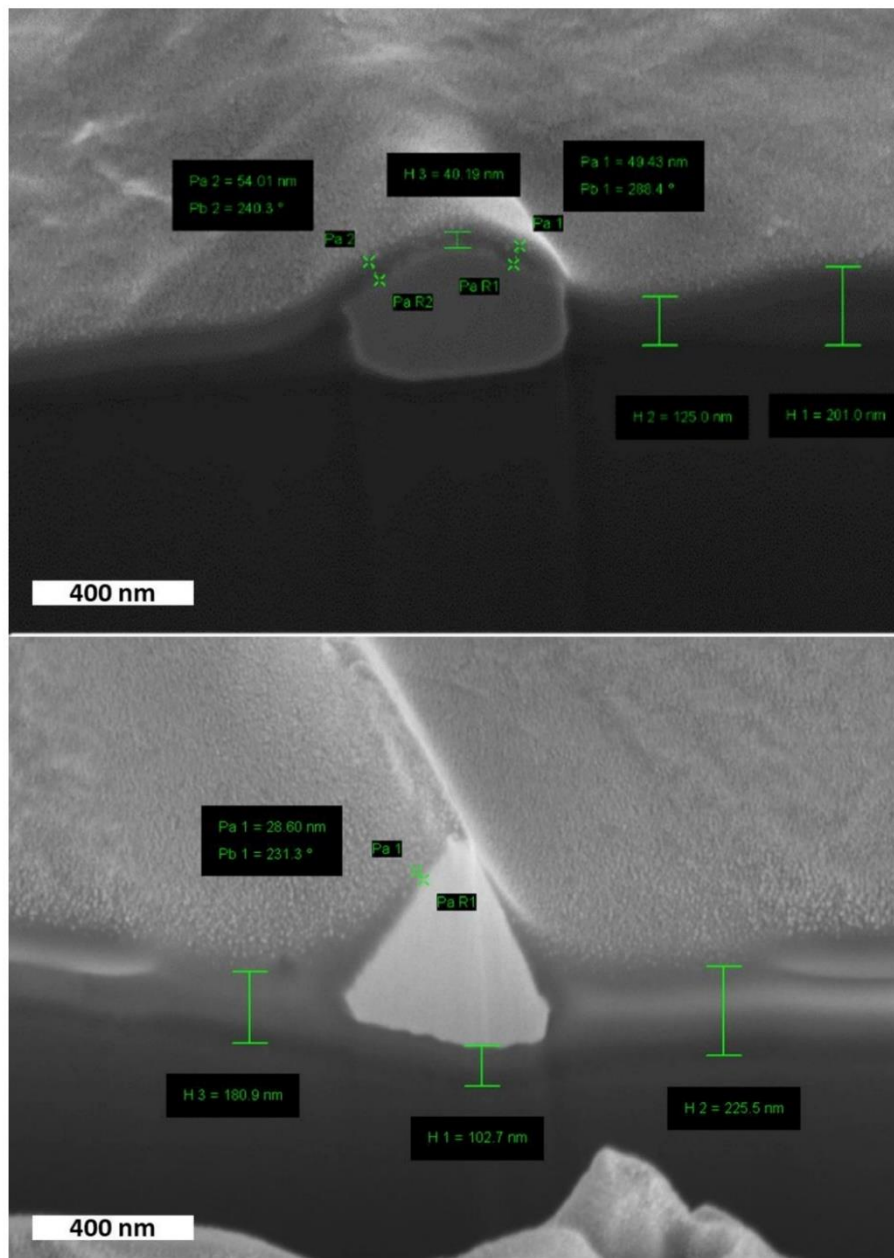


Figure S10. SEM images with FIB profiles of spray coatings with ZnO TP/ PAA on PP foil after shear test with measurements of the PAA layers.

To test the surfaces of the PP foils without spray coatings the blanc substrates were joined under similar conditions. After shear tests, the free surfaces were analysed with FE-SEM and the results are displayed in Figure S11.

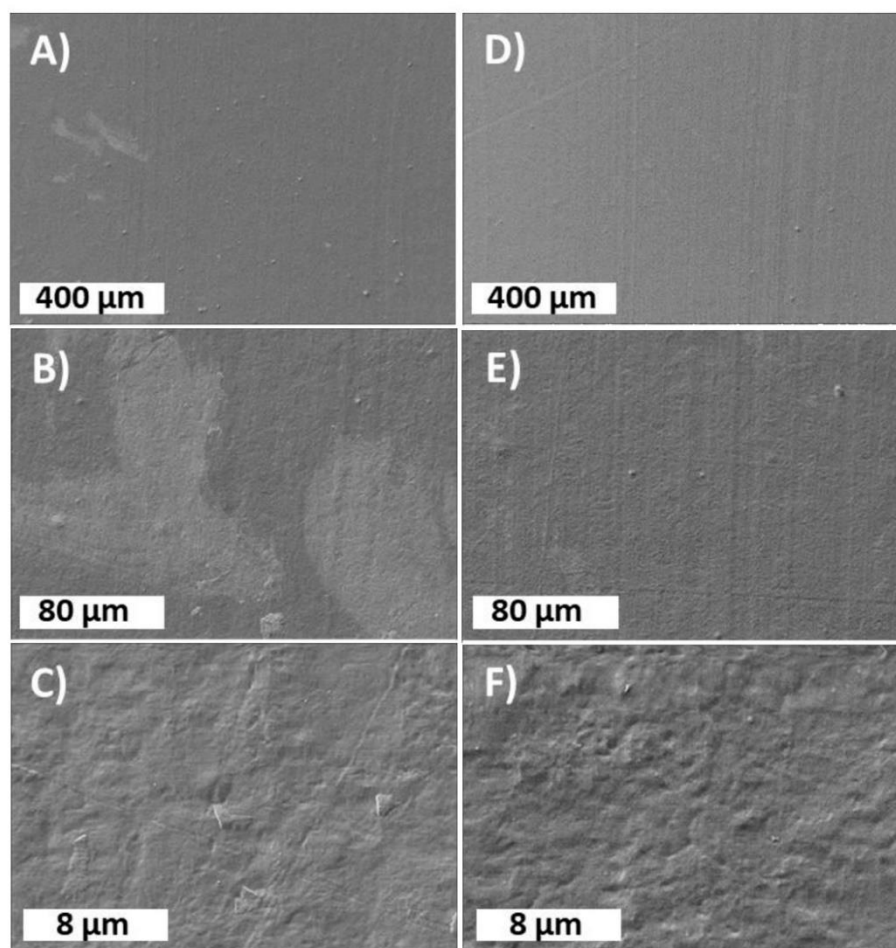


Figure S11. SEM images of PP foils after shear test. A)-C) solvent cleaned with three different magnifications and D)-F) both sides were plasma activated. The counter parts look similar (data not shown).

The behavior of the pure PAA spray coatings after shear tests are shown in the FE-SEM images in Figure S12.

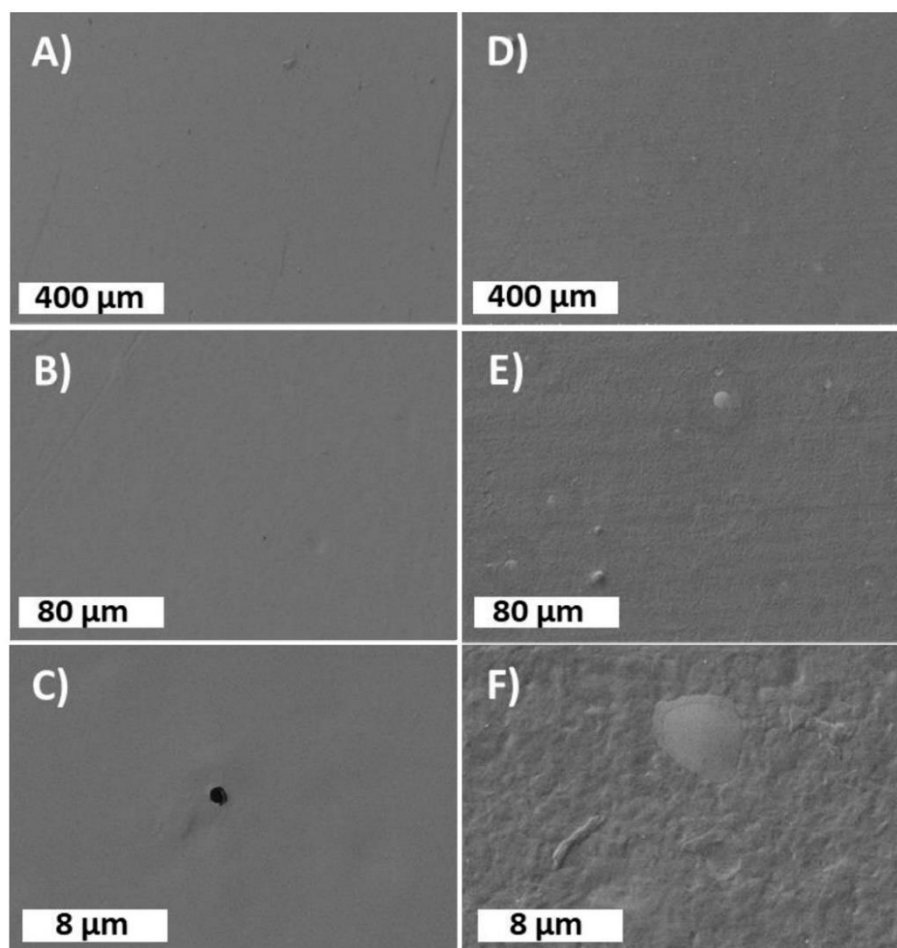


Figure S12. SEM images after shear test of the backsides of the PP foils. A)-C) spray coated with PAA and D)-F) only plasma activated counter part of the joining.

4 Overall discussion and conclusions

The fundamental understanding of interfacial reactions and bonding processes for long-term stable joints based on hybrid constructions are of significant importance in different sectors such as automotive or aerospace industry.³⁰⁸ Consequently, the scientific investigations regarding adhesion mechanisms for different industrially relevant materials like stainless steel, ZnO coatings and nanostructured HDG steel in combination with a low-cost, physiologically harmless and adhesion promoting polymer like PAA is of high interest for many technical and engineering applications. Therefore, this cumulative dissertation intensely contributes with the following four publications peer-reviewed in international journals to the adhesion science and engineering community with promising potential to be transferred to technical applications:

1. **Dennis Meinderink**, Alejandro Gonzalez Orive, Simon Ewertowski, Ignacio Giner, Guido Grundmeier, *Dependence of Poly(acrylic acid) Interfacial Adhesion on the Nanostructure of Electrodeposited ZnO Films*, ACS Applied Nano Mater. 2,2 (2019) 831-843
(abbreviated as **1. publication** in this thesis)
2. **D. Meinderink**, C. Kielar, O. Sobol, L. Ruhm, F. Rieker, K. Nolkemper, A. G. Orive, O. Ozcan, G. Grundmeier, *Effect of PAA-induced surface etching on the adhesion properties of ZnO nanostructured films*, International Journal of Adhesion and Adhesives 106 (2021) 102812
(abbreviated as **2. publication** in this thesis)
3. **D. Meinderink**, A. G. Orive, G. Grundmeier, *Electrodeposition of poly(acrylic acid) on stainless steel with enhanced adhesion properties*, Surface and Interface Analysis 50 (2018) 1224-1229
(abbreviated as **3. publication** in this thesis)
4. **Dennis Meinderink**, Karlo J.R. Nolkemper, Julius Bürger, Alejandro G. Orive, Jörg K.N. Lindner, Guido Grundmeier, *Spray Coating of Poly(acrylic Acid)/ZnO Tetrapod Adhesion Promoting Nanocomposite Films for Polymer Laminates*, Surface & Coatings Technology 375 (2019) 112-122
(abbreviated as **4. publication** in this thesis)

Within the **1. publication** of this PhD thesis, the focus was set on the molecular understanding of the adhesion mechanisms of PAA on stainless steel and different ZnO nanostructured surfaces. Interestingly, the single molecule force spectroscopy measurements on stainless steel showed only weak equilibrium desorption forces as plateaus in the corresponding force distance curves. Consequently, the carboxylate functions are basically physisorbed on the stainless steel surface in the aqueous solution. These results seem to be in contrast to the measured macroscopic desorption

forces in the **3. publication**, indicating strong interactions based on, for instance, acid-base behavior.

However, it has to be noted that the PAA chains are protonated in the **3. publication** caused by an additional cleaning step with hydrochloric acid (HCl) and the SMFS studies were performed in liquid solutions under deprotonating conditions. In addition, in the case of electropolymerisation the films were grown from acrylic acid monomers, while in the SMFS long PAA chains (450.000 g/mol) were attached to the cantilevers. Therefore, it is difficult to fully compare these two studies. Nevertheless, it can be seen that PAA has high potential to promote the adhesion between the epoxy-amine mode resin and the chosen stainless steel alloy in the **3. publication**. In addition, the SMFS results are reasonable when taking the preconditioning of the stainless steel by the enrichment of hydroxyl groups on the surface stated out in **1. publication** into account. Here, only weak adhesion interactions based on van der Waals and hydrogen bridges could be expected. Indeed, these fundamental studies were performed under model and precisely controlled conditions (pH, concentration, temperature, pre-treatments, etc). This fact underpins the need of surface pre-treatments to generate high adhesion performances. Nevertheless, the high work output leads to an overall understanding of the interfacial structure and bonding character of stainless steel and PAA which opens the door for further applications. Indeed, no further surface pre-treatments are necessary in the case of electropolymerisation demonstrated in the **3. publication** to reach high adhesion promoting effects.

Moreover, the SMFS were extended to the analysis of PAA on two different ZnO nanostructures deposited on stainless steel: ZnO nanorods and nanocrystalline ZnO films. As demonstrated in the graphical abstract of the **1. publication**, the molecular adhesion mechanisms could be proposed. In fact, the ZnO nanorods with a higher aspect ratio and therefore a higher amount of nonpolar surface areas exhibits a lot of accessible Zn^{II} atoms as reviewed in the introduction regarding the surface chemistry of ZnO crystals with wurtzite structure. The ZnO nanostructure and dwell time dependence of the molecular adhesion as evidenced by this SMFS work leads to a better understanding of the interfacial bond formation.¹⁶⁷ Intense multiple rupture events in the case of the ZnO nanorods and less multiple rupture events with low force levels and even with plateaus under increasing dwell times underline the effectivity of deprotonated PAA chains to efficiently bind to ZnO nanostructures.¹⁶⁷ Within this work, the SMFS shows the controllable measurement of molecular forces in the range to pN on technically interesting ZnO nanostructured surfaces on stainless steel. The combination of precise electrochemical deposition setups and the surface analysis by different methods like infrared based spectroscopy, X-ray photoelectron spectroscopy, and field-emission scanning electron microscopy lead to an accurate prediction of molecular forces.

4 Overall discussion and conclusions

Moreover, the **2. publication** highlights the increased understanding of the adhesion properties of ZnO nanostructures deposited via hydrothermal growth on hot-dipped galvanized steel as technically and industrially relevant substrates with the use of PAA containing solutions. These investigations underline the strong interactions between ZnO wurtzite crystals and carboxylate groups of the used PAA. The adhesion promoting after an immersion into dilute PAA aqueous solutions depends on the ZnO nanostructure (nanorods and platelet-like/nanocrystalline films). In other words, the aspect ratio of ZnO wurtzite crystals influences the effectivity of the enhancement of the adhesion with the immersion into PAA containing water-based solutions at neutral pH values. Discussing the molecular adhesion mechanisms in the **1. publication**, the results of the **2. publication** underline the macroscopic adhesion measured with the use of a model epoxy-amine adhesive which is additionally interesting for industrial applications. However, this work also demonstrates the difficulty in the identification of low surface concentrations of PAA, for example, with similar chemical functionalities such as adsorbed carbonates from the atmosphere, which is typical for metal oxide surfaces like ZnO. The building of the bridge between the molecular and macroscopic adhesion properties of poly(acrylic acid) and ZnO nanostructured films deposited via electrochemical and hydrothermal methods on technically relevant samples has been completed within this PhD work (combination of the **1. publication** and **2. publication**).

In the course of this scientific work, the macroscopic substantial adhesion promoting properties associated with the coating of stainless steel with a thin PAA layer were shown in the **3. publication** in figure 3. The surface chemical composition measured with infrared spectroscopy after different deposition times performed with precisely controllable electroinitiated polymerization (compare **3. publication**, figure 1¹⁷⁵) evidences the deposition of a thin layer of PAA. In addition, AFM measurements supported the successful modification with PAA layers of different thicknesses underpinning the precise deposition achieved by electropolymerisation. However, the peel-test results depending on the PAA layer thicknesses indicated an interfacial failure in the PAA films after a deposition time of around 150 s as displayed in Figure 26.

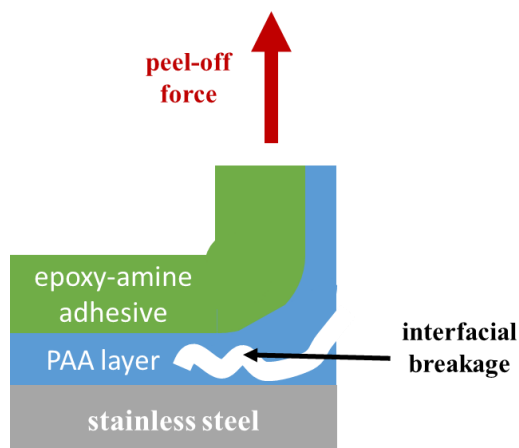


Figure 26. Schematic illustration of interfacial breakage in the PAA layer by reaching a critical PAA thickness.

4 Overall discussion and conclusions

Here, the backside analysis of the detached epoxy-amine films could give a hint of the adhesion failure by measuring, for instance, the surface concentration of transferred elements such as iron to the polymer side or nitrogen from the epoxy-amine resin to the metallic part. The need of an oxygen free electrolyte provides a difficult transfer to technical processes in industrial applications. However, it could be seen that even at low deposition times like 75 s the measured adhesion of the epoxy-amine adhesive on stainless steel is promoted by a factor of around 1.5. Therefore, the coating of metals with thin PAA layers by means of electrodeposition could lead to highly interesting pre-treatments. A main question is whether it is necessary to build up the PAA layer from monomers by polymerization to reach a grafted polymer film or if it is even better to deposit macromolecular PAA directly onto stainless steel by other deposition methods such as short-times spray coating. On the one hand, the stepwise monomer growth might lead to a higher coverage of PAA molecules caused by the lower steric hindering for the monomers to diffuse into poorly accessible edges and pores. On the other hand, the control of a radical-anionic polymerization comes with a lot of difficulties like the already mentioned oxygen free conditions and the electrochemical setup limiting the range of applications.

However, the application of these nanostructures to industrially relevant substrates like hot-dipped galvanized steel or polymer foils as mentioned in the introduction of this thesis is not as prominent as expected. To the best of our knowledge, no publications concerning the application of poly(acrylic acid) in combination with ZnO nanostructured dispersed in water-based solutions are available so far. Therefore, the **4. publication** contributes to a novel fast adhesion promoting application by spray coating with dilute aqueous ZnO TP/PAA dispersions supporting the “green chemistry” idea. Figure 27 summarizes the composition of the generated thin hybrid films on poly(propylene) foils after joining to sandwich structures.

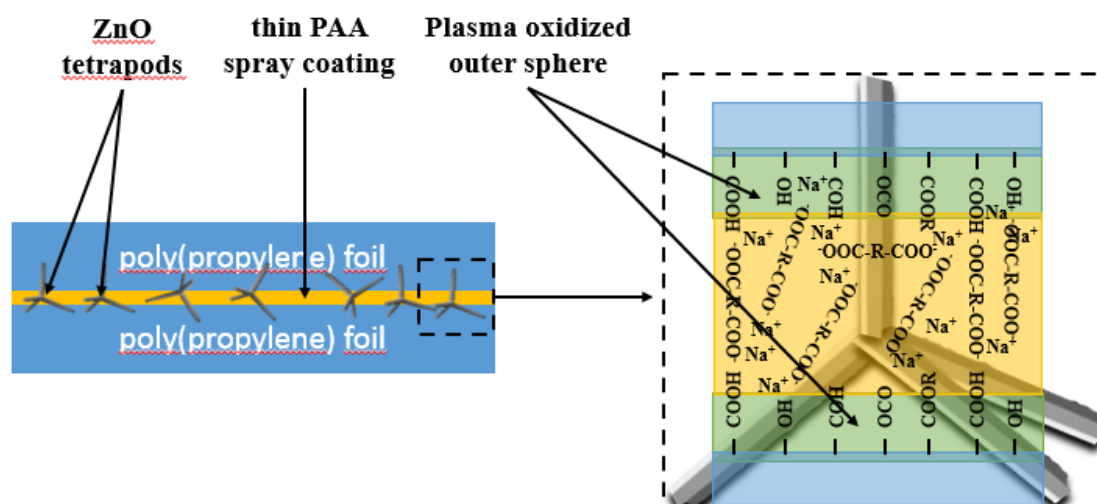


Figure 27. Illustration of the interfacial region of the poly(propylene)-poly(propylene) foil sandwich. Both foils were oxidized in an oxygen plasma and one of them was spray coated with a ZnO tetrapod/PAA dispersion.

The shear strength tests of PP-PP laminates without and with hybrid composite films showed a significant improvement in the adhesion. Even the coating with pure PAA films increased the shear strength by a factor of around 1.6. The proposed adhesion mechanisms could be summarized as mechanical interlocking by means of ZnO tetrapod structures embedded in the polymeric materials and chemical adhesion based on strong interactions between the oxidized surfaces of the poly(propylene) foils and the PAA molecules. These interactions could be based on electrostatic interactions, hydrogen bridges and a diffusive penetration of all materials where the latter one could increase even the total mechanical interlocking. The increasing of the hydrophilicity checked with water contact angle measurements before and after plasma oxidation could be taken into account by discussing the high wetting of the water-based dispersions by means of spray coating. Indeed, this fact could additionally explain the high adhesion performances.

All in all, all four publications contribute to the scientific understanding of molecular and macroscopic adhesion of PAA and ZnO nanostructures. The investigations support the possibility of using ZnO nanostructures in technical and industrial applications. On the one hand, the fundamental analysis with SMFS in the **1. publication** explained the high macroscopic adhesion performances after the treatment with PAA containing solutions from the **2. publication**. On the other hand, the application in industrial line processes of the spray coating (**4. publication**) and pre-treatment with PAA containing solutions (**2. publication**) could be discussed. Indeed, the experimental approaches both by means of SMFS and of macroscopic adhesion measurements in combination with surface analytics are building the bridge between the understanding of molecular and microscopic interfacial formation of interactions (see Figure 1 and Figure 4 in the introduction). Furthermore, in all experiments the depositions and pre-treatments were performed with dilute water-based solutions, which supports the green chemistry rules and underlines the appeal of using these approaches in applied technologies.

5 Outlook

The fundamental investigations of the molecular adhesion mechanisms measured by SMFS depending on the deposited ZnO nanostructure in the **1. publication** led to the prediction of macroscopic adhesion promoting performances as shown in the **2. publication**. Therefore, this approach can be applied to other highly adhesion promoting systems in future experiments. For example, the work of Mosebach et al. showed that the molecular adhesion forces between non-polar $\text{Al}_2\text{O}_3(11\text{-}20)$ single-crystals and $-\text{NH}_2/-\text{OH}$ functionalized cantilevers are based on acid-base interactions.³⁰⁹ This is in good agreement with the results of the works of Barthés-Labrousse investigating the model (amino-alcohol) molecules on pre-treated aluminum surfaces.^{310,311} However, these approaches can be extended to nanostructured aluminum samples prepared by the hydrothermal growth method as shown by Mattia et al.³¹² Furthermore, the understanding of molecular interactions of phosphonic acids as used by Thissen et al. on aluminum single-crystals³¹³ could be used in further SMFS experiments.

The principle of SMFS can be applied to the investigations of biologically relevant systems such as adhesins.^{314,315} The understanding of the interfacial interaction properties of these adhesion dominating proteins could give hints about the adsorption and colonization behavior of several bacteria on metal surfaces. Thus, the prediction, especially the optimization of implants and, in general, the development of materials with antibacterial adsorption performances lead to the reduction of infections of implants. Here, a manuscript is already in preparation.

The nanoetching effect of PAA on ZnO films demonstrated especially in the **2. publication** can be extended to in-situ experiments. With an in-situ Quartz Crystal Microbalance (QCM) and an ex-situ IRRAS and FE-SEM approach, the understanding of the nanoetching effect could be increased even further. Here, the deposition of ZnO nanostructured films on QCM crystals can be used for model systems comparable to the already used ZnO films. Then, the adsorption of PAA molecules can be followed with the QCM results. In addition, the ex-situ experiments could show the selective etching of the ZnO films and possible adsorptions of PAA chains. Indeed, results of previous experiments performed during this PhD work showed the dissolution of the ZnO crystals. Therefore, the exploration of the corrosion science of such ZnO films could also be helpful and necessary.

The precise deposition of poly(acrylic acid) by means of electropolymerisation and spray coating methods was successfully performed on stainless steel and poly(propylene) foils (**3. publication** and **4. publication**). However, the fundamental analysis and increased understanding of the adhesion mechanisms lead to further possible investigations based on these methods. Both methods could be extended to more industrially relevant substrates like the HDG substrate and aluminum and magnesium alloys. Moreover, the analysis of the difference between spray coated and electropolymerized substrates could be interesting regarding the adhesion failure.

For instance, the hypothesis could be that the electropolymerisation starting from small monomer molecules which are able to diffuse into pores and gaps of the substrate leads to a better adhesion performance than the spray coated substrates. In the latter case, the spray coated long polymer chains are probably not capable of diffusing into rough surface areas, which would result in lower adhesion forces. However, the spray coating method has the advantage that it can be used for up-scaled processes, while the same is difficult to achieve in the case of the electropolymerisation due to the need of removing oxygen from the electrolyte. Influencing parameters for the electropolymerisation such as the concentrations of initiator and monomer, applied current density/potential and solvent could have interesting effects. Indeed, in the case of the deposition of poly(acrylic acid) on stainless steel, the understanding of the adhesion promoting effect could be improved with the surface analysis of the detached films after peel-tests. Especially the identification of the transfer of zinc species from the stainless steel and the adhesive films should give a deeper understanding on: i) electrochemically initiated deposition in early deposition times of < 5 s and ii) adhesion promoting mechanisms. Here, a manuscript is already in preparation. Moreover, the pH-dependence on the deposition of the different samples could be useful for finding optimized adhesion promoting performances.

6 List of references

- (1) Özgür, Ü.; Alivov, Y. I.; Liu, C.; Teke, A.; Reshchikov, M. A.; Doğan, S.; Avrutin, V.; Cho, S.-J.; Morkoç, H. A comprehensive review of ZnO materials and devices. *Journal of Applied Physics* **2005**, 98 (4), 41301. DOI: 10.1063/1.1992666.
- (2) Schmidt-Mende, L.; MacManus-Driscoll, J. L. ZnO – nanostructures, defects, and devices. *Materials Today* **2007**, 10 (5), 40–48. DOI: 10.1016/S1369-7021(07)70078-0.
- (3) Ellmer, K.; Klein, A. ZnO and Its Applications. In *Transparent Conductive Zinc Oxide*; Ellmer, K., Klein, A., Rech, B., Eds.; Springer Series in Materials Science, 104; Springer, 2008; pp 1–33. DOI: 10.1007/978-3-540-73612-7_1.
- (4) Kołodziejczak-Radzimska, A.; Jesionowski, T. Zinc Oxide-From Synthesis to Application: A Review. *Materials (Basel, Switzerland)* **2014**, 7 (4), 2833–2881. DOI: 10.3390/ma7042833.
- (5) Wang, Y. W.; Zhang, L. D.; Wang, G. Z.; Peng, X. S.; Chu, Z. Q.; Liang, C. H. Catalytic growth of semiconducting zinc oxide nanowires and their photoluminescence properties. *Journal of Crystal Growth* **2002**, 234 (1), 171–175. DOI: 10.1016/S0022-0248(01)01661-X.
- (6) Holleman, A. F.; Wiberg, E.; Wiberg, N. *Lehrbuch der anorganischen Chemie*, 102., stark umgearb. u. verb. Aufl.; de Gruyter, 2007. DOI: 10.1515/9783110177701.
- (7) Masaru Saito; Shinobu Fujihara. Large photocurrent generation in dye -sensitized ZnO solar cells. *Energy & Environmental Science* **2008**, 1 (2), 280–283. DOI: 10.1039/B806096G.
- (8) Zhang, Q.; Dandeneau, C. S.; Zhou, X.; Cao, G. ZnO Nanostructures for Dye-Sensitized Solar Cells. *Advanced Materials* **2009**, 21 (41), 4087–4108. DOI: 10.1002/adma.200803827.
- (9) Ong, C. B.; Ng, L. Y.; Mohammad, A. W. A review of ZnO nanoparticles as solar photocatalysts: Synthesis, mechanisms and applications. *Renewable and Sustainable Energy Reviews* **2018**, 81, 536–551. DOI: 10.1016/j.rser.2017.08.020.
- (10) Zuzanna A.Lewicka; William W. Yu; Brittany L.Oliva; Elizabeth QuevedoContreras; Vicki L.Colvin. Photochemical behavior of nanoscale TiO₂ and ZnO sunscreen ingredients. *Journal of Photochemistry and Photobiology A: Chemistry* **2013**, 263, 24–33. DOI: 10.1016/j.jphotochem.2013.04.019.
- (11) Therias, S.; Larché, J.-F.; Bussière, P.-O.; Gardette, J.-L.; Murariu, M.; Dubois, P. Photochemical behavior of polylactide/ZnO nanocomposite films. *Biomacromolecules* **2012**, 13 (10), 3283–3291. DOI: 10.1021/bm301071w.
- (12) Valdez, C. N.; Braten, M.; Soria, A.; Gamelin, D. R.; Mayer, J. M. Effect of protons on the redox chemistry of colloidal zinc oxide nanocrystals. *Journal of the American Chemical Society* **2013**, 135 (23), 8492–8495. DOI: 10.1021/ja4035945.
- (13) Zuh, L.; Zeng, W. Room-temperature gas sensing of ZnO-based gas sensor: A review. *Sensors and Actuators A: Physical* **2017**, 267, 242–261. DOI: 10.1016/j.sna.2017.10.021.

- (14) Butt, H.-J.; Graf, K.; Kappl, M. *Physics and chemistry of interfaces*, 1. ed.; Physics textbook; Wiley-VCH, 2003. DOI: 10.1002/3527602313.
- (15) Butt, H.-J.; Kapple, M. *Surface and interfacial forces*; Physics textbook; Wiley-VCH Verlag GmbH & Co, 2010.
- (16) Sirelkhatim, A.; Mahmud, S.; Seeni, A.; Kaus, N. H. M.; Ann, L. C.; Bakhori, S. K. M.; Hasan, H.; Mohamad, D. Review on Zinc Oxide Nanoparticles: Antibacterial Activity and Toxicity Mechanism. *Nano-Micro Lett.* **2015**, 7 (3), 219–242. DOI: 10.1007/s40820-015-0040-x.
- (17) Paisoonsin, S.; Pornsunthorntawee, O.; Rujiravanit, R. Preparation and characterization of ZnO-deposited DBD plasma-treated PP packaging film with antibacterial activities. *Applied Surface Science* **2013**, 273, 824–835. DOI: 10.1016/j.apsusc.2013.03.026.
- (18) Dong, Y.; Argai, M.; He, B.; Tomovska, R.; Sun, T.; Martín-Fabiani, I. Zinc Oxide Superstructures in Colloidal Polymer Nanocomposite Films: Enhanced Antibacterial Activity through Slow Drying. *ACS Appl. Polym. Mater.* **2020**. DOI: 10.1021/acsapm.9b00991.
- (19) Tankhiwale, R.; Bajpai, S. K. Preparation, characterization and antibacterial applications of ZnO-nanoparticles coated polyethylene films for food packaging. *Colloids and surfaces. B, Biointerfaces* **2012**, 90, 16–20. DOI: 10.1016/j.colsurfb.2011.09.031.
- (20) Lin, C.-C.; Lee, M.-H.; Chi, M.-H.; Chen, C.-J.; Lin, H.-Y. Preparation of Zinc Oxide Nanoparticles Containing Spray and Barrier Films for Potential Photoprotection on Wound Healing. *ACS Omega* **2019**, 4 (1), 1801–1809. DOI: 10.1021/acsomega.8b02321.
- (21) Fahimmunisha, B. A.; Ishwarya, R.; AlSalhi, M. S.; Devanesan, S.; Govindarajan, M.; Vaseeharan, B. Green fabrication, characterization and antibacterial potential of zinc oxide nanoparticles using Aloe socotrina leaf extract: A novel drug delivery approach. *Journal of Drug Delivery Science and Technology* **2020**, 55, 101465. DOI: 10.1016/j.jddst.2019.101465.
- (22) Surwade, P.; Luxton, T.; Clar, J.; Xin, F.; Shah, V. Impact of the changes in bacterial outer membrane structure on the anti-bacterial activity of zinc oxide nanoparticles. *Journal of Nanoparticle Research* **2020**, 22 (2), 43. DOI: 10.1007/s11051-020-4767-z.
- (23) Liu, Y.; He, L.; Mustapha, A.; Li, H.; Hu, Z. Q.; Lin, M. Antibacterial activities of zinc oxide nanoparticles against Escherichia coli O157:H7. *Journal of Applied Microbiology* **2009**, 107 (4), 1193–1201. DOI: 10.1111/j.1365-2672.2009.04303.x.
- (24) Yamamoto, O. Influence of particle size on the antibacterial activity of zinc oxide. *International Journal of Inorganic Materials* **2001**, 3 (7), 643–646. DOI: 10.1016/S1466-6049(01)00197-0.
- (25) Raghupathi, K. R.; Koodali, R. T.; Manna, A. C. Size-dependent bacterial growth inhibition and mechanism of antibacterial activity of zinc oxide nanoparticles. *Langmuir: the ACS journal of surfaces and colloids* **2011**, 27 (7), 4020–4028. DOI: 10.1021/la104825u.

- (26) Kendall, K. *Molecular adhesion and its applications: The sticky universe*; Kluwer Academic/Plenum Publ, 2001.
- (27) Valtiner, M.; Grundmeier, G. Atomistic Understanding of Structure, Stability and Adhesion at ZnO/Electrolyte Interfaces. PhD thesis, Technische Universität Wien, Fakultät der technischen Chemie Wien, Austria, Wien, 2008.
- (28) Liufu, S.; Xiao, H.; Li, Y. Investigation of PEG adsorption on the surface of zinc oxide nanoparticles. *Powder Technology* **2004**, *145* (1), 20–24. DOI: 10.1016/j.powtec.2004.05.007.
- (29) Grundmeier, G.; Schmidt, W.; Stratmann, M. Corrosion protection by organic coatings: electrochemical mechanism and novel methods of investigation. *Electrochimica Acta* **2000**, *45* (15), 2515–2533. DOI: 10.1016/S0013-4686(00)00348-0.
- (30) Sørensen, P. A.; Kiil, S.; Dam-Johansen, K.; Weinell, C. E. Anticorrosive coatings: a review. *Journal of Coatings Technology and Research* **2009**, *6* (2), 135–176. DOI: 10.1007/s11998-008-9144-2.
- (31) Aung, M. M.; Li, W. J.; Lim, H. N. Improvement of Anticorrosion Coating Properties in Bio-Based Polymer Epoxy Acrylate Incorporated with Nano Zinc Oxide Particles. *Ind. Eng. Chem. Res.* **2020**, *59* (5), 1753–1763. DOI: 10.1021/acs.iecr.9b05639.
- (32) Lin, Y.-Y.; Lee, Y.-Y.; Chang, L.; Wu, J.-J.; Chen, C.-W. The influence of interface modifier on the performance of nanostructured ZnO/polymer hybrid solar cells. *Appl. Phys. Lett.* **2009**, *94* (6), 63308. DOI: 10.1063/1.3080203.
- (33) Wu, G.; Li, Z.; Zhang, X.; Lu, G. Charge Separation and Exciton Dynamics at Polymer/ZnO Interface from First-Principles Simulations. *The journal of physical chemistry letters* **2014**, *5* (15), 2649–2656. DOI: 10.1021/jz500980q.
- (34) Ozcan, O.; Pohl, K.; Ozkaya, B.; Grundmeier, G. Molecular Studies of Adhesion and De-Adhesion on ZnO Nanorod Film-Covered Metals. *The Journal of Adhesion* **2013**, *89* (2), 128–139. DOI: 10.1080/00218464.2012.731928.
- (35) Pohl, K.; Otte, J.; Thissen, P.; Giza, M.; Maxisch, M.; Schuhmacher, B.; Grundmeier, G. Adsorption and stability of self-assembled organophosphonic acid monolayers on plasma modified Zn–Mg–Al alloy surfaces. *Surface and Coatings Technology* **2013**, *218*, 99–107. DOI: 10.1016/j.surfcoat.2012.12.035.
- (36) Torun, B.; Giner, I.; Grundmeier, G.; Ozcan, O. In situ PM-IRRAS studies of organothiols and organosilane monolayers-ZnO interfaces at high water activities. *Surf. Interface Anal.* **2017**, *49* (1), 71–74. DOI: 10.1002/sia.6058.
- (37) Kandada, A. R. S.; Guarnera, S.; Tassone, F.; Lanzani, G.; Petrozza, A. Charge Generation at Polymer/Metal Oxide Interface: from Molecular Scale Dynamics to Mesoscopic Effects. *Adv. Funct. Mater.* **2014**, *24* (20), 3094–3099. DOI: 10.1002/adfm.201303689.

- (38) A. González-Orive; I. Giner; T. de los Arcos; A. Keller; G. Grundmeier. Analysis of polymer/oxide interfaces under ambient conditions – An experimental perspective. *Applied Surface Science* **2018**, *442*, 581–594. DOI: 10.1016/j.apsusc.2018.02.155.
- (39) Zhang, B.; Kong, T.; Xu, W.; Su, R.; Gao, Y.; Cheng, G. Surface functionalization of zinc oxide by carboxyalkylphosphonic acid self-assembled monolayers. *Langmuir: the ACS journal of surfaces and colloids* **2010**, *26* (6), 4514–4522. DOI: 10.1021/la9042827.
- (40) Yang, C.; Han, R.; Nie, M.; Wang, Q. Interfacial reinforcement mechanism in poly(lactic acid)/natural fiber biocomposites featuring ZnO nanowires at the interface. *Materials & Design* **2020**, *186*, 108332. DOI: 10.1016/j.matdes.2019.108332.
- (41) Lixiang Ma; Jingwei Zhang; Cuiqing Teng. Covalent functionalization of aramid fibers with zinc oxide nano-interphase for improved UV resistance and interfacial strength in composites. *Composites Science and Technology* **2020**, *188*, 107996. DOI: 10.1016/j.compscitech.2020.107996.
- (42) Fockaert, L.-L. I.; Ganzinga-Jurg, D.; Versluis, J.; Boelen, B.; Bakker, H. J.; Terryn, H.; Mol, J. M. C. Studying Chemisorption at Metal–Polymer Interfaces by Complementary Use of Attenuated Total Reflection–Fourier Transform Infrared Spectroscopy (ATR-FTIR) in the Kretschmann Geometry and Visible–Infrared Sum-Frequency Generation Spectroscopy (SFG). *J. Phys. Chem. C* **2020**, *124* (13), 7127–7138. DOI: 10.1021/acs.jpcc.9b10775.
- (43) Valtiner, M.; Grundmeier, G. Single molecules as sensors for local molecular adhesion studies. *Langmuir: the ACS journal of surfaces and colloids* **2010**, *26* (2), 815–820. DOI: 10.1021/la9022322.
- (44) Abdul Karim, M.; Park, Y.-D. A Review on Welding of Dissimilar Metals in Car Body Manufacturing. *Journal of Welding and Joining* **2020**, *38* (1), 8–23. DOI: 10.5781/JWJ.2020.38.1.1.
- (45) Goede, M.; Stehlin, M.; Rafflenbeul, L.; Kopp, G.; Beeh, E. Super Light Car—lightweight construction thanks to a multi-material design and function integration. *Eur. Transp. Res. Rev.* **2009**, *1* (1), 5–10. DOI: 10.1007/s12544-008-0001-2.
- (46) Sobek, W. Ultra-lightweight construction. *International Journal of Space Structures* **2016**, *31* (1), 74–80. DOI: 10.1177/0266351116643246.
- (47) Critchlow, G. W.; Brewis, D. M. Review of surface pretreatments for aluminium alloys. *International Journal of Adhesion and Adhesives* **1996**, *16* (4), 255–275. DOI: 10.1016/S0143-7496(96)00014-0.
- (48) Liston, E. M. Plasma Treatment for Improved Bonding: A Review. *The Journal of Adhesion* **1989**, *30* (1-4), 199–218. DOI: 10.1080/00218468908048206.

- (49) Mallick, P. K. Joining for lightweight vehicles. In *Materials, design and manufacturing for lightweight vehicles*; Mallick, P. K., Ed.; Woodhead Publishing in materials; CRC Press, 2010; pp 275–308. DOI: 10.1533/9781845697822.2.275.
- (50) Diebold, U.; Li, S.-C.; Schmid, M. Oxide surface science. *Annual review of physical chemistry* **2010**, *61*, 129–148. DOI: 10.1146/annurev.physchem.012809.103254.
- (51) Venables, J. D. Adhesion and durability of metal-polymer bonds. *Journal of Materials Science* **1984**, *19* (8), 2431–2453. DOI: 10.1007/BF00550796.
- (52) Abdeen, D. H.; El Hachach, M.; Koc, M.; Atieh, M. A. A Review on the Corrosion Behaviour of Nanocoatings on Metallic Substrates. *Materials (Basel, Switzerland)* **2019**, *12* (2). DOI: 10.3390/ma12020210.
- (53) Dennis Meinderink; Karlo J.R. Nolkemper; Julius Bürger; Alejandro G.Orive; Jörg K.N. Lindner; Guido Grundmeier. Spray coating of poly(acrylic acid)/ZnO tetrapod adhesion promoting nanocomposite films for polymer laminates. *Surface and Coatings Technology* **2019**, *375*, 112–122. DOI: 10.1016/j.surfcoat.2019.06.083.
- (54) Noei, H.; Jin, L.; Qiu, H.; Xu, M.; Gao, Y.; Zhao, J.; Kauer, M.; Wöll, C.; Muhler, M.; Wang, Y. Vibrational spectroscopic studies on pure and metal-covered metal oxide surfaces. *Phys. Status Solidi B* **2013**, *250* (6), 1204–1221. DOI: 10.1002/pssb.201248534.
- (55) Baruah, S.; Dutta, J. Hydrothermal growth of ZnO nanostructures. *Sci. Technol. Adv. Mater.* **2009**, *10* (1), 13001. DOI: 10.1088/1468-6996/10/1/013001.
- (56) Parker, T. M.; Condon, N. G.; Lindsay, R.; Leibsle, F. M.; Thornton, G. Imaging the polar (0001) and non-polar (1010) surfaces of ZnO with STM. *Surface Science* **1998**, *415* (3), L1046-L1050. DOI: 10.1016/S0039-6028(98)00563-9.
- (57) Kresse, G.; Dulub, O.; Diebold, U. Competing stabilization mechanism for the polar ZnO(0001)-Zn surface. *Phys. Rev. B* **2003**, *68* (24), 245409. DOI: 10.1103/PhysRevB.68.245409.
- (58) Levine, J. D.; Willis, A.; Bottoms, W. R.; Mark, P. Correlation of electronic, leed, and auger diagnostics on ZnO surfaces. *Surface Science* **1972**, *29* (1), 144–164. DOI: 10.1016/0039-6028(72)90075-1.
- (59) Kunat, M.; St. Girol, G.; Burghaus, U.; Wöll, C. The Interaction of Water with the Oxygen-Terminated, Polar Surface of ZnO. *J. Phys. Chem. B* **2003**, *107* (51), 14350–14356. DOI: 10.1021/jp030675z.
- (60) Wander, A.; Harrison, N. M. The stability of polar oxide surfaces: The interaction of H₂O with ZnO(0001) and ZnO(0001̄). *The Journal of Chemical Physics* **2001**, *115* (5), 2312–2316. DOI: 10.1063/1.1384030.
- (61) Wander, A.; Schedin, F.; Steadman, P.; Norris, A.; McGrath, R.; Turner, T. S.; Thornton, G.; Harrison, N. M. Stability of polar oxide surfaces. *Physical review letters* **2001**, *86* (17), 3811–3814. DOI: 10.1103/PhysRevLett.86.3811.

- (62) Valtiner, M.; Borodin, S.; Grundmeier, G. Preparation and characterisation of hydroxide stabilised ZnO(0001)-Zn-OH surfaces. *Physical chemistry chemical physics: PCCP* **2007**, 9 (19), 2406–2412. DOI: 10.1039/b617600c.
- (63) Valtiner, M.; Borodin, S.; Grundmeier, G. Stabilization and acidic dissolution mechanism of single-crystalline ZnO(0001) surfaces in electrolytes studied by in-situ AFM imaging and ex-situ LEED. *Langmuir: the ACS journal of surfaces and colloids* **2008**, 24 (10), 5350–5358. DOI: 10.1021/la7037697.
- (64) Valtiner, M.; Todorova, M.; Grundmeier, G.; Neugebauer, J. Temperature stabilized surface reconstructions at polar ZnO(0001). *Physical review letters* **2009**, 103 (6), 65502. DOI: 10.1103/PhysRevLett.103.065502.
- (65) Girard, R. T.; Tjernberg, O.; Chiaia, G.; Söderholm, S.; Karlsson, U. O.; Wigren, C.; Nylén, H.; Lindau, I. Electronic structure of ZnO(0001) studied by angle-resolved photoelectron spectroscopy. *Surface Science* **1997**, 373 (2), 409–417. DOI: 10.1016/S0039-6028(96)01181-8.
- (66) Valtiner, M.; Torrelles, X.; Pareek, A.; Borodin, S.; Gies, H.; Grundmeier, G. In Situ Study of the Polar ZnO(0001)–Zn Surface in Alkaline Electrolytes. *J. Phys. Chem. C* **2010**, 114 (36), 15440–15447. DOI: 10.1021/jp1047024.
- (67) P. Mitra; A.P. Chatterjee; H.S. Maiti. ZnO thin film sensor. *Materials Letters* **1998**, 35 (1-2), 33–38. DOI: 10.1016/S0167-577X(97)00215-2.
- (68) Gurlo, A. Nanosensors: towards morphological control of gas sensing activity. SnO₂, In₂O₃, ZnO and WO₃ case studies. *Nanoscale* **2011**, 3 (1), 154–165. DOI: 10.1039/c0nr00560f.
- (69) Li-Jian Bie; Xiao-Na Yan; Jing Yin; Yue-Qin Duan; Zhi-Hao Yuan. Nanopillar ZnO gas sensor for hydrogen and ethanol. *Sensors and Actuators B: Chemical* **2007**, 126 (2), 604–608. DOI: 10.1016/j.snb.2007.04.011.
- (70) Zhang, Y.; Ram, M. K.; Stefanakos, E. K.; Goswami, D. Y. Synthesis, Characterization, and Applications of ZnO Nanowires. *Journal of Nanomaterials* **2012**, 2012 (12), 1–22. DOI: 10.1155/2012/624520.
- (71) Skompska, M.; Zarębska, K. Electrodeposition of ZnO Nanorod Arrays on Transparent Conducting Substrates—a Review. *Electrochimica Acta* **2014**, 127, 467–488. DOI: 10.1016/j.electacta.2014.02.049.
- (72) Ahmad, M.; Zhu, J. ZnO based advanced functional nanostructures: synthesis, properties and applications. *J. Mater. Chem.* **2010**, 21 (3), 599–614. DOI: 10.1039/C0JM01645D.
- (73) Laurenti, M.; Porro, S.; Pirri, C. F.; Ricciardi, C.; Chiolerio, A. Zinc Oxide Thin Films for Memristive Devices: A Review. *Critical Reviews in Solid State and Materials Sciences* **2017**, 42 (2), 153–172. DOI: 10.1080/10408436.2016.1192988.
- (74) Marco Laurenti; Valentina Cauda. Porous Zinc Oxide Thin Films: Synthesis Approaches and Applications. *Coatings* **2018**, 8 (2), 67. DOI: 10.3390/coatings8020067.

- (75) Zhiqing Zhang; Jin Mu. Hydrothermal synthesis of ZnO nanobundles controlled by PEO–PPO–PEO block copolymers. *Journal of Colloid and Interface Science* **2007**, 307 (1), 79–82. DOI: 10.1016/j.jcis.2006.10.035.
- (76) Grothe, R.; Knust, S.; Meinderink, D.; Voigt, M.; Orive, A. G.; Grundmeier, G. Spray pyrolysis of thin adhesion-promoting ZnO films on ZnMgAl coated steel. *Surface and Coatings Technology* **2020**, 394, 125869. DOI: 10.1016/j.surfcoat.2020.125869.
- (77) Arca, E.; Fleischer, K.; Shvets, I. V. Influence of the Precursors and Chemical Composition of the Solution on the Properties of ZnO Thin Films Grown by Spray Pyrolysis. *J. Phys. Chem. C* **2009**, 113 (50), 21074–21081. DOI: 10.1021/jp907990z.
- (78) Aladko, L. S.; Komarov, V. Y.; Manakov, A. Y.; Ancharov, A. I. Phase diagram of the hexamethylenetetramine: water system. *Journal of Inclusion Phenomena and Macrocyclic Chemistry* **2007**, 59 (3), 389–391. DOI: 10.1007/s10847-007-9342-z.
- (79) Wang, L.; Dai, L.; Lei, M.; Chen, Y. Solubility of Hexamethylenetetramine in a Pure Water, Methanol, Acetic Acid, and Ethanol + Water Mixture from (299.38 to 340.35) K. *J. Chem. Eng. Data* **2008**, 53 (12), 2907–2909. DOI: 10.1021/je800662m.
- (80) Goux, A.; Pauporté, T.; Chivot, J.; Lincot, D. Temperature effects on ZnO electrodeposition. *Electrochimica Acta* **2005**, 50 (11), 2239–2248. DOI: 10.1016/j.electacta.2004.10.007.
- (81) Jung, M.-H.; Chu, M.-J. Synthesis of hexagonal ZnO nanodrums, nanosheets and nanowires by the ionic effect during the growth of hexagonal ZnO crystals. *J. Mater. Chem. C* **2014**, 2 (32), 6675–6682. DOI: 10.1039/C4TC01132E.
- (82) Wang, Z. L. ZnO nanowire and nanobelt platform for nanotechnology. *Materials Science and Engineering: R: Reports* **2009**, 64 (3), 33–71. DOI: 10.1016/j.mser.2009.02.001.
- (83) Mujtaba, J.; Sun, H.; Fang, F.; Ahmad, M.; Zhu, J. Fine control over the morphology and photocatalytic activity of 3D ZnO hierarchical nanostructures: capping vs. etching. *RSC Adv.* **2015**, 5 (69), 56232–56238. DOI: 10.1039/C5RA08325G.
- (84) Izaki, M. Preparation of Transparent and Conductive Zinc Oxide Films by Optimization of the Two-Step Electrolysis Technique. *J. Electrochem. Soc.* **1999**, 146 (12), 4517. DOI: 10.1149/1.1392667.
- (85) Yoshida, T.; Komatsu, D.; Shimokawa, N.; Minoura, H. Mechanism of cathodic electrodeposition of zinc oxide thin films from aqueous zinc nitrate baths. *Thin Solid Films* **2004**, 451-452, 166–169. DOI: 10.1016/j.tsf.2003.10.097.
- (86) Lin, Y.; Yang, J.; Zhou, X. Controlled synthesis of oriented ZnO nanorod arrays by seed-layer-free electrochemical deposition. *Applied Surface Science* **2011**, 258 (4), 1491–1494. DOI: 10.1016/j.apsusc.2011.09.113.
- (87) Xue, B.; Liang, Y.; Donglai, L.; Eryong, N.; Congli, S.; Huanhuan, F.; jingjing, X.; Yong, J.; Zhifeng, J.; Xiaosong, S. Electrodeposition from ZnO nano-rods to nano-sheets with only zinc

- nitrate electrolyte and its photoluminescence. *Applied Surface Science* **2011**, 257 (24), 10317–10321. DOI: 10.1016/j.apsusc.2011.05.132.
- (88) Newton, M. C.; Firth, S.; Matsuura, T.; Warburton, P. A. Synthesis and characterisation of zinc oxide tetrapod nanocrystals. *J. Phys.: Conf. Ser.*, 26 (1), 251. DOI: 10.1088/1742-6596/26/1/060.
- (89) Ronning, C.; Shang, N. G.; Gerhards, I.; Hofsäss, H.; Seibt, M. Nucleation mechanism of the seed of tetrapod ZnO nanostructures. *Journal of Applied Physics* **2005**, 98 (3), 34307. DOI: 10.1063/1.1997290.
- (90) Calestani, D.; Zha, M.; Mosca, R.; Zappettini, A.; Carotta, M. C.; Di Natale, V.; Zanolli, L. Growth of ZnO tetrapods for nanostructure-based gas sensors. *Sensors and Actuators B: Chemical* **2010**, 144 (2), 472–478. DOI: 10.1016/j.snb.2009.11.009.
- (91) Carotta, M. C.; Cervi, A.; Di Natale, V.; Gherardi, S.; Giberti, A.; Guidi, V.; Puzzovio, D.; Vendemiati, B.; Martinelli, G.; Sacerdoti, M.; Calestani, D.; Zappettini, A.; Zha, M.; Zanolli, L. ZnO gas sensors: A comparison between nanoparticles and nanotetrapods-based thick films. *Sensors and Actuators B: Chemical* **2009**, 137 (1), 164–169. DOI: 10.1016/j.snb.2008.11.007.
- (92) Roy, V. A. L.; Djurišić, A. B.; Chan, W. K.; Gao, J.; Lui, H. F.; Surya, C. Luminescent and structural properties of ZnO nanorods prepared under different conditions. *Appl. Phys. Lett.* **2003**, 83 (1), 141–143. DOI: 10.1063/1.1589184.
- (93) Xiangfeng, C.; Dongli, J.; Djurišić, A. B.; Leung, Y. H. Gas-sensing properties of thick film based on ZnO nano-tetrapods. *Chemical Physics Letters* **2005**, 401 (4-6), 426–429. DOI: 10.1016/j.cplett.2004.11.091.
- (94) Wan, Q.; Yu, K.; Wang, T. H.; Lin, C. L. Low-field electron emission from tetrapod-like ZnO nanostructures synthesized by rapid evaporation. *Appl. Phys. Lett.* **2003**, 83 (11), 2253–2255. DOI: 10.1063/1.1612899.
- (95) Han, J.; Zhu, Z.; Ray, S.; Azad, A. K.; Zhang, W.; He, M.; Li, S.; Zhao, Y. Optical and dielectric properties of ZnO tetrapod structures at terahertz frequencies. *Appl. Phys. Lett.* **2006**, 89 (3), 31107. DOI: 10.1063/1.2222329.
- (96) Mondia, J. P.; Sharma, R.; Schäfer, J.; Smith, W.; Zhao, Y. P.; Lu, Z. H.; Wang, L. J. An electrodynamically confined single ZnO tetrapod laser. *Appl. Phys. Lett.* **2008**, 93 (12), 121102. DOI: 10.1063/1.2987520.
- (97) Rackauskas, S.; Mustonen, K.; Järvinen, T.; Mattila, M.; Klimova, O.; Jiang, H.; Tolochko, O.; Lipsanen, H.; Kauppinen, E. I.; Nasibulin, A. G. Synthesis of ZnO tetrapods for flexible and transparent UV sensors. *Nanotechnology* **2012**, 23 (9), 95502. DOI: 10.1088/0957-4484/23/9/095502.

- (98) Tawale, J. S.; Dey, K. K.; Pasricha, R.; Sood, K. N.; Srivastava, A. K. Synthesis and characterization of ZnO tetrapods for optical and antibacterial applications. *Thin Solid Films* **2010**, *519* (3), 1244–1247. DOI: 10.1016/j.tsf.2010.08.077.
- (99) Wang, Y. G.; Sakurai, M.; Aono, M. Mass production of ZnO nanotetrapods by a flowing gas phase reaction method. *Nanotechnology* **2008**, *19* (24), 245610. DOI: 10.1088/0957-4484/19/24/245610.
- (100) Newton, M. C.; Warburton, P. A. ZnO tetrapod nanocrystals. *Materials Today* **2007**, *10* (5), 50–54. DOI: 10.1016/S1369-7021(07)70079-2.
- (101) Modi, G. Zinc oxide tetrapod: a morphology with multifunctional applications. *Adv. Nat. Sci: Nanosci. Nanotechnol.* **2015**, *6* (3), 33002. DOI: 10.1088/2043-6262/6/3/033002.
- (102) Yan, L.; Uddin, A.; Wang, H. ZnO Tetrapods: Synthesis and Applications in Solar Cells. *Nanomaterials and Nanotechnology* **2015**, *5*, 19. DOI: 10.5772/60939.
- (103) Mishra, Y. K.; Kaps, S.; Schuchardt, A.; Paulowicz, I.; Jin, X.; Gedamu, D.; Wille, S.; Lupan, O.; Adelung, R. Versatile Fabrication of Complex Shaped Metal Oxide Nano-Microstructures and Their Interconnected Networks for Multifunctional Applications. *KONA* **2014**, *31* (0), 92–110. DOI: 10.14356/kona.2014015.
- (104) Mishra, Y. K.; Adelung, R. ZnO tetrapod materials for functional applications. *Materials Today* **2018**, *21* (6), 631–651. DOI: 10.1016/j.mattod.2017.11.003.
- (105) Jin, X.; Strueben, J.; Heepe, L.; Kovalev, A.; Mishra, Y. K.; Adelung, R.; Gorb, S. N.; Staubitz, A. Joining the un-joinable: adhesion between low surface energy polymers using tetrapodal ZnO linkers. *Advanced materials (Deerfield Beach, Fla.)* **2012**, *24* (42), 5676–5680. DOI: 10.1002/adma.201201780.
- (106) Nasajpour, A.; Mandla, S.; Shree, S.; Mostafavi, E.; Sharifi, R.; Khalilpour, A.; Saghazadeh, S.; Hassan, S.; Mitchell, M. J.; Leijten, J.; Hou, X.; Moshaverinia, A.; Annabi, N.; Adelung, R.; Mishra, Y. K.; Shin, S. R.; Tamayol, A.; Khademhosseini, A. Nanostructured Fibrous Membranes with Rose Spike-Like Architecture. *Nano letters* **2017**, *17* (10), 6235–6240. DOI: 10.1021/acs.nanolett.7b02929.
- (107) Lupan, O.; Chow, L.; Chai, G.; Roldan, B.; Naitabdi, A.; Schulte, A.; Heinrich, H. Nanofabrication and characterization of ZnO nanorod arrays and branched microrods by aqueous solution route and rapid thermal processing. *Materials Science and Engineering: B* **2007**, *145* (1-3), 57–66. DOI: 10.1016/j.mseb.2007.10.004.
- (108) Gedamu, D.; Paulowicz, I.; Kaps, S.; Lupan, O.; Wille, S.; Haidarschin, G.; Mishra, Y. K.; Adelung, R. Rapid fabrication technique for interpenetrated ZnO nanotetrapod networks for fast UV sensors. *Advanced materials (Deerfield Beach, Fla.)* **2014**, *26* (10), 1541–1550. DOI: 10.1002/adma.201304363.

- (109) Mishra, Y. K.; Kaps, S.; Schuchardt, A.; Paulowicz, I.; Jin, X.; Gedamu, D.; Freitag, S.; Claus, M.; Wille, S.; Kovalev, A.; Gorb, S. N.; Adelung, R. Fabrication of Macroscopically Flexible and Highly Porous 3D Semiconductor Networks from Interpenetrating Nanostructures by a Simple Flame Transport Approach. *Part. Part. Syst. Charact.* **2013**, *30* (9), 775–783. DOI: 10.1002/ppsc.201300197.
- (110) Shiojiri, M.; Kaito, C. Structure and growth of ZnO smoke particles prepared by gas evaporation technique. *Journal of Crystal Growth* **1981**, *52*, 173–177. DOI: 10.1016/0022-0248(81)90189-5.
- (111) Nishio, K.; Isshiki, T.; Kitano, M.; Shiojiri, M. Structure and growth mechanism of tetrapod-like ZnO particles. *Philosophical Magazine A* **1997**, *76* (4), 889–904. DOI: 10.1080/01418619708214216.
- (112) Takeuchi, S.; Iwanaga, H.; Fujii, M. Octahedral multiple-twin model of tetrapod ZnO crystals. *Philosophical Magazine A* **1994**, *69* (6), 1125–1129. DOI: 10.1080/01418619408242243.
- (113) Yu, W. D.; Li, X. M.; Gao, X. D. Homogeneous-catalytic synthesis of tetrapodlike ZnO nanocrystals and their photoluminescence properties. *Chemical Physics Letters* **2004**, *390* (1), 296–300. DOI: 10.1016/j.cplett.2004.04.032.
- (114) Manna, L.; Milliron, D. J.; Meisel, A.; Scher, E. C.; Alivisatos, A. P. Controlled growth of tetrapod-branched inorganic nanocrystals. *Nature Mater* **2003**, *2* (6), 382–385. DOI: 10.1038/nmat902.
- (115) Iwanaga, H.; Fujii, M.; Takeuchi, S. Growth model of tetrapod zinc oxide particles. *Journal of Crystal Growth* **1993**, *134* (3), 275–280. DOI: 10.1016/0022-0248(93)90136-K.
- (116) Fujii, M.; Iwanaga, H.; Ichihara, M.; Takeuchi, S. Structure of tetrapod-like ZnO crystals. *Journal of Crystal Growth* **1993**, *128* (1-4), 1095–1098. DOI: 10.1016/S0022-0248(07)80104-7.
- (117) Iwanaga, H.; Fujii, M.; Ichihara, M.; Takeuchi, S. Some evidence for the octa-twin model of tetrapod ZnO particles. *Journal of Crystal Growth* **1994**, *141* (1), 234–238. DOI: 10.1016/0022-0248(94)90116-3.
- (118) Ebnesajjad, S., Ed. *Handbook of Adhesives and Surface Preparation: Plastics Design Library*; William Andrew Publishing, 2011.
- (119) Habenicht, G. *Kleben: Grundlagen, Technologie, Anwendungen*, 2., völlig Neubearb. und erw. Aufl.; Springer, 1990.
- (120) Lieng-Huang Lee. *Fundamentals of Adhesion*; Springer US, 1991.
- (121) Lee, L.-H., Ed. *Fundamentals of adhesion*; Plenum Press, 1991.
- (122) Fowkes, F. M. Role of acid-base interfacial bonding in adhesion. *Journal of Adhesion Science and Technology* **1987**, *1* (1), 7–27. DOI: 10.1163/156856187X00049.
- (123) Atkins, P. W.; Paula, J. de. *Physikalische Chemie*, 4., vollst. überarb. Aufl.; Wiley-VCH, 2006.

- (124) Leite, F. L.; Bueno, C. C.; Da Róz, A. L.; Ziemath, E. C.; Oliveira, O. N. Theoretical models for surface forces and adhesion and their measurement using atomic force microscopy. *International journal of molecular sciences* **2012**, *13* (10), 12773–12856. DOI: 10.3390/ijms131012773.
- (125) Hamaker, H. C. The London—van der Waals attraction between spherical particles. *Physica* **1937**, *4* (10), 1058–1072. DOI: 10.1016/S0031-8914(37)80203-7.
- (126) VanOss, C. J. *Interfacial forces in aqueous media*; Dekker, 1994.
- (127) Pletincx, S.; Fockaert, L. L. I.; Mol, J. M. C.; Hauffman, T.; Terryn, H. Probing the formation and degradation of chemical interactions from model molecule/metal oxide to buried polymer/metal oxide interfaces. *npj Mater Degrad* **2019**, *3* (1), 17. DOI: 10.1038/s41529-019-0085-2.
- (128) Watts, J. F.; Chehimi, M. M.; Gibson, E. M. Acid-Base Interactions in Adhesion: The Characterization of Surfaces & Interfaces by XPS. *The Journal of Adhesion* **1992**, *39* (2-3), 145–156. DOI: 10.1080/00218469208026546.
- (129) Hoffmann, R. A chemical and theoretical way to look at bonding on surfaces. *Rev. Mod. Phys.* **1988**, *60* (3), 601–628. DOI: 10.1103/RevModPhys.60.601.
- (130) Landoulsi, J.; Dupres, V. Probing peptide-inorganic surface interaction at the single molecule level using force spectroscopy. *Chemphyschem : a European journal of chemical physics and physical chemistry* **2011**, *12* (7), 1310–1316. DOI: 10.1002/cphc.201100007.
- (131) McCafferty, E. Lewis Acid/Lewis Base Effects in Corrosion and Polymer Adhesion at Aluminum Surfaces. *J. Electrochem. Soc.* **2003**, *150* (7), B342. DOI: 10.1149/1.1580135.
- (132) McCafferty, E. Acid-base effects in polymer adhesion at metal surfaces. *Journal of Adhesion Science and Technology* **2002**, *16* (3), 239–255. DOI: 10.1163/156856102317295478.
- (133) Mercier, D.; Rouchaud, J.-C.; Barthés-Labrousse, M.-G. Interaction of amines with native aluminium oxide layers in non-aqueous environment: Application to the understanding of the formation of epoxy-amine/metal interphases. *Applied Surface Science* **2008**, *254* (20), 6495–6503. DOI: 10.1016/j.apsusc.2008.04.010.
- (134) Fritah, Z.; Drouet, C.; Thouron, C.; Aufray, M. Direct evidence of amine-metal reaction in epoxy systems: An in situ calorimetry study of the interphase formation. *Progress in Organic Coatings* **2020**, *148*, 105769. DOI: 10.1016/j.porgcoat.2020.105769.
- (135) Bockenheimer, C.; Valeske, B.; Possart, W. Network structure in epoxy aluminium bonds after mechanical treatment. *International Journal of Adhesion and Adhesives* **2002**, *22* (5), 349–356. DOI: 10.1016/S0143-7496(02)00014-3.
- (136) Shchukin, D. G.; Skorb, E.; Belova, V.; Möhwald, H. Ultrasonic cavitation at solid surfaces. *Advanced Materials* **2011**, *23* (17), 1922–1934. DOI: 10.1002/adma.201004494.

- (137) Brotschie, A.; Borisova, D.; Belova, V.; Möhwald, H.; Shchukin, D. Ultrasonic Modification of Aluminum Surfaces: Comparison between Thermal and Ultrasonic Effects. *J. Phys. Chem. C* **2012**, *116* (14), 7952–7956. DOI: 10.1021/jp3016408.
- (138) Johnsen, B. B.; Lapique, F.; Bjørgum, A.; Walmsley, J.; Tanem, B. S.; Luksepp, T. The effect of pre-bond moisture on epoxy-bonded sulphuric acid anodised aluminium. *International Journal of Adhesion and Adhesives* **2004**, *24* (3), 183–191. DOI: 10.1016/j.ijadhadh.2003.09.002.
- (139) Baldan, A. Adhesively-bonded joints and repairs in metallic alloys, polymers and composite materials: Adhesives, adhesion theories and surface pretreatment. *J Mater Sci* **2004**, *39* (1), 1–49. DOI: 10.1023/B:JMSC.0000007726.58758.e4.
- (140) Das, K.; Bose, S.; Bandyopadhyay, A. TiO₂ nanotubes on Ti: Influence of nanoscale morphology on bone cell-materials interaction. *Journal of biomedical materials research. Part A* **2009**, *90* (1), 225–237. DOI: 10.1002/jbm.a.32088.
- (141) Park, J.; Bauer, S.; Schlegel, K. A.; Neukam, F. W.; Mark, K. von der; Schmuki, P. TiO₂ nanotube surfaces: 15 nm—an optimal length scale of surface topography for cell adhesion and differentiation. *Small (Weinheim an der Bergstrasse, Germany)* **2009**, *5* (6), 666–671. DOI: 10.1002/smll.200801476.
- (142) Venables, J. D.; McNamara, D. K.; Chen, J. M.; Sun, T. S.; Hopping, R. L. Oxide morphologies on aluminum prepared for adhesive bonding. *Applications of Surface Science* **1979**, *3* (1), 88–98. DOI: 10.1016/0378-5963(79)90063-1.
- (143) Dillingham, R. G.; Boerio, F. J. Interphase Composition in Aluminum/Epoxy Adhesive Joints. *The Journal of Adhesion* **1987**, *24* (2-4), 315–335. DOI: 10.1080/00218468708075434.
- (144) Bromberg, L. Polyether-Modified Poly(acrylic acid): Synthesis and Applications. *Ind. Eng. Chem. Res.* **1998**, *37* (11), 4267–4274. DOI: 10.1021/ie980358s.
- (145) Fresnais, J.; Yan, M.; Courtois, J.; Bostelmann, T.; Bée, A.; Berret, J.-F. Poly(acrylic acid)-coated iron oxide nanoparticles: quantitative evaluation of the coating properties and applications for the removal of a pollutant dye. *Journal of Colloid and Interface Science* **2013**, *395*, 24–30. DOI: 10.1016/j.jcis.2012.12.011.
- (146) Tan, A. L.; Khoo, L. J.; Alias, S. S.; Mohamad, A. A. ZnO nanoparticles and poly(acrylic) acid-based polymer gel electrolyte for photo electrochemical cell. *J Sol-Gel Sci Technol* **2012**, *64* (1), 184–192. DOI: 10.1007/s10971-012-2846-z.
- (147) Tian, B.; Liu, S.; Wu, S.; Lu, W.; Wang, D.; Jin, L.; Hu, B.; Li, K.; Wang, Z.; Quan, Z. pH-responsive poly (acrylic acid)-gated mesoporous silica and its application in oral colon targeted drug delivery for doxorubicin. *Colloids and surfaces. B, Biointerfaces* **2017**, *154*, 287–296. DOI: 10.1016/j.colsurfb.2017.03.024.

- (148) Yang, S.; Fu, Y.; Jeong, S. H.; Park, K. Application of poly(acrylic acid) superporous hydrogel microparticles as a super-disintegrant in fast-disintegrating tablets. *The Journal of pharmacy and pharmacology* **2004**, *56* (4), 429–436. DOI: 10.1211/0022357023015.
- (149) Qingchun, Z.; Changling, L. Synthesis and characterization superabsorbent-ethanol polyacrylic acid gels. *J. Appl. Polym. Sci.* **2007**, *105* (6), 3458–3461. DOI: 10.1002/app.26398.
- (150) Roma-Luciw, R.; Sarraf, L.; Morcellet, M. Concentration effects during the formation of poly (acrylic acid)-metal complexes in aqueous solutions. *Polymer Bulletin* **2000**, *45* (4), 411–418. DOI: 10.1007/s002890070015.
- (151) Tomida, T.; Hamaguchi, K.; Tunashima, S.; Katoh, M.; Masuda, S. Binding Properties of a Water-Soluble Chelating Polymer with Divalent Metal Ions Measured by Ultrafiltration. Poly(acrylic acid). *Ind. Eng. Chem. Res.* **2001**, *40* (16), 3557–3562. DOI: 10.1021/ie0009839.
- (152) Yan, R.; He, W.; Zhai, T.; Ma, H. Anticorrosion organic–inorganic hybrid films constructed on iron substrates using self-assembled polyacrylic acid as a functional bottom layer. *Electrochimica Acta* **2019**, *295*, 942–955. DOI: 10.1016/j.electacta.2018.11.117.
- (153) Abzaeva, K. A.; Voronkov, M. G.; Zhilitskaya, L. V.; Burovik, D. A.; Makarov, V. A.; Belozerskaya, G. G. Pharmacological activity of ziacryl, a zinc salt of polyacrylic acid. *Pharm Chem J* **2009**, *43* (12), 661–664. DOI: 10.1007/s11094-010-0376-y.
- (154) Hill, R. G.; Labok, S. A. The influence of polyacrylic acid molecular weight on the fracture of zinc polycarboxylate cements. *J Mater Sci* **1991**, *26* (1), 67–74. DOI: 10.1007/BF00576034.
- (155) Smith, D. C. Development of glass-ionomer cement systems. *Biomaterials* **1998**, *19* (6), 467–478. DOI: 10.1016/S0142-9612(97)00126-9.
- (156) Gao, D.; Zhao, P.; Lyu, B.; Ma, J.; Zhang, Y. Composite based on poly(acrylic acid)/modified attapulgite/zinc oxide as a flame retardant of cotton fabrics. *Cellulose*, 1–14. DOI: 10.1007/s10570-019-02948-2.
- (157) Padilla, A.; Vázquez, A.; Castaño, V. M. Synthesis and characterization of polyacrylic acid–zinc oxide composites. *J. Mater. Res.* **1991**, *6* (11), 2452–2456. DOI: 10.1557/JMR.1991.2452.
- (158) Chen, W.-S.; Huang, D.-A.; Chen, H.-C.; Shie, T.-Y.; Hsieh, C.-H.; Liao, J.-D.; Kuo, C. Fabrication of Polycrystalline ZnO Nanotubes from the Electrospinning of Zn ²⁺ /Poly(acrylic acid). *Crystal Growth & Design* **2009**, *9* (9), 4070–4077. DOI: 10.1021/cg900297q.
- (159) Brostow, W.; Castaño, V. M.; Huanosta, A.; Icaza, M. de; Nicho, M. E.; Saniger, J. M. Poly(acrylic acid) + zinc diacetate composites: High temperature service and electric conductivity. *Materials Research Innovations* **1999**, *3* (2), 85–91. DOI: 10.1007/s100190050130.
- (160) Leadley, S. R.; Watts, J. F. The use of XPS to examine the interaction of poly(acrylic acid) with oxidised metal substrates. *Journal of Electron Spectroscopy and Related Phenomena* **1997**, *85* (1), 107–121. DOI: 10.1016/S0368-2048(97)00028-5.

- (161) Wu, H.-S.; Jone, H.-C. Kinetic Study and Characterization of Poly(acrylic acid) and Metal Oxide. *Ind. Eng. Chem. Res.* **1997**, *36* (6), 2006–2011. DOI: 10.1021/ie960789f.
- (162) Wu, H.-S.; Jone, H.-C.; Hwang, J. Reaction of polyacrylic acid and metal oxides: Infrared spectroscopic kinetic study and solvent effect. *J. Appl. Polym. Sci.* **1997**, *63* (1), 89–101. DOI: 10.1002/(SICI)1097-4628(19970103)63:1<89:AID-APP9>3.0.CO;2-O.
- (163) Degen, A.; Kosec, M. Influence of pH and Ionic Impurities on the Adsorption of Poly(acrylic) Dispersant onto a Zinc Oxide Surface. *Journal of the American Ceramic Society* **2003**, *86* (12), 2001–2010. DOI: 10.1111/j.1151-2916.2003.tb03600.x.
- (164) C. Dange; T.N.T. Phan; V. André; J. Rieger; J. Persello; A. Foissy. Adsorption mechanism and dispersion efficiency of three anionic additives [poly(acrylic acid), poly(styrene sulfonate) and HEDP] on zinc oxide. *Journal of Colloid and Interface Science* **2007**, *315* (1), 107–115. DOI: 10.1016/j.jcis.2007.03.068.
- (165) Sugama, T.; Kukacka, L. E.; Carciello, N. Nature of interfacial interaction mechanisms between polyacrylic acid macromolecules and oxide metal surfaces. *J Mater Sci* **1984**, *19* (12), 4045–4056. DOI: 10.1007/BF00980770.
- (166) Kunze, C.; Valtiner, M.; Michels, R.; Huber, K.; Grundmeier, G. Self-localization of polyacrylic acid molecules on polar ZnO(0001)-Zn surfaces. *Physical chemistry chemical physics: PCCP* **2011**, *13* (28), 12959–12967. DOI: 10.1039/c1cp20913b.
- (167) Meinderink, D.; Orive, A. G.; Ewertowski, S.; Giner, I.; Grundmeier, G. Dependence of Poly(acrylic acid) Interfacial Adhesion on the Nanostructure of Electrodeposited ZnO Films. *ACS Appl. Nano Mater.* **2019**, *2* (2), 831–843. DOI: 10.1021/acsanm.8b02091.
- (168) Bélanger, D.; Pinson, J. Electrografting: a powerful method for surface modification. *Chemical Society reviews* **2011**, *40* (7), 3995–4048. DOI: 10.1039/c0cs00149j.
- (169) Teng, F. S.; Mahalingam, R. Mechanism and evaluation in electroinitiated copolymerization coatings of acrylonitrile and acrylic acid. *J. Appl. Polym. Sci.* **1979**, *23* (1), 101–113. DOI: 10.1002/app.1979.070230109.
- (170) Hung, K.-B.; Li, J.; Fan, Q.; Chen, Z.-H. The enhancement of carbon fiber modified with electropolymer coating to the mechanical properties of epoxy resin composites. *Composites Part A: Applied Science and Manufacturing* **2008**, *39* (7), 1133–1140. DOI: 10.1016/j.compositesa.2008.04.004.
- (171) Beck, F. Electrodeposition of polymer coatings. *Electrochimica Acta* **1988**, *33* (7), 839–850. DOI: 10.1016/0013-4686(88)80080-X.
- (172) Deng, Z.; Smyrl, W. H.; White, H. S. Stabilization of Metal-Metal Oxide Surfaces Using Electroactive Polymer Films. *J. Electrochem. Soc.*, *136* (8), 2152. DOI: 10.1149/1.2097233.
- (173) Li, C.; Bai, H.; Shi, G. Conducting polymer nanomaterials: electrosynthesis and applications. *Chem. Soc. Rev.* **2009**, *38* (8), 2397–2409. DOI: 10.1039/B816681C.

- (174) Giglio, E. de; Cometa, S.; Cioffi, N.; Torsi, L.; Sabbatini, L. Analytical investigations of poly(acrylic acid) coatings electrodeposited on titanium-based implants: a versatile approach to biocompatibility enhancement. *Analytical and bioanalytical chemistry* **2007**, 389 (7-8), 2055–2063. DOI: 10.1007/s00216-007-1299-7.
- (175) Meinderink, D.; Orive, A. G.; Grundmeier, G. Electrodeposition of poly(acrylic acid) on stainless steel with enhanced adhesion properties. *Surf. Interface Anal.* **2018**, 50 (11), 1224–1229. DOI: 10.1002/sia.6440.
- (176) Wang, X.; Bohn, P. W. Anisotropic in-plane gradients of poly(acrylic acid) formed by electropolymerization with spatiotemporal control of the electrochemical potential. *Journal of the American Chemical Society* **2004**, 126 (21), 6825–6832. DOI: 10.1021/ja0400436.
- (177) Najafisayar, P.; Bahrololoom, M. E. The effect of pulse electropolymerization on the electrochemical properties of polythiophene films. *Electrochimica Acta* **2013**, 114, 462–473. DOI: 10.1016/j.electacta.2013.10.063.
- (178) Su, W.; Iroh, J. O. Electropolymerization of pyrrole on steel substrate in the presence of oxalic acid and amines. *Electrochimica Acta* **1999**, 44 (13), 2173–2184. DOI: 10.1016/S0013-4686(98)00343-0.
- (179) Wencheng, S.; Iroh, J. O. Effects of electrochemical process parameters on the synthesis and properties of polypyrrole coatings on steel. *Synthetic Metals* **1998**, 95 (3), 159–167. DOI: 10.1016/S0379-6779(97)04112-X.
- (180) Bauer, A.; Meinderink, D.; Giner, I.; Steger, H.; Weitzl, J.; Grundmeier, G. Electropolymerization of acrylic acid on carbon fibers for improved epoxy/fiber adhesion. *Surface and Coatings Technology* **2017**, 321, 128–135. DOI: 10.1016/j.surfcoat.2017.04.039.
- (181) Subramanian, R. V.; Jakubowski, J. J. Electropolymerization on graphite fibers. *Polymer Engineering & Science* **1978**, 18 (7), 590–600. DOI: 10.1002/pen.760180708.
- (182) Subramanian, R. V.; Jakubowski, J. J.; Williams, F. D. Interfacial Aspects of Polymer Coating by Electropolymerization. *The Journal of Adhesion* **1978**, 9 (3), 185–195. DOI: 10.1080/00218467808075113.
- (183) Subramanian, R. V.; Sundaram, V.; Patel, A. K. *Electrodeposition of Polymers of Graphite Fibers: Effects on Composite Properties*. <https://apps.dtic.mil/dtic/tr/fulltext/u2/a055020.pdf>.
- (184) Uyama, Y.; Kato, K.; Ikada, Y. Surface Modification of Polymers by Grafting. In *Grafting/Characterization Techniques/Kinetic Modeling*; Galina, H., Ikada, Y., Kato, K., Kitamaru, R., Lechowicz, J., Uyama, Y., Wu, C., Eds.; Springer Berlin Heidelberg, 1998; pp 1–39. DOI: 10.1007/3-540-69685-7_1.
- (185) Barroso-Bujans, F.; Serna, R.; Sow, E.; Fierro, J. L. G.; Veith, M. Grafting of poly(acrylic acid) onto an aluminum surface. *Langmuir: the ACS journal of surfaces and colloids* **2009**, 25 (16), 9094–9100. DOI: 10.1021/la900518s.

- (186) Katz, E.; Lacey, A. L. de; Fierro, J. L.; Palacios, J. M.; Fernandez, V. M. Covalent binding of viologen to electrode surfaces coated with poly(acrylic acid) formed by electropolymerization of acrylate ions: I. Electrode preparation and characterization. *Journal of Electroanalytical Chemistry* **1993**, 358 (1), 247–259. DOI: 10.1016/0022-0728(93)80442-K.
- (187) Chegel, V. I.; Raitman, O. A.; Lioubashevski, O.; Shirshov, Y.; Katz, E.; Willner, I. Redox-Switching of Electrorefractive, Electrochromic, and Conductivity Functions of Cu²⁺/Polyacrylic Acid Films Associated with Electrodes. *Advanced Materials* **2002**, 14 (21), 1549–1553. DOI: 10.1002/1521-4095(20021104)14:21<1549:AID-ADMA1549>3.0.CO;2-C.
- (188) Lechner, M. D.; Gehrke, K.; Nordmeier, E. H. *Makromolekulare Chemie: Ein Lehrbuch für Chemiker, Physiker, Materialwissenschaftler und Verfahrenstechniker*, 5. Aufl.; Springer Spektrum, 2014. DOI: 10.1007/978-3-642-41769-6.
- (189) DECKER, C.; VATAJ, R.; LOUATI, A. Synthesis of acrylic polymer networks by electroinitiated polymerization. *Progress in Organic Coatings* **2004**, 50 (4), 263–268. DOI: 10.1016/j.porgcoat.2004.03.005.
- (190) Saïd Sadki; Philippe Schottland; Nancy Brodie; Guillaume Sabouraud. The mechanisms of pyrrole electropolymerization. *Chemical Society reviews* **2000**, 29 (5), 283–293. DOI: 10.1039/A807124A.
- (191) Di Wei; Kvarnström, C.; Lindfors, T.; Kronberg, L.; Sjöholm, R.; Ivaska, A. Electropolymerization mechanism of N-methylaniline. *Synthetic Metals* **2006**, 156 (7), 541–548. DOI: 10.1016/j.synthmet.2006.02.009.
- (192) Collins, G. L.; Thomas, N. W. Mechanism of coating by electropolymerization on metal cathodes from zinc chloride solutions of acrylamide. *Journal of Polymer Science: Polymer Chemistry Edition* **1977**, 15 (8), 1819–1831. DOI: 10.1002/pol.1977.170150804.
- (193) Heping Chen; T. Fuhlbrigge; Xiongzi Li. Automated industrial robot path planning for spray painting process: A review. In *2008 IEEE International Conference on Automation Science and Engineering*, 2008; pp 522–527. DOI: 10.1109/COASE.2008.4626515.
- (194) Pawlowski, L. Suspension and solution thermal spray coatings. *Surface and Coatings Technology* **2009**, 203 (19), 2807–2829. DOI: 10.1016/j.surfcoat.2009.03.005.
- (195) Bala, N.; Singh, H.; Karthikeyan, J.; Prakash, S. Cold spray coating process for corrosion protection: a review. *Surface Engineering* **2014**, 30 (6), 414–421. DOI: 10.1179/1743294413Y.0000000148.
- (196) Hassani-Gangaraj, S. M.; Moridi, A.; Guagliano, M. Critical review of corrosion protection by cold spray coatings. *Surface Engineering* **2015**, 31 (11), 803–815. DOI: 10.1179/1743294415Y.0000000018.

- (197) Moridi, A.; Hassani-Gangaraj, S. M.; Guagliano, M.; Dao, M. Cold spray coating: review of material systems and future perspectives. *Surface Engineering* **2014**, *30* (6), 369–395. DOI: 10.1179/1743294414Y.00000000270.
- (198) Hardwicke, C. U.; Lau, Y.-C. Advances in Thermal Spray Coatings for Gas Turbines and Energy Generation: A Review. *J Therm Spray Tech* **2013**, *22* (5), 564–576. DOI: 10.1007/s11666-013-9904-0.
- (199) Matthews, S.; James, B. Review of Thermal Spray Coating Applications in the Steel Industry: Part 1—Hardware in Steel Making to the Continuous Annealing Process. *J Therm Spray Tech* **2010**, *19* (6), 1267–1276. DOI: 10.1007/s11666-010-9518-8.
- (200) Fauchais, P.; Vardelle, M.; Vardelle, A.; Bianchi, L. Plasma spray: Study of the coating generation. *Ceramics International* **1996**, *22* (4), 295–303. DOI: 10.1016/0272-8842(95)00106-9.
- (201) Gill, B. J.; Tucker, R. C. Plasma spray coating processes. *Materials Science and Technology* **1986**, *2* (3), 207–213. DOI: 10.1179/mst.1986.2.3.207.
- (202) Perednis, D.; Gauckler, L. J. Thin Film Deposition Using Spray Pyrolysis. *J Electroceram* **2005**, *14* (2), 103–111. DOI: 10.1007/s10832-005-0870-x.
- (203) Bastwros, M.; Kim, G.-Y. Ultrasonic spray deposition of SiC nanoparticles for laminate metal composite fabrication. *Powder Technology* **2016**, *288*, 279–285. DOI: 10.1016/j.powtec.2015.10.039.
- (204) Tait, J. G.; Rand, B. P.; Heremans, P. Concurrently pumped ultrasonic spray coating for donor:acceptor and thickness optimization of organic solar cells. *Organic Electronics* **2013**, *14* (3), 1002–1008. DOI: 10.1016/j.orgel.2013.01.023.
- (205) Yang, Q.; Ma, Y.; Zhu, J.; Chow, K.; Shi, K. An update on electrostatic powder coating for pharmaceuticals. *Particuology* **2017**, *31*, 1–7. DOI: 10.1016/j.partic.2016.10.001.
- (206) Tang, K.; Gomez, A. On the structure of an electrostatic spray of monodisperse droplets. *Physics of Fluids* **1994**, *6* (7), 2317–2332. DOI: 10.1063/1.868182.
- (207) Kolasinska, M.; Krastev, R.; Gutberlet, T.; Warszynski, P. Layer-by-layer deposition of polyelectrolytes. Dipping versus spraying. *Langmuir: the ACS journal of surfaces and colloids* **2009**, *25* (2), 1224–1232. DOI: 10.1021/la803428f.
- (208) Schönhoff, M. Self-assembled polyelectrolyte multilayers. *Current Opinion in Colloid & Interface Science* **2003**, *8* (1), 86–95. DOI: 10.1016/S1359-0294(03)00003-7.
- (209) Vak, D.; Kim, S.-S.; Jo, J.; Oh, S.-H.; Na, S.-I.; Kim, J.; Kim, D.-Y. Fabrication of organic bulk heterojunction solar cells by a spray deposition method for low-cost power generation. *Appl. Phys. Lett.* **2007**, *91* (8), 81102. DOI: 10.1063/1.2772766.
- (210) Levingstone, T. J.; Ardhaoui, M.; Benyounis, K.; Looney, L.; Stokes, J. T. Plasma sprayed hydroxyapatite coatings: Understanding process relationships using design of experiment analysis. *Surface and Coatings Technology* **2015**, *283*, 29–36. DOI: 10.1016/j.surfcoat.2015.10.044.

- (211) Bian, J. M.; Li, X. M.; Zhang, C. Y.; Chen, L. D.; Yao, Q. Synthesis and characterization of two-layer-structured ZnO p-n homojunctions by ultrasonic spray pyrolysis. *Appl. Phys. Lett.* **2004**, *84* (19), 3783–3785. DOI: 10.1063/1.1739280.
- (212) Studenikin, S. A.; Golego, N.; Cocivera, M. Optical and electrical properties of undoped ZnO films grown by spray pyrolysis of zinc nitrate solution. *Journal of Applied Physics* **1998**, *83* (4), 2104–2111. DOI: 10.1063/1.366944.
- (213) Kim, T.; Canlier, A.; Kim, G. H.; Choi, J.; Park, M.; Han, S. M. Electrostatic spray deposition of highly transparent silver nanowire electrode on flexible substrate. *ACS applied materials & interfaces* **2013**, *5* (3), 788–794. DOI: 10.1021/am3023543.
- (214) Chang, C.-L.; Hwang, B.-H. Microstructure and Electrochemical Characterization of Sm 0.5 Sr 0.5 CoO 3 Films as SOFC Cathode Prepared by the Electrostatic-Assisted Ultrasonic Spray Pyrolysis Method. *International Journal of Applied Ceramic Technology* **2008**, *5* (6), 582–588. DOI: 10.1111/j.1744-7402.2008.02288.x.
- (215) Eita, M.; Wågberg, L.; Muhammed, M. Thin Films of Zinc Oxide Nanoparticles and Poly(acrylic acid) Fabricated by the Layer-by-Layer Technique: a Facile Platform for Outstanding Properties. *J. Phys. Chem. C* **2012**, *116* (7), 4621–4627. DOI: 10.1021/jp2095328.
- (216) Shaik, M. R.; Kuniyil, M.; Khan, M.; Ahmad, N.; Al-Warthan, A.; Siddiqui, M. R. H.; Adil, S. F. Modified Polyacrylic Acid-Zinc Composites: Synthesis, Characterization and Biological Activity. *Molecules* **2016**, *21* (3), 292. DOI: 10.3390/molecules21030292.
- (217) Kislenko, V. N.; Verlinskaya, R. M. Colloidal and Chemical Processes during the Interaction between Polyacrylic Acid and Zinc Oxide Dispersion. *Colloid Journal* **2002**, *64* (4), 447–450. DOI: 10.1023/A:1016815919708.
- (218) Kislenko, V. N.; Verlinskaya, R. M. Adsorption of Polyacrylic Acid and Its Copolymers with Acrylonitrile on Zinc Oxide Particles. *Journal of Colloid and Interface Science* **2002**, *250* (2), 478–483. DOI: 10.1006/jcis.2002.8344.
- (219) Rabie, S. M.; Sawaby, A.; Moharam, M. A.; Nassar, A. M.; Tahon, K. H. Temperature dependence of the reaction between some metal oxides and polyacrylic acid. *J. Appl. Polym. Sci.* **1990**, *41* (34), 445–453. DOI: 10.1002/app.1990.070410301.
- (220) Radyum Ikono, Nurwenda Novan Maulana, Tanti Dewinggih, Mukhtar Effendi, Wahyu Bambang Widayanto, Agus Sukarto, Nurul Taufiqu Rochman. Effect of Polyacrylic Acid Addition to Improve Nano Zinc Oxide Dispersion Stability. *International Journal of Engineering & Technology IJET-IJENS* **2012** (12), 95–99.
- (221) Gutkowski, R.; Schäfer, D.; Nagaiah, T. C.; Heras, J. E. Y.; Busser, W.; Muhler, M.; Schuhmann, W. Efficient Deposition of Semiconductor Powders for Photoelectrocatalysis by Airbrush Spraying. *Electroanalysis* **2015**, *27* (2), 285–292. DOI: 10.1002/elan.201400363.

- (222) Li, Z.; Kandel, H. R.; Dervishi, E.; Saini, V.; Xu, Y.; Biris, A. R.; Lupu, D.; Salamo, G. J.; Biris, A. S. Comparative study on different carbon nanotube materials in terms of transparent conductive coatings. *Langmuir: the ACS journal of surfaces and colloids* **2008**, *24* (6), 2655–2662. DOI: 10.1021/la701880h.
- (223) Chan, C. K.; Richter, L. J.; Dinardo, B.; Jaye, C.; Conrad, B. R.; Ro, H. W.; Germack, D. S.; Fischer, D. A.; DeLongchamp, D. M.; Gundlach, D. J. High performance airbrushed organic thin film transistors. *Appl. Phys. Lett.* **2010**, *96* (13), 133304. DOI: 10.1063/1.3360230.
- (224) De, S.; Lutkenhaus, J. L. Corrosion behaviour of eco-friendly airbrushed reduced graphene oxide-poly(vinyl alcohol) coatings. *Green Chem.* **2018**, *20* (2), 506–514. DOI: 10.1039/C7GC02882B.
- (225) Tu, C.-W.; Tsai, C.-H.; Wang, C.-F.; Kuo, S.-W.; Chang, F.-C. Fabrication of Superhydrophobic and Superoleophilic Polystyrene Surfaces by a Facile One-Step Method. *Macromol. Rapid Commun.* **2007**, *28* (23), 2262–2266. DOI: 10.1002/marc.200700447.
- (226) Westedt, U.; Wittmar, M.; Hellwig, M.; Hanefeld, P.; Greiner, A.; Schaper, A. K.; Kissel, T. Paclitaxel releasing films consisting of poly(vinyl alcohol)-graft-poly(lactide-co-glycolide) and their potential as biodegradable stent coatings. *Journal of controlled release: official journal of the Controlled Release Society* **2006**, *111* (1-2), 235–246. DOI: 10.1016/j.jconrel.2005.12.012.
- (227) Sabbatini, L., Ed. *Surface characterization of advanced polymers*; VCH, 1993.
- (228) Otto, M. *Analytische Chemie*, 3., vollst. überarb. und erw. Aufl.; Wiley-VCH, 2006.
- (229) Hollas, J. M. *Modern spectroscopy*, 4. ed., reprinted.; Wiley, 2004.
- (230) Bluhm, H. X-ray photoelectron spectroscopy (XPS) for in situ characterization of thin film growth. In *In situ characterization of thin film growth*; Koster, G., Rijnders, G., Eds.; Woodhead Publishing Series in Electronic and Optical Materials; Woodhead Pub, 2011; pp 75–98. DOI: 10.1533/9780857094957.2.75.
- (231) Kunze, C.; Torun, B.; Giner, I.; Grundmeier, G. Surface chemistry and nonadecanoic acid adsorbate layers on TiO₂(100) surfaces prepared at ambient conditions. *Surface Science* **2012**, *606* (19-20), 1527–1533. DOI: 10.1016/j.susc.2012.05.025.
- (232) Hofmann, S. *Auger- and X-Ray Photoelectron Spectroscopy in Materials Science: A User-Oriented Guide*; Springer Series in Surface Sciences, Vol. 49; Springer, 2013. DOI: 10.1007/978-3-642-27381-0.
- (233) Watts, J. F.; Wolstenholme, J. *An introduction to surface analysis by XPS and AES*, second edition; Wiley, 2020.
- (234) Larkin, P., Ed. *Infrared and Raman Spectroscopy*; Elsevier, 2011.
- (235) Günzler, H.; Gremlich, H.-U. *IR-Spektroskopie: Eine Einführung*, 4., vollständig überarbeitete und aktualisierte Aufl.; Wiley; Wiley-VCH, 2003. DOI: 10.1002/9783527662852.

- (236) Grundmeier, G.; Keudell, A. von; los Arcos, T. de. Fundamentals and Applications of Reflection FTIR Spectroscopy for the Analysis of Plasma Processes at Materials Interfaces. *Plasma Process. Polym.* **2015**, *12* (9), 926–940. DOI: 10.1002/ppap.201500087.
- (237) Greenler, R. G. Infrared Study of Adsorbed Molecules on Metal Surfaces by Reflection Techniques. *The Journal of Chemical Physics* **1966**, *44* (1), 310–315. DOI: 10.1063/1.1726462.
- (238) Suëtaka, W. *Surface Infrared and Raman Spectroscopy: Methods and Applications*; Methods of Surface Characterization, Vol. 3; Springer, 1995. DOI: 10.1007/978-1-4899-0942-8.
- (239) Krishna, R.; Unsworth, T. J.; Edge, R. Raman Spectroscopy and Microscopy. In *Reference Module in Materials Science and Materials Engineering*; Hashmi, S., Ed.; Elsevier, 2016. DOI: 10.1016/B978-0-12-803581-8.03091-5.
- (240) Egerton, R. F. *Physical principles of electron microscopy: An introduction to TEM, SEM, and AEM*; Springer, 2005.
- (241) Zhou, W.; Wang, Z. *Advanced Scanning Microscopy for Nanotechnology: in Chapter 1 Fundamentals of Scanning Electron Microscopy*; HEP Frontiers Online Higher Education Press, 2007.
- (242) Vickerman, J. C.; Briggs, D., Eds. *ToF-SIMS: materials analysis by mass spectrometry*, 2nd edition; Surface Spectra Limited; imp IM Publications, 2013.
- (243) Hutter, J. L.; Bechhoefer, J. Calibration of atomic-force microscope tips. *Review of Scientific Instruments* **1993**, *64* (7), 1868–1873. DOI: 10.1063/1.1143970.
- (244) Bouchiat, C.; Wang, M. D.; Allemand, J.-F.; Strick, T.; Block, S. M.; Croquette, V. Estimating the Persistence Length of a Worm-Like Chain Molecule from Force-Extension Measurements. *Biophysical journal* **1999**, *76* (1), 409–413. DOI: 10.1016/S0006-3495(99)77207-3.
- (245) Kaupp, G. *Atomic force microscopy, scanning nearfield optical microscopy and nanoscratching: Application to rough and natural surfaces*; Nanoscience and technology; Springer-Verlag Berlin Heidelberg, 2006. DOI: 10.1007/978-3-540-28472-7.
- (246) Carpick, R. W.; Salmeron, M. Scratching the Surface: Fundamental Investigations of Tribology with Atomic Force Microscopy. *Chemical Reviews* **1997**, *97* (4), 1163–1194. DOI: 10.1021/cr960068q.
- (247) García, R. Dynamic atomic force microscopy methods. *Surface Science Reports* **2002**, *47* (6-8), 197–301. DOI: 10.1016/S0167-5729(02)00077-8.
- (248) Noy, A. *Handbook of Molecular Force Spectroscopy*; Springer Science+Business Media LLC, 2008. DOI: 10.1007/978-0-387-49989-5.
- (249) Binnig; Quate; Gerber. Atomic force microscope. *Physical review letters* **1986**, *56* (9), 930–933. DOI: 10.1103/PhysRevLett.56.930.

- (250) Butt, H.-J.; Cappella, B.; Kappl, M. Force measurements with the atomic force microscope: Technique, interpretation and applications. *Surface Science Reports* **2005**, *59* (1-6), 1–152. DOI: 10.1016/j.surfrep.2005.08.003.
- (251) Cappella, B.; Dietler, G. Force-distance curves by atomic force microscopy. *Surface Science Reports* **1999**, *34* (1-3), 1–104. DOI: 10.1016/S0167-5729(99)00003-5.
- (252) Noy, A.; Vezenov, D. V.; Lieber, C. M. CHEMICAL FORCE MICROSCOPY. *Annu. Rev. Mater. Sci.* **1997**, *27* (1), 381–421. DOI: 10.1146/annurev.matsci.27.1.381.
- (253) Frisbie, C. D.; Rozsnyai, L. F.; Noy, A.; Wrighton, M. S.; Lieber, C. M. Functional group imaging by chemical force microscopy. *Science (New York, N.Y.)* **1994**, *265* (5181), 2071–2074. DOI: 10.1126/science.265.5181.2071.
- (254) McKendry, R.; Theoclitou, M.-E.; Rayment, T.; Abell, C. Chiral discrimination by chemical force microscopy. *Nature* **1998**, *391* (6667), 566–568. DOI: 10.1038/35339.
- (255) Noy, A.; Frisbie, C. D.; Rozsnyai, L. F.; Wrighton, M. S.; Lieber, C. M. Chemical Force Microscopy: Exploiting Chemically-Modified Tips To Quantify Adhesion, Friction, and Functional Group Distributions in Molecular Assemblies. *Journal of the American Chemical Society* **1995**, *117* (30), 7943–7951. DOI: 10.1021/ja00135a012.
- (256) Dague, E.; Alsteens, D.; Latgé, J.-P.; Verbelen, C.; Raze, D.; Baulard, A. R.; Dufrêne, Y. F. Chemical force microscopy of single live cells. *Nano letters* **2007**, *7* (10), 3026–3030. DOI: 10.1021/nl071476k.
- (257) Clear; Nealey. Chemical Force Microscopy Study of Adhesion and Friction between Surfaces Functionalized with Self-Assembled Monolayers and Immersed in Solvents. *Journal of Colloid and Interface Science* **1999**, *213* (1), 238–250. DOI: 10.1006/jcis.1999.6139.
- (258) Senden, T. J. Force microscopy and surface interactions. *Current Opinion in Colloid & Interface Science* **2001**, *6* (2), 95–101. DOI: 10.1016/S1359-0294(01)00067-X.
- (259) Clark, S. C.; Walz, J. Y.; Ducker, W. A. Atomic force microscopy colloid-probe measurements with explicit measurement of particle-solid separation. *Langmuir: the ACS journal of surfaces and colloids* **2004**, *20* (18), 7616–7622. DOI: 10.1021/la0497752.
- (260) Pasche, S.; Textor, M.; Meagher, L.; Spencer, N. D.; Griesser, H. J. Relationship between interfacial forces measured by colloid-probe atomic force microscopy and protein resistance of poly(ethylene glycol)-grafted poly(L-lysine) adlayers on niobia surfaces. *Langmuir: the ACS journal of surfaces and colloids* **2005**, *21* (14), 6508–6520. DOI: 10.1021/la050386x.
- (261) Ducker, W. A.; Senden, T. J.; Pashley, R. M. Direct measurement of colloidal forces using an atomic force microscope. *Nature* **1991**, *353* (6341), 239–241. DOI: 10.1038/353239a0.
- (262) Kappl, M.; Butt, H.-J. The Colloidal Probe Technique and its Application to Adhesion Force Measurements. *Part. Part. Syst. Charact.* **2002**, *19* (3), 129. DOI: 10.1002/1521-4117(200207)19:3<129:AID-PPSC129>3.0.CO;2-G.

- (263) Rabinovich, Y. I.; Singh, A.; Hahn, M.; Brown, S.; Moudgil, B. Kinetics of liquid annulus formation and capillary forces. *Langmuir: the ACS journal of surfaces and colloids* **2011**, *27* (22), 13514–13523. DOI: 10.1021/la202191c.
- (264) Harrison, A. J.; Corti, D. S.; Beaudoin, S. P. Capillary Forces in Nanoparticle Adhesion: A Review of AFM Methods. *Particulate Science and Technology* **2015**, *33* (5), 526–538. DOI: 10.1080/02726351.2015.1045641.
- (265) Bartels, F. W.; McIntosh, M.; Fuhrmann, A.; Metzendorf, C.; Plattner, P.; Sewald, N.; Anselmetti, D.; Ros, R.; Becker, A. Effector-stimulated single molecule protein-DNA interactions of a quorum-sensing system in *Sinorhizobium meliloti*. *Biophysical journal* **2007**, *92* (12), 4391–4400. DOI: 10.1529/biophysj.106.082016.
- (266) Evans, E. Probing the relation between force—lifetime—and chemistry in single molecular bonds. *Annual review of biophysics and biomolecular structure* **2001**, *30*, 105–128. DOI: 10.1146/annurev.biophys.30.1.105.
- (267) Noy, A.; Friddle, R. W. Practical single molecule force spectroscopy: how to determine fundamental thermodynamic parameters of intermolecular bonds with an atomic force microscope. *Methods (San Diego, Calif.)* **2013**, *60* (2), 142–150. DOI: 10.1016/j.ymeth.2013.03.014.
- (268) Geisler, M.; Horinek, D.; Hugel, T. Single Molecule Adhesion Mechanics on Rough Surfaces. *Macromolecules* **2009**, *42* (23), 9338–9343. DOI: 10.1021/ma9017372.
- (269) Schröder, T.; Geisler, T.; Walhorn, V.; Schnatwinkel, B.; Anselmetti, D.; Mattay, J. Single-molecule force spectroscopy of supramolecular heterodimeric capsules. *Physical chemistry chemical physics: PCCP* **2010**, *12* (36), 10981–10987. DOI: 10.1039/c0cp00227e.
- (270) Biggs, S.; Spinks, G. Atomic force microscopy investigation of the adhesion between a single polymer sphere and a flat surface. *Journal of Adhesion Science and Technology* **1998**, *12* (5), 461–478. DOI: 10.1163/156856198X00164.
- (271) Wong, S. S.; Woolley, A. T.; Joselevich, E.; Cheung, C. L.; Lieber, C. M. Covalently-Functionalized Single-Walled Carbon Nanotube Probe Tips for Chemical Force Microscopy. *Journal of the American Chemical Society* **1998**, *120* (33), 8557–8558. DOI: 10.1021/ja9817803.
- (272) Wong, S. S.; Harper, J. D.; Lansbury, P. T.; Lieber, C. M. Carbon Nanotube Tips: High-Resolution Probes for Imaging Biological Systems. *Journal of the American Chemical Society* **1998**, *120* (3), 603–604. DOI: 10.1021/ja9737735.
- (273) Fuji, M.; Machida, K.; Takei, T.; Watanabe, T.; Chikazawa, M. Effect of Surface Geometric Structure on the Adhesion Force between Silica Particles. *J. Phys. Chem. B* **1998**, *102* (44), 8782–8787. DOI: 10.1021/jp981978.
- (274) Li, H.; Zhang, W.; Xu, W.; Zhang, X. Hydrogen Bonding Governs the Elastic Properties of Poly(vinyl alcohol) in Water: Single-Molecule Force Spectroscopic Studies of PVA by AFM. *Macromolecules* **2000**, *33* (2), 465–469. DOI: 10.1021/ma990878e.

- (275) Hugel, T.; Grosholz, M.; Clausen-Schaumann, H.; Pfau, A.; Gaub, H.; Seitz, M. Elasticity of Single Polyelectrolyte Chains and Their Desorption from Solid Supports Studied by AFM Based Single Molecule Force Spectroscopy. *Macromolecules* **2001**, *34* (4), 1039–1047. DOI: 10.1021/ma0009404.
- (276) Geisler, M.; Balzer, B. N.; Hugel, T. Polymer adhesion at the solid-liquid interface probed by a single-molecule force sensor. *Small (Weinheim an der Bergstrasse, Germany)* **2009**, *5* (24), 2864–2869. DOI: 10.1002/sml.200901237.
- (277) Friedsam, C.; Gaub, H. E.; Netz, R. R. Probing surfaces with single-polymer atomic force microscope experiments. *Biointerphases* **2006**, *1* (1), MR1-MR21. DOI: 10.1116/1.2171996.
- (278) Dos Santos Ferreira, O.; Gelinck, E.; Graaf, D. de; Fischer, H. Adhesion experiments using an AFM—Parameters of influence. *Applied Surface Science* **2010**, *257* (1), 48–55. DOI: 10.1016/j.apsusc.2010.06.031.
- (279) Friedsam, C.; Seitz, M.; Gaub, H. E. Investigation of polyelectrolyte desorption by single molecule force spectroscopy. *J. Phys.: Condens. Matter* **2004**, *16* (26), S2369-S2382. DOI: 10.1088/0953-8984/16/26/010.
- (280) Lee, C.-K.; Wang, Y.-M.; Huang, L.-S.; Lin, S. Atomic force microscopy: determination of unbinding force, off rate and energy barrier for protein-ligand interaction. *Micron (Oxford, England : 1993)* **2007**, *38* (5), 446–461. DOI: 10.1016/j.micron.2006.06.014.
- (281) Bizzarri, A. R.; Cannistraro, S. The application of atomic force spectroscopy to the study of biological complexes undergoing a biorecognition process. *Chem. Soc. Rev.* **2010**, *39* (2), 734–749. DOI: 10.1039/b811426a.
- (282) Hugel, T.; Seitz, M. The Study of Molecular Interactions by AFM Force Spectroscopy. *Macromol. Rapid Commun.* **2001**, *22* (13), 989–1016. DOI: 10.1002/1521-3927(20010901)22:13<989:AID-MARC989>3.0.CO;2-D.
- (283) Friedsam, C.; Gaub, H. E.; Netz, R. R. Adsorption energies of single charged polymers. *Europhysics Letters (EPL)* **2005**, *72* (5), 844–850. DOI: 10.1209/epl/i2005-10316-7.
- (284) Seitz, M.; Friedsam, C.; Jöstl, W.; Hugel, T.; Gaub, H. E. Probing solid surfaces with single polymers. *Chemphyschem : a European journal of chemical physics and physical chemistry* **2003**, *4* (9), 986–990. DOI: 10.1002/cphc.200300760.
- (285) Friedsam, C.; Bécares, A. D. C.; Jonas, U.; Seitz, M.; Gaub, H. E. Adsorption of polyacrylic acid on self-assembled monolayers investigated by single-molecule force spectroscopy. *New Journal of Physics* **2004**, *6*, 9. DOI: 10.1088/1367-2630/6/1/009.
- (286) Geisler, M.; Pirzer, T.; Ackerschott, C.; Lud, S.; Garrido, J.; Scheibel, T.; Hugel, T. Hydrophobic and Hofmeister effects on the adhesion of spider silk proteins onto solid substrates: an AFM-based single-molecule study. *Langmuir: the ACS journal of surfaces and colloids* **2008**, *24* (4), 1350–1355. DOI: 10.1021/la702341j.

- (287) Gilbert, Y.; Deghorain, M.; Wang, L.; Xu, B.; Pollheimer, P. D.; Gruber, H. J.; Errington, J.; Hallet, B.; Haulot, X.; Verbelen, C.; Hols, P.; Dufrêne, Y. F. Single-molecule force spectroscopy and imaging of the vancomycin/D-Ala-D-Ala interaction. *Nano letters* **2007**, 7 (3), 796–801. DOI: 10.1021/nl0700853.
- (288) Sonnenberg, L.; Luo, Y.; Schlaad, H.; Seitz, M.; Cölfen, H.; Gaub, H. E. Quantitative single molecule measurements on the interaction forces of poly(L-glutamic acid) with calcite crystals. *Journal of the American Chemical Society* **2007**, 129 (49), 15364–15371. DOI: 10.1021/ja074070i.
- (289) Friedsam, C.; Del Campo Bécares, A.; Jonas, U.; Gaub, H. E.; Seitz, M. Polymer functionalized AFM tips for long-term measurements in single-molecule force spectroscopy. *Chemphyschem: a European journal of chemical physics and physical chemistry* **2004**, 5 (3), 388–393. DOI: 10.1002/cphc.200300797.
- (290) Pensa, E.; Cortés, E.; Corthey, G.; Carro, P.; Vericat, C.; Fonticelli, M. H.; Benítez, G.; Rubert, A. A.; Salvarezza, R. C. The chemistry of the sulfur-gold interface: in search of a unified model. *Accounts of chemical research* **2012**, 45 (8), 1183–1192. DOI: 10.1021/ar200260p.
- (291) Vericat, C.; Vela, M. E.; Benitez, G.; Carro, P.; Salvarezza, R. C. Self-assembled monolayers of thiols and dithiols on gold: new challenges for a well-known system. *Chemical Society reviews* **2010**, 39 (5), 1805–1834. DOI: 10.1039/b907301a.
- (292) Grandbois; Beyer; Rief; Clausen-Schaumann; Gaub. How strong is a covalent bond? *Science (New York, N.Y.)* **1999**, 283 (5408), 1727–1730. DOI: 10.1126/science.283.5408.1727.
- (293) Xue, Y.; Li, X.; Li, H.; Zhang, W. Quantifying thiol-gold interactions towards the efficient strength control. *Nature communications* **2014**, 5, 4348. DOI: 10.1038/ncomms5348.
- (294) Kienle, S.; Gallei, M.; Yu, H.; Zhang, B.; Krysiak, S.; Balzer, B. N.; Rehahn, M.; Schlüter, A. D.; Hugel, T. Effect of molecular architecture on single polymer adhesion. *Langmuir: the ACS journal of surfaces and colloids* **2014**, 30 (15), 4351–4357. DOI: 10.1021/la500783n.
- (295) Li, Y.; Liu, H.; Wang, T.; Qin, M.; Cao, Y.; Wang, W. Single-Molecule Force Spectroscopy Reveals Multiple Binding Modes between DOPA and Different Rutile Surfaces. *Chemphyschem : a European journal of chemical physics and physical chemistry* **2017**, 18 (11), 1466–1469. DOI: 10.1002/cphc.201600374.
- (296) Li, Y.; Qin, M.; Li, Y.; Cao, Y.; Wang, W. Single molecule evidence for the adaptive binding of DOPA to different wet surfaces. *Langmuir: the ACS journal of surfaces and colloids* **2014**, 30 (15), 4358–4366. DOI: 10.1021/la501189n.
- (297) Bell, G. I. Models for the specific adhesion of cells to cells. *Science (New York, N.Y.)* **1978**, 200 (4342), 618–627. DOI: 10.1126/science.347575.
- (298) Evans, E.; Ritchie, K. Dynamic strength of molecular adhesion bonds. *Biophysical journal* **1997**, 72 (4), 1541–1555. DOI: 10.1016/S0006-3495(97)78802-7.

- (299) Hinterdorfer, P.; Dufrêne, Y. F. Detection and localization of single molecular recognition events using atomic force microscopy. *Nature methods* **2006**, 3 (5), 347–355. DOI: 10.1038/nmeth871.
- (300) Evans, E. A.; Calderwood, D. A. Forces and bond dynamics in cell adhesion. *Science (New York, N.Y.)* **2007**, 316 (5828), 1148–1153. DOI: 10.1126/science.1137592.
- (301) Casalini, S.; Dumitru, A. C.; Leonardi, F.; Bortolotti, C. A.; Herruzo, E. T.; Campana, A.; Oliveira, R. F. de; Cramer, T.; Garcia, R.; Biscarini, F. Multiscale sensing of antibody-antigen interactions by organic transistors and single-molecule force spectroscopy. *ACS nano* **2015**, 9 (5), 5051–5062. DOI: 10.1021/acsnano.5b00136.
- (302) Razvag, Y.; Gutkin, V.; Reches, M. Probing the interaction of individual amino acids with inorganic surfaces using atomic force spectroscopy. *Langmuir: the ACS journal of surfaces and colloids* **2013**, 29 (32), 10102–10109. DOI: 10.1021/la4015866.
- (303) Eyring, H. The Activated Complex in Chemical Reactions. *The Journal of Chemical Physics* **1935**, 3 (2), 107–115. DOI: 10.1063/1.1749604.
- (304) Crocombe, A. D.; Adams, R. D. Peel Analysis Using the Finite Element Method. *The Journal of Adhesion* **1981**, 12 (2), 127–139. DOI: 10.1080/00218468108071194.
- (305) Zhang, L.; Wang, J. A generalized cohesive zone model of the peel test for pressure-sensitive adhesives. *International Journal of Adhesion and Adhesives* **2009**, 29 (3), 217–224. DOI: 10.1016/j.ijadhadh.2008.05.002.
- (306) G'Sell, C.; Boni, S.; Shrivastava, S. Application of the plane simple shear test for determination of the plastic behaviour of solid polymers at large strains. *J Mater Sci* **1983**, 18 (3), 903–918. DOI: 10.1007/BF00745590.
- (307) Schammler, G.; Buschick, K.; Hahn, R.; Reichl, H. Shear test for adhesion measurement of small structures. In *1996 IEEE International Integrated Reliability Workshop Final Report*; IEEE: Piscataway, 1997; pp 31–36. DOI: 10.1109/IRWS.1996.583379.
- (308) Silva, L. F. M. d.; Pirondi, A.; Öchsner, A. *Hybrid Adhesive Joints*; Advanced Structured Materials, Vol. 6; Springer-Verlag Berlin Heidelberg, 2011. DOI: 10.1007/978-3-642-16623-5.
- (309) Mosebach, B.; Ozkaya, B.; Giner, I.; Keller, A.; Grundmeier, G. Analysis of acid-base interactions at Al₂O₃ (11-20) interfaces by means of single molecule force spectroscopy. *Applied Surface Science* **2017**, 420, 296–302. DOI: 10.1016/j.apsusc.2017.05.105.
- (310) Barthés-Labrousse, M. G. Adhesion Mechanisms at Amine-Cured Epoxy/Aluminium Interfaces. *The Journal of Adhesion* **1996**, 57 (1-4), 65–75. DOI: 10.1080/00218469608013644.
- (311) Barthés-Labrousse, M.-G. Mechanisms of Formation of the Interphase in Epoxy-Amine/Aluminium Joints. *The Journal of Adhesion* **2012**, 88 (8), 699–719. DOI: 10.1080/00218464.2012.682933.

- (312) Mattia, D.; Leese, H. Controlled hydrothermal pore reduction in anodic alumina membranes. *Nanoscale* **2014**, 6 (22), 13952–13957. DOI: 10.1039/c4nr04661g.
- (313) Thissen, P.; Valtiner, M.; Grundmeier, G. Stability of phosphonic acid self-assembled monolayers on amorphous and single-crystalline aluminum oxide surfaces in aqueous solution. *Langmuir: the ACS journal of surfaces and colloids* **2010**, 26 (1), 156–164. DOI: 10.1021/la900935s.
- (314) Dupres, V.; Menozzi, F. D.; Loch, C.; Clare, B. H.; Abbott, N. L.; Cuenot, S.; Bompard, C.; Raze, D.; Dufrêne, Y. F. Nanoscale mapping and functional analysis of individual adhesins on living bacteria. *Nature methods* **2005**, 2 (7), 515–520. DOI: 10.1038/nmeth769.
- (315) El-Kirat-Chatel, S.; Beaussart, A.; Boyd, C. D.; O'Toole, G. A.; Dufrêne, Y. F. Single-Cell and Single-Molecule Analysis Deciphers the Localization, Adhesion, and Mechanics of the Biofilm Adhesin LapA. *ACS Chemical Biology* **2014**, 9 (2), 485–494. DOI: 10.1021/cb400794e.
- (316) Meinderink, D.; Kielar, C.; Sobol, O.; Ruhm, L.; Rieker, F.; Nolkemper, K.; Orive, A. G.; Ozcan, O.; Grundmeier, G. Effect of PAA-induced surface etching on the adhesion properties of ZnO nanostructured films. *International Journal of Adhesion and Adhesives* **2021**, 106, 102812. DOI: 10.1016/j.ijadhadh.2021.102812.

7 List of publications and presentations

7.1 Peer-reviewed publications

1. A. Bauer, D. Meinderink, I. Giner, H. Steger, J. Weitzl, G. Grundmeier, *Electropolymerization of acrylic acid on carbon fibers for improved epoxy/fiber adhesion*, Surface and Coatings Technology 321 (2017) 128-135
2. R. Grothe, M. Wiesing, I. Giner, D. Meinderink, G. Grundmeier, *Scanning Kelvin probe blister studies of the delamination of epoxy films on organosilane modified ZnMgAl alloy coated steel*, Materials and Corrosion 9999 (2017) 1–7
3. D. Meinderink, A. G. Orive, G. Grundmeier, *Electrodeposition of poly(acrylic acid) on stainless steel with enhanced adhesion properties*, Surface and Interface Analysis 50 (2018) 1224-1229
4. I. Giner, B. Torun, Y. Han, B. Duderija, D. Meinderink, A.G. Orive, T.d.l. Arcos, C. Weinberger, M. Tiemann, Hans-Joachim Schmid, G. Grundmeier, *Water adsorption and capillary bridge formation on silica micro-particle layers modified with perfluorinated organosilane monolayers*, Applied Surface Science 475 (2019) 873-879
5. D. Meinderink, Alejandro Gonzalez Orive, Simon Ewertowski, Ignacio Giner, Guido Grundmeier, *Dependence of Poly(acrylic acid) Interfacial Adhesion on the Nanostructure of Electrodeposited ZnO Films*, ACS Applied Nano Mater. 2,2 (2019) 831-843
6. Dennis Meinderink, Karlo J.R. Nolkemper, Julius Bürger, Alejandro G. Orive, Jörg K.N. Lindner, Guido Grundmeier, *Spray Coating of Poly(acrylic Acid)/ZnO Tetrapod Adhesion Promoting Nanocomposite Films for Polymer Laminates*, Surface & Coatings Technology 375 (2019) 112-122
7. R. Grothe, S. Knust, D. Meinderink, M. Voigt, A. González Orive, G. Grundmeier, *Spray pyrolysis of thin adhesion-promoting ZnO films on ZnMgAl coated steel*, Surface & Coatings Technology 394 (2020) 125869
8. D. Meinderink, C. Kielar, O. Sobol, L. Ruhm, F. Rieker, K. Nolkemper, A. G. Orive, O. Ozcan, G. Grundmeier, *Effect of PAA-induced surface etching on the adhesion properties of ZnO nanostructured films*, International Journal of Adhesion and Adhesives 106 (2021) 102812

7.2 Conference presentations

1. 4th Fachsymposiums Polymerverguss at the IFAM in Bremen in Germany with the oral talk “Einfluss der oxidischen Oberflächenstruktur auf Haftung und Enthaftung“, Dennis Meinderink, Guido Grundmeier (**21.09.17 - 22.09.2017**)
2. European Conference on Applications of Surface and Interface Analysis (ECASIA'17) with a poster presentation, *Electropolymerisation of acrylic acid on carbon fibers for improved epoxy/fiber adhesion*, A. Bauer, D. Meinderink, I. Giner, G. Grundmeier (**24.09.2017 - 29.09.2017**), (winner of the WILEY poster price)
3. 12th European Adhesion Conference and 4th Luso-Brazilian Conference on Adhesion and Adhesives (EURADH 2018 and CLBA 2018) with a plenary oral talk, *Molecular adhesion studies on ZnO nanorod coated stainless steel*, Dennis Meinderink, A. G. Orive, G. Grundmeier (**05.09.2018 - 07.09.2018**)
4. 3th International Conference on Applied Surface Science (ICASS'19) with a poster presentation, *Application of AFM-based single molecule force spectroscopy for the analysis of macromolecular adsorption on nanostructured ZnO films*, D. Meinderink, A. G. Orive, S. Ewertowski, I. Giner, G. Grundmeier (**17.06.2019 - 20.06.2019**)

7.3 Participations at conference contributions

1. 12th European Adhesion Conference and 4th Luso-Brazilian Conference on Adhesion and Adhesives (EURADH 2018 and CLBA 2018), *Electropolymerization of acrylic acid on stainless steel for improved adhesion properties*, A González-Orive, D Meinderink, F. Sahin, HC Schmidt, W Homberg, G Grundmeier (**05.09.2018 - 07.09.2018**)
2. 70th Annual Meeting of the International Society of Electrochemistry (ISE), *Electrografting of Acrylic Acid on Steel for Enhanced Adhesion Properties*, A. González-Orive, D. Meinderink, F. Sahin, J. C. Calderón-Gómez, G. Grundmeier (**04.08 - 09.08.2019**)
3. Verhandlungen der Deutschen Physikalischen Gesellschaft e.V. (DPG-Verhandlungen), *Atomic Resolution Differential Phase Contrast STEM investigations of electric fields in ZnO nanostructures*, Julius Bürger, Julia Weiß, Dennis Meinderink, Katja Engelkemeier, Wolfgang Bremser, Guido Grundmeier, Mirko Schaper, Jörg K. N. Lindner (**31.03 – 06.04.2019**)
4. The Annual Congress of the European Federation of Corrosion (EUROCORR), Richard Grothe, Dennis Meinderink, Jan Striewe, Jannik Kowatz, Thomas Tröster, Gerson Meschut, Guido Grundmeier (**09.09 - 13.09.2019**)

8 Attachment

8.1 List of figures

Figure 1. Illustration of the fundamental understanding of interfacial adhesion science resembling different macroscopic and molecular phenomena depending on the wide length scale and time scales of interfacial processes.	1
Figure 2. Schematic illustration of join partners with matched surface pre-treatments (orange) and coated with a resin (green) for a possible bonding to other materials.....	4
Figure 3. Schematic model of the hexagonal (indicated with blue lines and blue dashed lines) crystal wurtzite structure (based on Noei et al. ⁵⁴).	6
Figure 4. Schematic demonstration of the bridging between the microscopic, molecular interfacial adhesion processes and the macroscopic adhesion theory and praxis. Closing the gap between these two differently scaled “worlds” is necessary for optimized long-term constructions.....	15
Figure 5. Theoretical mechanism theories for adhesion (based on the text published by Ebnesajjad ¹¹⁸).	15
Figure 6. One possible classification of basic adhesion mechanisms and binding forces	16
Figure 7. “Lennard-Jones potential“ (based on Kendall ²⁶).	17
Figure 8. Principal structure of the electric double layer based on the Stern model (adapted from Butt et al. including literature in there ¹⁵).	21
Figure 9. Schematic summary of orbital interactions - left side: interactions in discrete molecules, right side: molecule-surface orbital interactions (based on Hoffmann et al. ¹²⁹ including literature in there).	29
Figure 10. Schematic illustration of equilibrium reactions at different pH values ranging from alkaline values to acidic pH values for an ideal polar ZnO(0001)-Zn surface (based on Valtiner et al. ^{27,62–64}).	31
Figure 11. Schematic demonstration of deposited polymers on metallic substrates. The images in A) show physisorbed polymers: 1) diblock copolymer where one block strongly adsorbs on the passive layer, 2) homopolymer interacting with the passive layer. The grafted polymers in the images in B) show the “mushroom” like state in 3) and in 4) the “brush” state is illustrated. Both situations in B) could be generated via a “direct coupling reaction” or a “graft polymerization” with monomers (images adapted from and based on Butt et al. ¹⁵ and from Uyama et al. ¹⁸⁴ including literature in there).	37
Figure 12. Basic illustration of an experimental spray-coating setup.	39
Figure 13. Schematic illustration of the photo effect releasing one photoelectron from inner core shell 2s excited by X-ray radiation (based on Sabbatini et al. ²²⁷).	42

Figure 14. Illustration of the geometrical pathway of the X-radiation and the emitted photoelectrons from a metallic substrate (based on Bluhm ²³⁰ and Sabbatini et al. ²²⁷ including literature in there).	43
Figure 15. Basically construction of an conventional Michelson interferometer (based on Günzler, Gremlich ²³⁵ including literature in there).	45
Figure 16. Schematic illustration of the application of infrared reflection absorption spectroscopy (IRRAS) on a metallic sample with a coating (based on Grundmeier et al. ²³⁶ including literature in there).	46
Figure 17. Schematic illustration of reflected infrared radiation with decomposition of the electric field vector (based on Grundmeier et al. ²³⁶ including literature in there).	47
Figure 18. Schematic construction of the main elements in a typical scanning electron microscope (based on Egerton et al. ²⁴⁰ including literature in there).	49
Figure 19. Schematic illustration of secondary ions fabricated by collisional process with primary particle (based on Vickerman and Briggs ²⁴² including literature in there).	50
Figure 20. Schematic illustration of surface tension and contact angle (adapted from Habenicht ¹¹⁹ and Butt et al. ¹⁵ including literature in there).	51
Figure 21. Schematic image of the experimental setup of an atomic force microscopy (AFM) (based on the poster presentation at the ICAS conference in Pisa in 2019 and on Butt et al. ¹⁵ including literature in there).	52
Figure 22. Combination of sensitivity and spring constant with law of Hook for the generation of final units. The result is a force in nN versus distance in μm curves, for example (based on the own poster presentation at the ICAS conference in Pisa in 2019).	56
Figure 23. Schematic illustration of the explanation of rupture events in force distance curves in single molecules force spectroscopy (based on Lee et al. ²⁸⁰ and Bizzarri et al. ²⁸¹ including literature in there).	57
Figure 24. Schematic image of the measurement principle of a peel-test (based on Crocombe and Adams ³⁰⁴ including literature in there).	61
Figure 25. Schematic image of a simple shear test (left side, based on G'Sell et al. ³⁰⁶ including literature in there) and the used approach in the 3. publication ⁵³ of this thesis (right side).	62
Figure 26. Schematic illustration of interfacial breakage in the PAA layer by reaching a critical PAA thickness.	159
Figure 27. Illustration of the interfacial region of the poly(propylene)-poly(propylene) foil sandwich. Both foils were oxidized in an oxygen plasma and one of them was spray coated with a ZnO tetrapod/PAA dispersion.	160

8.2 List of tables

Table 1. Summary of the parameters containing in the Bell-Evans theory.....	60
Table 2. Summary of the author contributions involved in the publication “ <i>Dependence of Poly(acrylic acid) Interfacial Adhesion on the Nanostructure of Electrodeposited ZnO Films</i> ”.	67
Table 3. Summary of the author contributions involved in the publication “ <i>Effect of PAA-induced surface etching on the adhesion properties of ZnO nanostructured films</i> ”.	107
Table 4. Summary of the author contributions involved in the publication “ <i>Electrodeposition of poly(acrylic acid) on stainless steel with enhanced adhesion properties</i> ”.	126
Table 5. Summary of the author contributions involved in the publication “ <i>Spray coating of poly(acrylic acid)/ZnO tetrapod adhesion promoting nanocomposite films for polymer laminates</i> ”.	134

8.3 List of abbreviations and acronyms

PAA	poly(acrylic acid)
AA	acrylic acid
ZnO	zinc oxide
PP	poly(propylene)
HDG	hot dipped galvanized steel
ODT	<i>1</i> -octadecanethiol
ODS	octadecyltriethoxysilane
-OH	hydroxyl group
APPA	3-aminopropylphosphonic acid
FTIR	<i>Fourier-transformed infrared spectroscopy</i>
AR-HR-XPS	Angle-Resolved High-Resolution X-ray Photoelectron Spectroscopy
PEO-PPO-PEO	poly(ethylene oxide)-poly(propylene oxide)-poly(ethylene oxide)
ZnO TP	zinc oxide tetrapods
HMTA	hexamethylenetetramine
LbL	Layer-by-Layer
EDL	electric double layer
IHP	inner Helmholtz plane
OHP	outer Helmholtz plane
IEP	isoelectric point
PZC	Point of zero charge
DLVO	from Derjaguin, Landau, Verwey, Overbeek
m-rd	monopole-rotating dipole
rd-rd	two rotating dipoles
id	induced dipole
m-id	monopole-induced
surf	surface
HSAB	Hard-Soft Acid-Base principle
HOMO	highest occupied molecule orbital
LUMO	lowest occupied molecule orbital
D-Ala-D-Ala	D-alanyl-D-alanine
UV	ultraviolet
AFM	atomic force microscopy
XPS	X-ray photoelectron spectroscopy
FT-IRRAS	Fourier-transformed infrared reflection absorption spectroscopy

IRRAS	infrared reflection absorption spectroscopy
SCS	single channel spectrum
FT	Fourier-Transformation
PM-FT-IRRAS	Polarization-modulated Fourier-transformed infrared reflection absorption spectroscopy
IR	infrared
PEM	photoelastic modulator
ZnS	zinc selenite
CCD	charge-coupled device
SEM	scanning electron microscope
FIB	focused ion beam
TEM	transmission electron microscopy
FE	field-emission
PE	primary electron
SE	secondary electrons
BSE	back scattered electrons
TE	transmitted, diffracted electrons
EDX	energy disperse microscopy X-ray spectroscopy
ToF-SIMS	time-of-flight secondary ion mass spectroscopy
SFA	surface force apparatus
CFM	chemical force microscopy
CFS	colloidal force spectroscopy
SMFS	single molecule force spectroscopy
SAM	self-assembled monolayer
SWNTs	single-walled carbon nanotubes
A β 40	amyloid- β 1-40 fibrils
FIB	focused ion beam
EDA	ethylenediamine
S-NHS	<i>N</i> -Hydroxysulfonosuccinimide sodium salt
EDC hydrochloride	<i>N</i> -(3-(dimethylamino)propyl)- <i>N'</i> -ethylcarbodiimide
PLE	poly(<i>L</i> -glutamic acid)
DOPA	3,4-dihydroxyphenylalanine
DNA	deoxyribonucleic acid
WLC	worm-like chain

8.4 Documentation of experimental details and approaches

According to the requirements for a cumulative PhD thesis at the Paderborn University (Department of Science), this chapter lists all experimental details, analytical methods and advanced approaches used and mentioned in the selected four peer-reviewed publications in this PhD thesis:

1. D. Meinderink, A. G. Orive, S. Ewertowski, I. Giner and G. Grundmeier, *Dependence of Poly(acrylic acid) Interfacial Adhesion on the Nanostructure of Electrodeposited ZnO Films* with permission from American Chemical Society (ACS) Appl. Nano Mater. **2019**, 2, 831-843 (Copyright 2019 American Chemical Society) with permission from American Chemical Society.
<https://pubs.acs.org/doi/10.1021/acsanm.8b02091>
2. D. Meinderink, C. Kielar, O. Sobol, L. Ruhm, F. Rieker, K. Nolkemper, A. G. Orive, O. Ozcan, Guido Grundmeier, *Effect of PAA-induced surface etching on the adhesion properties of ZnO nanostructured films*, International Journal of Adhesion and Adhesives 106 (**2021**) 102812 (Copyright Elsevier 2021) with permission from Elsevier.
<https://doi.org/10.1016/j.ijadhadh.2021.102812>
3. D. Meinderink, A. G. Orive, G. Grundmeier, *Electrodeposition of poly(acrylic acid) on stainless steel with enhanced adhesion properties* from Surface and Interface Analysis, Volume 50 (**2018**) on pages 1224-1229 (Copyright Wiley & Sons, Ltd. 2018) with permission from Wiley & Sons, Ltd. (License Numbers 4731840123016, 4987720158233)
<https://doi.org/10.1002/sia.6440>
4. Dennis Meinderink, Karlo J.R. Nolkemper, Julius Bürger, Alejandro G. Orive, Jörg K.N. Lindner, Guido Grundmeier, *Spray coating of poly(acrylic acid)/ZnO tetrapod adhesion promoting nanocomposite films for polymer laminates* in Surface and Coatings Technology 375 (**2019**) 112-122. (Copyright Elsevier 2019) with permission from Elsevier.
<https://doi.org/10.1016/j.surfcoat.2019.06.083>

8.4.1 Dependence of Poly(acrylic acid) Interfacial Adhesion on the Nanostructure of Electrodeposited ZnO Films

The text elements presented below are available in the publication (embedded as **1. Publication** in this PhD thesis): D. Meinderink, A. G. Orive, S. Ewertowski, I. Giner and G. Grundmeier with the title “*Dependence of Poly(acrylic acid) Interfacial Adhesion on the Nanostructure of Electrodeposited ZnO Films*” Appl. Nano Mater. 2019, 2, 831-843 (Copyright 2019 American Chemical Society) reused with permission from American Chemical Society (ACS). We acknowledge the American Chemical Society for the permission of reusing and embedding this publication in this PhD thesis: <https://pubs.acs.org/doi/10.1021/acsanm.8b02091>

Materials, chemicals and sample preparations (based on 1. publication of this PhD thesis):

- Preconditioning of stainless steel samples for SMFS measurements:
 - mirror polished stainless steel foil (type 1.4301, X5CrNi18-10, supplied by Thyssen Krupp SE)
 - coated with Al foil before cutting with guillotine shears into 2 x 2 cm² pieces
 - consecutively solvent cleaning steps in ultrasonic bath for 15 min for each step: tetrahydrofuran (p.a. grade, stabilized, supplied by Merck KGaA, Darmstadt, Germany), isopropanol (p.a. grade, supplied by Merck KGaA, Darmstadt, Germany) and ethanol (p.a. grade, supplied by Merck KGaA, Darmstadt, Germany) and dried in a nitrogen stream (99.999 %, supplied by Linde Gas AG, Germany)
 - plasma cleaning for removing organic contaminations: in pure oxygen (99.999 %, supplied by Linde Gas AG, Germany) atmosphere for 1 min at a pressure lower than 0.4 mbar with a volume speed of oxygen higher than 40 l/h
 - immersion into aqueous 2 mM NaClO₄ (98+%, Sigma-Aldrich, pH 7 adjusted with 0.1 M NaOH) for 72 h, rinsed with water and dried in a nitrogen stream before usage in SMFS experiments
- electrochemical deposition of ZnO films:
 - samples after solvent cleaning (without plasma cleaning)
 - cathodic deposition in aqueous 0.01 M HMTA and 0.01 M Zn(NO₃)₂·6 H₂O at 80 °C ± 3 °C for 900 s at -0.5 mA/cm² using a Reference 600 potentiostat (Gamry Instruments) (zinc nitrate precursor and HMTA solutions were freshly merged before usage in the three electrode setup)
 - electrodes:
 - reference: Ag/AgCl (saturated with KCl) connected to a salt bridge (filled with aqueous 0.1 M NaNO₃ solution) with a glass frit (model G0300 4 mm, AMETEK GmbH, Meerbusch, Germany)
 - working: 2 x 6 cm² cut stainless steel type 1.4301, X5CrNi18-10, supplied by Thyssen Krupp SE) samples, coated with isolating tape to form a total area of 2 x 2 cm²
 - counter electrode: cylindrical tube made of stainless steel (type 1.4301, supplied by Ullner u. Ullner GmbH, Paderborn, Germany)
 - after deposition, the samples were rinsed with ultrapure water (0.055 µS/cm, Ultra Clear TWF, SG water, Hamburg, Germany) and dried in nitrogen stream
- AFM tip preparation:
 - used cantilevers: gold-coated Si cantilevers (HQ:CSC17/Cr-Au, MikroMash, 10-17 kHz, 0.2 N/m) without further cleaning steps

- 1. functionalization step: immersion into aqueous 0.05 mmol HS-PEG-NH₂ x HCl (10.000 Da, Rapp Polymere GmbH, Germany) for 5.25 h at room temperature without stirring in ultrapure water (0.055 µS/cm, Ultra Clear TWF, SG water, Hamburg, Germany)
- dipping 3 times in ultrapure water before switching into the next solution
- 2. functionalization step:
 - stock solution: solving 26 mmol *N*-Hydroxysulfonosuccinimide sodium salt (S-NHS, Sigma-Aldrich) with 96 mmol *N*-(3-(dimethylamino)propyl)-*N'*-ethylcarbodiimide hydrochloride (EDC hydrochloride; ≥98%, 75 mg, 96 mmol; Sigma-Aldrich) in 5 ml of 4-(2-hydroxyethyl)-1-piperazineethanesulfonic acid buffer (HEPES, high-purity grade, Amresco, USA; 10 mM; pH tuned to 7.1 with NaOH solution)
 - 100 µl of the stock solution were added to an aqueous 10 ml PAA solution (5 g/l, 450.000 g/mol, Sigma-Aldrich) in 10 mM HEPES buffer solution – shaken gently for 1 min
 - -NH₂-functionalized cantilevers were immersed into the latter solution for 90 min at room temperature without stirring
- cleaning and storage: dipping 3 times in ultrapure water before immersing into aqueous 1 mM EDTA solution overnight (~ 12 h), then in ultrapure water for ~6 h followed by the storage in aqueous 100 mM EDTA solution
- Si wafers cut into 1 cm x 1 cm pieces coated with around 200 nm - 300 nm gold deposited via PVD (rinsed with EtOH and dried in nitrogen stream) were used for analytical characterizations after the two functionalization steps

Analytical methods (based on 1. publication of this PhD thesis):

1. FE-SEM (NEON 40 FE-SEM, Carl Zeiss SMT AG, Germany) for high-resolution SEM images (base pressure lower than $10.0 \cdot 10^{-5}$ mbar, InLens and SE2 detectors, tilt angle 0 °, EHT 2.00 kV, different magnifications)
2. PM-IRRAS (Vertex 70, with ZnSe photo-elastic modulator PMA50, Bruker, Germany) with a resolution of 4 cm^{-1} at an angle of 80 ° with respect to the surface normal, 50 kHz modulation, LN-MCT detector, 1024 scans with 1x amplifications
3. AR-XPS (ESCA+ setup, Omicron NanoTechnology, Germany) with a base pressure lower than $5.0 \cdot 10^{-10}$ mbar, monochromatic Al-K α irradiation source (1486.7 eV), 60 ° with respect to the surface plane for the ZnO films and 20 ° and 80 ° with respect to the surface plane for the stainless steel samples, 0.05 eV step size and a pass energy of 20 eV (100 eV pass energy)

for survey spectra) were set. Evaluations were performed with CASA-XPS software (Casa Software Ltd., Teigmouth, UK). Internal calibration to C 1s peak: 285.0 eV

4. SMFS was performed with a JPK Nano-Wizard III AFM (JPK Instruments, Germany) in the force-volume mapping contact mode. Further details:

- first approach in dry conditions with 0.5 $\mu\text{m/s}$ extend speed in z-direction with a set point of 100 mV (around 2.0 nN after cantilever calibration)
- commercial electrochemical cell (JPK Instruments) in 2 mM NaClO_4 (pH 7 adjusted with 0.1 M NaOH)
- temperature 298 K measured at the sample in the electrolyte., The temperature at the tip was estimated to be 301 K due to the heating of the laser.
- constant flow rate of around 2.24 ml/min at the initial filling step, and 0.52 ml/min while performing the SMFS
- mapping approaches were done with a deflection setpoint of 4.0 nN
- 256 force-distance curves (map area: 2 x 2 μm^2 with 16 x 16 pixels) were collected at different positions of distinct but equally treated samples with different cantilevers prepared under similar experimental conditions to have comparable results to built up statistical consequences
- evaluations of the force-distance curves were done with the JPK data-processing software

8.4.2 Effect of PAA-induced surface etching on the adhesion properties of ZnO nanostructured films

The text elements presented below are available in the publication (embedded as **2. publication** in this PhD thesis): *D. Meinderink, C. Kielar, O. Sobol, L. Ruhm, F. Rieker, K. Nolkemper, A. G. Orive, O. Ozcan, Guido Grundmeier, International Journal of Adhesion and Adhesives 106 (2021) 102812* (Copyright Elsevier 2021) with permission from Elsevier for reuse and embedding this article in this PhD thesis. We acknowledge Elsevier for the permission of reusing this publication: <https://doi.org/10.1016/j.ijadhadh.2021.102812>

Materials, chemicals and sample preparations (based on 2. publication of this PhD thesis):

- solvent cleaning: “skin passed hot-dip galvanised steel substrates (supplied by Chemetall GmbH, Frankfurt, Germany) temporary coated with Al foil were cut to 2.0 cm x 4.5 cm size and subsequently cleaned in tetrahydrofuran (THF) (Merck, Darmstadt, Germany), isopropanol (IsOH) (Merck, Darmstadt, Germany) and ethanol (EtOH) (UN 1170 ethanol provided by Martin und Werner Mundo oHG, Mainz-Kostheim, Germany) after removing Al

foil for 15 min in an ultrasonic bath to remove the protective oil.”³¹⁶ (adapted from **2. publication**)

- “Gardo”-cleaning: solvent cleaned samples (SC) were then immersed in an alkaline cleaning solution (30 g/l Gardoclean S5176 and 5 g/l Additive H7376/1; provided by Chemetall GmbH, Frankfurt, Germany) under stirring at 55 °C for one minute.
- water: for all experiments in this work, de-ionized water ($< 0.075 \mu\text{S/cm}$ conductivity, Ultra Clear TWF, SG Water, Hamburg, Germany) was used.
- ZnO film deposition: “ZnO nanorod (ZnO NR) growth was performed by immersing the substrates in an aqueous solution of 25 mM zinc nitrate, $\text{Zn}(\text{NO}_3)_2 \cdot 6 \text{H}_2\text{O}$ (zinc nitrate hexahydrate, 98 % extra pure, ACROS Organics) and 25 mM hexamethylenetetramine $\text{C}_6\text{H}_{12}\text{N}_4$ (HMTA, AnaLaR NORMAPUR®, VWR Chemicals) for 30 min at 90 °C ($\pm 5^\circ\text{C}$) followed by directly rinsing with de-ionized water. The continuous ZnO nanocrystalline morphology (ZnO NC) was achieved by addition of 0.12 mM sodium citrate (sodium citrate dehydrate, ACS, 99.0%, ABCR GmbH & Co. KG, Karlsruhe, Germany) to an aqueous deposition bath consisting of 50 mM $\text{Zn}(\text{NO}_3)_2 \cdot 6 \text{H}_2\text{O}$ and 43 mM HMTA in this case. The deposition time was also 30 min at 90 °C ($\pm 5^\circ\text{C}$).”³¹⁶ (adapted from **2. publication**)
- PAA immersion solutions: “PAA adsorption was carried out by immersion of the substrates for 10 minutes in an aqueous 2.6 g/l PAA solution (poly(acrylic acid); $M_w \sim 250.000$, 35 wt. % in H_2O , Sigma Aldrich, Germany) with a final concentration of 3.64 μM PAA solution at 23 °C ($\pm 2^\circ\text{C}$) with a pH 7 (adjusted with solid NaOH) without stirring, followed by rinsing with milli-pure water and drying in a stream of nitrogen. At this pH value the PAA chains should be deprotonated ($\text{pK}_a = 4.7$) in the solution and mainly carboxylate groups ($-\text{COO}^-$) of the weak acid are present.”³¹⁶ (adapted from **2. publication**)
- 90°-Peel-Tests: “a hot-curing two component epoxy-amine resin (11.19 g epoxy resin, a diglycidyl ether of bisphenol A (D.E.R 331, DOW Chemicals, USA) and 6.78 g amine hardener (poly(propylene glycol) bis(2-aminopropyl ether), Sigma-Aldrich)) was employed as model adhesive and applied on the substrates after mixing and degassing. To control the thickness of the adhesive films the samples were coated with 4 commercial adhesive tapes (1 layer of Scotch Magic™ Tape, supplied by 3M, Germany, and 3 layers of Tesafilm, supplied by tesafilm®, Germany). An aluminum foil was used to form the sandwich geometry, which was removed after the hardening step to obtain an open polymer film. Before the application of the liquid adhesive the samples were stored in a glove box (filled with a mixture of dry air and nitrogen) with controlled relative humidity ($6.0 \% \pm 3.0 \%$) at room temperature ($21.5^\circ\text{C} \pm 1.0^\circ\text{C}$) for 15 min (± 5 min) to remove the most adsorbed water layers from the atmosphere. The completed sandwich geometry was kept under these conditions for 15 min (± 5 min) to be sure that all pores are filled with liquid adhesive before curing step (120 °C for 75 min). To

investigate the wet de-adhesion process the samples were exposed to humid atmosphere ($> 95\%$ r.h.) at $40\text{ }^{\circ}\text{C}$ for 24 h ($\pm 1\text{ h}$) before the peel-test measurements. Peel-tests have been performed at a constant perpendicular angle to the sample surface with 1 mm/min velocity using a force gauge (model ZP-5, Imada, Tokyo, Japan) and a motorized peel-tester (MV-220 Motorized Test Stand, Imada, Tokyo, Japan) at $> 95\%$ relative humidity at room temperature ($21.5 \pm 2.0\text{ }^{\circ}\text{C}$). At least 3 different samples prepared under equal experimental conditions with 3-4 released adhesive stripes per sample gives a sufficient statistic accuracy with at least 11 stripes under each condition used for the evaluation of the adhesion properties after the different surface treatments. The film thicknesses of the applied model adhesives were measured with a DUALSCOPE® FMP20 (magnetoinductive and eddy current method, Helmut Fischer GmbH, Germany) at five different positions on five different coated samples. Before the measurements the equipment was calibrated with defined foils provided by the supplier of the measurement equipment. The resulted mean averaged value of the total epoxy-amine adhesive films is $150\text{ }\mu\text{m}$ ($\pm 19\text{ }\mu\text{m}$).^{”316} (adapted from **2. publication**)

Analytical methods (based on **2. publication of this PhD thesis**):

1. **FE-SEM**: “morphological characterization of ZnO films and peeled adhesive surfaces was performed by means of a field-emission scanning electron microscope (NEON® 40 FE-SEM, Carl Zeiss SMT AG, Germany) using an InLens detector; base pressure lower than $10.0 \cdot 10^{-5}\text{ mbar}$, InLens and SE2 detectors, tilt angle 0° , EHT 2.00 kV , different magnifications). Some samples were milled with a focused ion beam (FIB) system (NEON® 40 FE-SEM, Carl Zeiss SMT AG, Germany) with a Ga liquid ion source (LMIS). In all FIB procedures a current of 50 pA and a beam of 30 keV were used. Prior to the measurements of polymeric films, 3 nm Au/Pd (80 wt\% Au , 20 wt\% Pd) thick sputter coatings were deposited.”³¹⁶ (adapted from **2. publication**)
2. **DRIFTS**: “for the identification of adsorbed PAA on SC, ZnO NR and ZnO NC films DRIFT measurements were done with a Vertex 70 spectrometer (Bruker Optics, Germany). A gold sample (300 nm gold deposited via PVD on silicon wafer (100)) was measured as a reference. A resolution of 4 cm^{-1} , 512 scans for each sample, and a LN-MCT detector were used.”³¹⁶ (adapted from **2. publication**)
3. **XPS** was performed in an ESCA+ setup (Omicron NanoTechnology, Germany). A monochromatic Al-K α irradiation source (1486.7 eV) and an angle of 30° with respect to the surface plane were used for all measurements. The base pressure was lower than $3.0 \cdot 10^{-10}\text{ mbar}$ and neutralization in the case of the polymer films after peel-tests was used. For the detection, a multichannel plate detector (Omicron Argus, Germany) was used. A convolution of a Gauss (30%) and Lorentzian (70%) shape was chosen (Shirley background) in the CASA-XPS

software (Casa Software Ltd., Teignmouth, UK) for peak fittings and the C 1s peak at position 285.0 eV was set as internal calibration.”³¹⁶ (adapted from **2. publication**)

4. “ToF-SIMS measurements were performed using a ToF-SIMS IV (IONTOF GmbH, Münster, Germany) equipped with a 25 keV BiMn liquid metal ion gun (LMIG). For the identification of PAA, spectra were acquired upon negative polarity. All measurements were performed using the spectrometry mode (high current bunched mode - HCBU) to enable good mass resolution, on a region of 100 μm \times 100 μm . Analyses were conducted in the interlaced mode, allowing to couple the analysis process with a sputter process within the acquisition cycle. Sputtering was done using a 1 kV Ar beam and a sputtered area of a 300 μm \times 300 μm (where the analyzed area is in the center of the sputtered area). Ar was selected as a sputter species to remove surface contaminations without obtaining a significant influence on the secondary ion yield. As control, SC and ZnO NC samples were spray-coated with the same PAA solution (3.64 μM PAA (250.000 g/mol) in water at pH 7 adjusted with solid NaOH) and analyzed via ToF-SIMS. The spray coating process of aqueous PAA solutions has been described elsewhere. A commercial spray coater (ND-SP 11/4 Precision Spray Coater, Nadetech Innovations S.L., Spain) with an installed hot-plate was used. The motor speed was fixed at 1200 mm/min. A volume speed of 200 ml/h, a nozzle distance to the substrate surface of 12 cm, an operating temperature of 75 °C and 4.0 bar pressure of nitrogen (99.999 %, supplied by Linde Gas AG, Germany) were selected in the equipment.”³¹⁶ (adapted from **2. publication**)

8.4.3 Electrodeposition of poly(acrylic acid) on stainless steel with enhanced adhesion properties

The text elements presented below are available in the publication (embedded as **3. publication** in this PhD thesis): *D. Meinderink, A. G. Orive, G. Grundmeier, Surface and Interface Analysis, Volume 50, pages 1224-1229* (Copyright Wiley & Sons, Ltd. 2018) with permission for reuse from Wiley & Sons, Ltd. (License Numbers 4731840123016, 4987720158233).

We acknowledge Wiley & Sons, Ltd. for the permission of reusing this publication:
<https://doi.org/10.1002/sia.6440>

Materials, chemicals and sample preparations (based on **3. publication of this PhD thesis**):

- water: de-ionized water (< 0.075 $\mu\text{S/cm}$ conductivity, Ultra Clear TWF, SG Water, Hamburg, Germany)
- substrate: polished stainless steel (ASIS 316L, Goodfellow GmbH, Germany) coated with protection foil, cut into 3.0 x 4.5 cm^2 pieces
- solvent cleaning: subsequently cleaned in tetrahydrofuran (THF) (Merck, Darmstadt, Germany), isopropanol (IsOH) (Merck, Darmstadt, Germany) and ethanol (EtOH) (UN 1170

ethanol provided by Martin und Werner Mundo oHG, Mainz-Kostheim, Germany) each step for 15 min in an ultrasonic bath, followed by drying in a nitrogen stream

- coating with isolating tape to have defined areas for the working electrode
- electrochemical initiated polymerization: “A typical 3-electrode setup with a potassium chloride saturated silver/silver chloride as reference electrode, the stainless steel substrates as working electrode (6.0 cm² front side, backside was taped), and a closely coiled platinum wire (219.9 cm²) in a lugging filled with an aqueous 0.025 M H₂SO₄ solution, was used. The 75 ml water-based electrolyte for each deposition experiment consisted of 2.0 M acrylic acid (monomer) with methoxyphenone (inhibitor) (Sigma-Aldrich), 0.2 M zinc chloride (initiator) (Merck KGaA), and 0.04 M *N,N'*-methylenebisacrylamide (cross-linker) (Sigma-Aldrich). The pH of the resulting solution is raised to 6.0 by adding solid NaOH. Before every deposition, the electrolyte was purged with nitrogen for 15 minutes to create oxygen-free conditions. Otherwise, the reaction will be stopped as a consequence of the biradical character of oxygen because it reacts with the radical AA breaking off the electropolymerization. The atmosphere was purged during the reaction time. A potentiostat Reference 600™ (Gamry Instruments) was used to reach a constant potential of −1.15 V vs Ag/AgCl. In this regard, chronocoulometry measurements were performed to apply a well-defined bias voltage at the working electrode for 75, 100, 150, 225, and 300 seconds at room temperature. After the electrodeposition, samples were cleaned for 4 minutes in 100 ml of pure water and analyzed with Fourier transformed infrared reflection absorption spectroscopy (FT-IRRAS) and atomic force microscopy (AFM). To remove all zinc species embedded in the polymer, the modified stainless steel substrates were dipped in 100 ml of an aqueous 0.1 M HCl solution for 4 min. This step was followed by the characterization with PM-IRRAS and AFM measurements.”¹⁷⁵ (adapted from **3. publication**)
- Application of a model adhesive and peel test experiments: “a 2-component epoxy amine adhesive consists of 11.19 g epoxy resin (D.E.R. 331, DOW Chemicals, Midland/USA) and 6.78 g of the amine (poly(propylene glycol)bis(2-aminopropyl ether), Sigma-Aldrich). After mixing the 2 components, the polymer mix was degassed in vacuum ($<1.0 \times 10^{-2}$ mbar) for 1 hour. To remove all bubbles, the mixture was treated in ultrasonic bath for 15 minutes followed by another hour in vacuum for additional degassing. The poly(acrylic acid)-coated samples and untreated stainless steel samples taken as references were covered with 6 commercial adhesive tapes (1 layer of Scotch Magic™ Tape, supplied by 3M, Germany, and 5 layers of Tesafilm, supplied by tesafilm®, Germany) of around 300-μm thickness to create well-defined spacers for the application of the epoxy amine mix between the tapes. The coating step was carried out in a dry nitrogen atmosphere (7.0% ± 2.0% r.h.) at 19°C ± 1°C. The

samples were put on Polytetrafluoroethylene blocks coated with aluminum foil and fixed with a constant pressure with clamps. This was followed by the hardening step at 120°C for 75 minutes in the oven. Then, the samples were subsequently exposed for 72 hours at 40°C to humid air (>95% RH). The freestanding model adhesive films were cut into stripes, and the 90° pull-off forces (force gauge of type Model ZP-5, Imada) were recorded from each stripe. To maintain the peel-off angle, a motorized peel tester (MV-220 Motorized Test Stand, Imada) with a constant haul-off speed of 1 mm second⁻¹ was used.¹⁷⁵ (adapted from **3. publication**)

Analytical methods (based on **3. publication of this PhD thesis**):

1. **IRRAS**: FT-IR microscope of type Hyperion 1000 connected to a Vertex 70 spectrometer (both Bruker Optics, Germany), 4 cm⁻¹ resolution, 512 scans, LN-MCT detector, with 1x amplifications
2. **PM-IRRAS**: equal to settings above
3. **AFM**: MFP-3D-SA (Asylum Research) equipped with an antivibration table and an acoustic enclosure in intermittent contact mode operating in ambient air conditions at a scan rate of 0.5 to 1.2 Hz. To this end, HQ:NSC15/AIBS (325 kHz and 40 N m⁻¹, nominal radius of 8 nm) and HQ:NSC18/AIBS tips (75 kHz and 2.8 N m⁻¹, nominal radius of 8 nm), purchased from Mikromasch, were used. Root mean square (RMS) roughness measurements, R_q, from at least 3 10 × 10 μm² AFM images taken from different but equivalent sample areas for every deposition time have been collected and averaged.

8.4.4 Spray coating of poly(acrylic acid)/ZnO tetrapod adhesion promoting nanocomposite films for polymer laminates

The text elements presented below are available in the publication (embedded as **4. publication** in this PhD thesis): *Dennis Meinderink, Karlo J.R. Nolkemper, Julius Bürger, Alejandro G. Orive, Jörg K.N. Lindner, Guido Grundmeier, Surface and Coatings Technology 375 (2019) 112-122* (Copyright Elsevier 2019) with permission from Elsevier for reuse and embedding this article in this PhD thesis. We acknowledge Elsevier for the permission of reusing this publication:

<https://doi.org/10.1016/j.surfcoat.2019.06.083>

Materials, chemicals and sample preparations (based on **4. publication of this PhD thesis**):

- **ZnO TP synthesis**:
 - quartz tube of 1200 mm length with an outer diameter of 34 mm
 - a conical SiO₂ tube (28mm and 5mm inner diameters) inside the quartz tube for the collection of the solid products

- before synthesis: heating up to 900 °C in nitrogen atmosphere (purging for 10 min with a volume speed of 16 l/h – removing water and oxygen)
- starting synthesis:
 - zinc powder (1.6 g, Riedel-de Haën, fine powder, for analysis) placed in an Al oxide vessel was placed in the center of the tube oven under nitrogen flow
 - oxygen flow: 1.6 l/h \pm 0.5 l/h with nitrogen flow of 6.0 l/h \pm 0.5 l/h
 - reaction time: 30 min (stopping gas flows, cooling down over night in nitrogen atmosphere)
- fluffy colorless powder (ZnO TP) can be collected at the end of the smaller glass tube
- pretreatments of the poly(propylene) (PP) foil:
 - poly(propylene) foil (thickness 0.1 mm, homopolymer, Goodfellow, England) was cut into 1 cm \times 4 cm pieces with a scalpel
 - substrates were placed in a sample holder with ethanol (UN 1170 ethanol provided by Martin und Werner Mundo oHG, Mainz-Kostheim, Germany) and cleaned in ultrasonic bath for 15 min
 - rinsing with ethanol and dried in nitrogen
 - plasma activation of PP foils:
 - performed directly before usage
 - Plasma Cleaner Setup (Plasma Surface Technology, Diener electronic GmbH, Germany) under pure oxygen with constant pressure controlled by the volume flux of oxygen (p \sim 0.34 mbar) for 1 min
- aqueous dispersions for spray coating process:
 - 0.085 mM poly(acrylic acid) (PAA) (from 250.000 g/mol, 35 wt% in H₂O, Sigma Aldrich) dissolved in ultrapure water, adjusted pH to 7 with solid NaOH pellets (Merck Millipore, Germany)
 - ZnO TP powders were added: 8 mg/ml (resulting in a pH of 8.8 \pm 0.2), 16 mg/ml (resulting in a pH of 8.6 \pm 0.2)
 - Stirring for 10 min at 150 rpm (50 ml of the dispersions)
 - loading into syringes for the spray coater – shaken shortly before usage
- spray coating:
 - conventional spray coater (ND-SP 11/4 Precision Spray Coater, Nadetech Innovations S.L., Spain) with a high viscosity liquid atomization spray nozzle (mini-atomized nozzle MMAE/MMA type, Nadetech Innovations S.L., Spain) made of 316 L stainless steel
 - mixture of water-based solution and nitrogen flow
 - spray parameters:

- 75 °C \pm 3 °C temperature (measured behind the substrate)
 - volume speed: 100 ml/min of PAA/ZnO TP dispersions
 - 10 cm distance between nozzle and substrate surface
 - 1200 mm/min nozzle speed (horizontal orientation while spray coating step)
 - pressure: 6.0 bar inlet, 3.50 bar at the nozzle (set in software)
 - cleaning before each spray coating step with ultrapure water
- samples were stored for 24 h in desiccator (filled with silica particles; pressure around 30 mbar)
- joining of two PP foils:
 - laboratory hydraulic press (CY-PCH-600D) with mirror polished stainless steel plates on both hotplates
 - 1 cm² joining/ overlapping area (counterparts were also plasma cleaned, except for the solvent cleaned samples)
 - hotplate temperatures: 65 °C \pm 0.5 °C
 - pressure while the joining: 0.5 MPa \pm 0.4 MPa (estimated variation)
 - application time: 30 s
 - number of samples: 7 resulting in a total area of 7 cm² in the equipment (0.5 MPa distributed to 7 cm²)
- shear strength tests:
 - exposure to 40 °C (\pm 2 °C) at high humidity (> 95 %) in a closed PMMA box for 48 h
 - shear strength tests were performed in a closed box with similar humidity conditions (24 °C \pm 2 °C, > 95 %) using a ZP recorder (force gauge of type Model ZP-5, Imada) with a movement speed of 1 mm/s while one side of the laminates were fixed on the ground plate

Analytical methods (based on 4. publication of this PhD thesis):

- FE-SEM: equal to the above-mentioned settings
- TEM: on a probe-side Cs-corrected JEOL JEM-ARM200F at an acceleration voltage of 200 kV, For TEM analysis a droplet of ZnO TP dispersed in isopropyl alcohol was placed on a carbon coated grid and dried. To analyze cracking behavior, a ZnO TP holding grid was first covered by a second grid (carbon side on top of carbon side). In a second step ZnO TP were ground by displacing the covering grid which leads to cracking of TPs
- XPS: equal to settings mentioned above
- Raman spectroscopy: InVia Renishaw Raman microscope (Renishaw, Germany) with a CCD detector, two lasers (532 nm and 785 nm) with corresponding gratings and filter and mirror systems; YAG-Laser (532 nm, 55mW max. power), 50 \times objective, precise power (measured

calibrated USB photodiode (DIN EN ISO 9001, THORLABS, Germany) was 6.16 mW, internal calibration: 520.0 cm^{-1} ($\pm 0.5 \text{ cm}^{-1}$) on silicon wafer

- static water contact angle: sessile drop method, contact angle system (OCA 15 plus, DataPhysics, Filderstadt, Germany) with the SCA20 Software (DataPhysics Instruments GmbH, Filderstadt, Germany) for calculating the contact angles with the Young-Laplace method, 5 μl ultrapure water drops at 3-5 different positions on at least 3 different batches resulting in 76 measurements for the plasma treated samples (different batches under similar experimental conditions)

Acknowledgements

Ich möchte mich ganz herzlich bei Herrn Professor Dr.-Ing. Guido Grundmeier für die vertrauensvolle Delegation aller herausfordernden Aufgabenstellungen im Rahmen meiner Tätigkeiten an Ihrem Lehrstuhl bedanken! Die wissenschaftlichen Diskussionen habe ich immer als sehr professionell und zielführend empfunden. Ihre fachliche Förderung und die verschiedenen Aufgaben im Zusammenhang mit dieser Dissertation haben fortschrittlich zum Erfolg der Arbeiten beigetragen. Auch für die Übertragung insbesondere von verschiedenen Lehrtätigkeiten im Rahmen von Übungen, Praktikumsbetreuungen und dem Fortbildungsbeitrag am IFAM in Bremen möchte ich mich bei Ihnen bedanken. Dies hat mich sowohl fachlich, als auch in meiner Persönlichkeit sehr gestärkt. Die Ermöglichung zur Präsentation von unseren Ergebnissen auf Tagungen und internationalen Konferenzen war eine spannende Abwechslung vom Alltagsgeschäft im Büro und Labor. Vielen Dank!

Herrn Prof. Dr. Wolfgang Bremser, Frau Prof. Dr. Sabine Fechner und Herrn PD Dr. Hans Egold danke ich ganz herzlich für die freundlichen und unkomplizierten Annahmen zur Prüfungskommission.

Ein besonderes Dankeschön möchte ich Herrn Dr. Alejandro González Orive aussprechen. Thank you very much for all discussions, supports, revisions and improvements of our common works! ¡Muchas gracias!

Ich danke zudem allen Arbeitskollegen deren aller Aufzählung hier einen zu großen Rahmen einnehmen würde. Ich danke euch allen, insbesondere für die freundlichen, hilfsbereiten, unkomplizierten und angenehmen Umgangsweisen!

Vielen Dank auch an alle (ehemaligen) SHK's, WHB's und Abschlussarbeitsabsolvent(inn)en für die spannenden Diskussionen und das entgegengebrachte Vertrauen. Ihr habt alle klasse Arbeiten abgeliefert!

Ein großer Dank geht auch an alle Korrekturleser u.a. Herrn Dr. Daniel Pieper, Herrn Steffen Knust, Herrn Nicolas Sommer und Herrn Dr. Alejandro González Orive! Vielen Dank für eure Verbesserungsvorschläge und Korrekturen!

Zum Schluss möchte ich mich herzlichst bei meiner lieben Familie, meiner Freundin und meinen Freunden bedanken, die mir immer zugehört und mich jederzeit unterstützt haben. Ich danke euch!!